



UNIVERSIDAD
DE MÁLAGA

FACULTAD DE CIENCIAS

DEPARTAMENTO DE INGENIERÍA QUÍMICA

Tesis Doctoral

**ACOPLAMIENTO DE TECNOLOGÍAS DE POST-TRATAMIENTO PARA
EMISIONES CERO EN VEHÍCULOS AUTOMÓVILES LIGEROS**

**COUPLING OF AFTER-TREATMENT TECHNOLOGIES
FOR ZERO EMISSIONS IN LIGHT VEHICLES**

**Directoras M^a ÁNGELES LARRUBIA VARGAS
M^a CONCEPCIÓN HERRERA DELGADO**

Química Avanzada. Preparación y Caracterización de Materiales

MARINA CORTÉS REYES


Málaga, 2016





UNIVERSIDAD
DE MÁLAGA

AUTOR: Marina Cortés Reyes

 <http://orcid.org/0000-0002-7314-3673>

EDITA: Publicaciones y Divulgación Científica. Universidad de Málaga



Esta obra está bajo una licencia de Creative Commons Reconocimiento-NoComercial-SinObraDerivada 4.0 Internacional:

<http://creativecommons.org/licenses/by-nc-nd/4.0/legalcode>

Cualquier parte de esta obra se puede reproducir sin autorización pero con el reconocimiento y atribución de los autores.

No se puede hacer uso comercial de la obra y no se puede alterar, transformar o hacer obras derivadas.

Esta Tesis Doctoral está depositada en el Repositorio Institucional de la Universidad de Málaga (RIUMA): riuma.uma.es



ACOPLAMIENTO DE TECNOLOGÍAS DE POST-TRATAMIENTO PARA
EMISIONES CERO EN VEHÍCULOS AUTOMÓVILES LIGEROS

COUPLING OF AFTER-TREATMENT TECHNOLOGIES
FOR ZERO EMISSION IN LIGHT VEHICLES

Visado en Málaga, Noviembre 2016

MEMORIA DE TESIS presentada para obtener el grado de DOCTOR
en Ingeniería Química por la Universidad de Málaga



Fdo. Marina Cortés Reyes

DIRECTORAS



Dra. Mª Ángeles Larrubia Vargas
Catedrática Ingeniería Química



Dra. Mª Concepción Herrera Delgado
Profesora Titular Ingeniería Química



UNIVERSIDAD
DE MÁLAGA

M^a Ángeles Larrubia Vargas, Catedrática de Ingeniería Química de la Universidad de Málaga, y M^a Concepción Herrera Delgado, Profesora Titular de Ingeniería Química de la Universidad de Málaga

ACREDITAN que la presente Memoria de Tesis titulada “ACOPLAMIENTO DE TECNOLOGÍAS DE POST-TRATAMIENTO PARA EMISIONES CERO EN VEHÍCULOS AUTOMÓVILES LIGEROS-COUPLING OF AFTER-TREATMENT TECHNOLOGIES FOR ZERO EMISSION IN LIGHT VEHICLES” presentada por D^a. Marina Cortés Reyes, ha sido realizada bajo su dirección y reuniendo, a nuestro juicio, los requisitos necesarios para que su autora pueda aspirar al grado de DOCTOR, autorizan su presentación para su defensa en la Facultad de Ciencias de la Universidad de Málaga.

Para que así conste, firman el presente certificado en Málaga, a 3 de noviembre de 2016



Dra. M^a Ángeles Larrubia Vargas



Dra. M^a Concepción Herrera Delgado



UNIVERSIDAD
DE MÁLAGA

Agradecimientos

Me gustaría agradecer a todas las personas que me han acompañado a lo largo de la Tesis ya que, cada uno en su medida, me han aportado cosas valiosas que me han hecho evolucionar tanto en el terreno profesional como en el personal. Es difícil resumirlo en pocas líneas, pero espero que todo el que sienta que ha contribuido, sepa que le estoy agradecida.

En primer lugar quería agradecerse a mis directoras, M^a Ángeles Larrubia Vargas y Concepción Herrera Delgado, por la confianza que han depositado en mí durante todo este tiempo. En especial, a M^a Ángeles por su apoyo incondicional y su fuerza en momentos clave; a Conchi por estar siempre ahí. A Luis J. Alemany, por sus orientaciones, los conocimientos transmitidos y su grado de dedicación a mi formación. A todos los compañeros que han pasado por el Grupo de Investigación PROCAT durante estos años: Ana, Abraham, Bea, Carlos, Nacho, Paco, Rafa y Vane, por todos los buenos momentos que hemos pasado en el laboratorio y fuera de él; a Sandra y Marina por ser un motor en esta última etapa; a Fer por su ánimo y alegría constante; a Rocío, por ser la mejor compañera que se puede tener, excelente profesional y mejor persona; y a Antonio, fundamental tanto en el laboratorio como fuera de él, haciendo que lo complicado se vuelva más fácil, aportando siempre un rayo de luz en el camino.

A todo el personal de la Facultad de Ciencias y del SCAI que han contribuido al desarrollo de la Tesis. A las personas, como Mary y María, con las que he compartido la aventura de ser doctoranda. En especial a todos los componentes del Departamento de Ingeniería Química, a Pedro Díaz por su inestimable ayuda en los problemas de laboratorio, a M^a José por los trámites administrativos y a Gema, por mantener un ambiente agradable de trabajo.

A todos los miembros del Grupo de Investigación TQSA de la Universidad del País Vasco, en especial a D. Juan Ramón González Velasco, por permitirme realizar una estancia en sus laboratorios y aprender mucho en todas las ocasiones en las que hemos coincidido y a Beñat, por compartir las experiencias y conocimientos. A todos los becarios: Adriana, Ainara, Andoni, Cristina, Jon Ander, Jonatan, Maitane, Miren, Miryam y Unai, por integrarme como una más y hacerme vivir momentos inolvidables. Eskerrik asko!

Ringraziare il Prof. Dr. Luca Lietti (Politecnico di Milano) e tutti i suoi collaboratori, specialmente la Dra. Lidia Castoldi per la loro disponibilità e aiuta durante il mio soggiorno nei loro laboratori. Anche, a tutti i ragazzi: Laura, Angelo, Riccardo, Eugenio, Mateo e Silvia per i giorni di divertimento e lavoro. Grazie! Special thanks to Lukasz!

Ringraziare il Prof. Dr. Guido Busca della Università di Genova, per la sua sapienza e disponibilità, a Dra. Elisabetta Finocchio per la sua aiuta e dedizione al mio lavoro e a Gabriella per condividere momenti divertenti.

Al Ministerio de Educación, Cultura y Deporte por la financiación de la Tesis mediante el Programa de Formación de Profesorado Universitario (FPU12/03826). Al Ministerio de Ciencia e Innovación por el Proyecto CTQ2013-47853R. A las compañías Albemarle, Sasol, Degussa y Johnson Matthey, por el suministro de los materiales. A la ayuda de la Universidad de Málaga. Campus de Excelencia Internacional Andalucía Tech.

Por último quiero agradecerse a esas personas que aunque no te forman académicamente son el apoyo para que lo consigas y disfrutan con tus alegrías y se entristecen por tus penas, mi familia y mis amigos. Dentro de mis amigos quiero resaltar la fuerza y el ánimo que me han transmitido Ángela, Fernando, Pablo y Patrick. En mi familia, no tengo palabras para agradecerles a mis padres y a mi hermana todo lo que hacen por mí, sin su ayuda, sus orientaciones y su confianza no sería ni un ápice de la persona que soy, este trabajo también es en parte vuestro. No quiero terminar sin agradecerle a mis abuelos ese pedacito que me han aportado, a mis abuelas por seguir en la batalla pendientes de mí en todo momento y a mis abuelos Paco y Vicente, que aunque me dejaron al inicio de esta etapa, sé que han sabido guiar mis pasos y espero que dónde estén se sientan orgullosos.

Gracias por todo, Marina

**A mis padres y
a mi hermana,**



UNIVERSIDAD
DE MÁLAGA

Index

Resumen	i
1. Introduction	1
<i>1.1. Diesel engine emissions and European legislative framework for their control</i>	4
<i>1.2. NO_x and soot removal technologies for diesel exhaust</i>	7
1.2.1. Selective Catalytic Reduction (SCR)	8
1.2.2. NO _x Storage and Reduction (NSR)	17
1.2.3. Soot removal	21
1.2.4. Diesel Particulate-NO _x Reduction System (DPNR)	23
1.2.5. Coupling of after-treatment technologies	25
1.3. Objective	28
2. Experimental	29
<i>2.1. Reagents</i>	31
<i>2.2. Gases</i>	32
<i>2.3. Equipment</i>	33
2.3.1. Autoclave	33
2.3.2. Ultrasonic Processor	33
2.3.3. Furnace	34
2.3.4. Fourier Transform Infrared Spectroscopy (FTIR)	34
2.3.5. Diffuse Reflectance Infrared Fourier Transform Spectroscopy (DRIFTS)	34
2.3.6. Thermobalance	35
2.3.7. Flow reaction systems	36
<i>2.4. Catalyst synthesis</i>	38
2.4.1. Powder catalysts	38
2.4.1.1. NSR catalysts	38
2.4.1.2. SCR catalysts	39
2.4.2. Conformed catalysts	41
<i>2.5. Characterization techniques</i>	41
2.5.1. X-Ray Diffraction (XRD)	42
2.5.1.1. Rietveld Refinement	42
2.5.1.2. Temperature Programmed X-Ray Diffraction (TPXRD)	42
2.5.2. X-Ray Photoelectron Spectroscopy (XPS)	43
2.5.3. Analysis of porous solids	43
2.5.4. X-Ray Fluorescence (XRF)	44
2.5.5. Transmission Electron Microscopy (TEM) and High Resolution TEM (HRTEM)	44
2.5.6. Scanning Emission Microscopy (SEM)	45
2.5.7. Ultraviolet-visible spectroscopy (UV-Vis)	45
2.5.8. Raman spectroscopy	45
2.5.9. Fourier Transform Infrared Spectroscopy (FTIR)	45
2.5.9.1. Superficial acidity and metal location	46
2.5.9.2. CO adsorption at low temperature	46

2.5.9.3. <i>NO</i> adsorption	46
2.5.10. Temperature Programmed Desorption (TPD) of ammonia	47
2.5.10.1. <i>Ammonia</i> adsorption	47
2.6. <i>Catalytic study</i>	48
2.6.1. Transient Response Method (TRM)	48
2.6.1.1. <i>Isothermal thermogravimetric study (TG-MS)</i>	51
2.6.1.2. <i>Isothermal DRIFT-MS study</i>	51
2.6.2. Soot removal study	51
2.6.3. SCR activity	52
2.6.4. NH_3 oxidation	53
2.6.5. Mechanistic study	53
2.6.5.1. <i>SCR in DRIFTS</i>	53
2.6.5.2. <i>Co-adsorption of probe molecules</i>	53
2.6.5.2.1. FTIR co-adsorption pulses	54
2.6.5.2.2. Flow co-adsorption runs	54
2.6.6. Coupling of technologies	54
2.6.6.1. <i>Powder catalytic performance</i>	54
2.6.6.2. <i>Monolithic structure performance</i>	54
3. Results and discussion. NSR technology	57
3.1. <i>Characterization of NSR catalysts</i>	59
3.2. <i>Transient Response Method over NSR catalysts</i>	65
3.2.1. Isothermal thermogravimetric analyses of NSR catalysts	68
3.2.2. NSR mechanism over Pt-Ba-K/ Al_2O_3	70
3.3. <i>Soot influence over NSR catalysts</i>	73
3.3.1. TRM over NSR catalysts + soot mixtures	74
3.3.2. Isothermal thermogravimetric analyses of NSR catalysts + soot mixtures	78
3.3.3. NSR mechanism over Pt-Ba-K/ Al_2O_3 + soot mixture	81
3.3.4. Soot removal mechanism over LNT-catalysts	84
3.4. <i>TRM study over NSR catalysts in quasi-real conditions</i>	105
3.5. <i>Conclusions</i>	110
4. Results and Discussion. SCR technology	111
4.1. <i>Zeolitic material synthesis for SCR applications</i>	113
4.1.1. SAPO-34	113
4.1.2. Copper incorporation in SAPO-34 materials	121
4.2. <i>Copper species differentiation and location for a model Cu-SAPO-34</i>	136
4.3. <i>Insights into the SCR mechanism</i>	148
4.4. <i>Conclusions</i>	168

5. Results and discussion. NSR-SCR coupled technologies	169
<i>5.1. Influence of quasi-real conditions over NSR-SCR systems with volume ratio 1:1</i>	173
<i>5.2. Efficiency in dual system configuration even varying the operation parameters</i>	177
<i>5.3. Synthesis and characterization of monoliths</i>	189
<i>5.4. Activity of NSR-SCR system structured in monolithic form</i>	199
<i>5.5. Conclusions</i>	205
6. Significance and future lines of research	207
7. References	209



UNIVERSIDAD
DE MÁLAGA

List of Figures

1. Introduction

- Figure 1.1.** Evolution of the Spanish private car fleet according to fuel. (Source. Ref [1]). 3
- Figure 1.2.** NO_x real emissions compared to the standards (Source: Transport&Environment and the ICCT [35]). 6
- Figure 1.3.** Temperature and residence time operation conditions of the automobile, from idle to full performance of the engine, in comparison with other catalyzed transformation conditions. The relative values of NO_x, HC and CO for a vehicle are included (Source. Ref. [36]). 7
- Figure 1.4.** Vehicle diagram of the Urea system and the detail of the mixture. 9
- Figure 1.5.** Several structures of zeolites used in the SCR process (Source: [46]). 11
- Figure 1.6.** Scheme of the lean phase in NSR technology. 18
- Figure 1.7.** Scheme of the rich phase in NSR technology. 18
- Figure 1.8.** Sketch of the flow through the channel wall of a DPF [137]. 22
- Figure 1.9.** Diagram of the D-CAT system of Toyota. 23
- Figure 1.10.** Possible distribution of the coupling of technologies in the exhaust gas. 25

2. Experimental

- Figure 2.1.** Nicolet Nexus 6700 Spectrometer with the DRIFT reaction chamber, which is shown in the inset. 35
- Figure 2.2.** SDT Q600 Thermobalance with the detail of the sample pans. 35
- Figure 2.3.** Flow reaction systems in a) Lab.1, b) Lab.3 and c) Lab. 4. 37
- Figure 2.4.** Rotation system for the synthesis of monoliths. 41
- Figure 2.5.** Scheme of NH₃-TPD protocol. 47
- Figure 2.6.** Scheme of TRM runs. 48
- Figure 2.7.** NO_x response profile to a rectangular pulse. 49
- Figure 2.8.** Scheme of soot combustion experiments. 52
- Figure 2.9.** Reaction system for the study of monoliths. 55

3. Results and discussion. NSR technology

- Figure 3.1.** XRD patterns of the samples with the identification of the following species: γ -Al₂O₃ (---), Pt (Δ), BaCO₃ (\odot), K₂O (\diamond), K₄H₂(CO₃)₃·1,5H₂O (\square) 60
- Figure 3.2.** TEM images of the samples: a) Pt/Al₂O₃; b) Pt-Ba/Al₂O₃; c) Pt-K/Al₂O₃; d) Pt-Ba-K/Al₂O₃. 61
- Figure 3.3.** Deconvolution of the Pt4d_{5/2} XPS signal for the Pt-Ba-K/Al₂O₃ catalyst. 63
- Figure 3.4.** Deconvolution of the Ba3d_{5/2} XPS signal for the Pt-Ba-K/Al₂O₃ catalyst. 64
- Figure 3.5.** Deconvolution of the K2p XPS signal for the Pt-Ba-K/Al₂O₃ catalyst. 64
- Figure 3.6.** NO_x storage–reduction cycles at 350°C for Pt–Ba-K/Al₂O₃. 66
- Figure 3.7.** TG-TD analyses of LNT catalysts under isothermal (350°C) cyclic conditions lean (20 min, 1000ppm of NO+3% of O₂ in He), rich (15 min, 2000ppm of H₂ in He). 68
- Figure 3.8.** Assignments of peak position in DRIFT spectra results. 71
- Figure 3.9.** DRIFT spectra recorded for storage–reduction cycles at 350°C over Pt–Ba-K/Al₂O₃ from a) 1 min to h) 15 min under lean phase flow and i) after the regeneration step. 72
- Figure 3.10.** Fresh Printex U characterization: a) TEM image and b) Raman spectra. 73
- Figure 3.11.** NO_x storage–reduction cycles at 350°C for Pt–Ba/Al₂O₃ + soot sample. 75
- Figure 3.12.** NO_x storage–reduction cycles at 350°C for Pt–K/Al₂O₃ + soot sample. 75
- Figure 3.13.** NO_x storage–reduction cycles at 350°C for Pt–Ba–K/Al₂O₃ + soot sample. 76

Figure 3.14. The amount of NO _x removed (coloured symbol) and CO ₂ (blank symbol) produced vs. cycle number over catalyst+soot mixtures.	77
Figure 3.15. TG-TD analyses of Pt-Ba-K/Al ₂ O ₃ + soot catalyst under isothermal (350°C) and cyclic conditions: lean (20 min, 1000ppm of NO + 3% of O ₂ in He) and rich (15 min, 2000ppm of H ₂ in He).	79
Figure 3.16. DRIFT spectra recorded at 350°C over Pt-Ba-K/Al ₂ O ₃ + soot in He under a) lean and b) rich phase flow from a) 1 min to i) 15 min.	82
Figure 3.17. Weight loss and product distribution vs. temperature in the presence of 3% of O ₂ in He for soot.	85
Figure 3.18. Weight loss and product distribution vs. temperature in the presence of 3% of O ₂ in He for Pt-Ba/Al ₂ O ₃ .	86
Figure 3.19. Weight loss and products distribution vs. temperature in the presence of 3% of O ₂ in He for Pt-K/Al ₂ O ₃ .	86
Figure 3.20. Weight loss and product distribution vs. temperature in the presence of 3% of O ₂ in He for Pt-Ba-K/Al ₂ O ₃ .	87
Figure 3.21. Weight loss and product distribution vs. temperature in the presence of 1000ppm of NO + 3% of O ₂ in He for soot.	88
Figure 3.22. Weight loss and product distribution vs. temperature in the presence of 1000ppm of NO + 3% of O ₂ in He Pt-Ba/Al ₂ O ₃ .	88
Figure 3.23. Weight loss and product distribution vs. temperature in the presence of 1000ppm of NO + 3% of O ₂ in He for Pt-K/Al ₂ O ₃ .	89
Figure 3.24. Weight loss and product distribution vs. temperature in the presence of 1000ppm of NO + 3% of O ₂ in He for Pt-Ba-K/Al ₂ O ₃ .	90
Figure 3.25. Specific heat flow during soot oxidation without catalyst participation and over prepared catalysts in different conditions (A) 3% O ₂ in He flow; (B) 1000 ppm of NO + 3% of O ₂ in He flow.	91
Figure 3.26. Distribution functions of activation energy for the uncatalyzed soot elimination in different atmospheres.	96
Figure 3.27. Distribution functions of activation energy and deconvolution of signals for the catalysed soot removal process in the presence of 3% of O ₂ in He.	98
Figure 3.28. Distribution functions of activation energy and deconvolution of signals for the catalysed soot removal process in the presence of 1000ppm of NO and 3% of O ₂ in He.	101
Figure 3.29. Storage–reduction stationary cycle for Pt-Ba-K/Al ₂ O ₃ in He at 200°C.	105
Figure 3.30. Storage–reduction stationary cycle for Pt-Ba-K/Al ₂ O ₃ in He at 350°C.	106
Figure 3.31. Storage–reduction stationary cycle for Pt-Ba-K/Al ₂ O ₃ in H ₂ O+CO ₂ at 200°C.	107
Figure 3.32. Storage–reduction stationary cycle for Pt-Ba-K/Al ₂ O ₃ in H ₂ O+CO ₂ at 350°C.	107
4. Results and Discussion. SCR technology	
Figure 4.1. X-ray diffraction patterns of SAPO-c, SAPO-0.2-200-72h, SAPO-0.2-200-4s and SAPO-200-4.	114
Figure 4.2. SEM images of a) SAPO-0.2-200-72h, b) SAPO-0.2-200-4s, c) SAPO-c and d) SAPO-200-4.	116
Figure 4.3. Increase of weight according to time in NH ₃ saturation (750ppm) experiments at 100°C for SAPO-c, SAPO-0.2-200-72h, SAPO-0.2-200-4s and SAPO-200-4.	117
Figure 4.4. FTIR spectra of 10 torr of NH ₃ i, ii, iii and iv) and NO v, vi, vii, and viii) adsorbed on SAPO-c, SAPO-0.2-200-72h, SAPO-0.2-200-4s and SAPO-200-4, respectively.	118
Figure 4.5. SCR conversion and selectivity values according to temperature for SAPO-0.2-200-4s and SAPO-200-4.	120
Figure 4.6. X-ray diffraction patterns of 2CuSAPO-0.2-200-4s, 2Cu-SAPO-200-4, 2Cu-SAPO-150-4, 2Cu-SAPO-150-30 and 4Cu-SAPO-150-30.	122

Figure 4.7. SEM images of a) 2Cu-SAPO-0.2-200-4s, b) 2Cu-SAPO-200-4, c) 2Cu-SAPO-150-4, d) 2Cu-SAPO-150-30 and e) 4Cu-SAPO-150-30.	125
Figure 4.8. UV-Vis-DR spectra of 2CuSAPO-0.2-200-4s, 2Cu-SAPO-200-4, 2Cu-SAPO-150-4, 2Cu-SAPO-150-30 and 4Cu-SAPO-150-30.	126
Figure 4.9. Increase of weight according to NH ₃ saturation (750ppm) at 100°C for 2Cu-SAPO-200-4s, 2Cu-SAPO-200-4, 2Cu-SAPO-150-4, 2Cu-SAPO-150-30 and 4Cu-SAPO-150-30.	128
Figure 4.10. FTIR spectra of 10 torr of NH ₃ adsorbed on i) 2Cu-SAPO-0.2-200-4s and ii) 2Cu-SAPO-150-30 from a) 100°C to e) 500°C.	129
Figure 4.11. FTIR spectra of 10 torr of NO adsorbed on 2Cu-SAPO-0.2-200-4s from a) 100°C to c) 300°C.	131
Figure 4.12. Co-adsorption flow experiments of 800ppm of NH ₃ and 1000ppm of NO + 3% of O ₂ over SAPO-0.2-200-4s at a) 200°C and b) 300°C.	132
Figure 4.13. Co-adsorption flow experiments of 800ppm of NH ₃ and 1000ppm of NO + 3% of O ₂ over 2Cu-SAPO-0.2-200-4s at a) 200°C and b) 300°C.	133
Figure 4.14. SCR conversion and selectivity values according to temperature for a) 2Cu-SAPO-0.2-200-4s, b) 2Cu-SAPO-200-4, c) 2Cu-SAPO-150-30 and d) 4Cu-SAPO-150-30. Feeding conditions: 750ppm NO+750ppmNH ₃ +3%O ₂ in He.	134
Figure 4.15. FT-IR skeletal spectra of a) SAPO-200-4, b) 2Cu-SAPO-150-30 and c) 4Cu-SAPO-150-30.	137
Figure 4.16. FTIR spectra of a) SAPO-200-4 after activation at 500°C and b) after further adsorption of water and brief outgassing at r.t.	138
Figure 4.17. FTIR spectra of pure powders after activation at 500°C of a) SAPO-200-4, b) 2Cu-SAPO-150-30 and c) 4Cu-SAPO-150-30.	139
Figure 4.18. EDX mapping of HRTEM for 2Cu-SAPO-150-30.	141
Figure 4.19. EDX mapping of HRTEM for 4Cu-SAPO-150-30.	141
Figure 4.20. FTIR spectra of surface species arising from low temperature CO adsorption over SAPO-200-4 sample: a) CO adsorbed at -140°C, (b-h) outgassing from -140°C to room temperature. The activated surface has been subtracted.	143
Figure 4.21. FTIR spectra of surface species arising from low temperature CO adsorption over 2Cu-SAPO-150-30 sample: a) CO adsorbed at -140°C, (b-o) outgassing from -140°C to 150°C. The activated surface has been subtracted.	144
Figure 4.22. FTIR spectra of surface species arising from low temperature CO adsorption over 4Cu-SAPO-150-30 sample: a) CO adsorbed at -140°C, (b-n) outgassing from -140°C to 200°C. The activated surface has been subtracted.	145
Figure 4.23. FTIR spectra of surface species arising from AN adsorption over sample (A) SAPO-200-4, (B) 2Cu-SAPO-150-30 (C) 4Cu-SAPO-150-30. a) In the presence of AN vapor, b) after outgassing at room temperature, c) at 100°C, d) at 150°C, e) at 200°C, f) at 250°C, g) at 300°C. The activated surface spectrum has been subtracted.	146
Figure 4.24. FTIR spectra of surface species arising from PN adsorption at room temperature over sample a) SAPO-200-4, b) 2Cu-SAPO-150-30 and c) 4Cu-SAPO-150-30. The activated surface spectrum has been subtracted.	147
Figure 4.25. FTIR spectra of 10 torr of NO adsorbed on 2Cu-SAPO-0.2-200-4s from r.T. to 300°C without evacuation (black line) and in evacuation (red line).	148
Figure 4.26. FTIR co-adsorption spectra over 2Cu-SAPO-150-30 at 300°C after: a) NH ₃ adsorption and evacuation, b-e) in NO + O ₂ atmosphere and f) the evacuation of all the gas phase.	150
Figure 4.27. Pathways of the SCR reaction over Copper-zeolites.	151
Figure 4.28. FTIR co-adsorption spectra over 2Cu-SAPO-150-30 at 300°C after: a) NH ₃ adsorption and evacuation, b) 15 min in NO + O ₂ atmosphere and c) the evacuation of all the gas phase.	152
Figure 4.29. DRIFT spectra of the simultaneous adsorption of 750ppm of NH ₃ + 750ppm of NO + 3% of O ₂ as the time increases over 2Cu-SAPO-150-30 at 40°C.	153

Figure 4.30. DRIFT spectra of the simultaneous adsorption of 750ppm of NH ₃ + 750ppm of NO + 3% of O ₂ as the time increases over 2Cu-SAPO-150-30 at 100°C.	154
Figure 4.31. DRIFT spectra of the simultaneous adsorption of 750ppm of NH ₃ + 750ppm of NO + 3% of O ₂ as the time increases over 2Cu-SAPO-150-30 at 200°C.	154
Figure 4.32. A) Weight loss vs. temperature in the presence of 1000ppm of NO + 3% of O ₂ in He for 4Cu-SAPO-150-30. B) Distribution functions of activation energy for 4Cu-SAPO-150-30 and uncatalyzed soot in NO+O ₂ atmosphere.	156
Figure 4.33. Weight and heat flow profiles for 2Cu-SAPO-200-4 during thermal aging in A) He and B) H ₂ O.	157
Figure 4.34. X-ray diffraction patterns of 2Cu-SAPO-200-4 (fresh and hydrothermally aged in He and in H ₂ O) and unit cell values (inset table).	158
Figure 4.35. NH ₃ profiles for NH ₃ -TPD experiments (750ppm of NH ₃) in He and in 1.5% H ₂ O and 0.3% CO ₂ at different temperatures.	159
Figure 4.36. FTIR co-adsorption spectra over 2Cu-SAPO-150-30 at 200°C after: a) H ₂ O adsorption, b) CO ₂ adsorption, c) NH ₃ adsorption in evacuation, d-g) in NO + O ₂ atmosphere and h) evacuation of all the gas phase.	161
Figure 4.37. FTIR spectra after water adsorption and outgassing at 100°C of a) SAPO-200-4 and b) 2Cu-SAPO-200-4.	162
Figure 4.38. SCR conversion and selectivity values according to the temperature for a and b) SAPO-200-4 and c and d) 2Cu-SAPO-200-4. Feeding conditions: 750ppm NO+750ppmNH ₃ +3%O ₂ in He. Dotted lines (H ₂ O+CO ₂), solid lines (He).	163
Figure 4.39. Conversion and selectivity values for NH ₃ oxidation over 2Cu-SAPO-200-4 in the presence of He (solid lines) and water and CO ₂ (dotted lines).	166
Figure 4.40. Scheme of possible copper location inside the SAPO-34 structure.	167
5. Results and discussion. NSR-SCR coupled technologies	
Figure 5.1. Double bed configuration.	172
Figure 5.2. Conversion and selectivity values for different NSR/SCR volume ratios in experiments with NSR conditions (1000ppm NO+3%O ₂ /2000ppm H ₂ in He, 15-15 min) at a) 200°C and b) 350°C.	172
Figure 5.3. Storage–reduction stationary cycle (15-15 min) for Pt-Ba-K/Al ₂ O ₃ + 2Cu-SAPO-150-30 at 350°C in (a) He and (b) H ₂ O+CO ₂ .	174
Figure 5.4. Storage–reduction cycles for Pt-Ba-K/Al ₂ O ₃ + 2Cu-SAPO-150-30 at 200°C with lean-rich periods of 150-20 s ($\theta = 7.5$) with a hydrogen concentration of a) 0.2% b) 1% and c) 2.5% in H ₂ O+CO ₂ .	179
Figure 5.5. Storage–reduction cycles for Pt-Ba-K/Al ₂ O ₃ + 2Cu-SAPO-150-30 at 350°C with lean-rich periods of 150-20 s ($\theta = 7.5$) with a hydrogen concentration of a) 0.2% b) 1% and c) 2.5% in H ₂ O+CO ₂ .	180
Figure 5.6. Storage–reduction cycles for Pt-Ba-K/Al ₂ O ₃ + 2Cu-SAPO-150-30 at 200°C with lean-rich periods of 60-20 s ($\theta = 3$) with a hydrogen concentration of a) 0.2% b) 1% and c) 2.5% in H ₂ O+CO ₂ .	183
Figure 5.7. Storage–reduction cycles for Pt-Ba-K/Al ₂ O ₃ + 2Cu-SAPO-150-30 at 350°C with lean-rich periods of 60-20 s ($\theta = 3$) with a hydrogen concentration of a) 0.2% b) 1% and c) 2.5% in H ₂ O+CO ₂ .	184
Figure 5.8. Storage–reduction cycles for Pt-Ba-K/Al ₂ O ₃ + 2Cu-SAPO-150-30 at 350°C with lean-rich periods of 60-60 s ($\theta = 1$) with a hydrogen concentration of a) 0.2% and b) 1% and 20-20 s ($\theta = 1$) with H ₂ % of c) 0.2% and d) 1% in H ₂ O+CO ₂ .	187
Figure 5.9. SEM images of the cross and axial sections of the cordierite monolith with Al ₂ O ₃ coverage and the composition analyzed by EDX (inset Table 5.7).	190
Figure 5.10. Synthesis of the NSR and SCR catalysts in the monolithic form	191
Figure 5.11. SEM images of the cross section of the Pt-Ba-K/Al ₂ O ₃ -M monolith	193
Figure 5.12. EDX mapping of SEM images of Pt-Ba-K/Al ₂ O ₃ -M sample.	194
Figure 5.13. XRD patterns of the Blank-M and 2Cu-SAPO-150-30-M monoliths.	197
Figure 5.14. SEM images of the cross and axial sections of 2Cu-SAPO-150-30-M.	198

Figure 5.15. Copper EDX mapping of SEM images of 2Cu-SAPO-150-30-M sample.	199
Figure 5.16. Double bed configuration system for experiments with monoliths.	200
Figure 5.17. Storage-reduction cycles to saturation for Pt-Ba-K/Al ₂ O ₃ -M + Cu-SAPO-150-30-M at 350°C with lean-rich periods of 17-8h with a hydrogen concentration of 0.2% in H ₂ O+CO ₂ .	201
Figure 5.18. Storage-reduction cycles for Pt-Ba-K/Al ₂ O ₃ -M + Cu-SAPO-150-30-M at 350°C with lean-rich periods of 7-7h with a hydrogen concentration of 0.2% in H ₂ O+CO ₂ .	202
Figure 5.19. Storage-reduction cycles for Pt-Ba-K/Al ₂ O ₃ -M + Cu-SAPO-150-30-M at 350°C with lean-rich periods of 7-1h with a hydrogen concentration of 1% in H ₂ O+CO ₂ .	203
Figure 5.20. Storage-reduction cycles for Pt-Ba-K/Al ₂ O ₃ -M + Cu-SAPO-150-30-M at 350°C with lean-rich periods of 7-0.5h with a hydrogen concentration of 2.5% in H ₂ O+CO ₂ .	204



UNIVERSIDAD
DE MÁLAGA

List of Tables

Table 1.1. Emission limits ($\text{g}\cdot\text{km}^{-1}$) in diesel light-vehicle exhausts according to Euro directives.	5
Table 2.1. Composition of LNT-catalysts.	38
Table 2.2. Identification and synthesis parameters of the SCR catalysts.	40
Table 3.1. Binding energies from XPS data in eV for the samples (% species concentration).	62
Table 3.2. $\text{Pt}^0/\text{Pt}_{\text{ox}}$ ($\text{Pt}_{\text{ox}}=\text{Pt}^{2+}+\text{Pt}^{4+}$) ratio of the samples.	63
Table 3.3. Reactivity data calculated during soot-free storage-reduction of NO_x experiments from isothermal TRM profiles at 350°C .	67
Table 3.4. Summary of soot removal processes in O_2 atmosphere.	103
Table 3.5. Summary of soot removal processes in $\text{NO}+\text{O}_2$ atmosphere.	103
Table 3.6. Reactivity data calculated during the storage-reduction of NO_x experiments from isothermal TRM profiles at 200 and 350°C .	108
Table 4.1. Unit cell volume, surface area and pore volume of SAPO-c, SAPO-0.2-200-72h, SAPO-0.2-200-4s and SAPO-200-4.	115
Table 4.2. Composition of some samples obtained by XRF.	123
Table 4.3. Unit cell volume, surface area and pore volume of the Cu-containing samples.	124
Table 4.4. XPS data of copper species for Cu-SAPO-34 materials.	127
Table 4.5. Amount of ammonia adsorbed per gram of 2Cu-SAPO-200-4 or SAPO-200-4 at different temperatures and atmospheres.	160
Table 5.1. Experimental parameters of the double catalytic bed configurations.	172
Table 5.2. Experimental conditions for the study of different NSR/SCR catalytic beds.	172
Table 5.3. Reactivity data calculated during the storage-reduction of NO_x experiments from isothermal TRM profiles at 200 and 350°C for Pt-Ba-K/ Al_2O_3 and Pt-Ba-K/ Al_2O_3 +2Cu-SAPO-150-30 systems.	175
Table 5.4. Flow conditions used in the TRM experiments over NSR-SCR systems.	178
Table 5.5. TRM parameter values for the experiments with lean/rich time ratio variation as a function of the hydrogen percentage and the temperature.	185
Table 5.6. Characteristics of the monolith.	189
Table 5.7. Composition of the blank monolith wall covered by Al_2O_3 .	190
Table 5.8. Composition data obtained by XPS of Pt-Ba-K/ Al_2O_3 -M.	194
Table 5.9. Binding energies from XPS data in eV for Pt-Ba-K- Al_2O_3 -M (% species concentration).	195
Table 5.10. Composition data obtained by XPS of 2Cu-SAPO-150-30-M.	199



UNIVERSIDAD
DE MÁLAGA

List of abbreviations

AN	Acetonitrile
a.u.	Arbitrary units
BAS	Brönsted Acid Sites
BE	Binding Energy
BET	Brunauer-Emmett-Teller
CCD	Charge Couple Device
CHA	Chabazite
CT	Charge Transfer
cp _{si}	Cell per square inch
D-CAT	Diesel Clean Advanced Technology
DEA	Diethylamine
DFT	Density Functional Theory
DME	Dimethyl ether
DOC	Diesel Oxidation Catalyst
DPF	Diesel Particulate Filter
DPNR	Diesel Particulate NO _x Removal
DR	Diffuse Reflectance
DRIFTS	Diffuse Reflectance Infrared Fourier Transform Spectroscopy
DSC	Differential Scanning Calorimetric
EDX	Energy Dispersion X-ray Spectroscopy
E-R	Eley-Rideal
FAME	Fatty Acid Methyl Esters
FTIR	Fourier Transform Infrared Spectroscopy
GHSV	Gas Hourly Space Velocity
HC	Hydrocarbon
HRTEM	High Resolution Transmission Electron Microscopy
IN	Isobutyronitrile
IPA	Aluminum isopropoxide
JCPDS	Joint Committee on Powder Diffraction Standards
L-H	Langmuir -Hinshelwood
LNT	Lean NO _x Traps
MS	Mass Spectrometry
MTO	Methanol-to-olefin
NSR	NO _x Storage and Reduction
OC	Oxidation Capacity
RDE	Real-world driving emissions
PM	Particulate matter
PN	Pivalonitrile
SAPO	Silicoaluminophosphate
SCO	Selective Catalytic Oxidation
SCR	Selective Catalytic Reduction
SEM	Scanning Electron Microscopy
SOF	Soluble Organic Fraction
TEM	Transmission Electron Microscopy
TEPA	Tetraethylenepentamine
TGA	Thermogravimetric Analysis
TPD	Temperature Programmed Desorption



TPXRD	Temperature Programmed X-Ray Diffraction
TRM	Transient Response Method
TWC	Three Way Catalyst
UV-vis	Ultraviolet-visible Spectroscopy
XANES	X-Ray Absorption Near Edge Structure
XPS	X-Ray Photoelectron Spectroscopy
XRD	X-Ray Diffraction
XRF	X-Ray Fluorescence

Resumen

Una de las principales causas que favorecen el desequilibrio en la calidad del aire son las emisiones de óxidos de nitrógeno. El principal responsable en los niveles de NO_x globales se atribuye al sector transporte, que llega a representar el 55 % del total y el resto se debe a sectores como el energético, fundamentalmente en plantas de producción y sector industrial. Se puede considerar que el transporte por carretera es el principal emisor de óxidos de nitrógeno, lo que repercute considerablemente, consecuencia del crecimiento exponencial del parque automovilístico en los últimos 50 años y, según las previsiones, mantendrá un crecimiento casi sostenido por el incremento de vehículos de pasajeros en los países en desarrollo.

Gran parte de la normativa legal está enfocada a limitar las emisiones contaminantes procedentes de los vehículos automóviles y de otros medios de transporte, aunque también regula las emisiones industriales, plantas de generación de energía, pequeños equipos domésticos equipados con motores y generadores. Los estándares generalmente regulan las emisiones de NO_x , CO, HC_{in} (hidrocarburos inquemados) y MP (material particulado).

Las estrategias de actuación para el control de las emisiones de los NO_x se pueden separar en dos categorías, aquellas que consideran el tratamiento del combustible o modificaciones en la combustión y que se denominan primarias o las de tratamiento al final de línea (*after-treatment*) o secundarias. A su vez, las secundarias se pueden clasificar por ser una tecnología en “seco” o en “húmedo” y dentro de las primeras (tecnología en seco) se engloban las tecnologías catalíticas, tanto de carácter selectivo como no selectivo.

A pesar de los enormes logros conseguidos con las tecnologías de post-tratamiento para el control de las emisiones procedentes de los gases de escape asociadas al sector automovilístico, las cada vez más exigentes restricciones impuestas por la legislación, a lo que se suma el creciente número de vehículos, hace que a día de hoy las emisiones de gases contaminantes representen un grave problema ambiental. La demanda de motores diésel sigue aumentando en todo el mundo como resultado de la expansión de la industrialización; esto se debe a que los motores diésel tienen ciertas ventajas en

comparación con los motores de encendido por chispa como el bajo consumo de combustible, alto par motor y la longevidad, entre otros. A pesar de estas ventajas, los motores diésel son hoy en día uno de los factores principales que causan la contaminación del aire y para ello, actualmente, los estudios que se llevan a cabo se centran en cambiar ciertos parámetros de funcionamiento del motor, tales como la sincronización de válvulas, sincronización de la inyección y la velocidad con el fin de disminuir las emisiones nocivas. Las restricciones impuestas por la legislación están llegando a un punto en el que los niveles permitidos son muy difíciles de alcanzar a través de modificaciones del motor sin comprometer la eficiencia del mismo y se necesita urgentemente el desarrollo de las técnicas de pos-tratamiento para la reducción posterior, principalmente de los NO_x y material particulado (*soot*).

El proceso SCR se presenta como una forma atractiva para reducir los NO_x en exceso de O_2 , con el uso de agentes reductores tales como amoníaco o urea entre otros, ésta es una alternativa efectiva para la reducción de NO_x cuando el motor funciona en condiciones de estado estacionario. Sin embargo, el rápido cambio de condiciones en el motor conduce a una modificación rápida en los gases de escape, lo que hace que sea difícil obtener la reducción esperada de NO_x . En consecuencia, el control mediante SCR sigue siendo un gran desafío en la práctica. La estabilidad térmica de los catalizadores juega un papel crucial para que puedan ser utilizados en este proceso, debido a las altas temperaturas que se llegan a alcanzar en el motor y el vanadio que es una muy buena opción en la eliminación de los NO_x en las aplicaciones en fuentes estacionarias no lo es en el sector automovilístico debido a que puede sublimar a las altas temperaturas alcanzadas. Hasta la fecha, los esfuerzos más importantes relativos a los materiales utilizados como catalizadores se centran en los nuevos sistemas libres de vanadio con alta selectividad y alta estabilidad térmica. Esta búsqueda se centra esencialmente en catalizadores tipo zeolitas con poros pequeños, por sus propiedades de acidez media y alta estabilidad hidrotérmica, intercambiadas con metales, como hierro o cobre, y más concretamente este último por su alta actividad a baja temperatura.

Otro de los enfoques más prometedores y que se viene estudiando y está implementado desde hace tiempo es la tecnología NSR (NO_x Storage Reduction) o también llamada LNT-trap (trampa de NO_x) que es una tecnología que alterna de forma cíclica períodos en condiciones oxidantes y períodos en condiciones reductoras. Se basa en el

almacenamiento de NO_x sobre centros básicos del catalizador (principalmente Ba) para formar nitratos durante la fase pobre en combustible (condiciones oxidantes) y su reducción a nitrógeno en una atmósfera rica en combustible. Estos catalizadores necesitan la participación de un metal noble, normalmente platino, que es uno de sus principales inconvenientes.

Un concepto todavía aplicado escasamente combina ambas tecnologías y está basado en la premisa de que el catalizador LNT genera NH_3 , esta limitación se convierte en una ventaja puesto que puede ser usado por el catalizador SCR posicionado secuencialmente en la parte posterior del sistema LNT evitando al mismo tiempo la necesidad de utilizar un sistema de dosificación de urea o proporcionar un suministro externo de NH_3 al catalizador SCR; por lo que la combinación de ambas tecnologías ofrece una interesante solución para superar las limitaciones de los sistemas individuales que integran sus funcionalidades. En el sistema híbrido LNT+SCR, los NO_x que se almacenan en el catalizador LNT se reducen selectivamente y el *slip* de NH_3 generado durante la fase rica es adsorbido por el catalizador SCR colocado en la proximidad del componente LNT. El sistema SCR+LNT combina la capacidad de generación de NH_3 del catalizador LNT y la capacidad de adsorción de NH_3 sobre los sitios ácidos y de reducción de NO_x del catalizador SCR. Así no sólo se mejora la conversión total de NO_x , sino también se consume el NH_3 generado por el catalizador LNT en el lecho SCR localizado aguas abajo.

Esta información inicial y las aplicaciones comerciales aún limitadas han estimulado la investigación que se ha desarrollado como trabajo en esta Tesis Doctoral de forma que el análisis individual de ambas tecnologías y posteriormente de forma conjunta permita introducir mejoras para conseguir una alta eficiencia en la eliminación de los óxidos de nitrógeno y *soot* en el amplio rango de condiciones de operación que se encuentran en la práctica. Estas mejoras han ido dirigidas a la composición y propiedades de los catalizadores utilizados, tanto mediante la tecnología SCR como la NSR; analizando la composición, inicialmente en forma de polvo, de los catalizadores en las distintas condiciones de operación encontrando la formulación mejorada que por separado y posteriormente de forma conjunta rindan los mejores resultados en el proceso en condiciones reales, trasladando la formulación óptima en polvo a nivel de conformado-monolito.

En este sentido se ha realizado una revisión de las tendencias en los catalizadores en ambos casos que conjuntamente con la experiencia en la temática demostrada por el Grupo de Investigación donde se ha desarrollado la Tesis, constatado por las Tesis previas realizadas sobre el tema y las publicaciones en el argumento ha permitido centrar el trabajo en la Memoria planteada.

La Tesis se ha estructurado en tres bloques que coinciden con las tres secciones de resultados y discusión: por un lado se ha analizado el proceso NSR de forma individualizada, profundizando en el conocimiento para obtener un catalizador tipo LNT soportado con recubrimiento superficial inferior a la máxima capacidad de dispersión del soporte, que se corresponde con la monocapa teórica, que combine las propiedades de máxima acumulación y regeneración y que la capacidad no se vea afectada por la presencia de agua, CO₂ o *soot*; en segundo lugar también se ha realizado un análisis detallado del proceso individual SCR, estableciendo una ruta de síntesis reproducible y escalable que permita manejar grandes cantidades de un catalizador modelo que maximice el contenido en cobre en el interior de una estructura zeolítica de poro pequeño que por confinamiento promueva la eliminación de NO_x mediante SCR con aporte externo de amoníaco y estableciendo un mecanismo probable del proceso y en tercer lugar el estudio de las tecnologías acopladas, tanto el estudio de cómo combinarlas como también el escalado a nivel de laboratorio de los catalizadores conformados en forma de monolitos para poder trabajar en condiciones de operación próximas a las reales. En la Memoria de Tesis se presentan los resultados obtenidos que van desde el planteamiento de los catalizadores, con el estudio de la síntesis de los materiales en forma de polvo, su caracterización convencional y el estudio de la actividad catalítica a través de diferentes test catalíticos que han permitido evaluar su comportamiento bajo diferentes condiciones de operación y que se encuentran detalladas en el capítulo correspondiente a la metodología.

En cuanto a la tecnología NSR, existe un acuerdo general en la literatura que el catalizador debe estar formado por un alcalino-alcalino térreo con participación de una alta carga de metal noble como Pt soportado sobre alúmina; sin embargo existe controversia sobre el alcalino en concreto y el metal noble, así como sobre diversos aspectos relativos al comportamiento en presencia de *soot*, SO_x, H₂O y/o CO₂, por lo que determinar la formulación óptima del catalizador NSR (LNT) es un aspecto de

análisis de interés. Se han preparado catalizadores modelo (con base Ba-Pt soportados sobre alúmina), variando la relación Ba/Pt y preparados por impregnación a humedad incipiente siguiendo una metodología de incorporación de los metales que ya había sido analizada en trabajos anteriores y establecida por el Grupo de Investigación como óptima, ofreciendo las mejores propiedades estructurales y morfológicas que permiten una mejor actuación en el proceso, incorporando en primer lugar el metal noble y a continuación el alcalino o alcalino-térreo o la mezcla de ambos con calcinaciones intermedias a 350°C y una calcinación final a 500°C (5°C·min⁻¹) durante 5 horas. En busca de la eliminación simultánea de NO_x y *soot* se han preparado catalizadores modificados, con la incorporación de otro componente almacenador, concretamente potasio. Así, se han preparado sistemas trimetálicos Pt-Ba-K/Al₂O₃ de forma que se ha conseguido una formulación con la presencia de Ba y K (3.5 y 1.5 at·nm⁻² de Ba y K, respectivamente) que proporciona una óptima razón Pt⁰/Pt_{ox}, alrededor de 1.8 próxima al catalizador modelo de Bario que es el que presenta mayor capacidad en almacenamiento de NO_x, permitiendo alcanzar con esta formulación conversiones (almacenamiento) próximas a las del catalizador modelo, pero con una mejora sustancial en la selectividad a N₂, fundamentalmente en presencia de *soot*, a través de un mecanismo prácticamente idéntico al de los catalizadores modelo. Para ello, se llevaron a cabo experimentos con método de respuesta transitoria, tanto en reactor de flujo acoplado con masas y μGC como en termobalanza acoplada a masas, alimentando condiciones cíclicas de 1000ppm de NO_x + 3% O₂ con 2000 ppm de hidrógeno hasta saturación (15-15 min). Con el catalizador trimetálico que presentó mayor actividad catalítica, se han alcanzado cantidad de almacenamiento de NO_x de 0.42 mmol·g_{cat}⁻¹, capacidad de oxidación del 33%, conversión del 88% y selectividad a nitrógeno del 97%. Mediante los experimentos realizados con las pruebas en la termobalanza se confirmó el comportamiento y se observó la diferencia en la tendencia en la línea base de la masa dependiendo del metal presente en la formulación, indicando la baja regenerabilidad de los catalizadores que incorporan potasio. Además los flujos de calor coincidieron con la reacción de los nitratos en la etapa rica en combustible y dos señales diferentes asociadas a dos tipos de nitratos se observaron en presencia de la combinación de los metales bario y potasio. El mecanismo de reacción fue estudiado alimentando idénticas condiciones cíclicas en DRIFTS y se comprobó que es similar al propuesto para los catalizadores modelo PtBa y PtK. En la etapa de oxidación se detectó una combinación de especies tipo nitratos, *bridging* o *chelating* bidentados,

monodentados o nitratos libres, que durante la etapa de regeneración son prácticamente eliminados quedando la superficie restablecida.

La presencia de material particulado también fue analizada, caracterizando previamente el *soot* modelo Printex U, experimentos iguales fueron llevados a cabo con las mezclas entre los catalizadores y un 10% de *soot* realizada mediante *tight contact*, obteniéndose que inicialmente existe una competencia de la atmósfera de reacción entre la adsorción como nitratos y la reacción con el *soot* presente, disminuyendo la capacidad de acumulación hasta $0.36 \text{ mmol} \cdot \text{g}_{\text{cat}}^{-1}$ a 350°C . Además, la forma de eliminar el material particulado parece modificarse según el metal alcalino o alcalino-térreo incorporado en la formulación. Por ello, mediante análisis termogravimétrico acoplado con un espectrómetro de masas se estudió el mecanismo de eliminación del *soot*, realizando análisis en régimen no isoterma, desde temperatura ambiente hasta 1000°C , en presencia de diferentes atmósferas oxidantes ($\text{O}_2/\text{NO}+\text{O}_2$) y registrando la variación de la masa, el flujo del calor y los productos formados. Se observó, fundamentalmente, la pérdida de masa, que varió en temperatura y cantidad según el metal presente, con formación principalmente de agua y CO_2 . Mediante un modelo matemático que fue desarrollado teniendo en cuenta que una serie de reacciones irreversibles, paralelas y de primer orden tienen lugar en la eliminación del *soot*, se obtuvo la función de distribución de energías de activación, que permite identificar la ocurrencia de procesos según la energía de activación y desacoplar los procesos que tienen lugar. De forma que, en consonancia con los datos obtenidos se puede afirmar que la atmósfera de reacción influye en el proceso de eliminación, adelantando la temperatura a la que tiene lugar y que en presencia de potasio, la reducción de la cantidad de materia particulada ocurre por intervención de centros hidroxilados tipo Pt-OH-M que son los responsables de la mejora en el proceso de eliminación de *soot* cuando se encuentra el potasio en la formulación catalítica.

La influencia de la presencia de agua (1.5%) y CO_2 (0.3%) también fue estudiada a diferentes temperaturas, observándose una disminución de la cantidad de NO_x adsorbidos por gramo de catalizador, debido a la competencia de los centros activos, y valores inferiores de conversión, indicando que estos reactivos están involucrados de alguna forma en el proceso de regeneración y evitan la recuperación completa de la superficie. Además, se apreciaron diferentes comportamientos según la temperatura de

operación, de forma que aunque a alta temperatura, donde la diferencia de los parámetros es menos pronunciada, se observa una disminución de los co-productos no deseados aumentando la selectividad a nitrógeno, a baja temperatura, la producción de amoníaco se ve aumentada. Cabe destacar que en cualquier caso, en presencia de agua y CO_2 no se observó formación de N_2O . Este efecto puede ser debido a que la regeneración del catalizador, que podría tener lugar con formación inicial de amoníaco que posteriormente reacciona con los nitratos, es tan rápida que sale en los productos de reacción, además, podrían formarse $-\text{NCO}$ especies que se hidrolizan con formación de amoníaco.

Se puede concluir, con respecto a la tecnología NSR, que los catalizadores preparados han sido ampliamente caracterizados con técnicas convencionales, y se ha evaluado su actividad utilizando diferentes pruebas que ponen de manifiesto estos altos valores de conversión y selectividad a nitrógeno en el rango de temperatura de trabajo, sin embargo, fundamentalmente a baja temperatura, hay cierta formación de N_2O y NH_3 . Estos sistemas con presencia de K en la formulación presentan una disminución de la regeneración de la superficie catalítica, a pesar de ello, especialmente en presencia de *soot*, estos sistemas se muestran como prometedores ya que el potasio mejora el proceso de eliminación por intervención de los centros hidroxilados superficiales. En condiciones reales, en presencia de H_2O y CO_2 , hay un efecto compensatorio o doble, dependiendo de la temperatura de operación. Hay competitividad por los centros activos para la adsorción, aunque el agua puede influir en la mejora del proceso de regeneración.

El desarrollo de catalizadores para su aplicación en el proceso SCR ha avanzado a un ritmo elevado en las dos últimas décadas. En la actualidad, las zeolitas de pequeño poro intercambiadas con metales se han propuesto para su uso con amoníaco para aplicaciones De NO_x en fuentes móviles; en particular, las zeolitas intercambiadas con cobre son los principales candidatos entre todos los catalizadores basados en zeolita. En este sentido se ha establecido un protocolo de síntesis de una zeolita (con estructura tipo chabacita) intercambiada con Cu analizando diferentes variables que pueden influir en las características finales del catalizador obtenido y que van desde la propia formulación del catalizador con presencia en distinta concentración de Cu hasta las condiciones del proceso de síntesis, analizando diferentes precursores, agentes directores, tiempos y

temperaturas en la síntesis así como la influencia beneficiosa relativa a la disminución del tiempo de cristalización y aumento de la cristalinidad de las muestras que puede ejercer la actuación de ultrasonido en la preparación del gel de síntesis, de forma que las propiedades estructurales, morfológicas (microporosidad) y la actividad catalítica de la chabacita varían en función del proceso de síntesis (tiempo y temperatura en el autoclave) y con el contenido en fósforo y cobre. Concretamente, el proceso de síntesis consistió en la preparación de un gel con composición 2DEA: 0.6SiO₂: 1Al₂O₃: (0.2-0.8) P₂O₅: 50H₂O, al que ha sido incorporado cobre hasta en un 4% en peso (expresado como cobre metálico). En primer lugar se preparó una suspensión de alúmina del isopropóxido en agua al 75%, a continuación se añadió agua y ácido fosfórico, agitando vigorosamente durante dos horas, se adicionó la cantidad correspondiente de sílica y fue mezclado durante 4 horas, finalmente se incorporó el agente director de estructura, DEA, y 5% de semillas. El gel fue sonicado durante 3 minutos e introducido en el autoclave a la temperatura y durante el tiempo indicados en cada caso. Finalmente fue lavado, secado y calcinado a 550°C (1.8°C·min⁻¹) durante 5 horas. El cobre fue introducido en el gel inicial en forma de complejo, empleando una solución de sulfato de cobre y TEPA como agente complejante.

Estos materiales sintetizados han sido caracterizados mediante diferentes técnicas convencionales; así, la Difracción de Rayos X (DRX) ha permitido corroborar la estructura cristalina tipo chabazita de los materiales y determinar la influencia del ultrasonidos en la cristalinidad. Mediante las isotermas de adsorción de N₂ se ha comprobado que los materiales sintetizados presentan valores de área superficial alrededor de 500 m²·g⁻¹, en consonancia con lo reportado por otros autores en bibliografía, y que la relación entre los microporos y los poros totales varía en función de las condiciones de síntesis y el contenido en cobre de la muestra. La adsorción de amoníaco, analizado tanto con pruebas realizadas en termobalanza como en reactor de lecho fijo a flujo, alimentando pulsos rectangulares, permitió comprobar que la velocidad de adsorción de amoníaco está relacionada con la cristalinidad de la muestra y con el contenido en fósforo de las mismas. Experimentos de adsorción de moléculas sonda mediante IR proporcionaron información acerca de las especies formadas por interacción entre los materiales y los reactivos del proceso SCR, NO y NH₃. De forma que la SAPO-34 en ausencia de metal, adsorbe amoníaco en especies fundamentalmente

tipo Brönsted, y en presencia de una cantidad excesiva de NO se nitra por sobreacumulación de especies NO, en forma de nitratos estables.

La SAPO-34 sin cobre actúa como una excelente trampa de amoníaco, principalmente con acidez tipo Brönsted, pero no tiene capacidad redox para que la reacción SCR tenga lugar, por lo que podría ser empleado en otros procesos como MTO (metanol a olefinas) o en reformado de DME. Por otro lado, se comprobó que el uso de ultrasonidos aumenta la cristalinidad de las muestras reduciendo el tiempo necesario en autoclave.

La síntesis de Cu-SAPO-34 fue llevada a cabo en un solo paso, con rendimientos a sólido superiores al 96%. No se observó la presencia de CuO o cobre metálico mediante DRX, además se mantuvieron valores altos de cristalinidad y de área superficial con respecto a los materiales en ausencia de cobre. No obstante, se apreció un aumento en los parámetros de la celda unidad obtenidos mediante análisis de Rietveld, indicativo de que el cobre altera la estructura, posiblemente por su incorporación interior.

Las especies de cobre fueron analizadas mediante diferentes técnicas complementarias. Así, mediante espectroscopia UV-vis de reflectancia difusa, se detectaron especies de Cu^{2+} en diferentes entornos, tetraédrico y octaédrico, la adsorción de CO a baja temperatura mediante IR permitió detectar especies Cu^+ , enlazándose a tres grupos carbonilo que, conforme aumenta la temperatura, evoluciona al bi y monocarbonilo, y por XPS se observó una combinación de Cu^+ y Cu^{2+} , cuya relación depende de las condiciones de síntesis.

La adsorción de amoníaco, estudiada tanto mediante IR como a flujo, indicó que, de nuevo, las condiciones de síntesis afectan a la cantidad adsorbida de amoníaco; no obstante, especies Brönsted y Lewis fueron detectadas en todos los casos, las primeras asociadas al soporte y las otras relacionadas fundamentalmente con la interacción entre el cobre y el amoníaco. La adsorción de NO, el otro reactivo principal de la reacción SCR, tiene lugar con formación de especies nitrato y por interacción con el cobre en estado +2, como $\text{Cu}^{2+}(\text{NO})$, que podrían ser las especies activas para la Reducción Catalítica Selectiva. Los materiales sintetizados son activos en el proceso, con conversiones de NO por encima del 90% a partir de 250°C.

Además, se realizó un estudio profundo por combinación de diferentes técnicas, aplicando fundamentalmente Espectroscopia IR, para discernir la situación de las especies cobre en la estructura. De forma que, se ha comprobado que el cobre se encuentra homogéneamente distribuido a lo largo de las partículas y que, por adsorción de moléculas de distinto tamaño y análisis profundo de los grupos OH, debe encontrarse en el interior de las cavidades, no siendo intercambiada sino incluida dentro de la propia estructura.

Por adsorción en IR y DRIFTS de distintas concentraciones y en diferente orden de NO, NH₃ y O₂ mediante experimentos en instantáneo y a equilibrio, se pudo proponer una posible ruta por la que tiene lugar el proceso SCR. Las especies Cu²⁺ en distintos ambientes de coordinación parecen ser las activas junto con el amoníaco adsorbido, tanto en centros Lewis como Brönsted, pudiendo transcurrir a través de dos vías diferentes: adsorción de amoníaco sobre centros Lewis (principalmente relacionados con la presencia de Cu) que rápidamente interaccionan con los NO_x de la fase gas mediante un mecanismo tipo Eley-Rideal (E-R); o por otro lado, el amoníaco adsorbido sobre cobre o sobre la zeolita interacciona con el NO también adsorbido como nitrito o nitrato tipo Langmuir-Hinshelwood (L-H).

También fue abordada la influencia de algunos compuestos externos que se encuentran en el gas de escape, tales como la presencia de material particulado o compuestos oxigenados, el envejecimiento térmico o la actividad en presencia de agua y CO₂. El *soot* no entra en el pequeño poro de la zeolita, no modifica su estructura ni altera las especies de cobre y es necesario subir en temperatura como en los filtros de partícula para eliminarlo. Aunque se ha comprobado también que es estable térmicamente, por lo que las altas temperaturas en este sentido no suponen un problema. Los compuestos oxigenados, como el metanol, pueden atravesar los poros de la zeolita y formar olefinas, oligomerizar, o craquear depositándose finalmente carbón en el interior, lo que haría que la actividad del catalizador disminuyese, sin embargo un aumento de la temperatura de operación origina una recuperación de la actividad. El pequeño tamaño de los poros de la SAPO-34 limita la entrada de compuestos de mayor tamaño por lo que su comportamiento no se vería afectado por la presencia de ellos.

La estabilidad térmica de las muestras fue analizada mediante experimentos en termobalanza, en los que se mantuvo el material un tiempo determinado a 750°C, tanto en Helio como en presencia de agua (1%), siendo caracterizado posteriormente. Se observó que durante todo el tiempo no hubo ningún proceso en el que variase la cantidad de masa o se alterase el flujo de calor y todas las propiedades estructurales fueron mantenidas después del tratamiento, indicando que los materiales son altamente resistentes al envejecimiento térmico.

En presencia de agua y CO₂, el catalizador podría presentar inferior conversión, la capacidad de almacenamiento de amoníaco se ve disminuida debido a la competencia en la adsorción entre el amoníaco y el agua en los sitios ácidos. No obstante, el agua modifica la coordinación del cobre, originando especies hidratadas o carbohidratadas que serían más activas en la reacción SCR, mejorando la actividad e inhibiendo la oxidación del amoníaco y la descomposición de los nitratos, tal y como se observó en los diferentes experimentos a flujo llevados a cabo.

Finalmente el análisis detallado de los resultados obtenidos en cada uno de los procesos individualizados y con cada uno de los catalizadores ensayados ha permitido avanzar en el estudio proponiendo el acoplamiento de las tecnologías, analizando los sistemas en forma de polvo, concretamente el sistema Pt-Ba-K/Al₂O₃ (0.4, 3.5 y 1.5 at·nm⁻² de Pt, Ba y K, respectivamente) para el proceso NSR y 2Cu-SAPO-34 (2%Cu en peso, relación P/Al igual a 0.8, sintetizada en un solo paso, con ultrasonidos, introducida en autoclave a 150°C durante 30 horas) para el proceso SCR. Aquí se plantea otro punto estratégico y es la relación óptima de lecho catalítico NSR/SCR, estableciéndose la relación 1/1 en volumen como la mejor de las estudiadas ya que, en condiciones secas que son las más desfavorables, permite disminuir considerablemente tanto el amoníaco como el N₂O.

El estudio del acoplamiento de ambas tecnologías abordado ha versado en el análisis de diferentes variables y parámetros de operación (temperatura, relación tiempo oxidación/tiempo reducción y la concentración de hidrógeno en la etapa reductora, entre otros aspectos). Para ello, se ha empleado un reactor de lecho fijo de flujo descendente, que ha permitido colocar los dos lechos en polvo separados por lana de cuarzo. Se alimentaron condiciones idénticas a las de los experimentos NSR hasta saturación y

regeneración completa empleando 2000ppm de hidrógeno (15 min-15 min). En todos los casos se ha observado que el sistema híbrido de los catalizadores NSR-SCR mejora la capacidad de eliminación de óxidos de nitrógeno y la selectividad del proceso, siendo el efecto más notable a temperaturas más bajas, en las que los parámetros de actividad catalítica de partida eran inferiores. La incorporación de un lecho SCR aguas abajo del catalizador NSR permite retener el amoniaco formado, que en la etapa siguiente reacciona con el NO_x que no es convertido, aumentando la selectividad a nitrógeno. Además, como se demostró para el capítulo SCR, los materiales Cu-SAPO-34 son capaces de descomponer el NO y el N_2O de forma directa, por lo que la cantidad de N_2O que se pudiera formar también se reduce por la actuación del material zeolítico.

En cuanto a la eficiencia del sistema dual variando los parámetros de operación, se han realizado en el mismo equipo experimental modificando las condiciones de cada experimento. De manera que, se comprobó que a concentraciones bajas de hidrógeno, próximas a la estequiométrica, son necesarias relaciones de tiempo 1:1 entre la etapa oxidante y la de reducción para alcanzar la regeneración del catalizador. Conforme aumenta la cantidad de hidrógeno, la producción de amoniaco en el lecho NSR es mayor, sin embargo, repercute favorablemente en el acoplamiento (doble lecho) necesitándose un menor tiempo para alcanzar la completa regeneración del catalizador. Una relación de tiempos de 3:1 entre oxidación y reducción con concentraciones de hidrógeno alrededor del 1% son suficientes para evitar un exceso en el consumo de agente reductor, pero consiguiéndose la regeneración del catalizador y emisiones cero de los contaminantes.

La parte final de la Memoria presentada en el Capítulo 5 consistió en el estudio del proceso combinado (NSR-SCR) con catalizadores conformados en forma de monolitos. Para ello, se ha desarrollado una metodología de síntesis reproducible de los catalizadores mediante impregnación de los monolitos de cordierita ($2\text{SiO}_2 \cdot 5\text{MgO} \cdot 2\text{Al}_2\text{O}_3$) recubiertos por una capa de Al_2O_3 (20% en peso). Para ello, se han preparado soluciones de los agentes precursores que han sido estabilizadas durante 48 horas con las cantidades correspondientes para mantener la formulación catalítica ensayada en polvo (0.4, 3.5 y 1.5 $\text{at} \cdot \text{nm}^{-2}$ de Pt, Ba y K, respectivamente) y la respectiva para la zeolita de forma que la relación en peso entre la fase activa de los dos lechos se mantenga en 1:1. Posteriormente, los monolitos han sido impregnados y mantenidos en

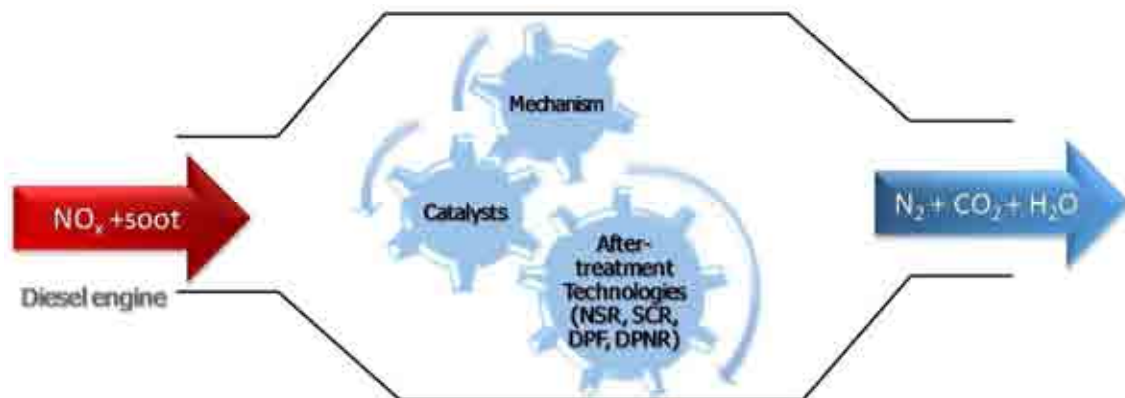
rotación durante al menos 24 horas y han sido secados y calcinados, manteniendo el mismo protocolo que para la síntesis de los catalizadores en polvo. Se ha comprobado, mediante diferentes técnicas de caracterización, que la incorporación de un 2% de fase activa, permite mantener las propiedades morfológicas del sistema que presentaban los catalizadores en forma de polvo, encontrándose las especies totalmente dispersas, con una buena adherencia y sin obstruir los canales.

Se estudió la actividad de estos materiales en eliminación de NO_x a escala de laboratorio, empleando un reactor tubular con un diámetro igual al de los monolitos y se estudiaron los parámetros de operación en las mismas condiciones que los materiales en polvo. En estas condiciones, se obtuvieron valores de eliminación de NO_x similares a los catalizadores en forma de polvo, $0.45 \text{ mmol NO}_x \cdot \text{g}_{\text{cat}}^{-1}$, aunque el tiempo para alcanzar la saturación fue alrededor de 17 horas, debido al bajo valor de la velocidad espacial y el tiempo de ruptura fue alrededor de 5.5 horas. El tiempo necesario para la regeneración también varía dependiendo de la cantidad de agente reductor, hidrógeno, empleada, de forma que para cantidades iguales adsorbidas una variación del contenido en hidrógeno entre 0.2 y 2.5% hace que el tiempo necesario para la regeneración del catalizador pase de 7 horas a media hora. Por lo tanto, se recomendaría trabajar con concentraciones entre 1 y 2.5% y tiempos de oxidación entre 7 y 14 veces mayores que el de reducción para conseguir alcanzar valores de conversión alrededor del 98%, con un slip mínimo de NO y total selectividad a nitrógeno en todo el rango de temperatura incluso en presencia de agua y CO_2 . Estos datos son indicativos del potencial que tienen los sistemas catalíticos acoplados de post-tratamiento para obtener emisiones cero en vehículos automóviles ligeros.



UNIVERSIDAD
DE MÁLAGA

1. Introduction





UNIVERSIDAD
DE MÁLAGA

1. Introduction

Nowadays, the industry and transport sectors are the main energy consumers and, in consequence, the major sources of environmental pollution. In this PhD Thesis, the emissions caused by vehicles will be considered. In Figure 1.1, the evolution of the Spanish fleet of light motor vehicles is represented according to fuel. As can be observed, in the last decades the sales of vehicles with diesel engines have been increasing even beyond of those with petrol, which have stabilized despite the economic crisis that has paralyzed the national market.

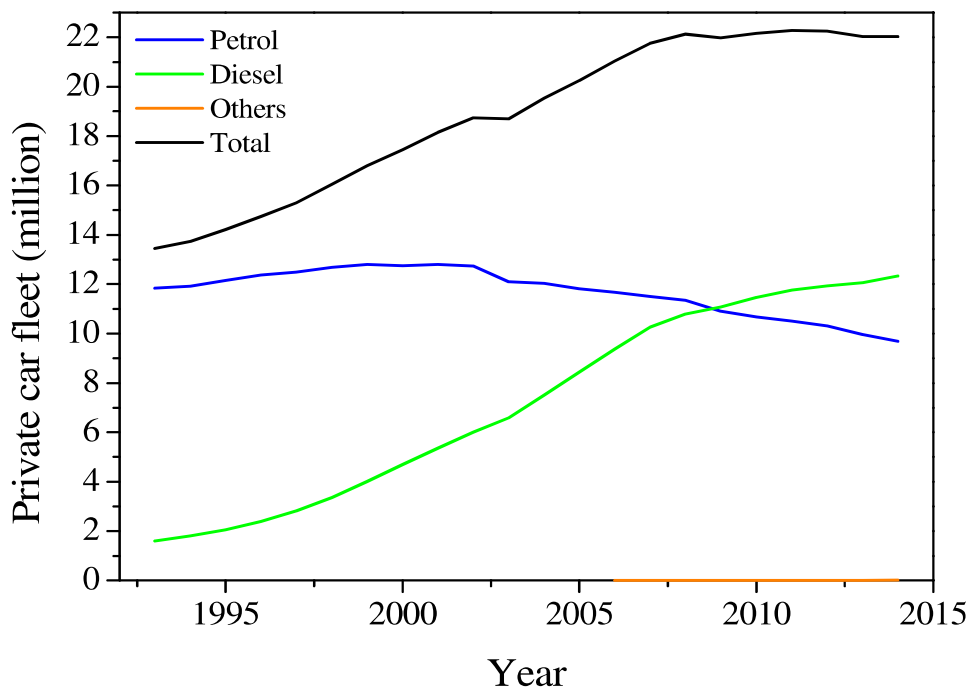


Figure 1.1. Evolution of the Spanish private car fleet according to fuel. (Source. Ref [1]).

The emergence of confidence in the diesel engines has emerged due to the fuel efficiency, reliability and durability [2–8]. The main drawback of this type of vehicle is the emission of contaminants, such as nitrogen oxides (NO_x) and particulate matter (soot) into the atmosphere, which are responsible for serious health and environmental problems [3,9–18].

Recently, many automobile manufacturers have proposed electricity as the future alternative, with plug-in hybrid, hybrid, electric and electric with hydrogen fuel cell vehicles. Nevertheless, as can be seen in the above figure, the number of these engines in the market is still low due to their limitations. Therefore, the demand for diesel

engines continues to increase worldwide and modifications, such as the incorporation of renewable fuels or changes in the operation parameters of the engine (e.g. valve timing, injection timing and speed) are being studied in order to reduce harmful emissions and preserve the reserves of fossil energy sources [19–23].

In particular, biodiesel, which can be defined as mono-alkyl esters of long chain fatty acids (FAME), is a type of green energy widely used nowadays blended with petrodiesel because of its non toxic and biodegradable nature and the decrease of CO_x and SO_x emissions; albeit a slight increase in nitrogen oxide (NO_x) emissions has been observed [24,25]. This negative effect is dependent on FAME/petrodiesel blends and the chain-length and double-bond content of fuels. The production of biodiesel starts with the choice of feedstock and even though several kinds of sources can be used such as vegetable oils, animal fats, waste or recycled cooking oil and algae, almost 95% of the biodiesel produced comes from vegetable oils such as soybean oil, rapeseed oil and palm oil the use of which directly competes with food uses [26]. The advantages of biodiesel as diesel fuel, in addition to its renewable character, are its minimal sulphur and aromatic content, its higher flash point, lubricity and cetane number and its non-toxic nature. However, biodiesel has some disadvantages such as a high viscosity, lower volatility, lower calorific value and lower oxidation stability and therefore up to now, its use in blends with petro-diesel is limited to 20% [27].

1.1. Diesel engine emissions and European legislative framework for their control

The main pollutants detected in the exhaust gases of vehicles are nitrogen oxides (NO_x), unburned hydrocarbons (HC), carbon oxides (CO_x), SO₂ and particulate matter (PM). The effects of these compounds are damaging to health and the environment. Nitrogen oxides could react with carbon monoxide and sunlight forming ozone, which irritates the respiratory system, destroys vegetation and becomes a greenhouse gas, causing ground-level photochemical smog [28]. NO₂ contributes considerably to acid rain [29]. Hydrocarbons, in addition to the already mentioned effect on photochemical smog, can cause cancer [30]. Additionally, carbon dioxide (CO₂) is one of the main causes of global warming [31] and carbon monoxide (CO) is a venom that reduces the oxygen flow in the blood and is particularly dangerous for people with heart disease. SO₂ causes acid rain, which is deposited in soils and lakes affecting forests and aquatic life. Finally,

particulate matter or soot refers to the fine particles mainly formed by carbonaceous matter, which can permeate the lungs, causing respiratory and cardiovascular diseases [32,33]. Of all these polluting substances, this PhD Thesis focuses on NO_x and soot emissions.

The terms “nitrogen oxides” encompasses the combination of NO and NO₂, which are produced during combustion in engines at high temperatures due to the reaction of nitrogen and oxygen, which does not take place at room temperature. The typical composition of a diesel engine consists of a blend of 95% NO and 5% NO₂; the latter is produced by the oxidation of NO in excess air.

The soot formation process consists of sequential nucleation, growth and coagulation steps and occurs during the combustion of carbonaceous fuels under substoichiometric conditions. Firstly, the initial formation of soot takes place in a laminar diffusion flame at temperatures between 1300 and 1430°C, where uncharged radicals and molecules appear as nucleation units. Then, these particles grow because of the addition of gaseous carbonaceous species that, finally, coagulate into aggregates.

Due to the ever increasing number of vehicles on the roads, regulation of emission limits was needed. However, the creation of laws that control air quality is recent. The first Directive on passenger vehicle emissions appeared in 1970 and it was not until 1988 that heavy-vehicle emissions were restricted. As far as the European Union is concerned, the first regulation (Euro 1) was signed in 1991 and since then, five more have been imposed, with never ending restrictions. In Table 1.1, a summary of the emission limits in diesel exhaust according to Euro directives is shown [34].

Table 1.1. Emission limits (g·km⁻¹) in diesel light-vehicle exhaust according to Euro directives.

Standard	Directive	Date	CO	NO _x	HC + NO _x	PM
Euro 1	91/441/EEC	07/1992	2.72	-	0.97	0.14
Euro 2	94/12/EC	01/1996	1.00	-	0.70	0.08
Euro 3	98/68/EC	01/2000	0.64	0.50	0.56	0.05
Euro 4		01/2005	0.5	0.25	0.30	0.025
Euro 5	2007/715/EC	09/2009	0.5	0.18	0.23	0.005
Euro 6		09/2014	0.5	0.08	0.17	0.005

The Euro 6 Standard came into force in November 2015 and, in comparison with the Euro 5, reduced the limits of NO_x from 180 to 80 mg·km⁻¹ and keeping the values of the particulate matter for diesel engines. The drastic reduction of the maximum pollutant

values, as a result of concern about the impact on health and the environment, requires an enormous effort on the part of manufacturers in order to adapt engines and exhaust to these impositions. In fact, it has been proved that nowadays not one single make complies with the latest air pollution limits (Euro 6) and there is a noticeable difference between the regulations and the real emissions as can be observed in Figure 1.2. Thus, the European Commission changed the normative and, from 2017 to 2020, the limit (80 mg·km⁻¹) can be exceeded in 110%, i.e. 168 mg·km⁻¹. In addition, from 2020 the limit can be surpassed by 50% (120 mg·km⁻¹).

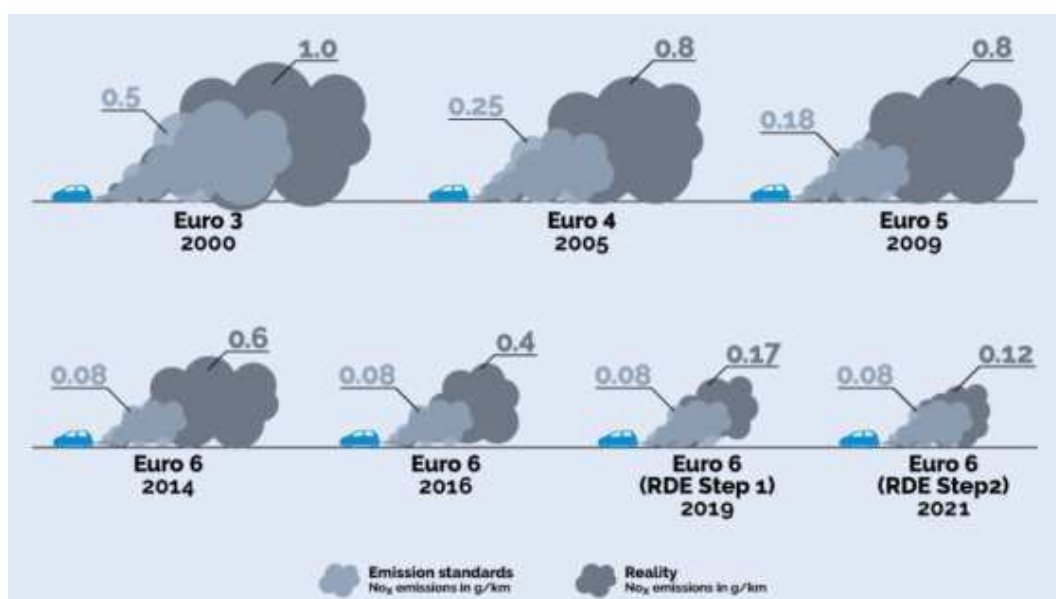


Figure 1.2. NO_x real emissions compared to the standards (Source: Transport&Environment and the ICCT [35]).

As is clear from the data, the technologies used up to now have not been effective enough to achieve the limits imposed by the regulations. Moreover, new systems are constantly being introduced to better analyze emissions, such as the real-world driving emissions (RDE), and thus, force manufactures to ensure the quality of their vehicles in terms of pollutant production. Therefore, the study and optimization of technologies to achieve these low emissions should be carefully investigated.

1.2. NO_x and soot removal technologies for diesel exhaust

There are several measures proposed for the reduction of pollutants, such as reducing vehicle weight, increasing the number of gears, recirculating the exhaust gases and modifying the air/fuel ratio. Nevertheless, the use of catalytic systems is needed if emissions are to be reduced below the regulation limits. In order to design suitable materials, the motor operation conditions must be known.

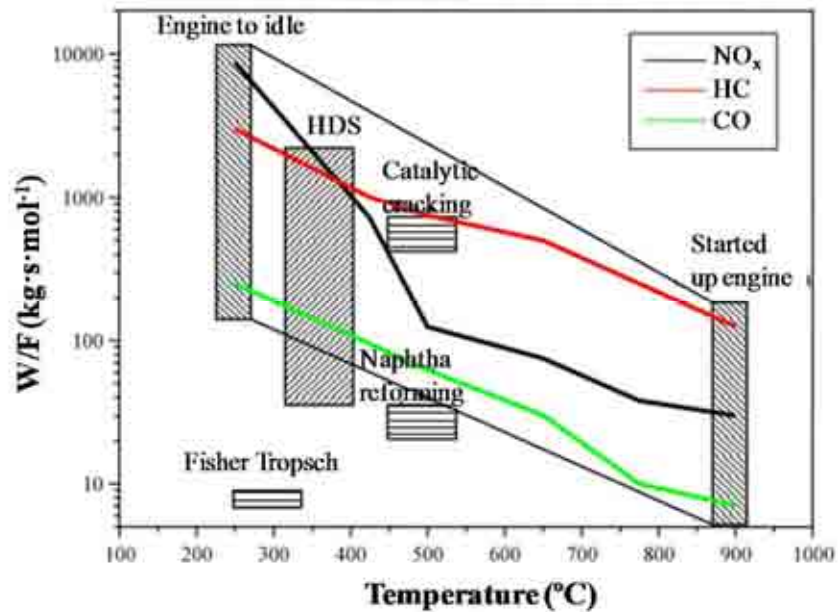


Figure 1.3. Temperature and residence time operation conditions of the automobile, from idle to full performance of the engine, in comparison with other catalyzed transformation conditions. The relative values of NO_x , HC and CO for a vehicle are included (Source. Ref. [36]).

As can be observed in Figure 1.3, industrial catalysts usually work under particular conditions and the optimization of a suitable formulation is possible. However, the catalyst design for use in vehicles is complicated, because the conditions (temperature and space velocity) oscillate over a wide range during the operation mode.

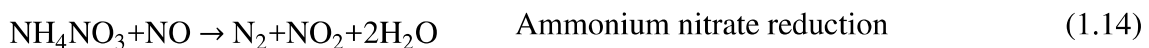
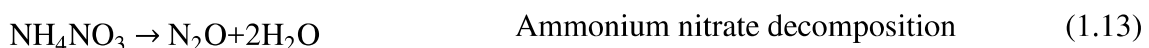
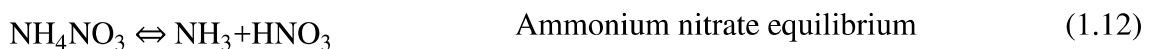
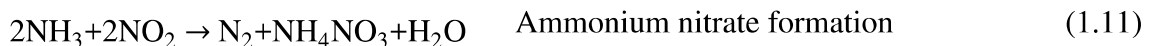
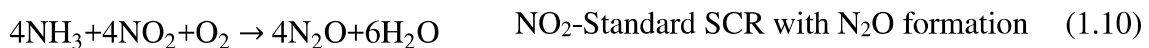
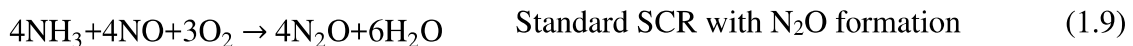
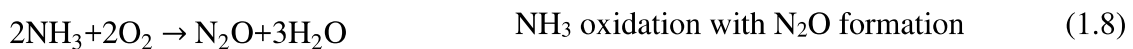
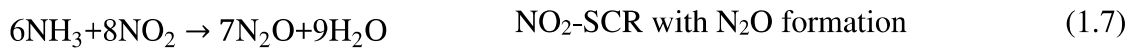
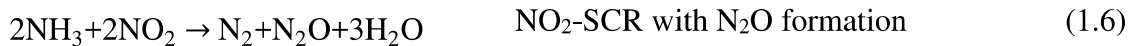
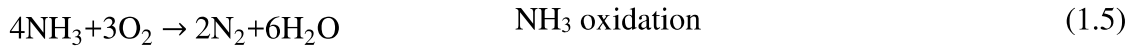
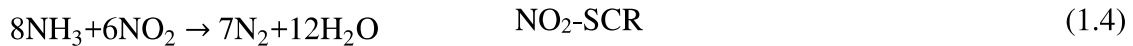
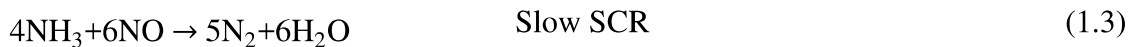
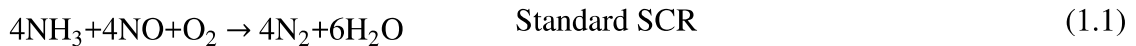
Regarding the air/fuel ratio fed into engines, whilst similar to the stoichiometric conditions (14.6) previously utilized in petrol engines, diesel vehicles work with an excess of air, obtaining a decrease in fuel consumption and CO, CO_2 and unburned hydrocarbon emissions; however, the NO_x emissions increase under these conditions. The Three Way Catalysts (TWC) are the most effective systems in NO_x reduction in almost absence of oxygen, with conversion values around 99%, and are able to simultaneously remove NO_x , CO and HC [33]. The key point of this technology is

found in the gas mixture, being necessary stoichiometric conditions with an ideal blend of fuel and air. An increase in the oxygen content, as is observed in diesel engines, could increase the reaction of oxygen with CO and HCs rather than with the NO_x; in consequence, this technology cannot be used in diesel engine vehicles. So, in this section, different techniques used in the NO_x and/or soot removal are included.

There are a large number of nitrogen oxide removal techniques which depending on the point of action can be divided in pre-combustion, during combustion and after-treatment. The most relevant after-treatment technologies are detailed forthwith.

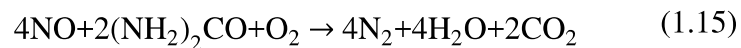
1.2.1. Selective Catalytic Reduction (SCR)

Selective Catalytic Reduction (SCR) consists of the use of ammonia from an external reducing agent, e.g. urea, which reacts with NO_x producing N₂ and H₂O, The reactions that could be involved in the process are now listed [37,38].



This technology is based on the eq 1.1-1.4 where ammonia and NO react with or without NO₂ involvement. Ammonia is always fed in sub-stoichiometric conditions in order to avoid its emission. The reaction 1.1 is called *Standard SCR* and takes place in the presence of NO and oxygen. The presence of NO₂ in exhaust gas makes the equations 1.2 and 1.4 relevant and furthermore the process is faster and occurs at lower temperatures. An increase of NO₂ up to the same level of ammonia could lead to the eq. 1.6 and cause N₂O formation, an undesired co-product. In addition, there are a series of parallel reactions that could occur with the formation of N₂O or other intermediates, such as nitrites or nitrates, which could decompose [39].

SCR technology is the most developed for the control of NO_x emissions in stationary sources, due to its efficiency, selectivity and cost. It allows the simultaneous removal of NO_x and SO_x, as well as NO_x and CO in power stations, industrial heaters and cogeneration plants [40]. Nevertheless, its incorporation in automobiles presents several problems, such as low activity at low temperatures, thermal stability at temperatures higher than 500°C and, more importantly, the necessity of incorporating a reducing agent in the vehicle, with the obvious space problems and security risks. The latter can be solved by the incorporation of a urea solution tank and then, reaction 1.15 would take place.



In 2005, this was put into practice in heavy duty commercial vehicles in Europe, where it is possible to situate the container with the solution [41]. In addition, some manufacturers have tried to apply the system in their own vehicles. In Figure 1.4, a diagram of the device is represented together with the detail of the mixture between the urea solution (commercially named Adblue) and the exhaust gas.



Figure 1.4. Vehicle diagram of the Urea system and the detail of the mixture.

Taking safety and toxicity into account, urea is the most suitable selective reducing agent for implementation in mobile sources. However, the chemistry of the DeNO_x process involves isocyanic acid formation with the consequent loss of activity [42]. Therefore, in order to incorporate SCR technology in light diesel vehicles, other possibilities should be considered so that another reducing agent can be used and the required space reduced.

SCR catalysts

In several studies it is possible to find a lot of materials widely described for their use as SCR catalysts, from vanadia-based systems to zeolites. Industrial catalysts for stationary sources are based on titanium oxide (TiO₂) as support in the anatase form with vanadium oxide (V₂O₅) and tungsten oxide (WO₃) as active phases. There is a proven synergetic effect from the combination of V and W oxide due to a strong interaction between them that results in a high reducibility of the catalyst [43]. These oxides have also been chosen because of their high activity in NO_x reduction at medium temperature range (300 – 450°C), their resistance to sulfur poisoning and affordability [44]. In spite of the well-known advantages, their implantation in mobile sources presents some inconveniences. The system is not effective at low loads or temperatures, which would be a difficulty for cold starts [42]. Their thermal stability is limited and the catalysts deteriorate at high temperatures. They are usually placed downstream to a Diesel Particulate Filter (DPF), as explained below and the temperature for DPF regeneration is high (T > 650°C). Therefore, the SCR catalyst would be exposed at high temperatures and the activity would quickly decrease. In addition, the release of toxic vanadium compounds from the catalyst at high temperatures is a main priority because of their toxic nature [45].

Nowadays, zeolitic materials are presented as more suitable NH₃-traps due to their acidity and structure [38], their high performance at low temperature conditions and their efficiency at high space velocities. Lots of zeolites have been proposed, such as ZSM5 or BETA, with completely different characteristics, framework types or Si/Al ratios, which are important factors for the catalytic properties of the materials. In Figure 1.5, the structures of the most studied zeolites for the SCR process are represented.

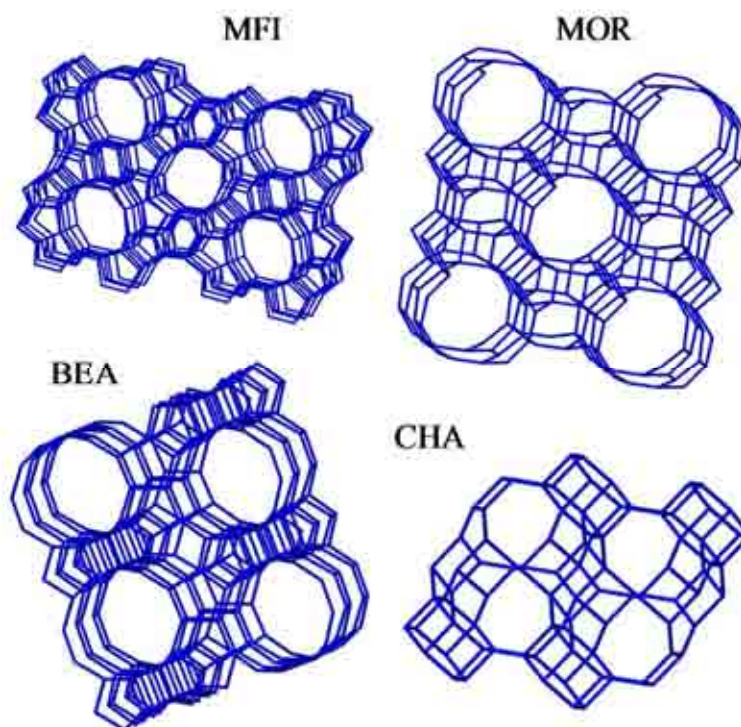


Figure 1.5. Several structures of zeolites used in the SCR process (Source: [46]).

The ZSM-5 zeolite, which has an MFI structure according to the IZA classification, displays two channels of 10 tetrahedra TO_4 , with a pore size of around 5.5 \AA and high Si/Al ratio. The Beta zeolite has a BEA structure and three systems of 12-rings channels and pore sizes of 6.4×7.6 and $5.5 \times 5.5 \text{ \AA}$, furthermore the ratio between Si and Al is found between 10 and 100. Both of them are catalogued as high-silica zeolites of medium and large pore, respectively. The Mordenite is an intermediate silica and large pore zeolite, with an 8 and 12 rings structure. The chabazite structure typical of SAPO-34 or SSZ-13 shows 6 and 8-rings, with sizes around 3.8 \AA , characteristic of small pore zeolites and, moreover, is an intermediate silica zeolite with Si/Al between 2 and 5.

Zeolites have to include a metal to have redox capacity; iron and copper have been the most studied in this technology. *M. Colombo et al.* [47] reported that copper-zeolites show a higher NH_3 and nitrate storage capacity, and present greater activity in ammonia oxidation. Besides, it is less sensitive to the feed ratio between NO and NO_2 and increases the effective range of the SCR process at lower temperatures [48].

Fe-ZSM5 and Cu-ZSM5 have been widely studied in this reaction in order to better understand the mechanism, compare the active phases and obtain the most active material; in addition, BEA and MOR interchanged with both metals have also been tested with the intention of clarifying the support influence on its catalytic properties.

The comparison between Fe-BEA, Fe-ZSM5 and Fe-MOR showed that the first presented the highest catalytic activity in the SCR due to the pseudo-tetrahedral Fe(III) species and a relatively high acidity whereas the others not only produced the side reaction of ammonia oxidation by oxygen on polynuclear octahedral Fe(III) but also participated in the N₂O decomposition caused by the stronger acidic sites [49]. On the other hand, when Cu-BETA and Cu-ZSM5 were compared, the latter was seen to be active at lower temperatures, related to the higher reducibility of copper that was detected [50]. Therefore, the catalytic properties depend not only on the support but also on the synthesis method and the active species as other authors have also tested [51].

There are several works in which the differences between the use of iron or copper are detailed [47,52]. Fe-zeolites usually have less ammonia storage capacity than Cu-zeolites and the latter being more active in the ammonia oxidation process and presenting higher SCR activity at low temperatures, as well as high efficiency in the N₂O decomposition process [53–55]. *P.S. Metkar et al.* [56] reported that the influence of the metal in the NO oxidation could be the rate determining step and concluded that the oxidation in the presence of iron is more active while the NO₂ is more strongly retained in copper. The content of metal is another key point since a high metal content could lead to extra-framework metal oxide clusters that are active for parallel reactions such as ammonia oxidation or nitrate formation [39,50,57,58]. One of the disadvantages of the use of copper is sulfur poisoning due to the stable CuSO₄-like compound formation, which affects the redox properties of the copper, inhibiting NO oxidation and, as a consequence, SCR activity [59,60]. However, the increase of the temperature above 500°C causes their thermal decomposition.

As mentioned above, the SCR catalyst would be placed downstream in the Diesel Particulate Filter (DPF), so, it has to tolerate high temperatures in the presence of water vapour. Large and medium pore zeolites, despite their excellent properties as SCR catalysts, have water stability problems [61]. The deactivation of large-pore materials is produced by the loss of the zeolite framework structure due to a poor metal/Al₂O₃ interaction [62] or the formation of oxides and metal-aluminate species [61]. Some authors [63] have shown that the impregnation of ZSM5 with phosphorous improves the hydrothermal stability of the aluminum framework. Nevertheless, such modifications are not sufficient for the suitable use of these catalysts in the process. Therefore, other types of materials have to be studied.

Recently, zeolites with small pore diameter such as chabazite (3.8Å) have been proposed to improve hydrothermal stability with regard to large pore zeolites [62,64,65]. Significant numbers of recent works compare this type of structure with other materials and ensure that SAPO-34 acts effectively in the SCR temperature range and has a better resistance to thermal aging and hydrothermal stability than others, such as SSZ-13, for example [66,67]. As a result, the search for SAPO-34 microporous materials to be used as a SCR bed is proven. However, there are some studies which indicate that the SCR-DeNO_x process is affected by strong diffusional limitations of ammonia and NO_x in the gas within the solid as catalyst. Therefore, a bimodal pore structure incorporating meso and macro pores in a monolithic structure for denoxing for stationary applications was proposed [68].

Silicoalumino phosphates (SAPOs) are a relevant type of microporous materials used mostly in the field of catalysis [69]. Their structure is similar to that of zeolites and AlPOs (i.e. microporous AlPO₄) with Brönsted acidity and they are formed from the substitution of Silicon by Phosphorus in AlPOs. SAPO-34 is probably the most interesting material in the SAPO family. It is isomorphous to the natural small pore zeolite chabazite (CHA), the topology of which might be described as layers of double six-member rings (6-MR) that are interconnected by units of 4-MR. The double 6-MR layers stack in an ABC sequence structure. This leads to a framework with a regular array of barrel-shaped cages with 9.4 Å diameter, interconnected by 8-MR windows (3.8 - 3.8 Å). Thus, SAPO-34 and CHA are small pore molecular sieves.

SAPO-34 in its protonic form is an excellent catalyst for the conversion of methanol to ethylene and propylene, in the so called Methanol to Olefin (MTO) process, developed by UOP and Norsk Hydro [70]. SAPO-34 is also an interesting material in selective adsorption technologies. In particular, it represents a promising material for N₂ rejection in natural gas processing, i.e. N₂ separation from CH₄ [71]. Similarly, it also has potential for CO₂/CH₄ separation in the treatment of natural gas or biogases [72]. Interestingly, in spite of its higher critical radius, methane is adsorbed preferentially with respect to N₂. Thus, in this case the separation capacity is not coming from a molecular sieving effect but from a preferential adsorption effect. On the other hand, the adsorption of CO₂ is stronger than that of CH₄. SAPO-34 is also found to be a potential

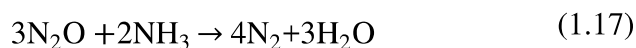
candidate for the kinetic separation of C3 hydrocarbon mixtures at near ambient conditions, due to the clearly stronger adsorption of propene than propane [73].

In spite of its very high technological interest, a number of unclarified points still affect preparation and use of this material. The effects of the preparation conditions on the properties of the resulting material in terms of phase purity and morphology are still to be fully understood and to be finely tuned [74]. A relevant factor also concerns the amount of silicon and the Al/P ratio in the final material, including the dispersion of silicon in the framework positions. It has, in fact, been reported that silicon can be substituted by phosphorus in the alternating Al-P framework positions of AIPO-34 giving rise to isolated centers, or alternatively, it can constitute silicalite-like islands [75]. As a third case, Si-Al alternating regions can be formed, similar to CHA. This determines the location and distribution of the protonic sites, including the possible interaction between the nearest Brönsted sites [76]. It seems that this strongly influences the interaction with water and also the stability of the solid associated with the tendency of Si-O-P bonds to hydrolyze.

Cu-SAPO-34 is also a crucial material, being very active and promising as the catalyst for the selective catalytic reduction of NO_x by ammonia [77–79]. Also for the preparation of this material a number of questions are still remaining open. They include preparation details, such as e.g. cationic exchange of pre-synthesized SAPO-34 [80] or one-pot hydrothermal coprecipitation, the effect of crystallinity [81] and morphology, the best composition in terms of silicon content and number of acid sites [82], the best copper loading [80], oxidation state, structure [83] and location [84] of copper active sites and their possible migration [85] during reaction or in pretreatments. Traditionally, these materials have been synthesized by hydrothermal processes, and metal-containing molecular sieves have been obtained by post-synthesis ion exchange procedures, such as wet ion exchange or chemical vapor deposition [86], that do not ensure good metal distribution inside the structure. Nevertheless, current studies are focused on the direct synthesis of these materials in one step, allowing the location of extra-framework copper species in the chabazite cages [64,87].

SCR mechanism

The SCR process mechanism has been widely studied over the years; for example, *G. Busca et al.* [88] revised the mechanisms proposed over different oxide catalysts, with possible intermediates and concluded that the reaction occurs on Lewis sites and NO is not adsorbed on V₂O₅-based catalysts before reacting, according to an Eley-Rideal mechanism. Nevertheless, the mechanism over Cu-SAPO-34 is still an open debate. All the above mentioned reactions (eqs. 1.1 – 1.15) could be involved in the processes that take place when ammonia, NO and oxygen are in contact with the zeolite. In addition, the N₂O formed on these materials could decompose to nitrogen and oxygen at high temperatures or react with ammonia by the reactions 1.16 and 1.17 [39] and NO decomposition or disproportionation could also take place.



The SCR mechanism and the active species of Cu-SSZ-13 (iso-structural material) has also been investigated [89–91]; with low copper contents, Cu²⁺ ions tends to stay close to the faces of 6-membered rings and some ions could also be positioned close to 8-membered rings when the copper load is increased. The latter could be more active in SCR and ammonia oxidation reactions due to the easier Cu²⁺/Cu⁺ redox cycling. The reaction mechanism for Cu-SAPO-34, as for Cu-SSZ-13 or vanadia-based systems, involves an acid site and a redox active species. Nowadays, these are under investigation and depend on the synthesis and properties of the material. In terms of acidity, Brönsted acid sites are recognized as the necessary species in this process [66]. Nevertheless, there is also controversy about this, as some authors have demonstrated that the Brönsted sites do not play a key role in this process or are always saturated by NH₄⁺ species [92] and others have explained that ammonia could also be adsorbed on Cu²⁺ sites [93] and the hydroxyl groups could store and supply ammonia. In DRIFTS experiments over a Cu/SAPO-34 synthesized by the ion-exchange method, other authors [94] have observed two adsorbed ammonia species (active and inactive) and the ammonia migration from the Brönsted acid sites to Lewis acid sites. The rate of this

process at low temperatures was lower than the SCR rate so it may be the rate determining step, whereas at high temperatures the rate determining step was the NH_3 adsorption. The Lewis acid sites are related to the copper content of the sample. The acid content can be adjusted by the modification of the Si proportion and, as other authors [95] have detected for different Cu/SAPO-34 synthesized by ion-exchange, the increase of acidic sites at high temperatures inhibits ammonia oxidation resulting in the improvement of SCR activity.

As far as active metal species are concerned, several authors have indicated the Cu^{2+} isolated species as the active species in the SCR reaction [80,84,96], where NO is oxidized to generate nitrites/nitrates, producing ammonia nitrites or N_2O , which act as intermediate decomposing to nitrogen and water [93]. In particular, some contributions [83] have specified that the active Cu^{2+} species are associated with the six-ring window and displaced into the ellipsoidal cavity of SAPO-34. On the other hand, other authors have detected the presence of Cu dimers and have assigned the activity of the process to these species. In this case, nitrosonium cations (NO^+) were identified as key surface intermediates in the process of NO oxidation to NO_2 and nitrates [97]. Other copper species could be formed in the zeolites and could lead to undesired parallel reactions. For example, the presence of Cu_xO_y clusters could promote ammonia oxidation by oxygen [80] or N_2O formation [98]. In addition, copper ionic pairs have been presented as active sites in N_2O decomposition [51,53,99,100].

Taking all these possible pathways into account, the SCR mechanism is still not clear. In spite of the Eley-Rideal (E-R) mechanism that has been proposed by many researchers, where ammonia is adsorbed on the Lewis acid center and then reacts directly or via an intermediate with NO or NO_2 in gas phase, the possibility of a Langmuir-Hinshelwood (L-H) with activated nitrite intermediate adsorbed on the catalyst surface cannot be discarded [101].

Hydrothermal behaviour of the zeolites

The hydrothermal stability of the zeolite and its behaviour in the presence of water are two main concerns in the use of these materials as SCR catalysts. As has been explained above, the small pore zeolites are suitable for this reaction due to the high hydrothermal stability that they present in comparison to the large pore zeolite, since the pore size is smaller than the diameter of $\text{Al}(\text{OH})_3$ and inhibits the dealumination [62,102]. In

addition, as has been demonstrated in the bibliography, copper species migrate from the external surface into the micropores during hydrothermal treatment at high temperatures [103] improving the redox ability of the aged Cu/SAPO-34 zeolite and maintaining its acidic properties [104,105]. The migration of surface clusters into the cavities also suppresses competitive ammonia oxidation [106]. During thermal aging the copper ions could be stronger bound as if structural Cu^{2+} were present [107]. However, several authors have exposed these materials to extreme conditions and have not always obtained good results. The exposure of a Cu-SAPO-34 synthesized in one-pot to a stream with 80% of humidity at 70°C produced the collapse of the structure; however, this effect decreased with an increase in copper content, and Cu^{2+} ions seem to be the active species and structure protective agents [108]. *K. Leistner et al.* [102] have also observed similar effects when a Cu/SAPO-34 synthesized by exchanged was exposed to a feed containing water vapour at temperatures below 100°C.

The study of the SCR reaction in the presence of water is also relevant because of the presence of this compound in exhaust gas. In the bibliography, some analyses about this can be found. *T. Yu et al.* [109] investigated the influence of water and CO_2 in the SCR reaction over a Cu/SAPO-34 synthesized by solid state ion exchange, and observed that the CO_2 did not present a high impact on the conversion, whereas the water presence improved the acidity of Brönsted acid sites and the reducibility of the Cu^{2+} species and, therefore, the SCR activity. As has been mentioned above, the isolated copper species are modified in the presence of water and converted into a hydrated copper species, which is the active site [91]. *U. De-La-Torre et al.* [110] observed an improvement in nitrogen selectivity at lower temperatures and did not detect a noticeable effect at medium-high temperatures. Therefore, the effect of water remains unclear in the literature.

1.2.2. NO_x Storage and Reduction (NSR)

NSR (NO_x Storage and Reduction) technology, also known as LNT (Lean- NO_x Traps) was considered the most effective method for nitrogen oxide removal in the exhaust of diesel engine vehicles in the last decade [111,112]. It consists of alternating cyclic lean-rich conditions. So that, when oxygen is in excess (lean fuel mixture), NO_x are retained and partially stored as nitrate and nitrite on the catalyst surface. These species react in the following phase (fuel rich) producing nitrogen and water [2,3,113–115].

Among NSR catalysts, Co-based oxide catalysts such as mixed oxides, perovskites and hydrotalcite-derived oxides have attracted much attention because of their excellent catalytic oxidation capacity [3]. However, standard NSR catalysts consist of precious metals and alkaline/alkaline-earth metal oxides, typically platinum and barium, respectively, dispersed on metal oxide supports such as alumina [114] with a high surface area. The noble metal catalyzes the oxidation and reduction processes and the metal oxide acts as a storage element [116,117].

During the lean phase, step in excess of oxygen, the NO_x are stored on the storage element, in the nitrate form, as can be observed in Figure 1.6.

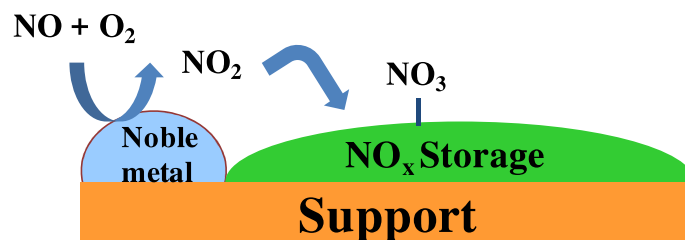


Figure 1.6. Scheme of the lean phase in NSR technology.

The process can take place along two parallel pathways [118]: the nitrate route, where NO is oxidized to NO_2 and then stored in nitrate form, and the nitrite route, with the direct oxidation of NO and its storage in nitrite form, which are subsequently oxidized to nitrates. In the rich phase, the reduction of the stored nitrogen oxides by reaction with the reducing agent takes place, as can be observed in Figure 1.7.

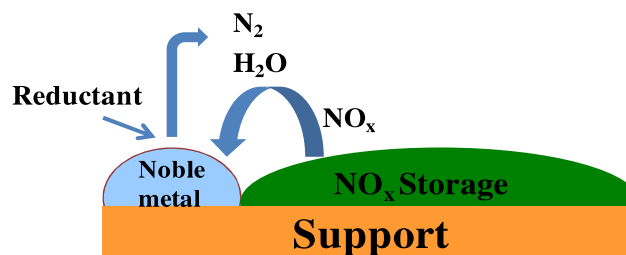


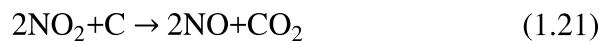
Figure 1.7. Scheme of the rich phase in NSR technology.

The rate of the NSR process depends on the proximity of the noble metal to the stored NO_x . Reducing conditions can be obtained by different procedures, such as an increase in the fuel injection, a reduction of the inlet air or a secondary fuel injection with the cylinder in full expansion. Although hydrogen, CO or unburned hydrocarbons are used as engine reductant gases in real conditions, hydrogen is usually utilized in the

experiments, because it is clean and allows the study of the catalysts simulating reducing conditions [117].

Nitrate decomposition takes place due to the decrease of the oxygen content, which reduces the stability of their equilibrium, or the temperature increase that produces the reduction [111]. In this step ammonia has been detected by several authors [119] and, in consequence, a decrease in nitrogen selectivity. This suggests that the process takes place in two steps: first, the formation of ammonia would be produced by the reaction between adsorbed NO_x and the reductant gas and then, the ammonia would react with the nitrates forming nitrogen [120]. Ammonia can also be toxic, causing irritation in the lungs and producing serious health problems, so its emission is not allowed. Therefore, solutions for ammonia control have to be proposed, such as the coupling of technologies, which is explained below.

The main disadvantages of this technology are sulfur poisoning, thermal aging, clusters formation and soot production. The latter causes a decrease in the NO_x storage capacity due to the carbonate deposition on the catalyst surface in the active sites of the storage element from the CO_2 produced in the soot combustion and the reaction between the carbon and NO_2 , which would reduce the nitrate production by the following reactions:



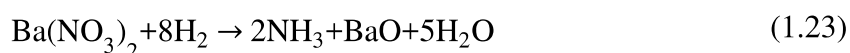
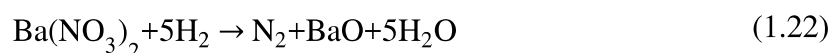
As soot removal is another key point of this PhD Thesis, it will be described in depth in the next section. The reaction between SO_2 , which is present in exhaust gas, and the catalyst surface oxygen is responsible for the catalyst deactivation by sulfur, since sulfates would be formed and are more thermally stable than nitrates and would cover the catalyst active surface reducing the amount of active centers for the adsorption [121]. The acidity of the support influences the resistance to sulfur poisoning, improving its behavior as the acidity of the catalyst increases and, consequently, the incorporation of TiO_2 to the support would allow a better resistance. Another possibility that has demonstrated high durability values consists of using a solid solution of ZrO_2 - TiO_2 in order to stabilize the alumina [122]. The addition of Ce to the support or the use of CeO_2 as support has shown a high performance in the sulfur poisoning [121]. Other

authors [123] have also observed an improvement in the sulfur poisoning resistance when tin is added to the formulation, since the sulfate stability is decreased.

Alumina has been widely used in these types of catalyst due to its capacity for maintaining properties constant irrespective of temperature. However, its characteristics can be improved, by adding CeO₂-ZrO₂ or ZrO₂-TiO₂, which would have high thermal stability and would sustain the high platinum dispersion [124]. In addition, the sintering of the metals over the support decreases the activity by the formation of clusters that are not effective in the process; in order to avoid the production of these species, several authors have proposed the use of ceria [125,126].

The most studied catalyst for the NSR process is Pt-Ba/Al₂O₃. Barium content above 10% produces a negative effect in the morphological properties of the catalyst and in the platinum dispersion, however, adsorption capacity increases, obtaining the maximum value for monolayer coverage [127]. The reduction of the Pt dispersion is caused by the fast exothermic decomposition of the barium precursor.

Ammonia formation has been detected when this catalyst is studied, as has been previously mentioned and, in consequence, the nitrogen selectivity decreases. This is due to the competition between two parallel reactions that can occur in the regeneration step and are now specified, supposing that the NO_x are stored in the barium as nitrates [113].



It has been demonstrated that the synthesis procedure influences both the properties and the catalytic activity of the materials. The use of diamminedinitroplatinum and barium acetate as precursors provokes a high activity in NO_x storage because of the interactions between the metals and between the metals and the support, since it causes a good dispersion of barium and there are plenty of accessible platinum sites [128]. The order in which the metals are added to the support also modifies their adsorption capacity, obtaining better results with the impregnation of the noble metal supported catalyst by the storage metal [129].

There are a lot of parameters that influence the catalytic properties of standard Pt-Ba/Al₂O₃ as well as several concerns that have to be studied, such as soot formation and ammonia production. In the following sections, these aspects are going to be detailed.

1.2.3. Soot removal

The particulate matter is mainly composed of carbon that adsorbs soluble organic fraction (SOF), sulphates and water. The ratio between SOF and soot is modified depending on engine operation conditions and is higher when the engine is working at low loads, i.e. at low temperatures. The amount of sulphate is usually less than 5% [10]. Soot consists of small fractions of particle agglomerates (15-30 nm of diameter) made up of carbon and ash traces of metal and covered by condensates of heavier organic compounds and sulphates together with nucleating particles composed of condensed hydrocarbons and sulphates [130]. The soot formation takes place in a series of phases [131,132], starting with the sequential nucleation in which gas phase molecules forms small centers of soot in a laminar diffusion flame. Then, these centers grow and coagulate by gas carbonaceous species addition. These aggregates can also adsorb other molecules and semivolatile polycyclic aromatic hydrocarbons.

There are two ways to remove the particulate matter (PM) effectively. One of them consists of using a Diesel Oxidation Catalyst (DOC), whose main function is to selectively oxidize CO and a wide range of hydrocarbons that are part of the soot. This type of system is located just downstream of the engine and is usually a cordierite support structure through which exhaust gas flows. It is covered with a high surface area washcoat where the active phase is supported. Catalysts based on cobalt, iron or manganese oxides with noble metals such as platinum or palladium are the most common [6,133,134]. The most widely used system in PM removal is the Diesel Particulate Filter (DPF). This filter consists of a monolithic device with porous walls, through which the gas from the engine passes, while the particles are retained [5,135–139], as can be observed in Figure 1.8.

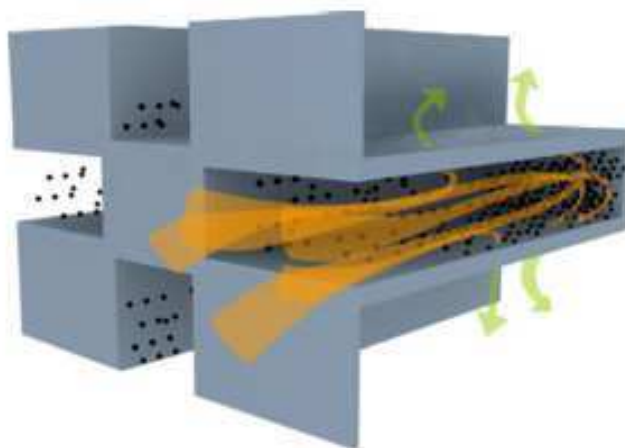


Figure 1.8. Sketch of the flow through the channel wall of a DPF [137].

To prevent these particles hindering the circulation of gas, when the pressure rises to a certain level, the system sends a small amount of fuel that causes an increase in temperature and burns the entire number of particles deposited on the filter. So, being completely regenerated, it can continue working in optimal conditions. A wide range of catalysts has been studied for this purpose, such as single and mixed metal oxides or perovskite- and spinel-type oxides [134,139–142]. Some authors believe that the addition of potassium combined with platinum to the catalyst formulation is one of the most promising options for soot oxidation [10,134]. The role played by alkali metals and alkaline-earth metals in removing soot is under investigation. *L. Castoldi et al.* [140] have indicated the beneficial effect of these metals in catalyst formulation for soot removal, both in the catalyst as in the particulate filter.

In order to improve catalyst formulation it is necessary to understand the behaviour of each of its elements in the particulate matter removal process. For this reason, the soot oxidation mechanism with and without catalysts has been extensively reported in literature [143,144]. This process has generally been studied using thermogravimetric analysis (TGA) since it allows for working with gas-solid reactions and distinguishing between competing models [141,145,146]. Besides this type of analysis, the physical contact between soot and the catalyst is another factor to consider, because soot combustion in air on a catalyst takes place via a three-phase reaction. Tight contact mode is the most used method to study this mechanism; although it does not represent the real situation, it makes the study of the intrinsic catalytic combustion of soot possible [9,141,146–148].

In the absence of a catalyst and in the presence of air *R. Lopez-Fonseca et al.* [149] postulated that combustion occurs through a single-rate process, which involves the penetration of oxygen and the subsequent combustion of soot inside the porous structure. This reaction could be via the dissociative chemisorption of oxygen, which leads to oxygen radicals that subsequently form (unstable) surface oxygen complexes that decompose forming CO and CO₂ [131,143].

The mechanism of soot removal in other oxidizing atmospheres has also been proposed [144,150]. When NO₂ and O₂ are both present in the gas mixture, it is assumed that the oxygenated carbon complexes are formed firstly by the reaction between soot and NO₂, enhancing soot oxidation at lower temperatures [114,144,150]. The metal-catalysed reaction mechanism could be similar to the non-catalytic reaction [2,143]. It has been shown that the presence of soot decreases the NO_x storage activity of the catalysts, due to an interaction between soot and the stored NO_x that provides an additional route for oxidation of the carbonaceous material [5,12,114,131,151,152]. However, the mechanism for soot removal in the presence of alkaline or alkaline-earth metals has to be better understood.

1.2.4. Diesel Particulate-NO_x Reduction System (DPNR)

In view of the limitations imposed by current legislation, nowadays the interest in simultaneous removal of NO_x and soot has increased. The most used technology for this purpose is known as Diesel Particulate-NO_x reduction (DPNR) developed by Toyota [11,12,114,134,151]. In fact, the DPNR system is the main part of the D-CAT (Diesel Clean Advanced Technology) technology, which has been introduced in several models and is represented in Figure 1.9.

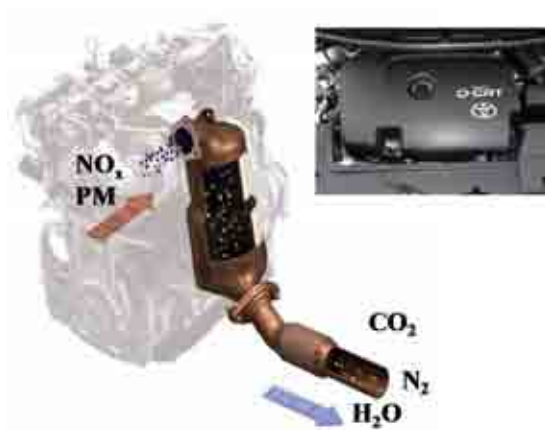


Figure 1.9. Diagram of the D-CAT system of Toyota.

This technique consists of using a porous ceramic filter coated with a catalytic layer composed of a high surface area support (such as a gamma Al_2O_3), a noble metal (Pt) and an alkali or alkaline-earth metal oxide, which present a high NO_x storage capacity. The procedure is similar to NSR technology as it works in cyclic conditions, alternating fuel-lean phases, during which the nitrogen oxides produced by the engine are adsorbed on the storage element, with rich fuel phases in which the nitrates are reduced to nitrogen, as was explained above [2,11,153–156]. The stored nitrates decrease the soot combustion temperature. However, it must be taken into account that there is a minimum combustion temperature, which cannot be reduced by the use of catalysts, since it depends on the characteristics of the soot [157].

Since the idea of simultaneous removal of NO_x and particulates (PM) in a single trap was proposed [158] many systems have been investigated for this purpose, but the catalytic technology of simultaneous emission control, especially at low temperatures, is still an open debate [153,159,160]. Although other catalysts have been proposed for this aim, such as noble metals [16,114,147], zeolites [161] perovskite-related oxides [162]; spinel phases [163] and hydrotalcite-derived compounds modified by transition metal ions [13,148], which exhibit excellent properties, the proposed NO_x storage-reduction mechanism in the Diesel Particle NO_x Reduction system (DPNR) is similar to that already announced by Toyota for Lean NO_x Traps [164–166] and, in consequence, similar catalysts are used. The Pt-Ba system supported on $\gamma\text{-Al}_2\text{O}_3$ is the most studied NSR catalyst, and catalyst modification by other components, such as Sn, K, Ag, Co, Fe or Ceria have been investigated [2,126,153–156,167,168]. Modified systems showed high stability, enhanced soot combustion and improved resistance to sulfur poisoning [2,153,156]. Although, the catalysts modified with potassium show a comparable and improved performance in soot removal aspects, compared to standard Pt-Ba systems, some concerns remain, especially related to the volatile nature of K-species, catalyst regeneration, NO and ammonia release [2,11,123,134,152,169,170]. In addition, other aspects to consider are active site dispersion and catalytic supports, since the latter can provide an optimal platinum dispersion, lower surface carbonation than barium and a good interaction between active centers [113,171–173].

1.2.5. Coupling of after-treatment technologies

At present, NSR technology is the most efficient in removing nitrogen oxides from diesel exhaust gases; however, it is not enough to achieve zero emissions at the outlet of the vehicles, due to the formation of an NH_3 slip that is strongly dependent on the formulation and the conditions. The SCR system, which is based on the mineralization of NO_x to N_2 and water with ammonia [134,174], requires the injection of an external reducing agent, which makes its implementation in mobile sources difficult. Therefore, the coupling of SCR and NSR technologies is being widely studied to solve this drawback [50,175–178].

The idea consists of placing a SCR catalytic bed downstream of the NSR catalyst, so that the ammonia produced during the lean phase in the LNT-catalyst can be stored in the SCR catalyst and, then, it would react with the unconverted NO_x in the oxidant phase, increasing the NO_x conversion and the nitrogen selectivity. A possible distribution of its implementation in the exhaust gas of a diesel engine vehicle is schematised in Figure 1.10. Commercially, the system was implemented in the Mercedes E320 Bluetec vehicle in 2007 [179]. The main advantages of this system as compared to the single NSR catalytic bed are: the increase in NO_x conversion values, a wider operating temperature window, the improvement of the catalyst durability and the reduction of unburned hydrocarbon production due to reaction in the SCR catalyst [175].

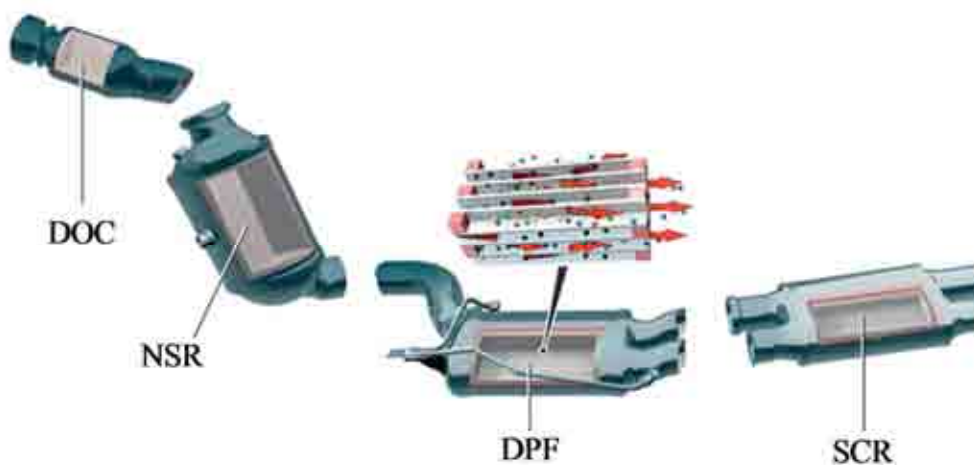


Figure 1.10. Possible distribution of the coupling of technologies in the exhaust gas.

Although there are a large number of contributions that have proposed this configuration as the most effective for NO_x removal, they have been mainly focused on the study of each catalytic bed independently. So, it is necessary to delve into the study of coupling of technologies and their possible application in real conditions. Several authors have studied the coupling of standard Pt-Ba/Al₂O₃ and the Fe-ZSM5 zeolite in powder [177,180,181], detecting higher nitrogen production in the overall cycle. In the double-bed configuration, higher levels of nitrogen are detected in the lean phase, due to the reaction of the nitrogen oxides with the ammonia that has been stored in the previous rich phase. The physical mixture of the catalysts produces a lower amount of nitrogen in the rich phase because one of the nitrogen production routes uses ammonia as intermediate and, with the zeolite being so close, the ammonia formed could be adsorbed on the zeolite and, thus, the nitrogen formation would decrease. Similar results have been obtained by other authors when the Cu-ZSM-5 was placed downstream of a Pt-Rh-Ba/Al₂O₃ [182] or when Cu-ZSM-5 is substituted for Co/Al₂O₃ [183]. The use of Ag/Al₂O₃ had no impact as an SCR catalyst.

With the intention of replacing the zeolites as SCR catalysts, some authors [184] have developed materials based on modified alumina and prepared by sol-gel method, with the required acidic and redox properties, by the introduction of metal ions such as cerium (for oxygen mobility), titanium, zirconium and silica. Although, these materials are effective in the NH₃-SCR reaction together with the NH₃-SCO (Selective Catalytic Oxidation), the zeolite with the incorporation of copper, as has been explained in the SCR section, is the most effective material that can be used in this technology up to now. Nevertheless, the incorporation of ceria to the LNT-formulation would enhance ammonia production and NO_x adsorption [126,185,186]. As far as copper zeolites are concerned, materials prepared by ion exchange or impregnation have been studied in granular and monolithic form [50,110,187]. In addition, large and small pore zeolites have been used and, again, a higher hydrothermal stability and a wider operation temperature window were observed when the small pore zeolites were analyzed. In all cases, ammonia formation was negligible and N₂O selectivity decreased with the use of double-bed configuration.

The formulations have also been tested in monolithic form, both in separate monoliths depending on the technology used and as layers within the same cordierite support. In addition, the simulation has been carried out and a theoretical optimal thickness has

been obtained between 45 and 20 μm depending on the cycle time [188]. The reduction time or the ratio between oxidation/reduction period times is another key point in the behaviour of these materials. A decrease in the rich pulse length causes a reduction in the NO_x removal efficiency, because insufficient time was available for the completely regeneration of the catalysts [183,189].

Therefore, the synthesis of Cu-zeolites materials in powder and monolithic structure and the study of these in double bed configuration is still an open debate, as are also the cyclic conditions that seem to influence catalytic behaviour.

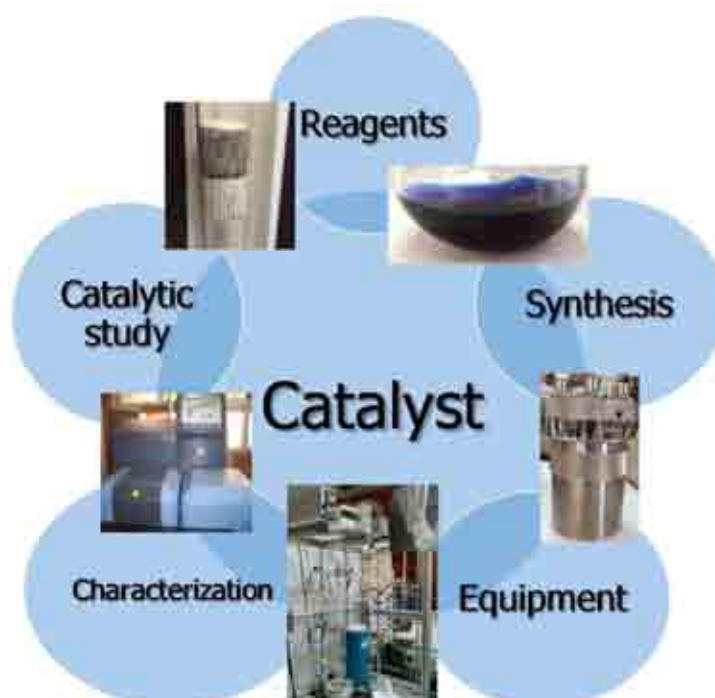
1.3. Objective

NSR and SCR after-treatment catalytic technologies for De-NO_x in diesel engines are far from being introduced in light vehicles in the short run obtaining zero emissions. Therefore, the overall aim responds to the title of the PhD Thesis "After-treatment technologies coupling for zero emissions in light vehicles". The individualization of both technologies is going to be addressed, from the catalyst synthesis, the study of the role of the active phases in the catalyst and their performance in *quasi*-real conditions to the coupling of the LNT with NH₃-SCR systems.

For this purpose, the PhD Thesis was organized in three targets that coincide with the three sections of results and discussion in which the PhD Thesis is divided:

- Going into detail about the knowledge for obtaining a supported LNT-catalyst with surface coverage lower than the monolayer, which combines the maximum NO_x adsorption and regeneration capacities without being modified by water, CO₂ or particulate matter presence together with the study of the chemistry of the soot removal process, differentiating the mechanism based on the reaction occurrence and the kinetic parameters.
- Determining an approachable synthesis route able to be expansible, with large amount of sample, of a model catalyst that maximizes the copper content inside the small pore zeolitic structure, which promotes the NO_x removal by SCR reaction with external ammonia supply. Moreover, clarifying a plausible mechanism approach for De-NO_x by SCR, analyzing the influence of other compounds in the performance.
- Studying how to couple the catalysts of both technologies for obtaining a hybrid system and how to scale at laboratory levels the catalysts in monolithic form to operate under close to real conditions.

2. Experimental





UNIVERSIDAD
DE MÁLAGA

2. Experimental

The materials used in the catalyst synthesis and in the reactivity studies, together with the experimental procedures and the data treatments, are explained in this chapter.

2.1. Reagents

- ***γ-Alumina Puralox TH***: γ -Alumina supplied by *Sasol*, with a total pore volume of $1 \text{ cm}^3 \cdot \text{g}^{-1}$ and surface area value of $144 \text{ m}^2 \cdot \text{g}^{-1}$.
- ***Diamminedinitroplatinum (II) (Pt(NH₃)₂(NO₂)₂)***: salt used as platinum precursor, provided by *Aldrich Chemical*, with a density of $1.05 \text{ g} \cdot \text{cm}^{-3}$, a molecular weight of $321.16 \text{ g} \cdot \text{mol}^{-1}$ and concentration of 3.4 % (w/w) in ammonium hydroxide solution.
- ***Barium acetate (Ba(CH₃COO)₂)***: salt employed as barium precursor, supplied by *Merck*, with a molecular weight of $255.43 \text{ g} \cdot \text{mol}^{-1}$ and 99% of purity.
- ***Potassium acetate (K(CH₃COO))***: salt utilised as potassium precursor, provided by *Fluka*, with a molecular weight of $98.14 \text{ g} \cdot \text{mol}^{-1}$ and 99% of purity.
- ***Printex U***: model soot supplied by *Degussa*, with a specific area of $97 \text{ m}^2 \cdot \text{g}^{-1}$ and the following composition: 97.17 % of C, 1.16 % of H, 0.19 % of N and 0.31 % of S (minimum ash content).
- ***Aluminum isopropoxide (Al[OCH(CH₃)₂]₃) or IPA***: precursor of the aluminium, provided by *Alfa Aesar* in granular form, with a molecular weight of $204.25 \text{ g} \cdot \text{mol}^{-1}$, a density of $1.035 \text{ g} \cdot \text{ml}^{-1}$ and purity higher than 98%.
- ***LUDOX® HS-40 colloidal silica***: used as silica precursor, supplied by *Sigma Aldrich* as a 40wt.% suspension in H₂O with a molecular weight value of $60.08 \text{ g} \cdot \text{mol}^{-1}$.
- ***ortho-Phosphoric Acid (H₃PO₄)***: provided by *Panreac*, with a molecular weight of $98.00 \text{ g} \cdot \text{mol}^{-1}$, 85% of purity, and a density of $1.7 \text{ g} \cdot \text{ml}^{-1}$.
- ***Diethylamine (C₄H₁₁N) or DEA***: employed as the structure director agent, supplied by *Sigma Aldrich* with a molecular weight of $73.14 \text{ g} \cdot \text{mol}^{-1}$, a density of $0.707 \text{ g} \cdot \text{ml}^{-1}$ and more than 99.5% of purity.

- **Copper sulphate (CuSO_4):** salt used as copper precursor, provided by VWR Chemicals, with a molecular weight of $159.61 \text{ g}\cdot\text{mol}^{-1}$ and 99.4% of purity.
- **Tetraethylenepentamine ($\text{C}_8\text{H}_{23}\text{N}_5$) or TEPA:** utilised as complexing agent, supplied by Sigma Aldrich with a molecular weight of $189.30 \text{ g}\cdot\text{mol}^{-1}$ and a density of $0.998 \text{ g}\cdot\text{ml}^{-1}$.
- **Acetonitrile (CH_3CN) or AN:** supplied by Sigma Aldrich, anhydrous and with a molecular weight of $41.05 \text{ g}\cdot\text{mol}^{-1}$.
- **Pivalonitrile ($(\text{CH}_3)_3\text{CCN}$) or PN:** provided by Sigma Aldrich, with a molecular weight of $83.13 \text{ g}\cdot\text{mol}^{-1}$ and more than 98% of purity.
- **Monolith (Core):** cylindrical cordierite structure ($2\text{SiO}_2\cdot 5\text{MgO}\cdot 2\text{Al}_2\text{O}_3$) impregnated with an Al_2O_3 layer (20wt.%) provided by Johnson Matthey, with 400 cpsi, 1x4" (inch), a specific surface area of $20 \text{ m}^2\cdot\text{g}^{-1}$ and a pore volume of $0.31 \text{ cm}^3\cdot\text{g}^{-1}$.

2.2. Gases

The gases used in the experiments for both in situ and flow reactivity are detailed below.

- **Nitrogen monoxide (NO):** with a molecular weight of $30 \text{ g}\cdot\text{mol}^{-1}$ was provided by Abelló Linde as a cylinder of pure gas for probe molecule adsorption experiments and in diluted form (3000ppm of NO and 1500ppm of Ar in He) for flow tests.
- **Ammonia (NH_3):** with a molecular weight of $15 \text{ g}\cdot\text{mol}^{-1}$ was supplied by Abelló Linde as a cylinder of pure gas for probe molecule adsorption experiments and in diluted form (3% of NH_3 and 3000ppm of Ar in He) for flow tests.
- **Oxygen (O_2):** with a molecular weight of $32 \text{ g}\cdot\text{mol}^{-1}$ was provided by Abelló Linde as a cylinder of pure gas for probe molecule adsorption experiments and in diluted form (20% of O_2 in He) for flow tests.
- **Hydrogen (H_2):** with a molecular weight value of $2 \text{ g}\cdot\text{mol}^{-1}$ was supplied by Abelló Linde with 3% of hydrogen and 3000ppm of Ar in He.
- **Helium (He):** with high purity and a molecular weight of $4 \text{ g}\cdot\text{mol}^{-1}$ was provided by Abelló Linde.

- **Nitrogen dioxide (NO_2):** with a molecular weight of $46 \text{ g}\cdot\text{mol}^{-1}$ was supplied by *Abelló Linde* as a cylinder with 3000ppm of NO_2 , 2% of O_2 , 2% of N_2 and 2000ppm of Ar in He.
- **Carbon monoxide (CO):** with a molecular weight of $28 \text{ g}\cdot\text{mol}^{-1}$ was provided by *Abelló Linde* as a cylinder of pure gas for probe molecule adsorption experiments.
- **Carbon dioxide (CO_2):** with a molecular weight of $44 \text{ g}\cdot\text{mol}^{-1}$ was supplied by *Abelló Linde* as a cylinder of 5% of CO_2 and 5000ppm of Ar in He for flow experiments.

2.3. Equipment

In this section, the equipment and instrumentation used in the experimental part of the PhD Thesis are described, indicating their purpose, technical characteristics and operation conditions (Laboratory 1 – University of Malaga, Laboratory 2 – University of Genoa, Laboratory 3 – Polytechnic of Milan, Laboratory 4 – University of the Basque Country).

2.3.1. Autoclave

For the hydrothermal synthesis process, an autoclave from *Parr Instruments* was utilized. It was composed of a Teflon glass with a capacity of 125 cm^3 and a stainless steel container, able to withstand a maximum temperature and pressure value of 250°C and 1900 psig, respectively.

2.3.2. Ultrasonic Processor

The Ultrasonic Processor UIP1000hd (Hielscher) with an unchangeable frequency of 20 kHz was used in the preparation of the gel precursor of the zeolitic materials using a titanium sonotrode. The ultrasonic power intensity was $300\text{W}\cdot\text{cm}^{-2}$.

2.3.3. Furnace

A tubular Carbolite-CST1000 model furnace, from *Heareus* was employed in order to thermally treat the materials. It consisted of a refractory inner tube that can reach a temperature of 1000°C (1273K). The temperature was adjusted by a Eurotherm 808 controller.

2.3.4. Fourier Transform Infrared Spectroscopy (FTIR)

Infrared studies were carried out in different conditions and with different equipment depending on the purpose of the experiment. In every case, 100 scans were registered in the range between 4000 and 400 cm^{-1} with a resolution of 4 cm^{-1} and KBr beam splitters. For IR skeletal studies, an Avatar 380 Nicolet FT Instrument with DTGS detector was used (Lab. 2). Probe molecule adsorption were carried out in an IR cell connected with a conventional outgassing/gas manipulation apparatus and spectra were recorded in a Nicolet Nexus 6700 spectrometer (Lab. 1) or Nicolet Nexus FT Instrument (Lab. 2), with MCT and DTGS detectors, respectively. The systems were also composed of a vertical furnace that allowed the thermal treatment of the samples. The samples were pressed into 13 mm disks using a hydraulic press and placed in the sample holder of a quartz cell with KBr windows, permanently connected to a conventional vacuum line ($\approx 1 \cdot 10^{-4}$ torr).

2.3.5. Diffuse Reflectance Infrared Fourier Transform Spectroscopy (DRIFTs)

FTIR in situ experiments were performed in a continuous flow DRIFT Harrick Praying Mantis™ reaction chamber, connected to the QMS 200 mass spectrometer. Spectra were registered in the Nicolet Nexus 6700 spectrometer, working with the same parameters as the FTIR experiments. The temperature was adjusted by the Harrick ATC low voltage controller with a K-type thermocouple.



Figure 2.1. Nicolet Nexus 6700 Spectrometer with the DRIFT reaction chamber, which is shown in the inset.

2.3.6. Thermobalance

The TG/DSC data were acquired using an SDT Q600 thermobalance from *T.A. Instrument*. The parameters were calculated as the difference between the sample and the empty reference pan. The measurement and control of the temperature were carried out by two platinum/platinum-rhodium thermocouples in the range between atmosphere temperature and 1500°C. The system was equipped with a horizontal furnace and two gas feeding tubes, one of them for the helium purge ($80 \text{ cm}^3 \cdot \text{min}^{-1}$) and the other for the reaction gases ($20 \text{ cm}^3 \cdot \text{min}^{-1}$). The gas control was performed by an external mass flow controller and the product distribution analysis was accomplished by the QMS 200 mass spectrometer.



Figure 2.2. SDT Q600 Thermobalance with the detail of the sample pans.

2.3.7. Flow reaction systems

Catalytic tests were carried out in three different systems with several analyzers depending on the University. In all cases, the feed gases flowed down through a fixed catalytic bed and the valve positions allowed the alternation of oxidant/reducing atmospheres.

Laboratory 1: the equipment consisted of a quartz tubular fixed bed reactor, where there is no radial diffusion and with a narrowing after the bed in order to prevent the occurrence of secondary reactions, located inside an electric furnace that was regulated by a PID controller (TIC, TOHO TTM-0005), where 60 mg of powder catalyst (100 – 120 mesh) was placed. The feed stream was adjusted by the PID 1831 mass flow controller, specifically calibrated for each gas. The total flow was $100 \text{ cm}^3 \cdot \text{min}^{-1}$, corresponding to a Gas Hourly Space Velocity (GHSV) of $3 \cdot 10^4 \text{ h}^{-1}$. The Pfeiffer Prisma™ Quadrupole Mass Spectrometer QMS 200 and the μGC 3000A from Agilent were used to analyze the product distribution. The following mass/charge ratios were used to monitor the evolution of the involved species concentration during the reactions: 2 (H_2), 4 (He), 15, (NH_3), 18 (H_2O), 28 (CO or N_2), 30 (NO), 32 (O_2), 40 (Ar), 44 (CO_2 or N_2O) and 46 (NO_2). The analysis of the mass/charge ratio 12 (C) and 14 (N) were registered to differentiate the lines in which two compounds coincide. The quantification of the QMS data was carried out using experimental factors that had been obtained during the calibration process, which was performed with calibration mixtures. In addition, the μGC allowed the identification of N_2O , CO , CO_2 , O_2 and N_2 .

For the experiments with the catalysts conformed in the monolithic structure, the same equipment was used, utilising another type of reactor that consisted of a quartz tube, with a diameter of 1" and a narrowing at the outlet, that allows the work in laminar flow conditions, similar to those that can be found in a vehicle.

Laboratory 3: this micro-reactor was composed of a quartz tube (7 mm I.D.) loaded with 60 mg of powder catalyst (100 – 120 mesh). The total flow was $100 \text{ cm}^3 \cdot \text{min}^{-1}$, corresponding to GHSV of $3 \cdot 10^4 \text{ h}^{-1}$. The reactor was directly connected to three analysers in parallel: i) a mass spectrometer (Thermostar 200, Pfeiffer), in which the same lines as in Lab. 1 were registered and an identical calibration protocol was carried out; ii) a UV- NO_x analyser (LIMAS 11 HW, ABB) to obtain the concentration of NO ,

NO₂ and NH₃; iii) a micro-gas chromatograph (3000A, Agilent) to obtain the N₂, N₂O, CO, CO₂ and O₂ composition.

Laboratory 4: the reaction system consisted of a stainless steel reactor with 1 cm³ of granular catalyst (35 – 50 mesh) that was placed in a 3-zone tube furnace. The temperature was measured at the top of the catalytic bed. Gases were fed via mass flow controllers and the total flow rate was set at 2·10³ cm³·min⁻¹, associated with a GHSV of 9·10⁴ h⁻¹. The total flow was changed in order to decrease the GHSV to 5·10⁴ h⁻¹. The analysis system was composed of an FTIR multigas analyser (MKS 2030) followed by a mass spectrometer (Quadrupole Mass Spectrometer).



Figure 2.3. Flow reaction systems in a) Lab.1, b) Lab.3 and c) Lab. 4.

2.4. Catalyst synthesis

2.4.1. Powder catalysts

2.4.1.1. NSR catalysts

The NSR catalysts consisted of a high surface area supporting material (γ -Al₂O₃), an oxidation component (noble metal, Pt) and a NO_x storage element (alkaline or alkaline-earth metal oxides). The synthesis method and the order of elements addition influence the catalyst properties. So, the catalysts were prepared by wetness impregnation by the following procedure. First, the Pt/ γ -Al₂O₃ monometallic catalyst was obtained after impregnation of the support (γ -Al₂O₃) with an aqueous solution of diamminedinitroplatinum (II), dried overnight at 90°C and calcined for 3 hours at 350°C in air. Then, Ba, K or a simultaneous mixture of both was introduced as aqueous solutions of barium acetate or potassium acetate in the Pt/ γ -Al₂O₃ catalyst to obtain the bimetallic or trimetallic catalysts. The final calcination was performed at 500°C (5°C·min⁻¹) for 5 hours in air.

From all the series that were prepared varying the ratio between the metals, the most representative and optimized powder catalysts obtained are presented in Table 2.1, where the identification and the components weight percentages are included.

Table 2.1. Composition of LNT-catalysts.

Catalyst		Pt (wt.%)	Ba (wt.%)	K (wt.%)	Al ₂ O ₃ (wt.%)
0.4Pt/ γ -Al ₂ O ₃	Pt/Al ₂ O ₃	1.9	-	-	98.1
0.4Pt-4Ba/ γ -Al ₂ O ₃	Pt-Ba/Al ₂ O ₃	1.9	13.1	-	85
0.4Pt-16K/ γ -Al ₂ O ₃	Pt-K/Al ₂ O ₃	1.9	-	14.9	83.2
0.4Pt-3.5Ba-1.5K/ γ -Al ₂ O ₃	Pt-Ba-K/Al ₂ O ₃	1.9	11.5	1.4	85.2

The metal loading is expressed as formal surface atomic density (atoms per square nanometer, at·nm⁻²) for comparison in terms of surface coverage. The overall metal loading for Platinum and Barium was as needed to obtain the theoretical monolayer coverage, as was reported for the most effective catalysts.

To obtain the soot + catalyst mixtures, the desired amount of soot was added to the catalyst in the presence of H₂O (powder to water ratio was 2000:1 w/w) using tight contact method and was then dried at 90°C for 24 h. The soot content was kept constant

at 10 wt%, except for DRIFTS experiments where the soot content was reduced to 1 wt%. Having tested different amounts of carbon, this low amount was used since its value was high enough to obtain an intense signal that could be analysed without overlapping the spectrum.

2.4.1.2. SCR catalysts

As far as SCR catalysts are concerned, this PhD Thesis has focused on the study of SAPO-34 zeolitic materials with copper as metal, due to their well-known properties of high hydrothermal stability and low temperature activity, respectively. In contrast to other authors, who use commercial materials or synthesize the support and incorporate the metal by exchange or impregnation, here a one-pot synthesis process has been proposed in order to decrease the synthesis time and introduce the copper inside the cavities.

SAPO-34 type materials were synthesized by hydrothermal method, using the molar gel composition: 2 DEA: 0.6 SiO₂: 1 Al₂O₃: (0.2-0.8) P₂O₅: 50 H₂O, incorporating copper up to 4wt% (expressed as copper metal). The following synthesis parameters were modified in order to study the influence on the morphology and the SCR activity: phosphorus and copper content, time and temperature in the autoclave and the use of ultrasound.

The gel preparation was carried out in the following way: firstly, an aluminium suspension was prepared by adding isopropoxide to water (75 wt%), then, water and phosphoric acid were added and stirred vigorously for 2 hours, after that, silica was mixed for 4 hours and finally, the structure-directing agent (DEA, diethylamine) and 5wt% of seeds were added. In most cases, the ultrasound assisted synthesis method was performed. For that, the gel was sonicated in pulses of 30 seconds for up to 3 minutes with the Ultrasound Processor explained above, introducing the glass beaker containing the gel in a glass crystallizer with water to prevent heating.

After the time in the autoclave, the solid product was washed several times with distilled water, filtered and dried overnight at 110°C. Finally, it was calcined at 550°C (1.8°C·min⁻¹) in air for 5h to remove the organic template molecules.

To introduce copper in the structure, a Cu-complex was prepared by mixing a 20wt% aqueous solution of copper (II) sulphate with the TEPA (tetraethylenepentamine) and

was stirred for 2h until complete dissolution. The molar ratio Cu:TEPA was 1:2 and the relation between the complex and the material Cu-TEPA/(Al+P) was 0.081. The complex was added to the precursor gel together with the phosphoric acid and the pH was adjusted with the structure-directing agent, always keeping it within basic values.

A factorial design of experiments was carried out in order to study all the parameters mentioned above. Nevertheless, in Table 2.2, only the synthesis conditions and the identification of the most representative materials are described. In general, the nomenclature consists of XCu-SAPO-P-T-t-h/s, where X is the copper percentage, SAPO refers to SAPO-34 material, P is the P/Al ratio, T and t are the temperature and time in the autoclave, respectively and h/s correspond to hydrothermal or ultrasound assisted synthesis method. All the catalysts with a P/Al ratio of 0.8, which are shown here, were prepared using ultrasound so these are not expressed in the identification. By way of example, 2Cu-SAPO-0.2-200-4s indicates that the material SAPO-34 was synthesized with 2 wt% of copper, 0.2 of P/Al ratio, the temperature and time in the autoclave were 200°C and 4 hours, respectively and the gel was previously sonicated before being introduced into the autoclave.

Table 2.2. Identification and synthesis parameters of the SCR catalysts.

Catalyst	Ultrasound	P/Al	Cu (wt%)	Temperature (°C)	Time (h)
SAPO-0.2-200-72h	-	0.2	-	200	72
SAPO-0.2-200-4s	✓	0.2	-	200	4
2Cu-SAPO-0.2-200-4s	✓	0.2	2	200	4
4Cu-SAPO-0.2-200-4s	✓	0.2	4	200	4
SAPO-200-4	✓	0.8	-	200	4
2Cu-SAPO-200-4	✓	0.8	2	200	4
4Cu-SAPO-200-4	✓	0.8	4	200	4
2Cu-SAPO-150-4	✓	0.8	2	150	4
4Cu-SAPO-150-4	✓	0.8	4	150	4
2Cu-SAPO-150-30	✓	0.8	2	150	30
4Cu-SAPO-150-30	✓	0.8	4	150	30

2.4.2. Conformed catalysts

With the intention of progressing in the study of both technologies, monolithic structures of the optimized formulations were prepared and were identified with the same notation ended in -M. The synthesis of NSR-M was carried out using the following steps: firstly, the monolith with an alumina covering was impregnated with the platinum precursor solution and, after 24 hours in rotation in the system displayed in Figure 2.4, was dried overnight at 90°C and calcined for 3 hours at 350°C in air; then, the mixture of barium and potassium precursors was added and kept in rotation for 24 hours and again dried overnight at 90°C; and, finally it was calcined at 500°C for 5 hours ($5^{\circ}\text{C}\cdot\text{min}^{-1}$) in air. All the precursor solutions were prepared 48 hours before the impregnation in order to ensure their stability. The Cu-SAPO-M monoliths were synthesized by impregnation of the support with the washed gel after the process in the autoclave. It was in rotation 24 hours and then was dried overnight at 110°C and calcined at 550°C ($1.8^{\circ}\text{C}\cdot\text{min}^{-1}$) for 5 hours.



Figure 2.4. Rotation system for the synthesis of monoliths.

2.5. Characterization techniques

Characterization techniques were used to obtain the physiochemical properties of the catalysts, going into detail about the structure, the composition and the detected species.

2.5.1. X-Ray Diffraction (XRD)

X-ray Powder Diffraction data were recorded with an EMPYREAN diffractometer (PANalytical), equipped with an automatic loader and a rotating sample holder, using Cu $K\alpha_{1,2}$ radiation ($\lambda = 1.54059 \text{ \AA}$). In the incident beam path, the optical system consisted of a group of divergence and anti-divergence slits that were set at $\frac{1}{2}^\circ$ and Soller slits (incident and diffracted beam) of 0.04 rad were used. The PIXcel detector was employed. The X-ray tube worked at 45 kV and 40 mA. The measurements were done from 5° to 80° (Bragg angle, 2θ) for 30 minutes, with measurement steps of 0.017° . During the measurement, the intensity of the reflected X-rays was recorded and the diffraction pattern peaks appeared when the Bragg equation is fulfilled. This equation relates the X-Ray wavelength and the interatomic distance with the incidence angle of the diffracted beam:

$$n\lambda=2d\sin\theta \quad (2.1)$$

where λ is the wavelength, d is the distance between atomic layers and θ is the angle between the incident rays and the crystal surface. These data provided information about the crystallinity of the structures and allowed the identification of the phases.

2.5.1.1. Rietveld Refinement

From XRD data, the Rietveld refinement [190] of the samples was carried out in order to study the structure modification due to the incorporation of cations, obtaining the unit cell volume and parameters a , b , and c . The SAPO-34 structure designed with the 168335 identification number was used as starting structure, keeping it as it is expressed in the bibliography and refining zero, background, peak shape and unit cell values.

2.5.1.2. Temperature Programmed X-Ray Diffraction (TPXRD)

The Temperature Programmed X-Ray Diffraction was carried out in a Philips X'Pert Pro MPD diffractometer (PANalytical) with similar characteristics to the other, using a primary monochromator with a crystal of Ge (1 1 1) and a RTMS (Real Time Multiple Strip) X'Celerator detector consisting of 128 Si detectors in line. The sample was heated at $10^\circ\text{C}\cdot\text{min}^{-1}$ in air with an Anton Paar (HTK1200N model) temperature chamber and the measurements were performed from 300 to 700°C at 50°C steps from 5 to 80° (2θ) for 40 min. This experiment allowed the study of the structure modification along the calcination process.

2.5.2. X-Ray Photoelectron Spectroscopy (XPS)

The XPS spectra were obtained in a Physical Electronic (PHI) 5701 spectrometer, equipped with a standard X-ray source with two Mg and Al anodes, PHI 04-548 model. The Precision Energy Analyzer/Multichannel Detector PHI 10-360 was employed to analyze in ultra-high vacuum the species presented in the powder catalysts that were supported in stainless steel cylinders with 0.5 cm² of area. During the XPS spectra data processing, binding energy values were referenced to the C1s peak from the adventitious contamination layer, 284.8 eV of binding energy, to determine peak positions within ± 0.2 eV accuracy. All deconvolutions of experimental curves were done with Gaussian-Lorentzian line fitting of varying proportions (60 – 80%), trying to minimize the X² value. This technique gave information about the surface atomic composition and the chemical or electronic state of each surface element. The following regions were analyzed: Al2p, O1s, N1s, Pt4d_{5/2}, Ba3d_{5/2}, K2p, P2p, Si2p, Cu2p, CuLMM, Mg2p. The full spectra analysis was done using MultiPak Software. Short acquisition time of 10 minutes was used to examine C1s, Cu2p and CuLLM XPS regions in order to minimize the photoreduction of Cu²⁺ species. However, a Cu²⁺ reduction in high vacuum during the analysis cannot be excluded.

2.5.3. Analysis of porous solids

N₂ adsorption-desorption isotherms were obtained at 77K (–196°C) using a Micromeritics ASAP 2020 Analyzer. Before the analysis, the samples were outgassed in vacuum (1·10⁻³ Pa) for 5h at 453K (180°C). The specific surface area was obtained by the BET (Brunauer-Emmett-Teller) method, applying the lineal form of:

$$\frac{P}{V(P_0-P)} = \frac{1}{V_m C} + \left[\frac{C-1}{V_m C} \right] \frac{P}{P_0} \quad (2.2)$$

where V is the adsorbed gas volume measured in normal conditions (760 mmHg and 0°C) at each adsorbate partial pressure (P), P₀ is the saturation pressure of the nitrogen at 77K (–196°C), V_m is the monolayer volume and C is a constant related to the adsorption energy. After having obtained volume of the monolayer, the specific surface area (S_{BET}) was calculated with the equation 2.3, where N_A is the Avogadro number and σ corresponds to the area occupied by a nitrogen molecule

$$S_{\text{BET}} = \frac{V_m}{22414} \cdot N_A \cdot \sigma \quad (2.3)$$

The external superficial area and the microporosity of the samples were determined by the t-plot method, from the slope and the y-intercept of the representation of the adsorbed nitrogen quantity and the thickness of the adsorbed gas, t, applying the Harkins and Jura equation (eq.2.4) for the estimation of the t:

$$t = \left(\frac{13.99}{0.034 - \log(P/P_0)} \right)^{1/2} \quad (2.4)$$

The total pore volume was also calculated with the maximum quantity of adsorbed nitrogen and the density conversion factor. In addition, the microporous distribution was obtained by the MP method.

2.5.4. X-Ray Fluorescence (XRF)

The XGT-5000WR Fluorescence spectrometer by X-ray dispersive energy was utilised to quantitatively analyze the composition of the samples. It consisted of a primary X-ray filter and a high purity Si detector. There was no sample preparation or vacuum required, the material was placed in the sample chamber and analyze at atmospheric pressure.

2.5.5. Transmission Electron Microscopy (TEM) and High Resolution TEM (HRTEM)

The acquisition of TEM images was carried out in a Philips CM200 (200 kV) microscope equipped with an Energy Dispersion X-ray Spectroscopy (EDX) analyser that allows the analysis of the elements present in the sample. For this technique, the sample was dispersed in a volatile liquid (ethanol) and deposited on a carbon holder, which is transparent to radiation, and dried in air. A Talos™ F200X instrument from FEI was used for the high resolution TEM images and the EDX mapping.

2.5.6. Scanning Emission Microscopy (SEM)

SEM micrographs were obtained with the Scanning Electron Microscope JEOL JSM – 840. Prior to recording the images, a fine gold layer was sprayed on the sample to assure conduction. Precise analyses of the elements were carried out in different points of the samples.

2.5.7. Ultraviolet-visible Spectroscopy (UV-Vis)

Diffuse Reflectance (DR) UV-Visible NIR analysis was carried out in air in wet conditions, using a T92+UV Spectrophotometer from *PG Instruments* (Lab. 1) or a Jasco V570 instrument (Lab. 2), both of them equipped with an integrating sphere accessory and an internal reference pattern, which allow the registration of data on wavelengths (λ) between 200 and 2500 nm. In all cases, the samples were pulverized in an agate mortar and, then, compacted and placed in the holder. The registered spectra were shown in the normalized form, by the Kubelka-Munk function:

$$F(R_{\infty}) = \frac{(1-R_{\infty})^2}{2-R_{\infty}} \quad (2.5)$$

where R_{∞} represented the reflectance value of the sample to infinite thickness. In practice, samples with 5 mm of thickness were used, enough quantity to ensure the R_{∞} measurement.

2.5.8. Raman Spectroscopy

Raman spectra were collected in a DXR Raman Microscope, from *Thermo Scientific*, working at an exciter line of 532 nm and 10 mW of power and incorporating a Charge Couple Device (CCD) detector. Spectra were recorded in the 60 – 3500 cm^{-1} raman shift range with an accumulation time of near 5 s.

2.5.9. Fourier Transform Infrared Spectroscopy (FTIR)

A wide variety of experiments was performed by Fourier Transform Infrared Spectroscopy (FTIR) and is detailed below.

For IR skeletal studies, the powder samples were diluted in KBr FT-IR grade (1wt.%) and pressed in disks. Spectra were recorded by an Avatar 380 Nicolet FT instrument. Any other FTIR experiment were carried out with self-supported disks that were activated at 500°C in vacuum for 2 hours in the quartz cells systems explained above.

Then, different analyses were performed in order to obtain information about the active species of the samples.

2.5.9.1. Superficial acidity and metal location

The superficial acidity analysis, of both Brönsted and Lewis acid sites, requires the use of a basic compound such as molecule probe to introduce a pulse and study its interaction with the catalyst surface by IR. The position of the metal in a porous material can be studied adsorbing molecules with different sizes, larger and smaller than the pore diameter. Taking all this into account, several series of adsorption experiments of basic molecules with different sizes were carried out. Pulses of ca. 4 torr of NH₃, acetonitrile (AN), isobutyronitrile (IN) and pivalonitrile (PN) with kinetic diameter of 3.57, 3.8, 5.6 and 6 Å, respectively, were adsorbed onto the activated samples at room temperature. The gas phase was then evacuated from the cell and the surface spectra were recorded from room temperature up to 500°C with 50°C steps.

2.5.9.2. CO adsorption at low temperature

To study in depth the copper species which were located in the samples, as well as the interaction with small molecules, CO adsorption experiments were carried out. The sample was introduced in a cell that allowed cooling by liquid nitrogen in an external jacket. CO adsorption was performed at -140°C (real temperature measured by a thermocouple), feeding 7 torr of CO gas. Then, IR spectra were recorded in evacuation and the disk was warmed to between -140°C and 200°C.

2.5.9.3. NO adsorption

NO adsorption experiments were carried out in order to analyse the interaction between this molecule and the catalysts, which is of great relevance in the SCR process. For this, the protocol was identical to the ammonia adsorption process, introducing a pulse of 5 torr at room temperature and registering spectra in evacuation up to 500°C. In addition, several adsorptions at different temperatures were carried out to observe the species that are formed in each temperature.

2.5.10. Temperature Programmed Desorption (TPD) of ammonia

The analysis of the ammonia adsorption capacity and the strength of the acid sites, complementary to the IR study, was performed in a flow reactor. The materials were activated at 500°C for 1 hour in inert atmosphere. Then, 750 ppm of NH₃ was adsorbed at room temperature the necessary time for reaching the saturation. A He purge was subsequently carried out in order to remove the physisorbed ammonia and, finally, the sample was warmed up to 500°C at 10°C·min⁻¹.

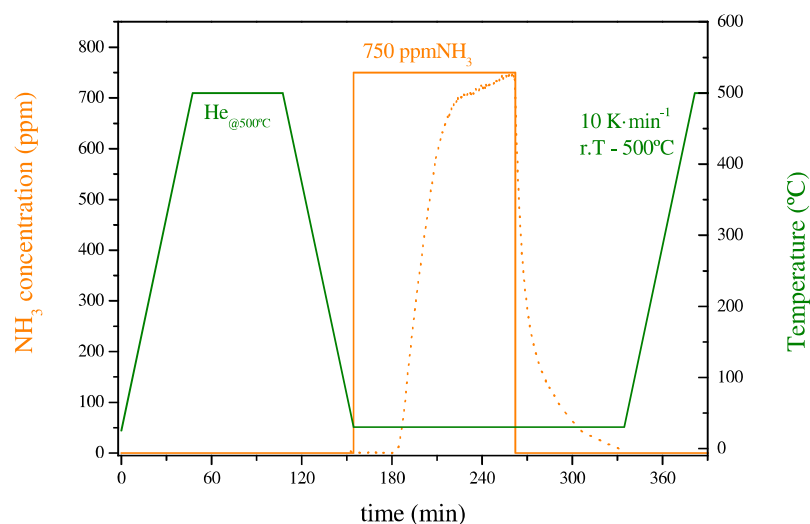


Figure 2.5. Scheme of NH₃-TPD protocol.

2.5.10.1. Ammonia adsorption

For the purposes of studying the behaviour of the catalysts as NH₃-traps, adsorption experiments at different temperatures were carried out. In a similar way to the NH₃-TPD tests, 750ppm of ammonia was adsorbed onto the catalyst (15mg) placed in the TG chamber or in the reactor. After the saturation time, a Helium flow was circulated and then, the sample was heated to 500°C. In all cases, the product distribution was analyzed by mass spectrometry and the ammonia adsorption capacity was calculated with the equation (2.7).

2.6. Catalytic study

The reaction mechanism and the activity parameters of the different technologies studied were addressed by a series of catalytic analyses, which are detailed in this section.

2.6.1. Transient Response Method (TRM)

The activity of the catalysts in the NSR and DPNR technologies was studied by the Transient Response Method (TRM) in the range between 150 and 500°C. This method consisted of the analysis of the response curves when alternated rectangular pulses were fed. For this, 60 mg of powder catalyst was introduced in the reactor, and was conditioned in 100 ml·min⁻¹ of He flow at 500°C for 1 hour to obtain surface dehydroxylation and decarbonation. For catalyst+soot mixtures, the activation temperature was modified to 350°C, to avoid particulate matter combustion. After that, at different temperatures, cyclic conditions were alternated using 100 cm³·min⁻¹ of total flow and 3·10⁴ h⁻¹ of GHSV. A rectangular pulse of NO (1000ppm) + O₂ (3%) balance in He, and H₂ (2000ppm) also in He flow, were subsequently fed during the oxidation (15 min) and reduction (15 min) steps, respectively. For all experiments, the N-balance was closed with a 3-5% deviation. In Figure 2.6, the scheme of the first five cycles is shown.

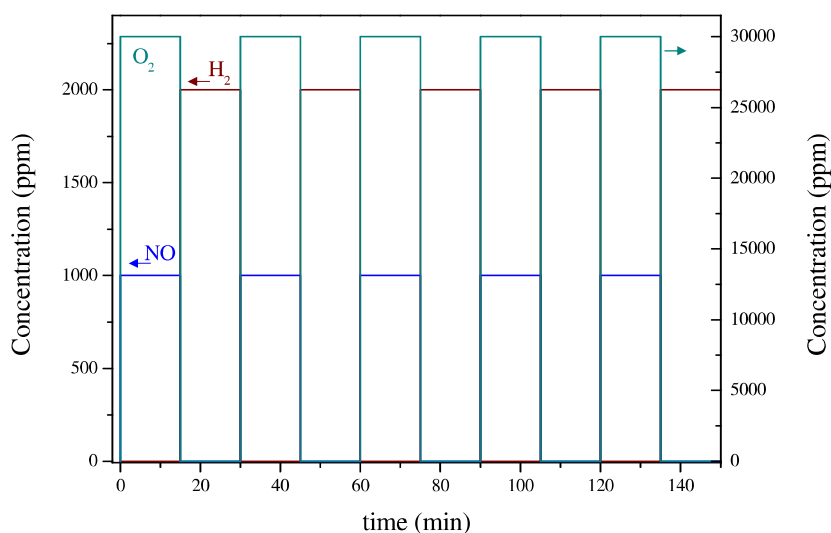


Figure 2.6. Scheme of TRM runs.

To study the influence of water and CO₂, the same rectangular pulses were performed in 1.5% of H₂O and 0.3% of CO₂ atmosphere. The water was introduced as vapour,

passing the Helium stream through a saturator that contained water at the corresponding temperature to incorporate to the gas phase that water concentration.

Quantitative analysis of the product distribution profiles was used to establish the activity parameters. In Figure 2.7, the NO_x profile of one of the cycles is represented in order to explain how the estimation of adsorbed nitrates was arrived at.

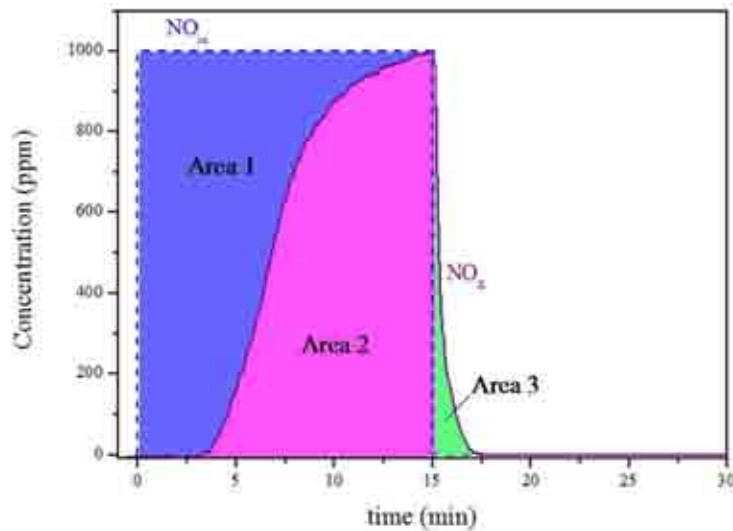


Figure 2.7. NO_x response profile to a rectangular pulse.

The amount of adsorbed NO_x was obtained by the substitution of the values as per this equation:

$$A_{NO_x}^{ox} = \text{Retained amount (ppm}\cdot\text{s)} = \text{Area 1} - (\text{Area 2} + \text{Area 3}) \quad (2.6)$$

where area 1 corresponds to the fed NO, and areas 2 and 3 are associated with the amount of NO registered in the outlet during the lean and initial part of the rich phase, respectively.

From the obtained NO_x area, the amount of adsorbed NO_x per gram of catalyst can be calculated using the equation 2.7. For this, the following operation conditions were taken into account: 100 cm³·min⁻¹ of flow (F), 60 mg of catalyst and the reaction temperature; as well as the assumption of ideal gas behaviour.

$$\frac{mol_{NO_x}}{g_{cat}} = \frac{A_{NO_x}^{ox} \left(\frac{cm^3_{NO_x} \cdot s}{m^3_{gas}} \right) \cdot F \left(\frac{cm^3_{gas}}{s} \right) \cdot 10^{-6} \left(\frac{m^3_{gas}}{cm^3_{gas}} \right) \cdot 10^{-3} \left(\frac{dm^3_{NO_x}}{cm^3_{NO_x}} \right) \cdot \frac{1}{22.4} \left(\frac{mol_{NO_x}}{dm^3_{NO_x}} \right)}{g_{cat}} \quad (2.7)$$

NO_x conversion was defined as the amount of nitrogen oxides that react from the adsorbed nitrates and was calculated with the Equation 2.8

$$X_{NO_x} = \frac{A_{NO_x}^{ox} - A_{NO_x}^{re}}{A_{NO_x}^{ox}} \quad (2.8)$$

where A_{NO_x}^{ox} has been previously explained and A_{NO_x}^{re} is the area under the NO_x curve in the reduction step. N₂-yield (R_{N₂}) was defined as the ratio between the nitrogen production and the amount of adsorbed NO_x and was calculated with the Equation 2.9.

$$R_{N_2} = \frac{2A_{N_2}^{re}}{A_{NO_x}^{ox}} \quad (2.9)$$

Selectivity of the different reaction products was obtained with the following equations, being defined as the ratio between the amount of product formed and the converted nitrates.

$$S_{N_2} = \frac{2A_{N_2}^{re}}{A_{NO_x}^{ox} - A_{NO_x}^{re}} \quad (2.10)$$

$$S_{NH_3} = \frac{A_{NH_3}^{re}}{A_{NO_x}^{ox} - A_{NO_x}^{re}} \quad (2.11)$$

$$S_{N_2O} = \frac{2A_{N_2O}^{re}}{A_{NO_x}^{ox} - A_{NO_x}^{re}} \quad (2.12)$$

Other relevant activity parameters were established: NO_x breakthrough time (the effective retention period, calculated as the intersection of the axis with the tangent at the inflection point of the NO_x profile), oxidation capacity (OC, determined as the amount of NO₂ produced during the lean phase and presented as a ratio NO₂ formed/the amount of NO at the end of the step) and the accumulation rate (defined as the adsorption capacity per reaction time in the lineal part of the profile).

2.6.1.1. Isothermal thermogravimetric study (TG-MS)

The same protocol described in the previous part was performed in the thermobalance. Isothermal thermogravimetric and differential analyses (TG-DTA-DSC) of soot free and catalyst+soot mixture samples were carried out under cyclic lean-rich NO_x storage-reduction conditions (20 min, 1000 ppm of NO + 3% of O₂ in He; 15 min, 2000 ppm of H₂ in He) at 350°C. Before the experiments all samples were treated in He in temperatures ranging from room temperature (RT) to 350°C at 10 K min⁻¹. At 350°C the NO/O₂ (He balance) was fed into the reactor until complete saturation as confirmed by MS. Then, cyclic conditions were alternated. Both, isothermal and non-isothermal thermogravimetric experiments were carried out using 20 mg of sample and 100 ml·min⁻¹ of total gas flow.

2.6.1.2. Isothermal DRIFT-MS study

To study the species involved in the process, the same protocol described for the TRM method in the previous section was performed in a DRIFTs continuous flow reaction chamber. The studies were carried out for catalyst and catalyst+soot mixtures. Before the experiments, He flow (350°C, 1h, 25 cm³·min⁻¹, GHSV = 1.8·10⁴ h⁻¹) was applied in order to clean the chamber and the catalyst surface. The reactions were carried out at a constant temperature of 350°C. The accumulation step (1000ppm of NO + 3% of O₂ in He flow, 15 min) was directly followed by the regeneration step (2000ppm of H₂ in He flow, 15 min). The temperature was adjusted and controlled by the Harrick ATC low voltage controller with a K-type thermocouple. Spectra were recorded in diffuse reflectance mode (DRIFT), and 64 scans were collected at resolution 1 cm⁻¹.

2.6.2. Soot removal study

Thermogravimetric analysis (TG-DSC) was employed for the kinetic study of the intrinsic reactivity of the synthesized catalysts in the soot removal process. The sample was loaded into the chamber and when the weight of the sample reached a constant value in He atmosphere, it was heated from room temperature to 1000°C at a rate of 10°C·min⁻¹ in an atmosphere of NO/O₂ (1000 ppm of NO+3% O₂ in He flow) or O₂ (3% of O₂ in He flow), maintaining a total gas flow rate of 100 ml·min⁻¹ (which was large enough to disregard the mass transfer resistance of the particle) for 10 mg of sample GHSV = 2·10⁴ h⁻¹ STP). No significant differences were recorded in TG-profiles indicating that intraparticle resistance is negligible for particles smaller than 0.9 μm in

diameter. The gas composition at the outlet of the thermobalance was temporally analysed on line by mass spectrometry.

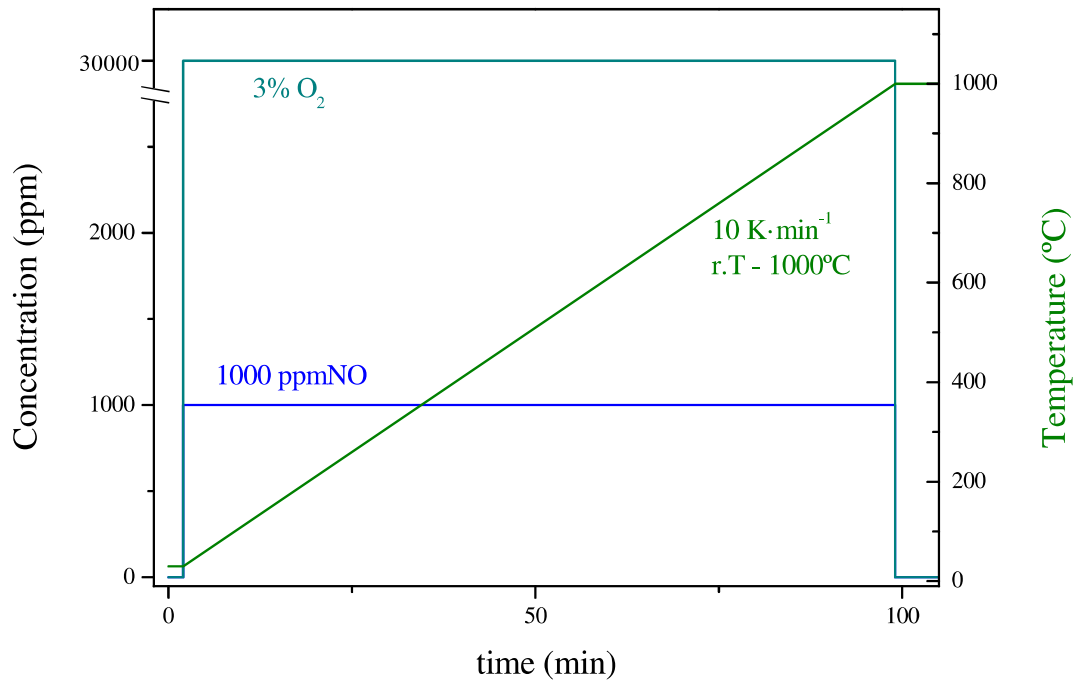


Figure 2.8. Scheme of soot combustion experiments.

2.6.3. SCR activity

SCR experiments were performed in the down flow reactors that were loaded with 60 mg (Lab. 1 and 3) or 1 ml (Lab.4). The composition of the feed gas mixture was 750ppm of NO, 750ppm of NH₃ and 3% (Lab. 1 and 3) or 6% (Lab. 4) of O₂. Argon was used as a tracer and Helium as a carrier gas. In addition, 1.5% of H₂O and 0.3% of CO₂ were also introduced into the reactor to study the influence of these components in SCR activity. The reaction temperature was varied from 150 to 500°C. All the nitrogen compounds were monitored and the concentration of each element at stationary state for each temperature was obtained. The activity of the catalysts was evaluated in terms of conversion (X) and selectivity (S), which was calculated with the following equations.

$$X_{\text{NO}} = \frac{C_{\text{NO}}^{\text{in}} - C_{\text{NO}}^{\text{out}}}{C_{\text{NO}}^{\text{in}}} \quad (2.13)$$

$$X_{\text{NH}_3} = \frac{C_{\text{NH}_3}^{\text{in}} - C_{\text{NH}_3}^{\text{out}}}{C_{\text{NH}_3}^{\text{in}}} \quad (2.14)$$

$$S_{\text{N}_2} = \frac{2C_{\text{N}_2}^{\text{out}}}{C_{\text{NO}}^{\text{in}} \cdot X_{\text{NO}} + C_{\text{NH}_3}^{\text{in}} \cdot X_{\text{NH}_3}} \quad (2.15)$$

$$S_{\text{NO}_2} = \frac{C_{\text{NO}_2}^{\text{out}}}{C_{\text{NO}}^{\text{in}} \cdot X_{\text{NO}} + C_{\text{NH}_3}^{\text{in}} \cdot X_{\text{NH}_3}} \quad (2.16)$$

$$S_{\text{N}_2\text{O}} = \frac{2C_{\text{N}_2\text{O}}^{\text{out}}}{C_{\text{NO}}^{\text{in}} \cdot X_{\text{NO}} + C_{\text{NH}_3}^{\text{in}} \cdot X_{\text{NH}_3}} \quad (2.17)$$

where C_i represents the concentration of the “i” species and the superscripts “in” and “out” indicate that the gas concentration was measured at the inlet and the outlet of the reactor, respectively.

2.6.4. NH_3 oxidation

In order to individualize the processes, NO was removed from the feeding stream and 750ppm of NH_3 and 3% of O_2 were introduced into the reactor. The process was studied at the same temperature range and the activity parameters were defined as has been explained, with the difference that NO was a product of the reaction.

2.6.5. Mechanistic study

2.6.5.1. SCR in DRIFTS

A mixture of 750ppm of NO, 750ppm of NH_3 and 3% of O_2 was also fed into the DRIFT chamber at different temperatures and spectra were recorded during the time in order to identify the species that were involved in the process.

2.6.5.2. Co-adsorption of probe molecules

Co-adsorption of ammonia, NO and O_2 were carried out in different pieces of equipment to study the SCR process with several complementary techniques.

2.6.5.2.1. FTIR co-adsorption pulses

Co-adsorption of probe molecules at different temperatures was performed in a cell connected to a vacuum system. Firstly, 1-5 torr of ammonia was adsorbed and, 20 minutes later the non-chemisorbed ammonia was evacuated. A mixture of NO and O₂ (1:1) was then introduced. Simultaneous gas phase and surface spectra were recorded throughout the time, as well as, the remaining surface after the final evacuation. The co-adsorption was also carried out, the disk having previously been saturated with 1 torr of H₂O and 1 torr of CO₂.

2.6.5.2.2. Flow co-adsorption runs

After conditioning the catalyst in helium for 1h at 500°C, 800ppm of ammonia was adsorbed for 20 min, and a purge of He was then fed for 40 min, at different temperatures. Finally, 1000ppm of NO and 3% of O₂ were introduced into the reactor. The process was repeated several times and the gas composition was analyzed by mass spectrometry.

2.6.6. Coupling of technologies

2.6.6.1. Powder catalytic performance

In order to study the coupling of the technologies in powder, the same feeding conditions as those explained in section 2.6.1 were used. The reactor was loaded with two catalytic beds of 60 mg each (w/w: 1/1), which were separated by a quartz wool layer. Firstly, the gas passed through the NSR catalytic bed and the products met the SCR catalytic bed downstream. The system was working in chemical regime and with the same volume as the NSR experiments and, therefore, the GHSV was kept at $3 \cdot 10^4 \text{ h}^{-1}$ with respect to each catalytic bed. The operational parameters were modified in order to study the operability limits of the materials. Thus, the weight ratio between the NSR and SCR catalytic beds, the time of the oxidant and reduction phases and the hydrogen content were varied.

2.6.6.2. Monolithic structure performance

The activity of the double catalytic bed configuration was studied for the catalysts in monolithic form. For this, the same equipment as for the TRM experiments over the powder catalysts was used with the variation of the reactor, which consisted of a quartz tube, with a 1 inch diameter and a narrowing at the outlet to increase the flow rate and prevent the modification of the product distribution, as can be observed in Figure 2.9.



Figure 2.9. Reaction system for the study of monoliths.

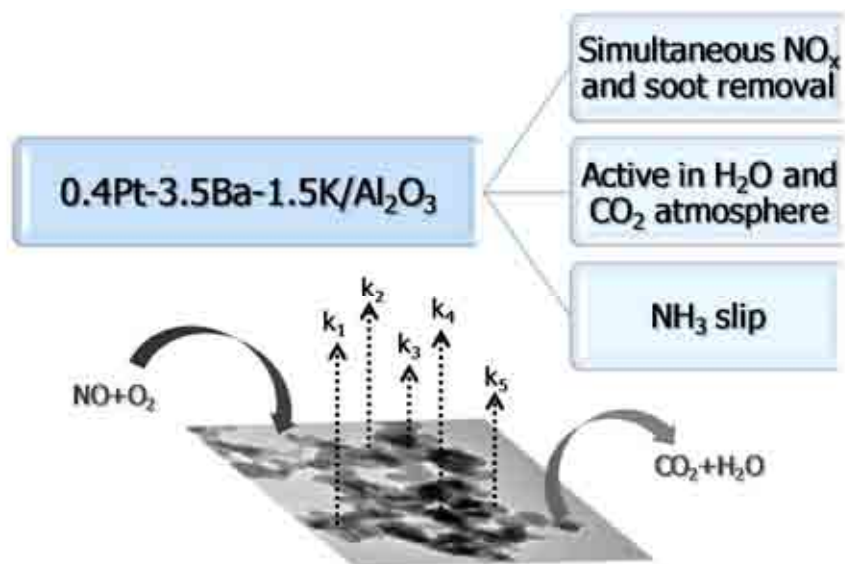
The reactor was loaded with two monoliths each 1x1 inches in diameter and height (w/w: 1/1), corresponding to a weight of around 6g, positioned in the same direction to prevent flow distortion. Cyclic conditions were used, alternating in the feed stream, oxidant phases of 1000ppm of NO + 3% of O₂ with reducing steps of different hydrogen concentrations (0.2 – 2.5 %) in atmosphere of 1.5% of H₂O + 0.3% of CO₂. The experiments were performed up to saturation and complete regeneration of the samples, so, the time for each period was modified according to the conditions. The system was working in laminar regime, with a total flow of 100 cm³·min⁻¹ owing to the equipment limitations and, therefore the GHSV was set at 10³ h⁻¹ with respect to each catalytic bed. The temperature was analyzed at the centre of the entire catalytic bed and at the reactor outlet.



UNIVERSIDAD
DE MÁLAGA

3. Results and Discussion.

NSR technology





UNIVERSIDAD
DE MÁLAGA

3. Results and discussion. NSR technology

The model and modified NSR catalysts were made up of a high surface area supporting material (γ -Al₂O₃), an oxidation component (noble metal, Pt) and a NO_x storage element (Ba and/or K) [170]. Our previous works [171,172] have pointed out the influence of the support in the catalytic activity. According to the results, the properties and the obtaining processes of different kinds of alumina, γ -Al₂O₃ TH with high hydrothermal stability was used in the synthesis of the catalysts. In addition, a percentage of platinum around 2wt% allowed a high dispersion over this support.

L. Castoldi et al. [127] demonstrated that barium percentage higher than 10wt% negatively affects both the catalyst morphological properties and the Pt dispersion in the samples, nevertheless, the NO_x adsorption capacity increases and, if the weight percentage is above 16wt%, an increase in ammonia production is observed. So, the amount of barium was maximized in order to obtain total monolayer coverage and, then, partially or completely replaced by potassium.

Catalysts were prepared by incipient wetness impregnation. The order of the impregnation steps is crucial especially when the catalysts undergo high temperature pulses (i.e. during the regeneration steps). *Lindholm et al.* [191] have reported that a higher storage capacity is obtained when Pt/ γ -Al₂O₃ is impregnated with barium than when Ba/ γ -Al₂O₃ is impregnated with platinum, increasing the storage value up to 54% when the first sequence is used. *Pereda-Ayo et al.* [129] also concluded that the preparation of Pt-BaO/Al₂O₃ monolith catalyst by the incorporation of platinum using adsorption procedure and then barium using dry impregnation, led to the uniform dispersal and distribution of both Pt and Ba which facilitates the close proximity of the metal on the catalyst surface. Therefore, the platinum precursor was incorporated first followed by the storage element solution with intermediate and final calcinations in order to obtain the studied catalysts.

3.1. Characterization of NSR catalysts

Herein, the results of the characterization of these materials, using several techniques such as XRD, TEM, porous solid analysis or XPS, are presented. In Figure 3.1, the XRD patterns of the samples are shown. In all cases, signals associated with gamma alumina (JCPDS 75-0921) and platinum in metallic state (JCPDS 4-0802) were

identified, with Bragg angle values of 37.5, 39.6, 45.9, 60.9 and 66.9° for the support and 39.8, 46.4 and 76.5° for the noble metal. As has been reported [152,156], witherite, orthorhombic carbonate species, was the barium dominant phase and is related to Bragg angle values of 23.9, 27.6, 34.3 and 42.1° (JCPDS 5-0378). For K-containing catalysts, two contributions were observed assigned to oxide (JCPDS 43-1020) and hydrated carbonate (JCPDS 20-0886) species. Signals at 26.5, 30.3, 41.9 and 66.9° were detected for the K₂O and peaks at 15.9, 28.9 and 31.6° were associated with K₄H₂(CO₃)₃·1,5H₂O.

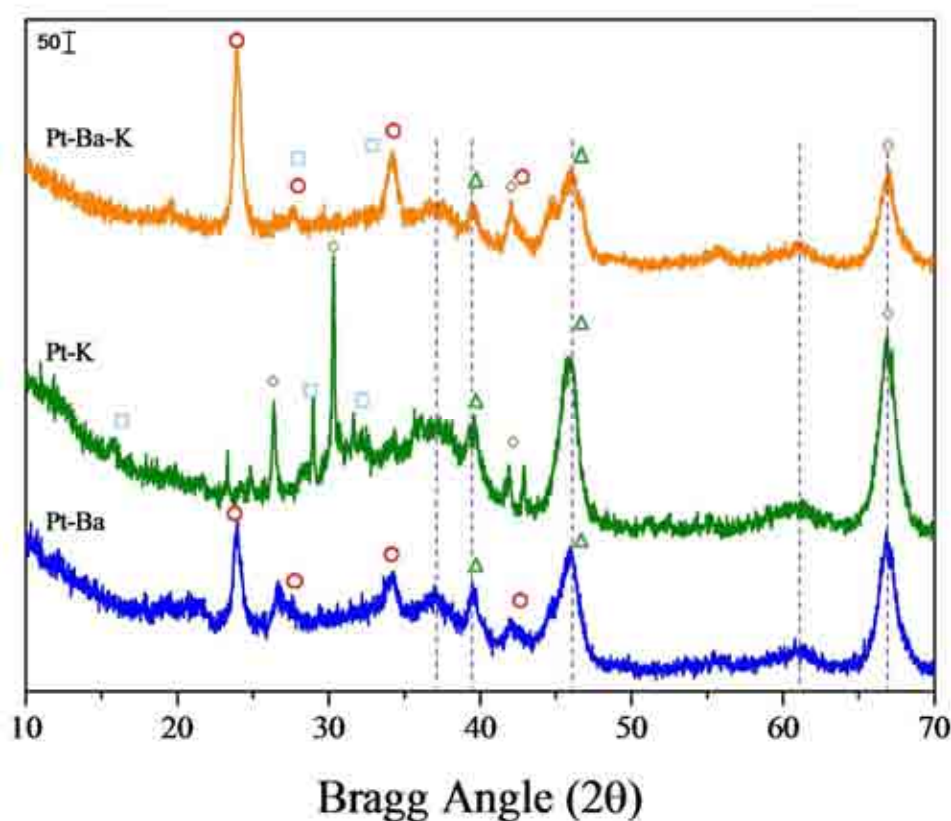


Figure 3.1. XRD patterns of the samples with the identification of the following species: γ -Al₂O₃ (---), Pt (▲), BaCO₃ (●), K₂O (◇), K₄H₂(CO₃)₃·1,5H₂O (□).

These species were also observed in the TEM images, which are represented in Figure 3.2. The γ -Al₂O₃ employed as support, with specific surface area of 144 m²·g⁻¹ and total pore volume of 1 cm³·g⁻¹, presented a homogeneous granular morphology, as can be observed in the images of Pt/Al₂O₃ (Fig. 3.2.a), which has been included for comparative purposes. In addition, small particles in the order of nm were detected and identified by EDX. In fact, a wide Pt particle size distribution from 2 to 60 nm has been informed for this catalyst [172], with two main sizes, between 2-5 nm and higher than

50 nm. This factor plays an important role in the DPNR technology, since small particles favour the oxidation of NO to NO₂.

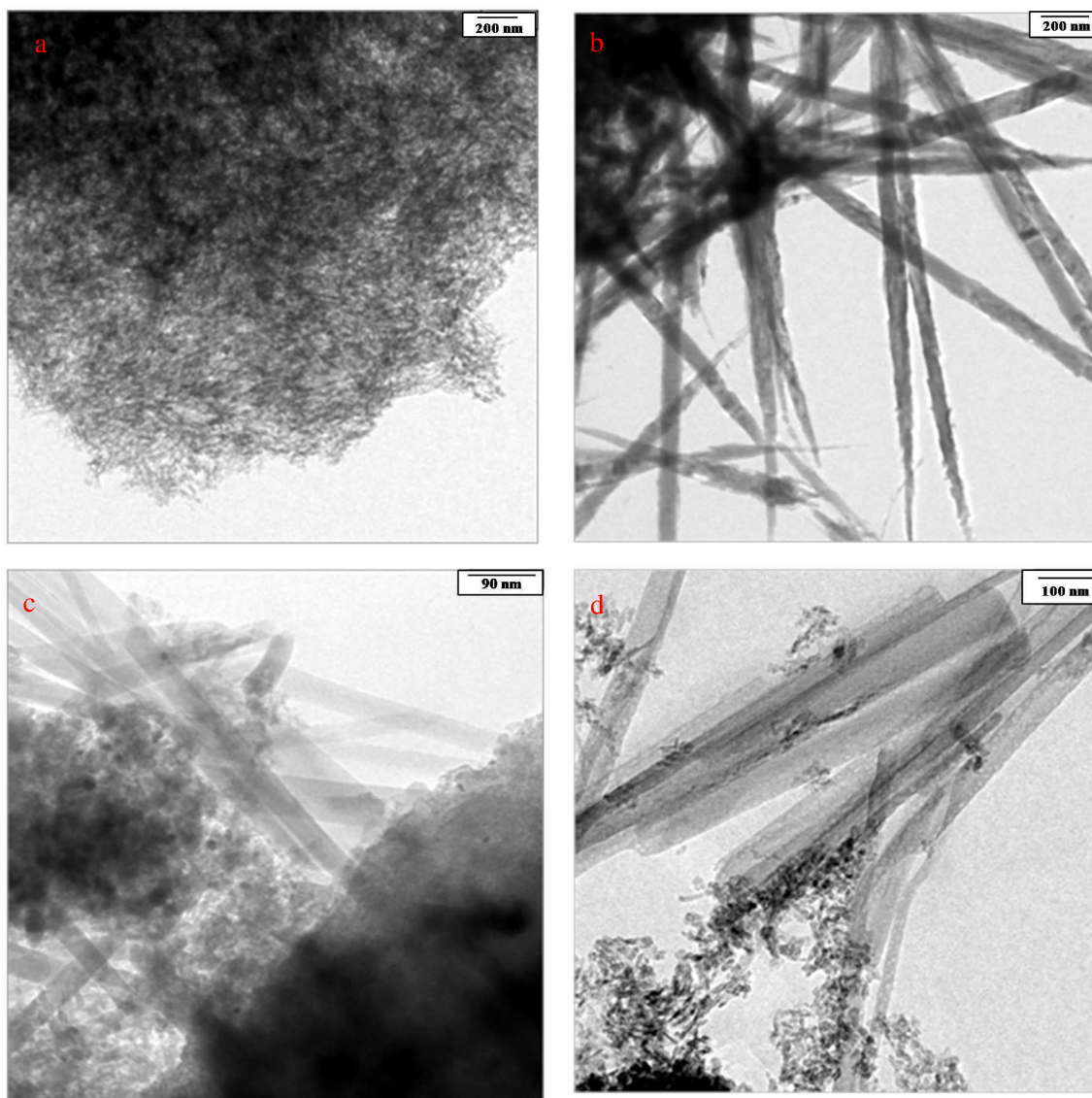


Figure 3.2. TEM images of the samples: a) Pt/Al₂O₃; b) Pt-Ba/Al₂O₃; c) Pt-K/Al₂O₃; d) Pt-Ba-K/Al₂O₃.

In the TEM image of Pt-Ba/Al₂O₃ (Fig. 3.2.b), the needle-like structure crystallites detected were associated with the presence of barium in the carbonate form. The granular form of the support was also observed and the EDX analysis confirmed the presence of platinum.

The presence of potassium (Fig. 3.2.c) was detected as needle-like and “melt-like” structures, due to the carbonate phase and the water retained in the catalyst. All the components were also analyzed by EDX.

The TEM image of Pt-Ba-K/Al₂O₃ (Fig. 3.2.b) was similar to the others and needle-like crystallites of the alkaline and alkaline-earth metals, Pt particles (around 15 nm) and the support morphology were observed and identified by EDX analysis.

To complete the characterization of the surface species of the metals, XPS spectra of the catalysts were registered and Binding Energy (BE) values were estimated. For each element, the relative percentages of the surface species were calculated by the deconvolution of the C1s, O1s, Al2p, Pt4d_{5/2}, Ba3d_{5/2} and K2p signals and these are represented in Table 3.1. In the case of Pt, the region 4d was analyzed instead of 4f (71.3 eV) because of the presence of Al and the strong overlapping Al2p signal [113], located around 74.4 eV [192].

Table 3.1. Binding energies from XPS data in eV for the samples (% species concentration).

Catalyst	Binding Energy ($\pm 0,2$ eV)					
	C	O	Al	Pt	Ba	K
Pt-Ba/Al ₂ O ₃	284.7 (63.8)	530.7 (88.5)	74.0	314.7 (64.8)	779.3 (31.0)	-
	286.8 (18.3)			316.8 (29.3)		
	289.5 (17.9)			318.4 (5.9)		
Pt-K/Al ₂ O ₃	284.8 (66.4)	531.1 (98.1)	74.1	314.1 (36.6)	-	292.6 (9.3)
	286.9 (3.4)			316.5 (53.0)		
	289.3 (30.2)			318.7 (10.4)		
Pt-Ba-K/Al ₂ O ₃	284.6 (64.7)	530.9 (96.0)	73.9	314.7 (64.8)	779.2 (29.2)	292.3 (19.1)
	286.6 (26.7)			316.9 (32.3)		
	289.0 (8.6)			318.6 (2.9)		

As can be observed in Table 3.2, the carbon region can be divided in three signals, being the majority associated with adventitious carbon (used as internal reference) and the others related to the presence of carbonaceous remains from the synthesis. The band in the range between 284.6–284.8 eV corresponds to carbon species, C-C, the intermediate contribution was assigned to the bond of C with O and the highest energy, around 289 eV, was associated with the carbonate species [171,192]. In the O1s region, two bands were distinguished. The main and less energetic signal, close to 531 eV, was attributed to the O lattice, found in the carbonates and oxides, principally of the support (Al₂O₃), whereas the other contribution could be assigned to surface hydroxyl groups. An intense signal, around 74 eV of binding energy, can be observed and related to aluminum in oxide phase.

Regarding the platinum, the deconvolution of the signal from Pt4d_{5/2} region provided three bands with binding energies, similar for all the catalysts and ca. 314, 317 and 319

eV, corresponding to Pt^0 , Pt^{2+} and Pt^{4+} , respectively. As an example, the deconvolution for the Pt-Ba-K/ Al_2O_3 is represented in Figure 3.3.

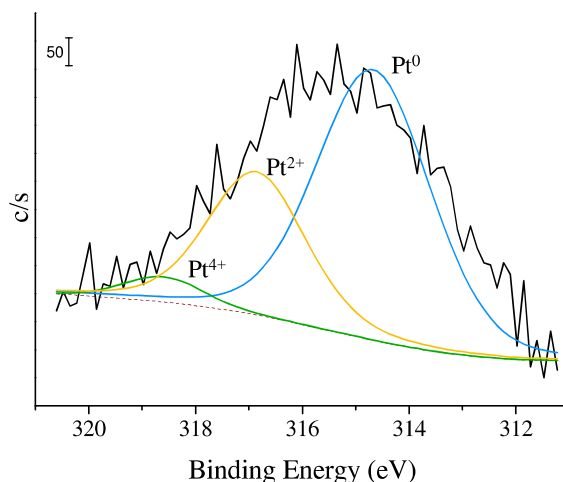


Figure 3.3. Deconvolution of the $\text{Pt}4d_{5/2}$ XPS signal for the Pt-Ba-K/ Al_2O_3 catalyst.

The ratio between both platinum states, metallic (Pt^0) and oxidised (Pt_{ox}), the latter being the result of adding Pt^{2+} and Pt^{4+} contributions, can be obtained from the deconvolution of the signal. This relationship was affected by the metal that was incorporated into the formulation and related to the catalytic behaviour. So, in Table 3.2, the $\text{Pt}^0/\text{Pt}_{\text{ox}}$ ratios for the studied catalysts are shown. Pt/ Al_2O_3 has also been included for comparison purposes.

Table 3.2. $\text{Pt}^0/\text{Pt}_{\text{ox}}$ ($\text{Pt}_{\text{ox}}=\text{Pt}^{2+}+\text{Pt}^{4+}$) ratio of the samples.

	Pt/ Al_2O_3	Pt-Ba/ Al_2O_3	Pt-K/ Al_2O_3	Pt-Ba-K/ Al_2O_3
$\text{Pt}^0/\text{Pt}_{\text{ox}}$	1.2	1.8	0.6	1.8

These data indicate that the metals present on the catalyst surface may modify $\text{Pt}^0/\text{Pt}_{\text{ox}}$ ratio increasing/decreasing Pt^0 surface site population. As has been previously reported [171,193], the interaction between platinum and the storage element is relevant in the NO_x removal activity. The highest value was obtained for Pt-Ba/ Al_2O_3 and Pt-Ba-K/ Al_2O_3 catalysts, indicating Pt^0 stabilization by Ba species, as has been observed elsewhere [113,140] with this kind of materials. In contrary, for Pt-K/ Al_2O_3 catalyst, the highest amount of Pt^{2+} and Pt^{4+} was detected, indicating that K incorporation could limit the reducibility of the catalyst active centers. The trimetallic system, Pt-Ba-K/ Al_2O_3 ,

despite containing potassium, showed a value almost identical to Pt-Ba/Al₂O₃ due to the close amount of barium surface load.

From the XPS data, the presence of barium, mainly as carbonate, was also evidenced by the band around 780 eV, in accordance with the others techniques. In addition, a less intense band at lower binding energy associated with barium oxide was observed. The deconvolution of the Ba3d_{5/2} region for Pt-Ba-K/Al₂O₃ is shown in Figure 3.4.

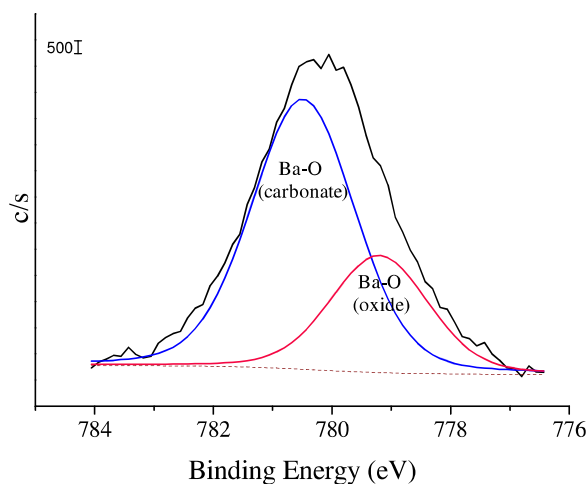


Figure 3.4. Deconvolution of the Ba3d_{5/2} XPS signal for the Pt-Ba-K/Al₂O₃ catalyst.

In the case of potassium, two contributions were also detected (Fig. 3.5); the most intense band was associated with the hydrated hydroxycarbonate species and the minority, at energy values lower than 293 eV, related to the oxide phase.

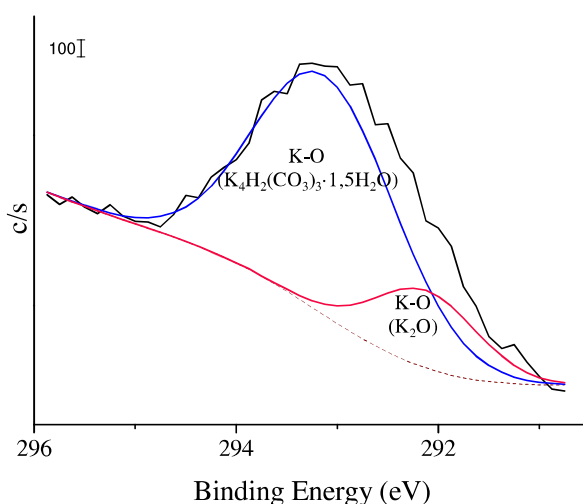


Figure 3.5. Deconvolution of the K2p XPS signal for the Pt-Ba-K/Al₂O₃ catalyst.

As have been explained, the results of different characterization techniques with regard to the metal species that were present in the catalyst agreed.

Regarding the specific surface area, the incorporation of the metals reduced the value in 18%, from 144 down to 118 $\text{m}^2\cdot\text{g}^{-1}$, as a consequence of the deposition of the components onto the surface. This decrease is in line with other authors that have observed reduction values between 10 and 30% with similar catalysts [171] or 20% of diminution is typically observed when 5% of Ag and 10% of Ba were incorporated to a $\gamma\text{-Al}_2\text{O}_3$ and is more pronounced at high loadings [1].

As partial conclusion, it is noteworthy that Ba-containing catalysts favour the stabilization of the metallic state of platinum, as was deduced from XPS data. All characterization techniques agree on the main species of the metals that are carbonate and hydrated hydroxycarbonate phases for barium and potassium, respectively; as well as the presence of metal oxides.

Taking these results into account, a similar catalytic behaviour between Pt-Ba/ Al_2O_3 and Pt-Ba-K/ Al_2O_3 could be expected. However, several authors have reported the beneficial role of the potassium incorporation in the formulation in order to simultaneously remove NO_x and soot [2,9,12]. Therefore, the trimetallic catalyst here showed with a Ba/K atomic ratio of 2.3, allowed the improvement of the process due to the potassium content, as will be explained below, keeping the Pt-Ba model catalyst surface characteristics and the *quasi*-theoretical monolayer coating, without clusters formation.

3.2. Transient Response Method over NSR catalysts

To analyse the catalytic behaviour of the LNT-catalysts, TRM experiments were carried out, alternating lean and rich phases, 1000ppm of NO + 3% of O_2 and 2000ppm of H_2 in He, respectively, in pulses of 15 min, in which the saturation of the samples was achieved. In Figure 3.6, the profile of the outlet gas distribution during the cycles for the Pt-Ba-K/ Al_2O_3 at 350°C is shown.

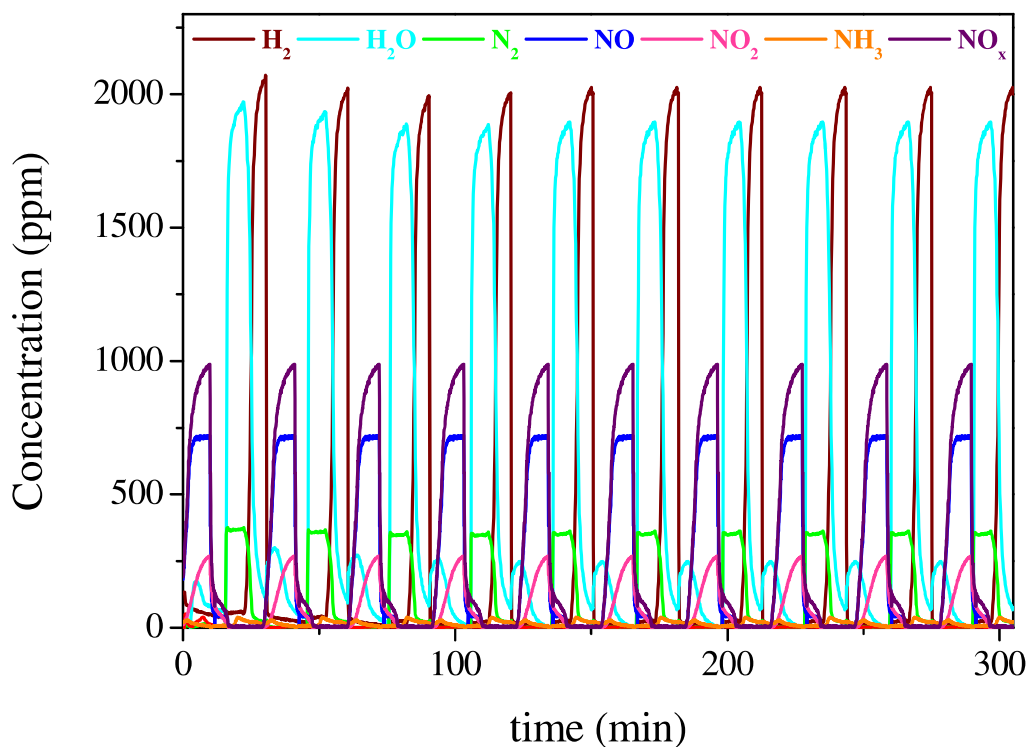


Figure 3.6. NO_x storage–reduction cycles at 350°C for Pt–Ba–K/Al₂O₃.

In the storage phase, NO₂ production was observed together with the unconverted NO distribution, as well as a small water formation, produced as a consequence of the NO_x adsorption process. In the reduction step, a simultaneous production of nitrogen and water was detected and associated with the reaction between the fed hydrogen and the adsorbed nitrates. At this temperature, only a little amount of NH₃ (< 50ppm) was noticed, whereas N₂O production was absent.

The same experimental procedure was carried out over Pt–Ba/Al₂O₃ and Pt–K/Al₂O₃ catalysts, obtaining similar profiles because the same process was happening, except for the amount of each species that was dependent on the elements of the formulation.

The activity parameters were obtained from the quantitative analysis of the last lean-rich cycle in which the catalysts were working in steady state. The performances at 350°C are summarized in Table 3.3. The data revealed that, from the point of view of the NO_x storage capacity, slightly higher values were detected for those systems with Ba loading (Pt–Ba/Al₂O₃ and Pt–Ba–K/Al₂O₃). Nevertheless, similar values were obtained for all the studied system, indicating that both, Ba and K presented a good performance as storage elements. The oxidation capacity of the Pt component (measured by the NO₂ at the end of the step) is lower over Pt–K catalyst as a consequence of the worsening Pt–K

cooperation due to platinum particle masking by K element as has been previously reported [2] with this type of catalysts and in agreement with the characterization data presented above.

Table 3.3. Reactivity data calculated during soot-free storage-reduction of NO_x experiments from isothermal TRM profiles at 350°C.

Catalyst	NO _x stored (· 10 ³ mol NO g _{cat} ⁻¹)	Oxidation Capacity (%)	NO _x Conversion (%)	N ₂ Selectivity (%)
Pt-Ba/Al ₂ O ₃	0.45	38	98	85
Pt-K/Al ₂ O ₃	0.37	11	78	100
Pt-Ba-K/Al ₂ O ₃	0.42	33	88	97

Over the studied catalysts and during the reduction step, the prompt formation of N₂ is detected for all catalysts. NH₃ is only observed (<100 ppm) for those catalysts containing Ba; although its formation is further dependent on the operation temperature [118,119]. During the regeneration cycle, the Pt-Ba/Al₂O₃ showed the best NO conversion, whereas the N₂ selectivity was 85%, the lowest value, due to the already mentioned ammonia formation. This system acts in a similar way to the standard Pt-Ba reported by other authors [153,173,194–196], who studied the formulation in powder or monolithic structures. The NO conversion over Pt-K catalysts was lower compared to Pt-Ba systems, whereas the N₂ selectivity reached the maximum value since no ammonia was detected. For trimetallic catalyst, the obtained conversion value was intermediate to that of the model catalysts (88%), nevertheless, the improvement in the N₂ selectivity for this system comparing to standard Pt-Ba is noteworthy, as a consequence of the presence of potassium in the formulation. In addition, Ba-containing catalysts presented higher values of NO_x storage and oxidation capacity. In relation to the NO_x adsorption capacity, although all the samples registered noteworthy values, close, or even higher, to those reported in the bibliography [113,117,197] studied in similar conditions, Barium has been reported [2,198] as a more suitable element for NO_x storage. The oxidation capacity is related to the Pt-metal cooperation and, as has been demonstrated in the previous section, was higher when barium was in the formulation.

3.2.1. Isothermal thermogravimetric analyses of NSR catalysts

Isothermal TG-MS experiments (350°C) under NO_x cyclic lean-rich conditions were carried out to check the LNT-catalysts performance in terms of weight gained during the lean step due to nitrates/nitrites trapping, the weight loss registered during the rich phase due to nitrates/nitrites removal by chemical reduction and also to evaluate the heat flow evolution during the lean-rich cycling. The weight (%) and the heat flow (W·g⁻¹) profiles are displayed in Figure 3.7 for the first's five cycles, from the first regeneration cycle, for Pt-Ba/Al₂O₃, Pt-K/Al₂O₃ and Pt-Ba-K/Al₂O₃ catalysts. MS profiles (not shown) were similar to those registered by TRM-runs under the given conditions.

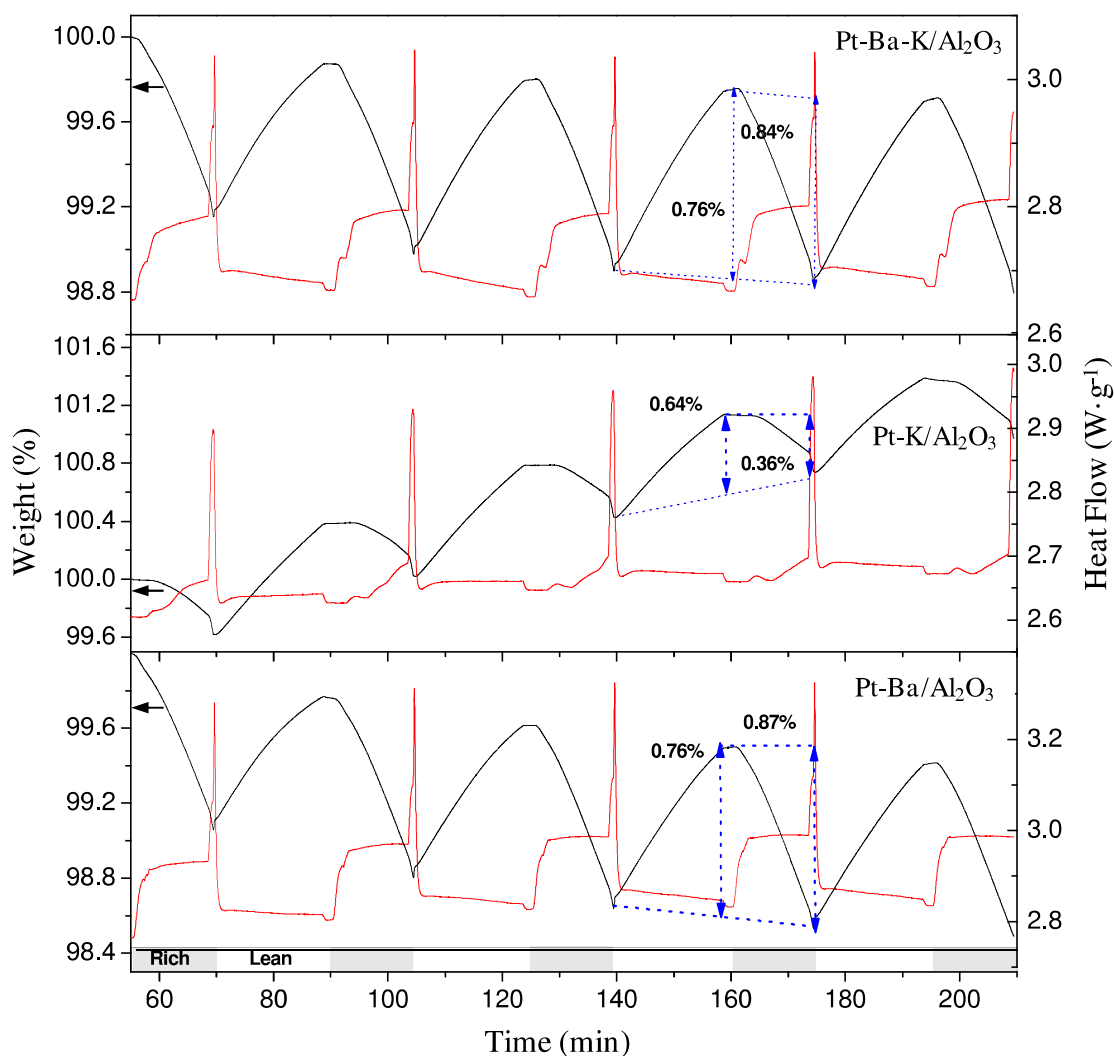


Figure 3.7. TG-TD analyses of LNT catalysts under isothermal (350°C) cyclic conditions lean (20 min, 1000ppm of NO+3% of O₂ in He), rich (15 min, 2000ppm of H₂ in He).

For Pt-Ba/Al₂O₃ sample a cyclic weight gain-loss (%) can be observed, that corresponds to lean-rich steps associated with nitrites/nitrates storage (weight gain: 0.76% of initial weight in this step) and the regeneration by nitrites/nitrates reduction (with a weight loss of 0.87%). Apart from the cyclic weight changes, a continuous trend of decrease in the weight baseline was evidenced; indeed, the difference between weight gain and mass loss up to 5th cycle was ca. 0.3 %, indicating that during catalyst regeneration the total weight of species removed was higher than total weight of stored nitrites/nitrates species. This data reveals that other species are involved such as water and carbonates, which decompose and are removed from the catalyst up to 5th lean-rich cycle. For the consecutive cycles, under dry condition, the deviation of weight gain and mass loss was lower than 0.05%.

The storage capacity of Pt-K/Al₂O₃ catalyst reached 0.64% of the initial weight in the step, which is similar to the value obtained by the TRM protocol, $3.7 \cdot 10^{-4} \text{ mol NO}_x \cdot \text{g}_{\text{cat}}^{-1}$ and lower than the result for the standard Pt-Ba/Al₂O₃. For Pt-K/Al₂O₃ sample, the opposite trend in the weight baseline to the Pt-Ba catalyst was evidenced, and the total weight of the stored species was higher than the total weight of decomposed/removed species. The weight decrease of 0.36% of the maximum weight reached in the lean phase was associated with an incomplete regeneration of the catalyst. As consequence, an ‘accumulation’ associated with species that resist catalyst regeneration can be observed, with a measurable total weight variation between 0.2-0.4 (%) and thus the total sample weight is continuously increasing in the subsequent cycles from 100 up to 101.6 for the five initial cycles. Another possible explanation for the increase in the baseline could be insufficient hydrogen content for the regeneration of the catalyst in the designated time.

For Pt-Ba-K/Al₂O₃ catalyst, the general trend observed for the Pt-Ba standard formulation was apparently reproduced, reaching a weight gain value of 0.76% that corresponds to the calculated value, $4.2 \cdot 10^{-4} \text{ molNO}_x \cdot \text{g}_{\text{cat}}^{-1}$. Ba-containing catalysts registered higher mass gain and better NO_x accumulation capacities. This mass change, attributed mostly to the amount of trapped NO_x and calculated for each catalyst from the 4th accumulation cycle, showed the same trend as the calculated stored NO_x (mmol NO_x g_{cat}⁻¹) given in Table 3.3. In the reduction stage, the loss of mass (0.84%) was associated with the total reduction of nitrate/nitrite accumulated in the storage phase with N₂ and

H₂O formation and, in addition, a minimal amount of NH₃ (<50 ppm) as consequence of an undesired nitrate reduction route.

The NO_x adsorption rate is another relevant parameter, since it can be modified depending on the formulation of the catalyst. From the TG data, the rate value can be obtained. So, barium containing catalyst showed values around $9.5 \cdot 10^{-3} \text{ mg} \cdot \text{min}^{-1}$, while for the Pt-K/Al₂O₃ catalyst the rate decreased to $8 \cdot 10^{-3} \text{ mg} \cdot \text{min}^{-1}$. This fact can be related to the lower NO_x adsorption capacity of the latter catalyst.

The heat flow values ($\text{W} \cdot \text{g}^{-1}$) for the storage and reduction steps in the different samples depend on the storage components (Ba, K or Ba+K) in the LNT-catalyst as can be observed in Figure 3.7. During the lean phase, no net heat flow modification was registered. In contrast, along the rich step, two ascendant signals (exothermic) were detected and attributed to different and subsequent reaction/desorption processes of two types of stored nitrates, which were accompanied by nitrogen and water formation. The net heat flow value is lower for Pt-K catalyst and the difference between both exothermic signals is more evident for K-containing catalysts. The so marked and sharp exothermic signals at the end of each reducing stage could be attributed to the change from oxidizing to reducing conditions. According to literature data, in the rich step, not only are nitrates reduced to N₂ by the excess of reducer agent, but Pt-oxide species also formed during the lean step can be reduced giving an exothermic response and leading to an increase of the heat as *W.S. Epling et al.* [199] have observed in monoliths. Moreover, a temperature variation (+0.5°C) in the catalytic bed at the end of each "isothermal" reduction step was observed, even in O₂ absence. As nitrate stability is associated with temperature, this small variation in the temperature detected does not affect the NO_x accumulation capacity in the subsequent lean-rich cycles.

3.2.2. NSR mechanism over Pt-Ba-K/Al₂O₃

Several works have focused on the NSR reaction mechanism over this type of materials using infrared spectroscopy in order to obtain data about the species involved in the process [2,194,198,200–209]. Understanding is made difficult by the wide range ($\approx 1100 - 1700 \text{ cm}^{-1}$) in which the NO_x adsorption species appeared. Based on this, Figure 3.8 has been prepared as a summary.

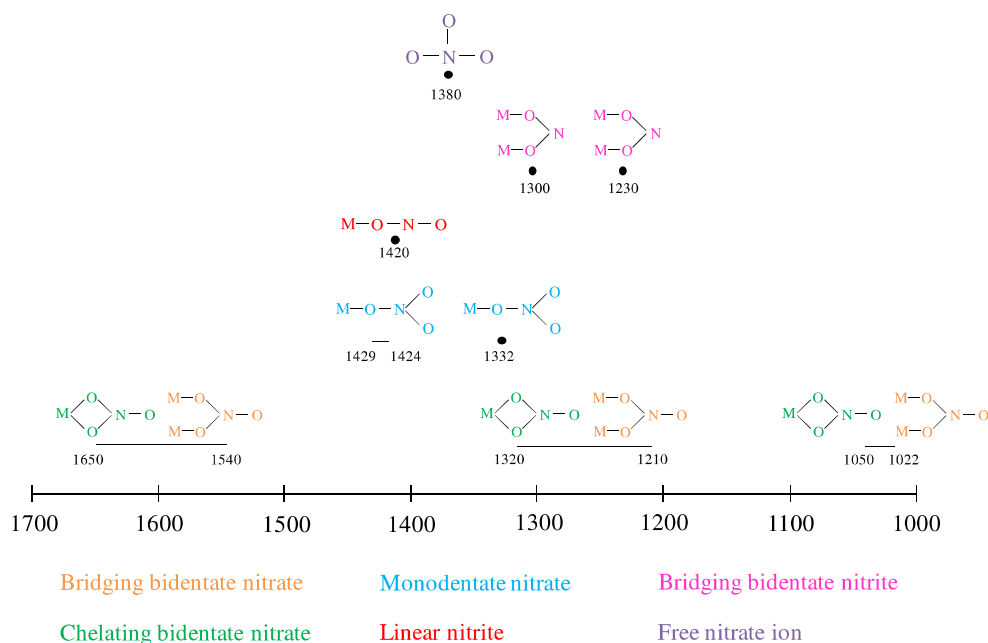


Figure 3.8. Assignments of peak position in DRIFT spectra results.

Taking this scheme into account, the mechanism over Pt-Ba/Al₂O₃ and Pt-K/Al₂O₃ has already been proposed [2,198,201,210,211]. It has been generally accepted that the storage occurs with the initial formation of nitrites, followed by the oxidation of nitrites to nitrates. Nevertheless, the direct formation of nitrate species could be a parallel reaction route. After a long period of oxidant conditions or upon reaching the saturation point, only nitrates were observed. Regarding the reduction mechanism, hydrogen reduces the adsorbed nitrates to N₂, either by direct reaction or via ammonia formation as an intermediate; NH₃ could also be an undesired product decreasing the selectivity of the process.

As far as involved species are concerned, it is noteworthy that the adsorption takes place via different species depending on the metal present in the formulation. So, over Pt-Ba/Al₂O₃ the main species are surface bidentate nitrates (bridging and/or chelating) and linear or monodentate nitrates whereas over Pt-K/Al₂O₃, although remarkable amounts of bidentate nitrates were observed, the predominant feature was associated with free nitrate ion. In addition, the surface properties of Pt-Ba/Al₂O₃ were fully restored in contrast to Pt-K/Al₂O₃ where the regeneration process is limited.

To study the involved species and confirm the mechanism over Pt-Ba-K/Al₂O₃, DRIFTs experiments were carried out in lean/rich conditions; alternating 15 min cycles of

1000ppm of NO + 3% of O₂ with 2000ppm of H₂ and registering spectra every 2 min. In Figure 3.9 the data obtained from the oxidation step and the final spectrum after the regeneration process are shown.

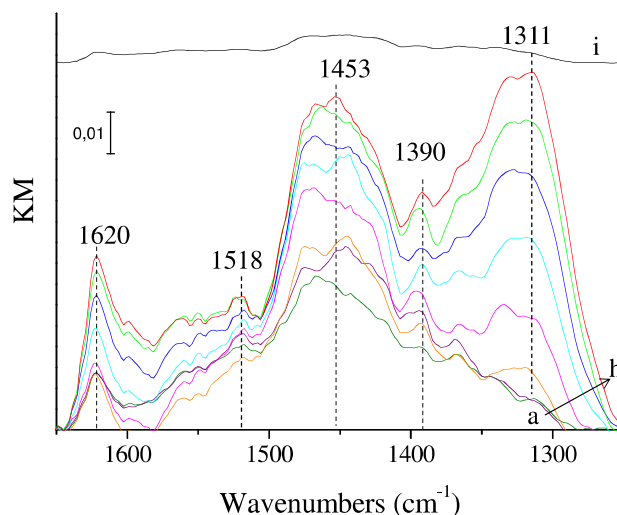


Figure 3.9. DRIFT spectra recorded for storage–reduction cycles at 350°C over Pt–Ba–K/Al₂O₃ from a) 1 min to h) 15 min under lean phase flow and i) after the regeneration step.

In the oxidation phase over Pt–Ba–K/Al₂O₃, the region between 1560 and 1190 cm⁻¹ was highly affected by a combination of nitrates. The signal around 1620 cm⁻¹ could be related to bridging bidentate nitrates as well as chemisorbed water. The modification of the region from 1500 to 1590 cm⁻¹ together with the band from 1250 to 1370 cm⁻¹ could be associated with bridging and chelating bidentate nitrates. Between 1410 and 1500 cm⁻¹, the band could be caused by the formation of monodentate nitrates. Nevertheless, some authors [201] have attributed the last two mentioned to ionic (“bulk-like”) nitrates. Finally, the peak around 1390 cm⁻¹ could be assigned to free nitrate ion without excluding the possibility of being a consequence of the potassium nitrate due to the interaction with the KBr windows. After the regeneration step the surface is almost completely restored. So, the mechanism was identical to the model Pt–Ba and Pt–K catalysts, involving a combination of nitrate species on barium and potassium.

After having demonstrated the high performance of the trimetallic catalyst in terms of NO_x adsorption capacity as well as the unchanged mechanism, the effect of the presence of soot was also studied.

3.3. Soot influence over NSR catalysts

Printex U was used as model soot, with a surface area of $97 \text{ m}^2 \cdot \text{g}^{-1}$, with a carbon percentage of 97.2% and 1.2% of hydrogen. Before the preparation of the mixtures between the catalysts and the soot by tight contact method, Printex U was characterized.

In Figure 3.10.a, the TEM image of this carbon is shown and small spherical particles with a diameter of between 20 and 50 nm were observed, as has been reported by other authors [212] and in line with the values of diesel particles that have been obtained in real engine operation conditions [213,214]. The Raman spectrum of fresh soot is displayed in Figure 3.10.b together with its deconvolution and gives an insight into the type of carbon species.

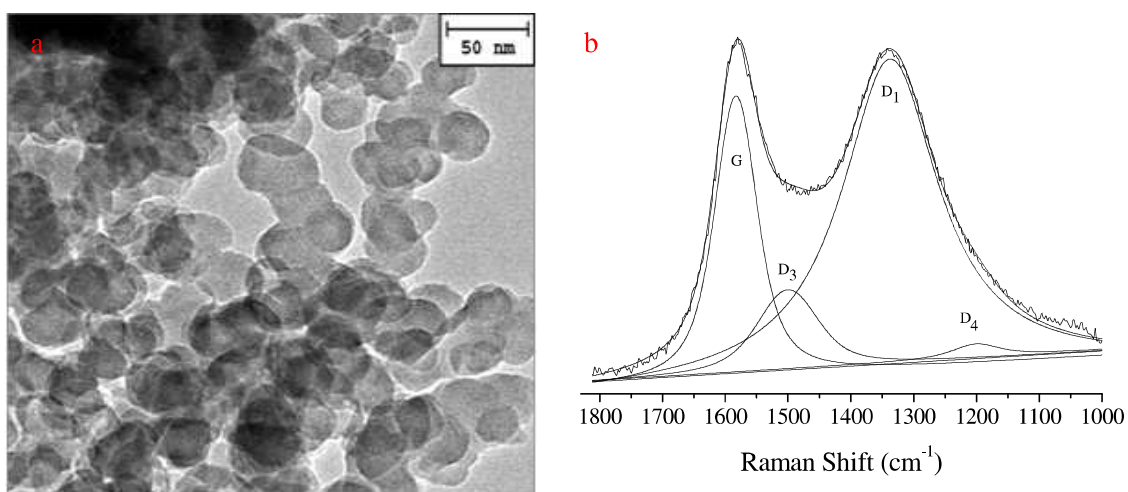


Figure 3.10. Fresh Printex U characterization: a) TEM image and b) Raman spectra.

In general, two bands, G (1580 cm^{-1}) and D₁ (1350 cm^{-1} , and also denoted as D) are representative of carbon, being associated with the ideal graphitic structure and the nature of disordered graphite, respectively. However, in a detailed analysis of the spectrum up to five signals could be considered. In that case, the D₂ band (around 1620 cm^{-1} and not detected in this material) is attributed to the disorder-induced graphitic lattice vibration mode, the D₃ signal (1500 cm^{-1}) is associated with amorphous sp^2 -bonded forms of carbon, and the D₄ band (1200 cm^{-1}) is related to disordered graphitic lattice, as other authors have previously reported [215–217] for other model and real kinds of particulate matter.

The model Printex U soot contained a combination of ideal and disordered graphitic lattices, where the main signals corresponded to disordered structures. The graphitization index, obtained as the ratio between G and D1 bands, was around 37%. This value was not too high in comparison with others previously reported and was indicative of the larger proportion of graphene layer edges that reacted in soot resulting in a high level of disorder.

XPS data were also analyzed and the deconvolution of the C1s region in three bands at 284.8, 285.9 and 288.8 eV was carried out. The predominant binding energy (64%), around 285 eV, as is common in this type of material [218], was associated with the C-C bond. The other contributions around 285.9 (20%) and 288.8 (16%) eV. were related to interactions between carbon and oxygen in different kinds of bonds.

The similarity between Printex U and real soot, which can be found in a vehicle working in real conditions, makes this model soot a suitable material with which to obtain realistic and reliable data at laboratory scale.

3.3.1. TRM over NSR catalysts + soot mixtures

In order to examine the influence of the particulate material in the NSR process, TRM studies were performed on mixtures of the catalysts with 10% of soot, alternating rectangular step feed of NO in lean condition (excess of oxygen) with rectangular step feed of H₂ in rich condition (absence of oxygen) as explained by the above named TRM experiment. The profiles of the product distribution for Pt-Ba/Al₂O₃, Pt-K/Al₂O₃ and Pt-Ba-K/Al₂O₃ and soot mixtures are displayed in Figures 3.11, 3.12 and 3.13, respectively.

In the lean phase of all catalysts, unconverted NO was observed together with NO₂ formation, due to the occurrence of the oxidation of NO by O₂ over Pt sites. However, the oxidation capacity in the initial cycles was decreased with respect to soot-free tests and could be caused by the masking of the active sites by the carbon. In addition, CO₂ production during this step was detected, as a consequence of the elimination of soot by the oxidant atmosphere and the amount decreased throughout the experiment. During the rich phase, N₂ and water were the main products of the reaction. Neither ammonia nor NO slips were observed, suggesting that the catalysts were more selective than their corresponding soot-free systems.

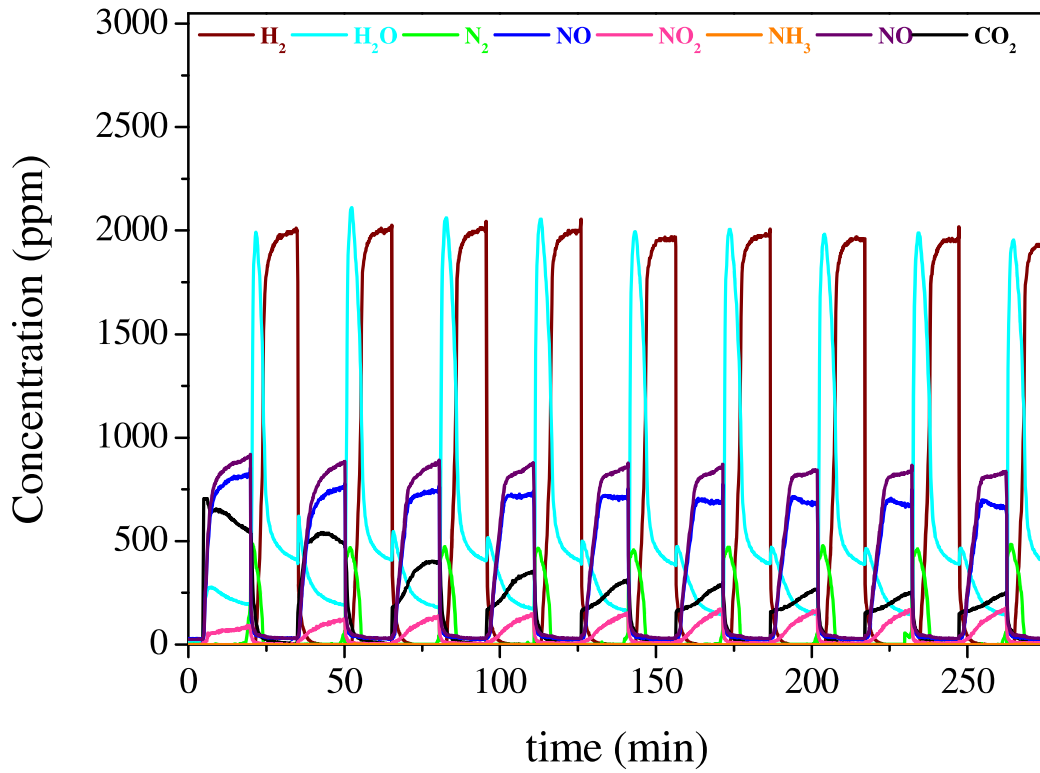


Figure 3.11. NO_x storage–reduction cycles at 350°C for Pt–Ba/Al₂O₃ + soot sample.

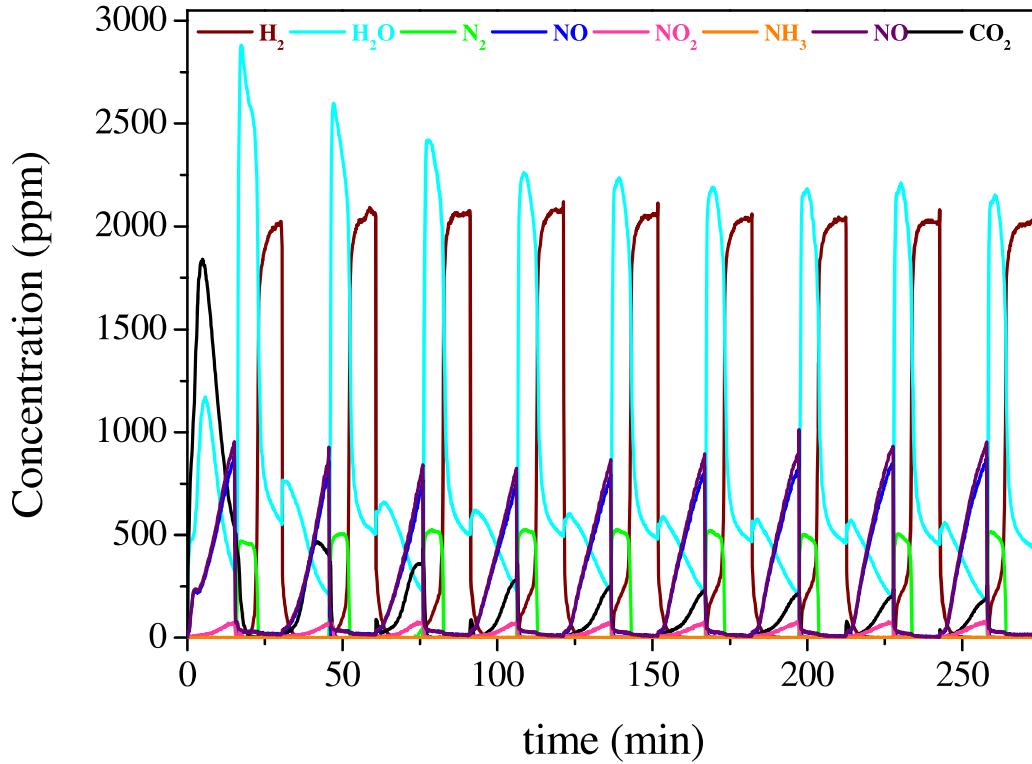


Figure 3.12. NO_x storage–reduction cycles at 350°C for Pt–K/Al₂O₃ + soot sample.

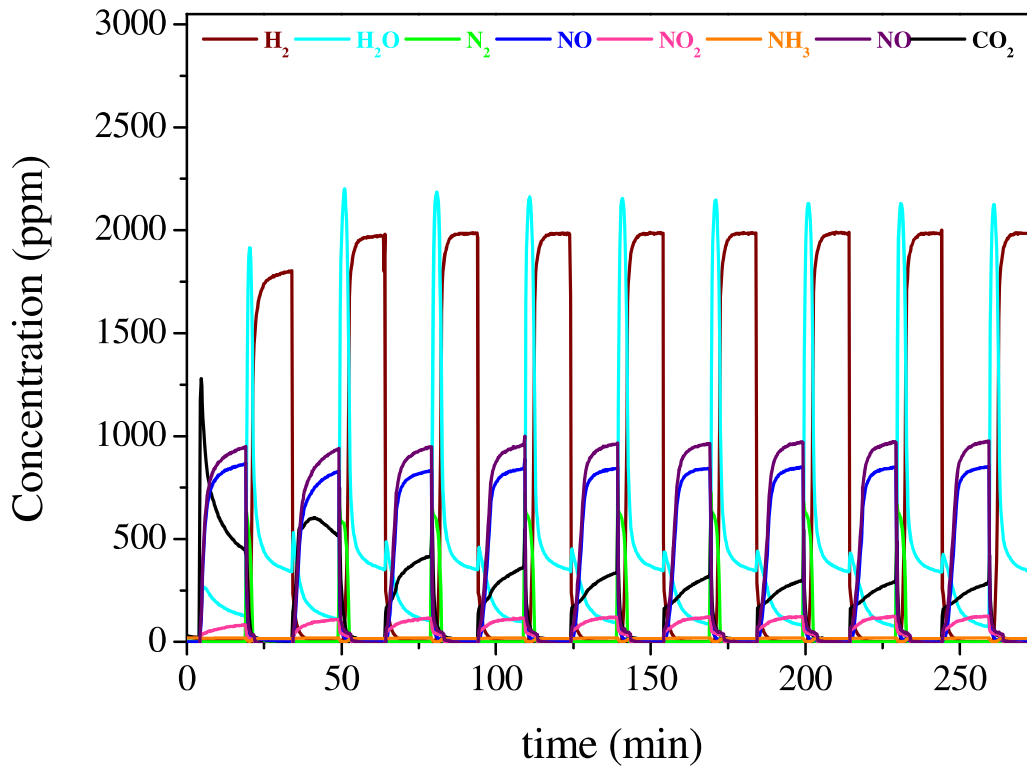


Figure 3.13. NO_x storage–reduction cycles at 350°C for Pt–Ba–K/Al₂O₃ + soot sample.

From the profiles, although the NSR process seems to occur in the same way, the NO_x adsorption in the lean phase accompanied by CO₂ production by soot elimination and the reduction of the adsorbed nitrates with N₂ and H₂O production, i.e. the processes of simultaneous removal of NO_x and soot, are modified depending on the element that is included in the formulation. In order to better understand the differences, the amount of NO_x removed and CO₂ produced over the systems were calculated and are plotted versus the cycle number in Figure 3.14.

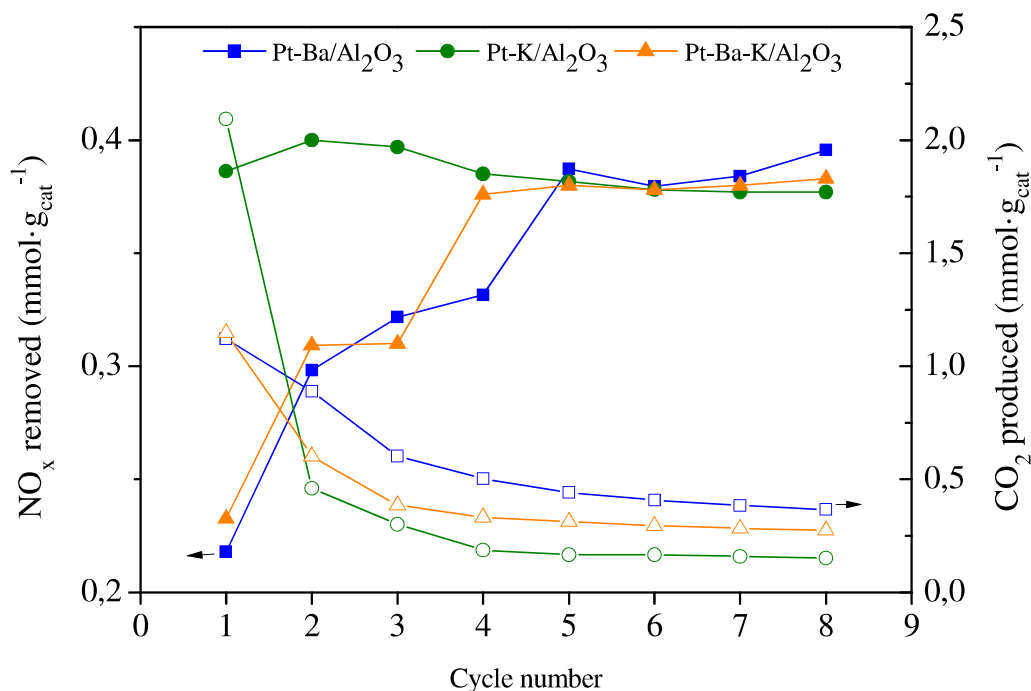


Figure 3.14. The amount of NO_x removed (coloured symbol) and CO₂ (blank symbol) produced vs. cycle number over catalyst+soot mixtures.

The TRM data obtained suggested that both, the alkali component and the composition have an influence on the general catalyst behaviour during reactions. Higher K loadings presented a better performance in terms of more rapid soot combustion; however, simultaneous soot and NO_x removal takes place with higher efficiency in the multicomponent system with higher Ba loading. Additionally, soot presence limits the adsorption of NO_x over the storage component and then the amount of NO_x accumulated diminishes as can be calculated for the last cycle where decreases from 0.42 mmol·g_{cat}⁻¹ to 0.36 mmol·g_{cat}⁻¹ for Pt-Ba-K/Al₂O₃ were observed. Regarding the amount of H₂O observed, it should be noted the evolution and concentration profile during the reducing step were delayed with respect to the N₂ concentration curve, which could indicate the rehydration of the catalyst during cycles. Moreover, due to the chemical nature of potassium and the surface structures observed, a higher production of water takes place, which facilitates the contact between soot and the active sites, promoting regeneration of the catalyst by the removal of particulate material through a process that involves water.

At this point, it is worth remembering the characterization of these systems that indicated the presence of a potassium carbonate phase, mostly K₄H₂(CO₃)₃·1.5H₂O and

K₂O, low melting point species that can moisten the surface of the catalysts improving their mobility and consequently their activity. The activity of Pt in NO oxidation is modified by the presence of storage components (Ba, K or Ba+K) having different electronic properties. High Ba content stabilized Pt⁰, playing an important role in NO_x adsorption.

The data showed the intermediate behaviour of the trimetallic catalyst with the performance of Pt-Ba/Al₂O₃ and Pt-K/Al₂O₃ catalysts. For Pt-Ba-K/Al₂O₃ + soot during the first 4 lean cycles, soot was removed efficiently giving off CO₂. This activity in terms of soot removal was most likely connected to the presence of K and its enhancing effect on the soot removal process. At the same time, NO_x storage and the concentration of NO₂ (lean phase) increased gradually with time, suggesting that CO₂ and NO/NO₂ competed for the same adsorption sites as other authors have previously reported [2,11,116,166]. From cycle 6, while soot oxidation took place at almost the same level, the catalyst performance in NO_x storage increased and was reproducible up to 50 cycles (data not shown). There was no evidence of strong deactivation suggesting that the addition of Ba improves catalytic regeneration.

The capacity for soot elimination is higher for the potassium-containing catalysts, which instantly eliminate a high proportion of the soot. Therefore, the behaviour of optimized trimetallic formulation (3.5 and 1.5 at/nm² of Ba and K, respectively) is similar to Pt-Ba in NO_x adsorption capacity with an improvement in the soot removal due to the presence of an amount of potassium that allows the theoretical monolayer coverage.

3.3.2. Isothermal thermogravimetric analyses of NSR catalysts + soot mixtures

An isothermal TG experiment (at 350 °C) under NO_x cyclic lean-rich conditions for Pt-Ba-K/Al₂O₃+soot mixture is presented in Figure 3.15. Before NO+O₂ admission, catalyst+soot mixture was treated in He flow from room temperature (rt.) to 350 °C, registering a weight loss value of 5.5% together with an exothermic signal attributed to a small amount of soot removal and the release of water and volatiles from the sample.

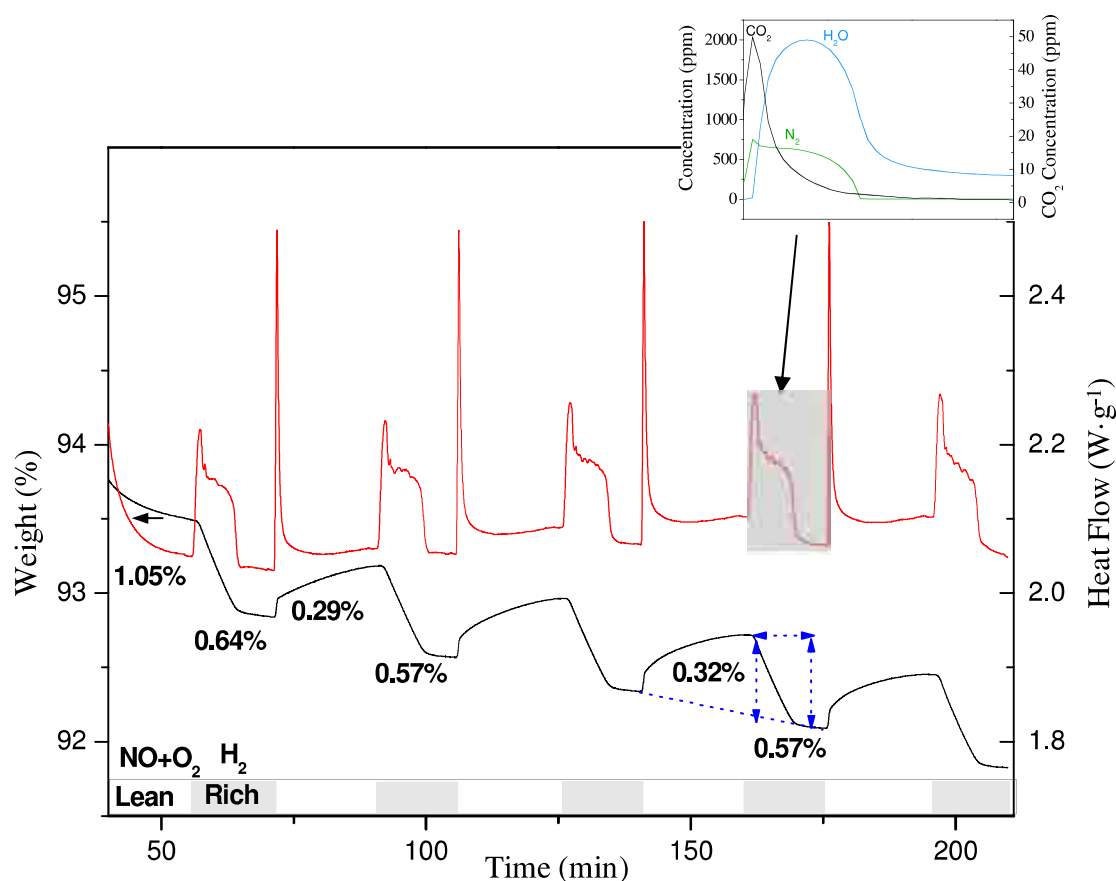


Figure 3.15. TG-TD analyses of Pt-Ba-K/Al₂O₃ + soot catalyst under isothermal (350°C) and cyclic conditions: lean (20 min, 1000ppm of NO + 3% of O₂ in He) and rich (15 min, 2000ppm of H₂ in He).

During lean-rich cycling, the behaviour of the investigated Pt-Ba-K/Al₂O₃+soot mixture was different in each cycle, mainly because the amount of soot gradually decreases continuously with time. During the first two cycles, noticeable soot removal activity was observed which corresponds to a 13.7 and 7.2% weight loss. The soot is progressively and completely oxidized after the 7th cycle (following the CO₂ signal in the MS). For LNT-catalyst + soot samples during the first storage cycle, despite the lean conditions (atmosphere NO/O₂), a mass loss of ca. 1% was observed. This weight decrease is directly related to soot removal, and the low storage capacity is associated with NO₂ consumption in the soot oxidation. CO₂ was produced during this reaction and part of it was stored on the catalyst in place of NO_x, however the amount of soot removed was still higher than the amount of CO₂ and NO_x trapped, thereby, giving a negative weight increase value. Moreover, the weight loss under rich condition can be divided into two steps, i.e. one with rapid mass loss and another with a near plateau line; this phenomenon can be observed for all cycles. The total weight loss is the highest during the first cycle (ca. 0.64 %) and later is roughly constant (0.57 %). This could

indicate that after 10 min. of sample treatment in H₂ atmosphere, the reduction of the stored species on the catalyst surface was complete. In fact the H₂ outlet signal registered in the MS after 10 min was equal to the H₂ inlet and H₂O, CO₂ and N₂ profiles approach zero. The heat flow profile during the rich phase also revealed two features, but completely different from the soot-free samples: one intense complex exothermic peak and then a near plateau baseline. The positive heat flow was similar to that explained above due to the regeneration of stored nitrites/nitrates, except for the intense initial peak that is accompanied by CO₂ formation and associated with the soot removal. The plateau line indicated that the soot removal took place only up to a certain point and the lower amount of adsorbed NO_x in the presence of soot was reduced in a shorter time.

In the presence of soot, the NO_x adsorption rate decreases from 9.5·10⁻³ to 4.5·10⁻³ mg·min⁻¹ in the initial cycles; however, when the catalyst is regenerated, after the 7th cycle, the adsorption rate of nitrogen oxides reaches values of around 9·10⁻³ mg·min⁻¹.

The TG profile for the second and additional steps of NO_x accumulation shows an increase of weight (0.29-0.33 %) together with a slight increase in the heat flow signal caused by an endothermic process. This could be associated with nitrite/nitrate accumulation and also to CO₂ adsorption onto the catalytic surface.

The difference between the weight loss and weight gain (%) during cycling, which is around 0.28% (for the second and additional cycles), can be attributed to several causes. The first could be the difference in mass of the reaction atmospheres to which the catalyst sample is exposed (NO/O₂ versus H₂); however, in soot-free isothermal experiments the difference is minimal. Another more likely cause could be connected with the occurrence of an interaction between stored nitrates and soot with CO₂ and NO formation, according to reaction (eq. 3.1). A third probable effect may suggest the gasification of soot in the presence of water (eq. 3.2) with the subsequent water gas shift reaction (eq. 3.3) promoted by platinum, hence no CO was observed.



The stored nitrate participation in soot removal has already been reported by different authors [12,163,219] and is a complex process because two solid phases are involved (catalyst and soot) together with a gas phase. The modification of the interface between these three components makes a detailed kinetic study difficult [220]. It has been proposed that the catalytic process provides for both CO and CO₂ formation as primary products and under non-catalytic conditions, the CO/CO₂ ratio is dependent on the oxygen supply and temperature [140]. The catalytic soot removal mechanism is based on the formation of surface oxygen complexes (SOCs) as soot oxidation intermediates, and when NO₂ was present together with O₂ in the gas mixture, the oxygenated carbon complexes were found to form firstly via the reaction of soot with NO₂. Moreover the study of soot combustion over alkaline and alkaline-earth oxide catalysts suggests the formation of alkaline oxygenated compounds which play a major role in the oxygen transfer process [140]. In addition, the formation of surface –OH groups or chemisorbed water was found to promote the elimination of soot, which is of particular importance for K-containing systems and is in line with previous studies [2].

The simultaneous soot and NO_x removal over Pt-Ba-K/Al₂O₃ catalysts under lean conditions proceed in a similar way as in the case of NO_x-assisted soot combustion [2]. The enhancement in the soot combustion rate in the presence of NO_x (lean phase) can be associated with the conversion of NO_x to NO₂ and stored nitrate species, which then react with soot. Under reduction conditions (rich phase), when H₂O is formed the removal of soot was possible most likely due to the participation of nitrite/nitrate species and the product of their partial decomposition, NO₂, which is a product of partial nitrite/nitrate reduction, as stated previously [2]. The LNT-trimetallic model catalyst modifies the released N-species distribution. In addition, the potassium influences water adsorption/desorption management, which most likely intensified the soot-catalyst surface contact and thus enhanced the overall system activity towards soot removal.

3.3.3. NSR mechanism over Pt-Ba-K/Al₂O₃ + soot mixture

For the purposes of studying the evolution of the catalytic surface during the DPNR process and evidencing the behaviour observed in the TRM flow runs, DRIFTS experiments were carried out in similar feeding conditions. So, pulses of 15 min of

1000ppm of NO + 3% of O₂ and 2000ppm of H₂ were alternated and spectra were registered every 2 min. DRIFT spectra of the nature and isothermal transformation of the surface NO_x species recorded from the storage-reduction cycles at 350°C for Pt-Ba-K/Al₂O₃ + soot are shown in Figure 3.16.

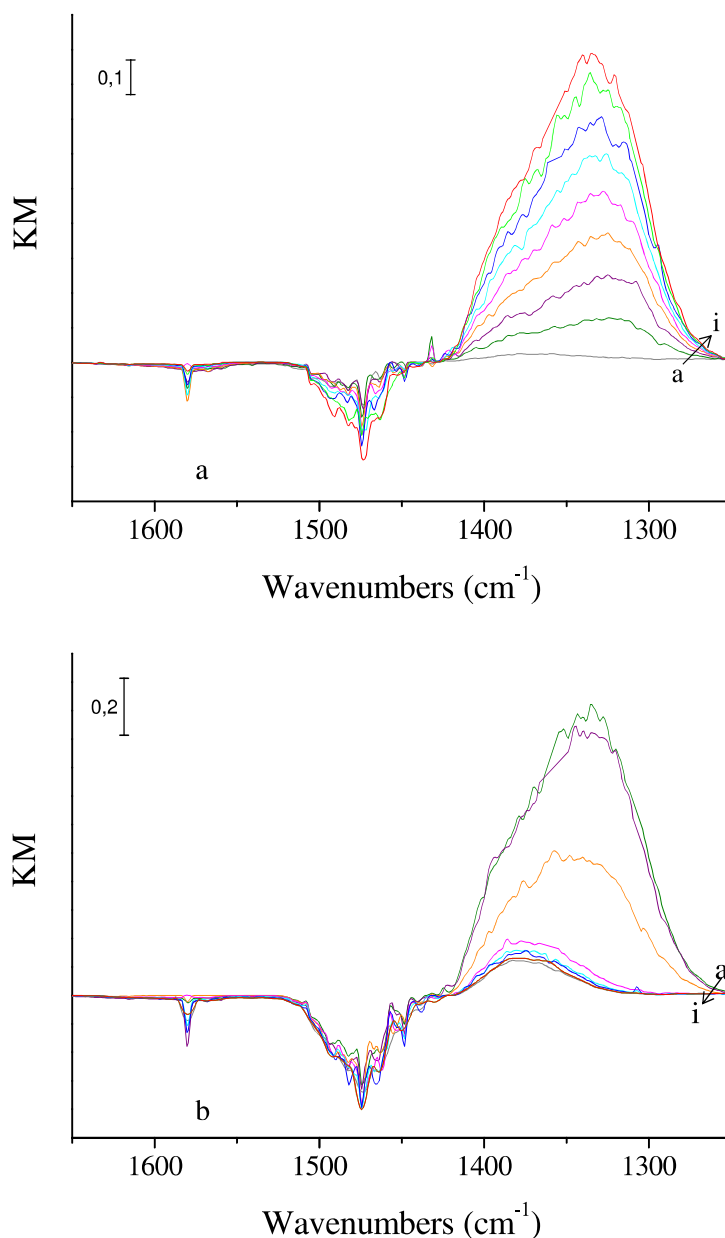


Figure 3.16. DRIFT spectra recorded at 350°C over Pt–Ba-K/Al₂O₃ + soot in He under a) lean and b) rich phase flow from a) 1 min to i) 15 min.

The DRIFT spectra discussion focuses on the wavenumber range between 1650 and 1250 cm⁻¹ where bands indicative of the formation and transformation of adsorbed NO_x species can be analyzed. As has been previously detailed, the peaks of the ν₃ mode of

monodentate, bidentate and bridged nitrates appear at $1530\text{--}1480\text{cm}^{-1}$, $1565\text{--}1500\text{cm}^{-1}$, and $1650\text{--}1600\text{cm}^{-1}$, respectively, while the ν_3 mode of monodentate nitrite, bridged nitrite, and nitro compounds are detected at $1470\text{--}1450\text{cm}^{-1}$, $1220\text{--}1205\text{cm}^{-1}$, and $1440\text{--}1335\text{cm}^{-1}$, respectively [221]. Some attribute the band at $1460\text{--}1300\text{cm}^{-1}$ to nitrates instead of nitro groups [222], and these authors also assign a peak at $1330\text{--}1320\text{cm}^{-1}$ to bidentate nitrites.

On the surface of the catalyst (Fig 3.16.a), the formation of monodentate and bidentate nitrates was noticed by the bands at 1310, 1320 and 1335 cm^{-1} . Additional bands due to ionic nitrate and free nitrate ions were also observed at 1380 and 1740 cm^{-1} . The bands observed at 1360 cm^{-1} and 1410 cm^{-1} were associated with chelating bidentate carbonates and carbonate ions as carbon base adsorbate due to the presence of soot. Nitrates were the prevailing sorption species suggesting that the high oxidation capacity of the catalyst makes the oxidation of NO to NO_2 and nitrate much faster. Although nitrites were not observed as intermediates in the reaction process, they may exist temporarily at the beginning of the step.

The appearance of negative bands at $1520\text{--}1570\text{ cm}^{-1}$ that increase in intensity was related to the adsorption/displacement of the surface carbonate species associated with potassium and barium. CO_2 produced during the lean phase (in agreement with TRM cycles) is partially retained by the compounds present on the catalysts surface.

During the reduction of stored nitrates/nitrites with H_2 the surface properties were only partially restored. A broad and less intense band with maximum at 1380 cm^{-1} was detected; this band and the negative peaks suggest that the removal of a part of the Ba carbonates took place. Additionally, a weak adsorption region was also detected between 2070 cm^{-1} and 1860 cm^{-1} (not shown) due to the remaining CO bonding with Pt species [2]. A second lean-rich cycle was carried out under the same experimental condition and the registered spectra were quite similar, suggesting that after the reduction by H_2 the remaining species do not cause the material deactivation.

In general, DRIFT spectra recorded for Pt-Ba-K/ Al_2O_3 + soot showed that the surface was dominated by the higher Ba presence, indeed, during the accumulation phase band assignment was similar to the Pt-Ba + soot system already published [2]. The complexity of the absorption peaks for these nitrates reflects the heterogeneity of the

surface sites (K and Ba sites), which results in the nitrate species coordinating with the catalyst surface in different ways.

All these data confirm that the incorporation of potassium to a Pt-Ba *quasi*-model catalyst causes almost instant soot removal when the catalyst is exposed to alternating conditions, with the NO_x adsorption capacity being recovered as the PM is eliminated. *Peralta et al.* [9] have proposed that the high reactivity of the alkali metal is due to the high mobility of some potassium compounds that improves the effective contact between soot and catalysts, whereas other authors [2,140,223] have suggested that another soot removal mechanism is involved in the presence of this metal. For this reason, a detailed study of the soot removal mechanism in the presence of LNT catalyst in different oxidant conditions is explained below.

3.3.4. Soot removal mechanism over LNT-catalysts

In order to better understand the soot removal pathway and the estimation of kinetic parameters; TG-MS curves were performed in different oxidation atmospheres measured at a constant rate of heating (10°C·min⁻¹) and obtained under chemical regime; i.e. out of mass transfer limitations. The TG curves had to be obtained under chemical regime in order to evaluate f(E) (distribution function of activation energy); so the mass transfer resistance for the current particle size (<1 mm in diameter) was negligible at a flow rate of 100 ml·min⁻¹ (STP).

The weight loss of soot in the presence of different catalysts in atmosphere of O₂ (3% He-balance) are shown in the following figures, together with the concentration of water and CO₂ measured by MS. The profile obtained for soot (free-catalyst) is also included.

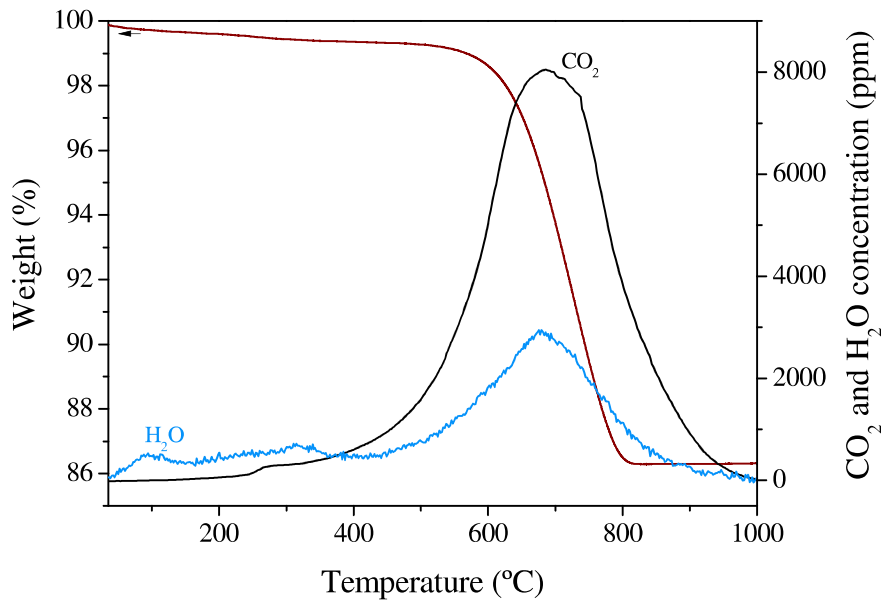


Figure 3.17. Weight loss and product distribution vs. temperature in the presence of 3% of O₂ in He for soot.

The weight loss observed for soot (Fig. 3.17), in oxygen atmosphere, is close to 10 % of the initial weight and having been produced in a single step and registered in the range between 600 and 800°C. However, the TG profiles for soot removal in O₂-atmosphere over alkaline-modified Pt alumina-supported catalysts (LNT improved catalysts) showed that the soot removal occurs in a different way even at lower temperatures. In the presence of Pt-Ba/Al₂O₃ (Fig. 3.18), standard formulation of LNT catalysts, the soot removal also took place in a single step but with a higher weight loss rate, and at a slightly lower temperature range than soot-free catalysts, indicating that it is an activated process.

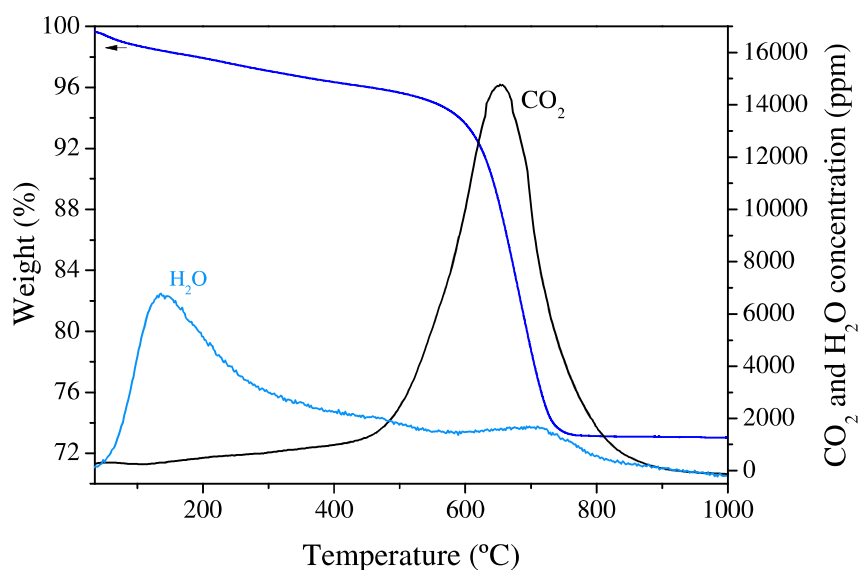


Figure 3.18. Weight loss and product distribution vs. temperature in the presence of 3% of O₂ in He for Pt-Ba/Al₂O₃.

For Pt-K/Al₂O₃ (Fig. 3.19), where the Ba was substituted by K, with a metal loading for the almost same surface coverage, the TG curve registered was completely different; in which three steps for the soot-removal process can be clearly differentiated. A region between 200 and 350°C with a loss of 7% was observed related to the dehydration of chemisorbed water. A second step, from 350 to 500°C, can be seen where 10% of soot was eliminated, and CO₂ and H₂O formations were registered. Finally, a third temperature window at higher temperatures with a weight loss of 4% was observed and is associated with the removal of the rest of the soot, by combustion, possibly due to less contact with the catalyst.

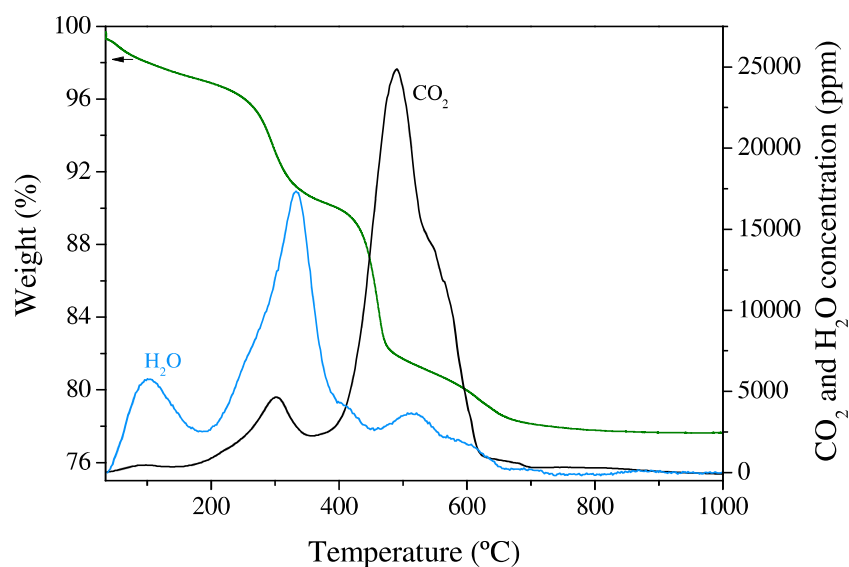


Figure 3.19. Weight loss and product distribution vs. temperature in the presence of 3% of O₂ in He for Pt-K/Al₂O₃.

The soot removal process over Pt-Ba-K/Al₂O₃ occurs in a wider temperature range, between 400 and 800°C and the weight loss corresponded to 11% of the total. An intermediate behaviour between Pt-Ba/Al₂O₃ and Pt-K/Al₂O₃ was found for the trimetallic catalyst; although, it was apparently closer to the Ba-containing catalyst due to the similar relative load of this element in the formulation. So that the expected reactivity in the catalytic soot oxidation depends on the electropositive character of the metal added to the catalyst formulation and the surface species. It is evidenced that the presence of K or Ba oxides modifies CO₂ production with regard to uncatalyzed soot oxidation and the H₂O released is more related to the K-containing catalysts.

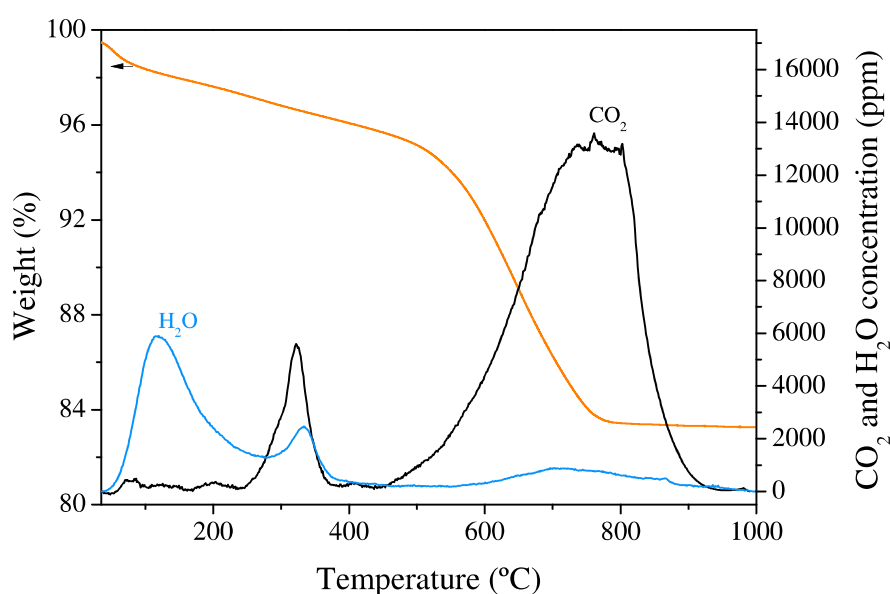


Figure 3.20. Weight loss and product distribution vs. temperature in the presence of 3% of O₂ in He for Pt-Ba-K/Al₂O₃.

TG-curves in atmosphere of NO+O₂ and the CO₂ and H₂O distribution profiles for the same materials are shown in the following figures. The uncatalyzed soot removal presented a weight loss of 10% and the temperature range is narrower than was observed in O₂-atmosphere, due to a more oxidizing environment.

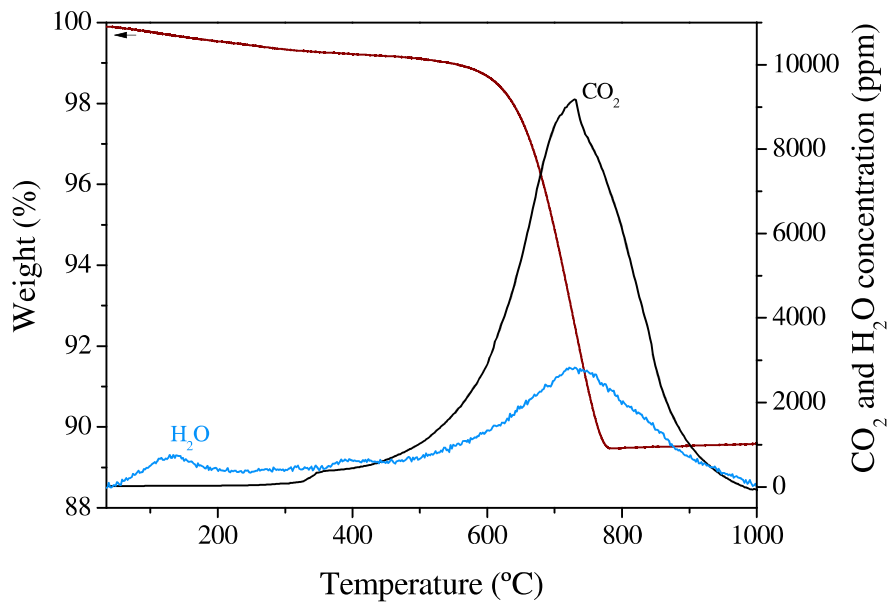


Figure 3.21. Weight loss and product distribution vs. temperature in the presence of 1000ppm of NO + 3% of O₂ in He for soot.

For the standard LNT-catalyst formulation (Pt-Ba/Al₂O₃, Fig. 3.22), the soot removal occurred in a single step between 500 and 800°C with a weight-loss close to 22%, associated with the elimination of the particulate matter and a further decarbonation of the catalyst. This process is activated and the temperature interval in which the soot combustion takes place is consistent with data reported by other authors [174].

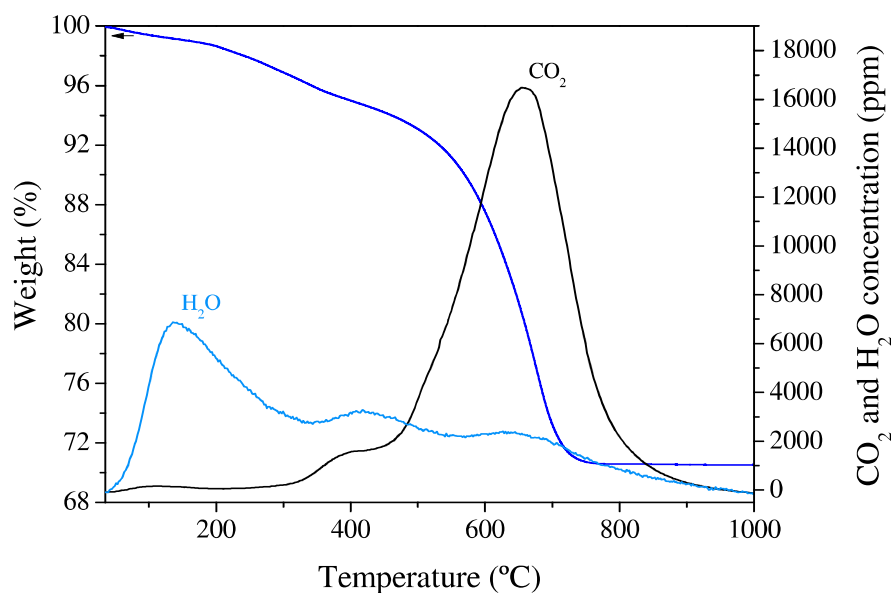


Figure 3.22. Weight loss and products distribution vs. temperature in the presence of 1000ppm of NO + 3% of O₂ in He Pt-Ba/Al₂O₃.

For Pt-K/Al₂O₃ the TG profile was completely different, and three consecutive weight losses were registered and associated with a sequential soot elimination process; with an additional partial dehydration by chemisorbed water at temperatures of between 200 and 350°C with a weight loss of 7%. The three sequential steps were detected at 350-500°C, 500-600°C and 600-750°C with weight losses of 9, 2.5 y 2%, respectively. Contrary to what was registered for the uncatalyzed and over the Pt-Ba/Al₂O₃ catalyst, the MS-signals for H₂O and CO₂ in the case of the K-containing catalyst were also different even in NO+O₂ atmosphere. So, four non-symmetrical signals for water evolution were registered, and a peak close to 300°C and an asymmetrical signal between 400 and 600°C in the CO₂ profile.

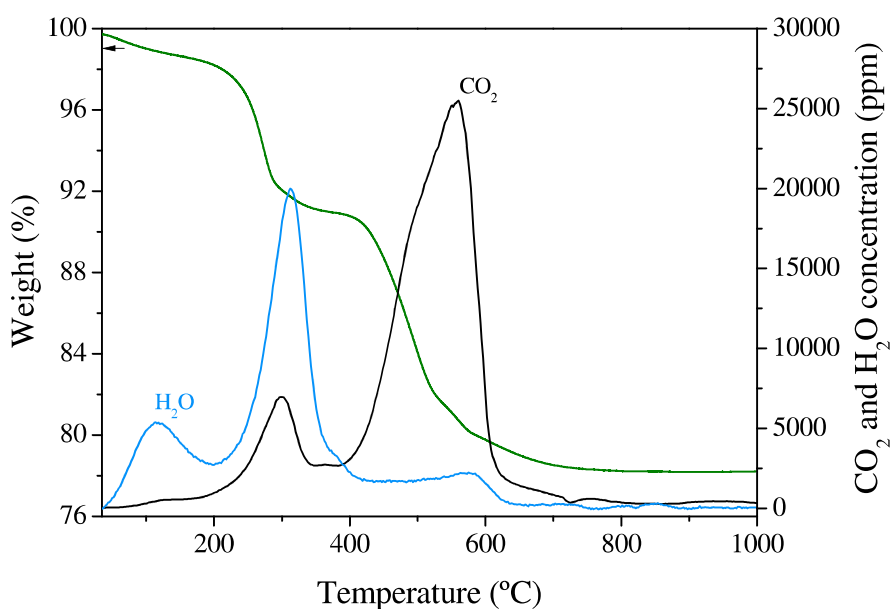


Figure 3.23. Weight loss and product distribution vs. temperature in the presence of 1000ppm of NO + 3% of O₂ in He for Pt-K/Al₂O₃.

The TG-curve obtained over Pt-Ba-K/Al₂O₃ was halfway between those observed for the Pt-Ba and Pt-K model catalysts, and it also showed sequential steps although it was closer to the catalyst that incorporates the alkaline-earth metal.

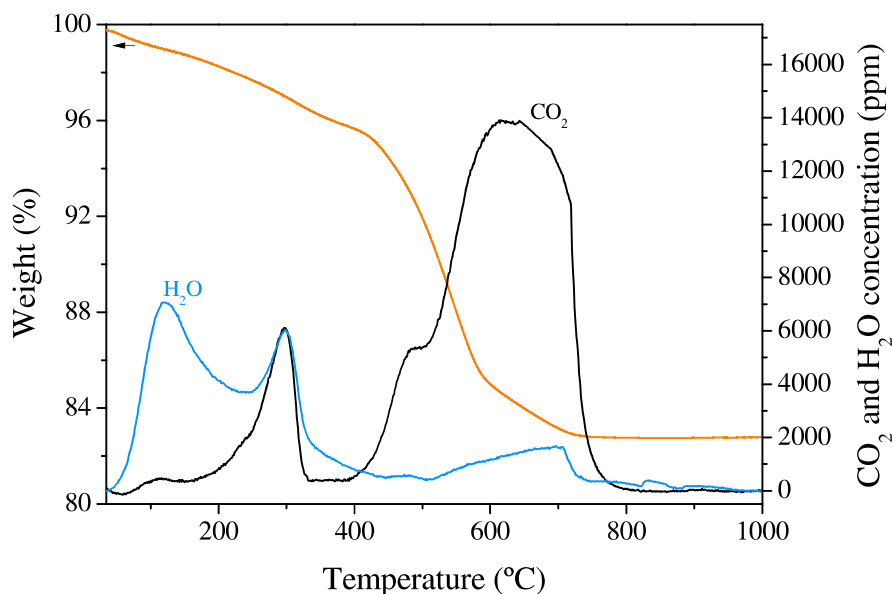


Figure 3.24. Weight loss and product distribution vs. temperature in the presence of 1000ppm of NO + 3% of O₂ in He for Pt-Ba-K/Al₂O₃.

The mass loss strongly increased in the presence of NO+O₂ although the total burn-off associated with ash remained practically unaffected. In addition, the soot elimination occurred in a lower temperature range compared to the same experiment in the absence of NO, due to a greater oxidizing environment [150]. The effect of Pt on the catalytic oxidation of soot for Pt-containing catalysts, facilitating NO-oxidation, has been discussed so far in the literature. NO₂ formation is enhanced by Pt and transported via the gas phase over soot particles, oxidizing carbon while itself being reduced to NO [224]. NO₂ is known to oxidize soot at lower temperatures than O₂, being a stronger oxidant [123,144,150]. However, some form of cooperative effect must exist, promoted by the alkali or alkaline earth in the LNT catalysts that modifies the curves and the profiles in the soot removal process. All samples exhibited a slight weight loss up to 350°C attributed to the desorption of water adsorbed on soot particle besides the chemisorbed water depending on chemical nature of the catalysts [224]. The peaks registered at higher temperatures, above 700°C, were associated with soot combustion albeit slightly shifted, as reported earlier by *L. Castoldi et al.* [140], by the presence of either the alkaline or the alkaline-earth oxide species. However, intermediate signals also improved the soot removal, and must be associated with other factors that are related to the formulation of catalysts and improve the overall process of the elimination of carbon particles.

In order to further study the soot removal process, the heat flow was also analyzed. In Figure 3.25, the heat flow curves of O₂ and NO+O₂ assisted soot elimination, with or without an LNT catalyst, in the temperature range of 50–950°C at a heating rate of 10°C·min⁻¹ are presented. Each exothermic signal is associated with the weight loss observed in the TG profile and the process that took place.

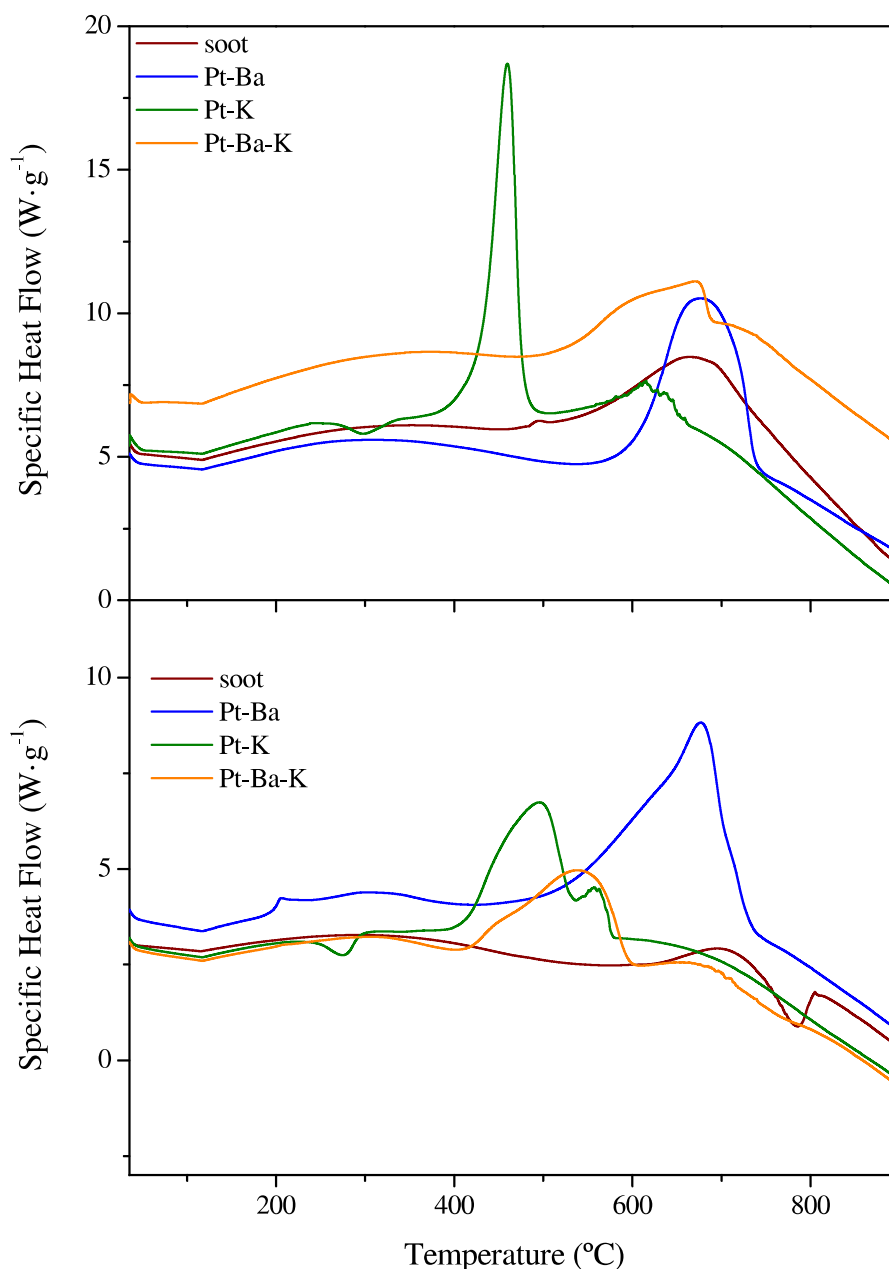


Figure 3.25. Specific heat flow during soot oxidation without catalyst participation and over prepared catalysts in different conditions (A) 3% O₂ in He flow; (B) 1000 ppm of NO + 3% of O₂ in He flow.

The heat flow curve for bare soot combustion in O₂ atmosphere shows two broad exothermic peaks, one at a lower temperature region i.e. 120-500°C, with a heat flow

increase up to 7%, and another at 675 °C, with a heat flow increase in ca. 50%. Those signals were most likely related to the slow gasification reaction of soot with the release of water and CO₂ (120-500°C) followed by the combustion of the soot sample (675°C). The exothermic nature of the soot removal process has been previously reported [225] in the study of titanates for diesel soot combustion. At the end of the test, an increase in heat flow was evidenced due to the gas composition change in the TG chamber. Similar heat effects were detected for soot elimination over Pt-Ba/Al₂O₃, but the increase in heat flow was higher than in the case of bare soot combustion. However, the main exothermic peak was still observed at 675°C. The heat profiles suggested that the main combustion region was narrower in the case of the Pt-Ba/Al₂O₃ catalyst. The heat profile for soot combustion over the Pt-K/Al₂O₃ catalyst differs from that of the Pt-Ba/Al₂O₃. Instead of two signals, the heat flow curve obtained during soot combustion over Pt-K/Al₂O₃ shows one endothermic and two sharp exothermic peaks, with centers at 275, 460 and 610°C, respectively, with values of 6W·g⁻¹ (275°C), 19W·g⁻¹ (460°C) and 8W·g⁻¹ (610°C). The endothermic process detected around 275°C corresponds to the desorption of crystallization water of the catalyst. The greatest exothermic process takes place ca. 460°C related to the intervention of potassium centers. For the Pt-Ba-K/Al₂O₃ catalyst the heat flow curve is similar to those obtained for soot combustion over the Pt-Ba sample, but with the baseline shifted towards ca. 50% higher values than in the case of Pt-K/Al₂O₃ and Pt-Ba/Al₂O₃ catalyst. This behaviour allows the individualization of the role of each element.

For NO+O₂ assisted soot combustion, the heat flow baseline was shifted to lower values, from 5W·g⁻¹ to 2.5W·g⁻¹ (Fig. 3.25) for all experiments with and without a catalyst. For Pt-Ba/Al₂O₃, the asymmetric exothermic peak, shoulder, evidenced around 600°C, with a maximum value at 675°C located at similar temperatures but with a relative heat flow value higher than O₂ assisted atmosphere, is associated with two coupled exothermic processes, which are related to the different oxidative species involved (adsorbed nitrate species and O₂ gas phase), according to the differences detected in the TG profile. For Pt-K/Al₂O₃, the endothermic dehydration process at low temperatures was also detected and associated with the first weight loss in the TG profile. The difference between the two exothermic peaks is narrower, with maximum values at 475 and 550°C, due to the additional interaction of soot with nitrate species, but with a similar total heat flow. For Pt-Ba-K/Al₂O₃, the heat profile reveals three

exothermic peaks that were shifted to lower temperatures, i.e. 475, 575 and 675°C compared to O₂ assisted soot removal, because of the more oxidizing atmosphere and the adsorbed species that are involved in a series of more exothermic and faster reactions. Those experiments revealed that there is a connection between heat flow and the mass loss stages observed during TG-DTA-MS in situ analysis that depends on the soot removal process which is a sequential process of coupled reactions. The main change in soot elimination and heat flow values were observed for LNT catalysts where K was incorporated, due to the process of soot removal by its centers.

The combination of TG-profiles, heat flows and gas-product distribution observed suggest that there are activated processes where the frequency of occurrence depends on the characteristics of the catalyst and the reaction atmosphere. The analysis of complex reactions to deduce the intrinsic removal mechanism of soot in the presence of different catalysts and reaction atmospheres has been approached through kinetic data, taking account of the variation of the frequency factor of the single processes. So, the decoupling of complex reactions allows the establishment of an explanation route for the soot removal process in the presence of LNT-catalysts. The kinetics was analyzed based on a model where the soot-removal reaction consists of a series of first-order reactions each of which has a different activation energy and frequency factor. The frequency factors were closely correlated by a function of the activation energy. The different activation energies were represented by a distribution curve obtained from the TG-curves measured at a constant heating rate. The weight loss during the removal process, in different environments, was predicted by using the curve determined by the proposed method.

It was assumed that the soot removal process takes place through a series of irreversible, independent and parallel first-order reactions. The differences in the reaction rate were represented by the activation energy and the frequency factor values. So, the weight loss of soot elimination of the i-th adsorbed species was represented by:

$$-\frac{dm_i}{dt} = k_{oi} \cdot e^{-E_i/RT} \cdot m_i \quad (3.4)$$

where m_i (mg) is the mass-weight, E_i and k_{oi} are, the activation energy (kJ·mol⁻¹) and the frequency factor (s⁻¹), respectively, if the rate equation of the Arrhenius type is assumed. *Anthony et al.* [226] analyzed the fast pyrolysis of coal based on a model

which accepts that the pyrolysis consists of a large number of first-order independent reactions, according to the model originally derived from *Vand* [227] for analyzing the irreversible change in the resistance of metallic films prepared by evaporation. According to this model the unconverted fraction $q(t)$ is given as a function of time and temperature as:

$$q(t) = \frac{m(t)}{m_0} = \int_0^{\infty} \exp \left[-k_0 \int_0^t e^{-E/RT} dt \right] f(E) dE \quad (3.5)$$

where $f(E)$ is the distribution function of activation energy defined so as to satisfy

$$\int_0^{\infty} f(E) dE = 1 \quad (3.6)$$

The value of the frequency factor is not constant and is related to the activation energy, based on a well-known experimental fact that the frequency factor increases with the increase of activation energy. The relationship between them, given by Eq. 3.7, is known as "compensation effect" in the field of chemical reaction kinetics [228]:

$$k_0 = \alpha \cdot e^{\beta E} \quad (3.7)$$

where α and β are positive constants determined experimentally, which vary depending on the nature of the process. In previous experiments on the decomposition of organic compounds adsorbed on these LNT-catalysts, it was found that the frequency factor (k_0) increases with the activation energy and the following equation (α and β) is as follows:

$$k_0 = \alpha \cdot e^{\beta E}; \quad k_0 = 10^7 \cdot e^{0.043E}$$

These data provides activation energy values that are within the ranges given in other literature using different routes for estimation, such as *Kissenger-Akahira-Sunose* isoconversional methods, *Coats-Redfern* model-fitting method or the equation proposed by *Brukh* and *Mitra* [138,141,142,146,149,150,229].

Substituting Eq. 3.7 in Eq. 3.5, the following expression was obtained:

$$q(t) = \int_0^{\infty} \exp \left[-\alpha \cdot e^{\beta E} \int_0^t e^{-E/RT} dt \right] f(E) dE \quad (3.8)$$

The equation 3.8 indicated that weight-loss can be estimated when the relationship between temperature and time are given, and α and β and $f(E)$ are predetermined. The distribution curve of activation energy, $f(E)$ was determined by the analysis of the thermogravimetric curve at a constant heat rate (a) and the Eq. 3.8 was rewritten as follows:

$$q(T) \cong \int_0^{\infty} \Phi(E,T)f(E)dE \quad (3.9)$$

where $\Phi(E, T)$, related to the temperature and the activation energy and considering the Poisson approximation, could be replaced by

$$\Phi(E, T) \cong \exp \left[-\frac{\alpha e^{\beta E T}}{a} \cdot \frac{e^{-E/RT}}{E/RT} \right] \quad (3.10)$$

By examining the change of $\Phi(E, T)$ with respect to E at fixed temperatures, $\Phi(E, T)$ was found to be approximated by the tangent line at the inflection point of $\Phi(E, T)$. Based on this estimation $f(E)$ is formulated as

$$f(\bar{E}) = -\frac{(1+S)^2}{R[P(P+M/P)(e/2+S)+P(2S-P)]} \cdot \frac{dq}{dT} \quad (3.11)$$

where P , S , \bar{E} and M are related to temperature (T), respectively, as seen in the following equations.

$$P = E_{in}/RT \quad (3.12)$$

$$S = P - \beta E_{in} \quad (3.13)$$

$$\bar{E} = [(2S + e)/2(S + 1)]E_{in} \quad (3.14)$$

$$M = P(2 + P)/(1 + S) \quad (3.15)$$

where E_{in} is the activation energy at the inflection point in Eq. 3.10, and is related to T by

$$\frac{\alpha E_{in}}{\alpha e^{\beta E_{in} RT^2}} \cong e^{-E_{in}/RT} \quad (3.16)$$

All values on the right hand side of Eq. 3.11 can be calculated in advance for select T values by the equations 3.12-3.15. The differential value on the right hand side of Eq.

3.11 can be obtained by numerical differentiation of the TG-curve at a constant heating rate.

The function of distribution of the activation energy obtained for the uncatalyzed soot removal in O_2 and $NO+O_2$ atmospheres are shown in Figure 3.26.

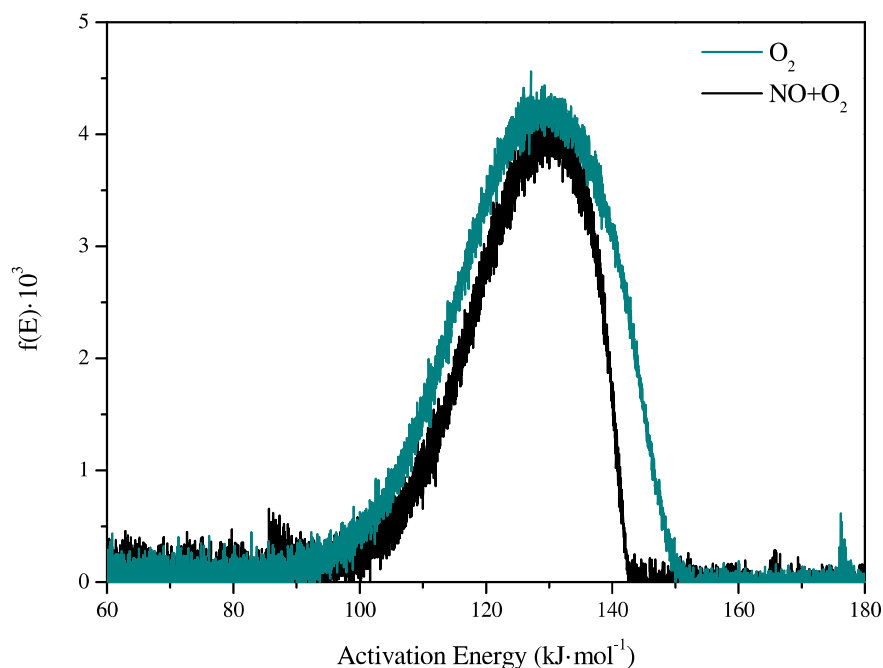
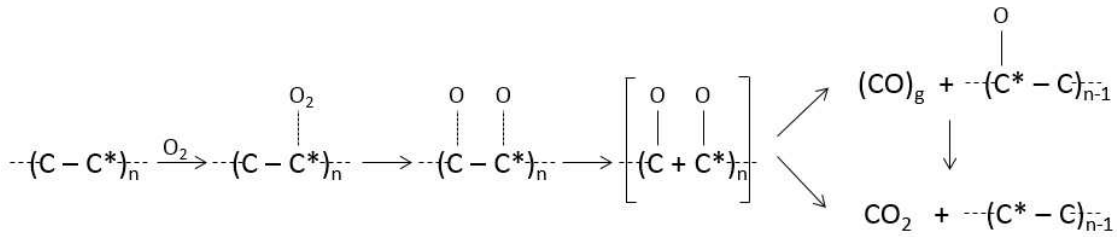


Figure 3.26. Distribution functions of activation energy for the uncatalyzed soot elimination in different atmospheres.

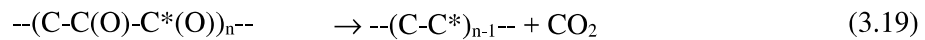
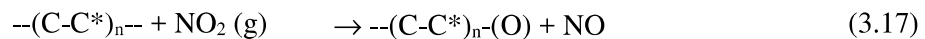
In the presence of oxygen, the distribution function is a quasi-symmetric monomodal Gaussian type curve with a maximum frequency value for activation energy close to $130 \text{ kJ}\cdot\text{mol}^{-1}$, where CO_2 was the main product detected in the temperature range between 550 and 850°C . This value is in agreement with other values of activation energy reported in bibliographies for particulate matter combustion reactions, when soot samples with similar characteristics to Printex U are used; although, the activation energy values could vary to between 130 and $160 \text{ kJ}\cdot\text{mol}^{-1}$, depending on the heterogeneity of the surface and structural properties of the soot [131,138,142,224,230]. It is generally accepted that soot combustion follows a mechanism based on surface nucleation with the subsequent movement of the resulting surface, which is consistent with the oxygen passing through the porous structure of the solid sample and finally the reduction in size of the spheres until total combustion (Scheme 1) where C^* is an available carbon site to be oxidized.



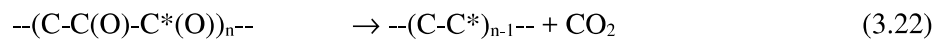
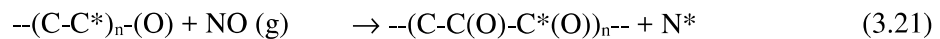
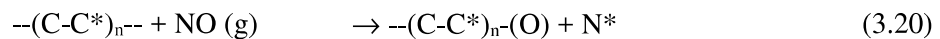
Scheme 1. Mechanism of uncatalyzed soot combustion under O₂ atmosphere.

For the elimination of uncatalyzed soot in NO+O₂ atmosphere, the function of distribution is an asymmetric and narrower curve with a single and relative maximum close to 130 kJ·mol⁻¹, in which an increase in the NO signal was detected by MS in the temperature range between 550 and 650°C and where CO₂ was the main product registered in a wider temperature range of between 560 and 750°C.

It is evident that the influence of NO_x in the gas phase improves the oxidation of the surface; but two possible mechanisms, depending on the main species present, NO₂ or NO, are both possible. In keeping with the MS data for product distribution, where NO detection and CO₂ formation were registered with a progressive shortening in the carbon chain and the data previously reported [150,151] for the NO₂, the following reactions (Eqs. 3.17-3.19) could represent the route for soot removal in the uncatalyzed process



In the case of the NO, where N₂ and CO₂ should be the products detected, the equation would be as follows:



The first route was apparently more convincing in concordance with the results obtained by mass spectrometry (data not shown), where an increase of the NO signal was observed in the temperature range between 550 and 700°C with simultaneous CO₂ production as well as an additional CO₂ formation that extended up to 950°C; indicating that the removal process occurs in greater proportions as a result of the influence of NO₂, due to its greater oxidizing potential according to the equilibrium reaction: $\text{NO} + \text{O}_2 \leftrightarrow \text{NO}_2$. It was also reported that the soot properties, including microstructure, elemental analysis, ash content and ash composition, determine its reactivity towards oxidation with synthetic air and NO_x [4,138,224,230].

The distribution functions for the catalyzed soot removal process in an oxygen atmosphere and the deconvolution of the signals are shown in Figure 3.27. For the Pt-Ba/Al₂O₃ with a LNT-catalyst standard formulation, the distribution function calculated was a *quasi*-symmetric curve with a maximum close to 120 kJ·mol⁻¹. However, the deconvolution showed that this oxidation process is a series of coupled processes due to the fact that two activation energy values were registered at 117 and 128 kJ·mol⁻¹; associated with the O₂-ads catalyst and the O₂ gas phase contributions, respectively.

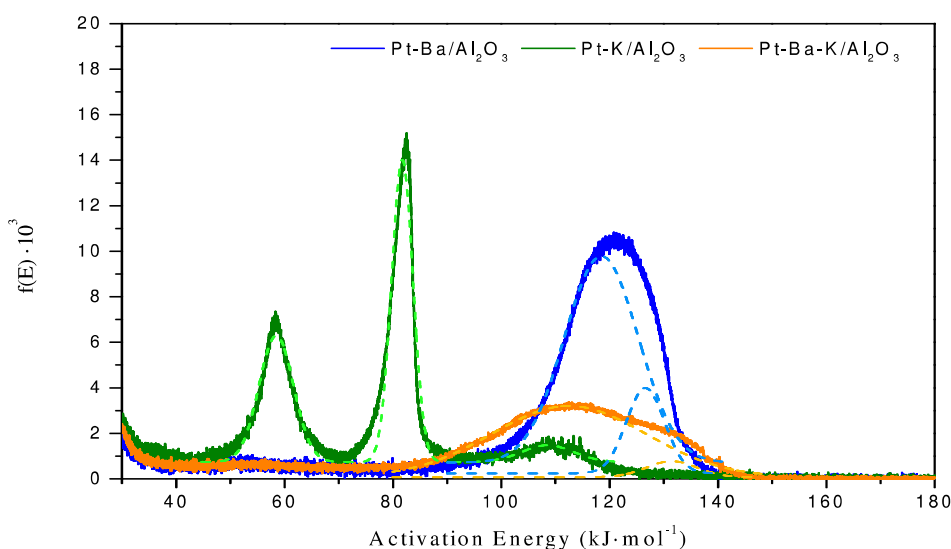
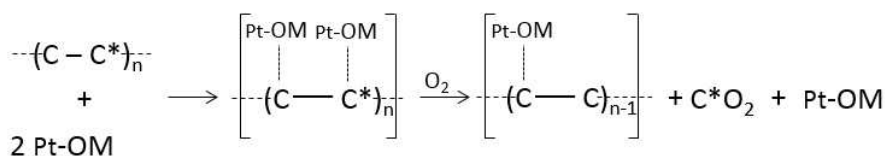


Figure 3.27. Distribution functions of activation energy and deconvolution of signals for the catalysed soot removal process in the presence of 3% of O₂ in He.

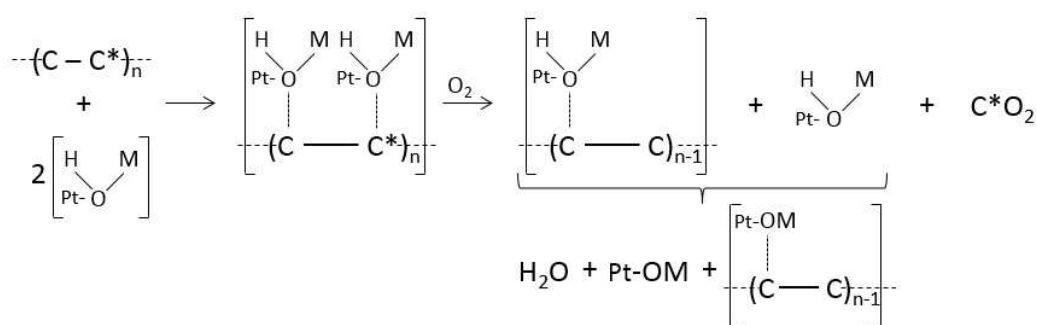
A totally different situation is observed over the Pt-K/Al₂O₃ catalyst, where soot elimination occurs in three steps, as can be observed by the maxima in the distribution curve obtained. Three values of activation energy at 60, 85 and 110 kJ·mol⁻¹ should be

noted, indicating that several coupled processes exist in the soot removal. The first activation energy value clearly corresponds to the removal of water and was associated with water physisorbed in the catalyst (water signal below 130°C accompanied by weight loss in the TG-curve) with 60 kJ·mol⁻¹ that coincides with the water condensation heat value. The second value of the activation energy, with the highest frequency value, may be associated with a second process, which mainly involves structural or chemisorbed surface water, due to the presence of potassium in the formulation and registering a parallel CO₂ formation during this step. It has also been suggested that K has high mobility and is able to remain in contact with the soot [9,14,15,134,231], which enhances its combustion away from the active sites (propagation of the combustion). The third activation energy, with a broader signal and with the lowest frequency value, is very close to those calculated for the Pt-Ba/Al₂O₃ catalyst, indicating that the final step should be related to soot assisted combustion, where the O₂ adsorbed species might be involved. For the trimetallic catalyst, Pt-Ba-K/Al₂O₃, a very broad and non-symmetrical distribution curve was obtained and its deconvolution provided two values of activation energy at 110 and 130 kJ·mol⁻¹, which would indicate the participation of the O₂-adsorbed on the mixed-alkaline surface sites and the molecular O₂ present in gas phase in the removal of soot. This further indicates that the behaviour of Pt-Ba-K/Al₂O₃ in the elimination of soot is closer to the bimetallic Pt-Ba/Al₂O₃ catalyst, probably related to the lower K/Ba ratio and the similarity in the Pt⁰/Pt_{ox} relationship.

Up to now it has been assumed that the oxidation of soot takes place via the participation of different metal centers that involve a series of activated steps and, although to less extent, by its reaction with molecular oxygen. This latter route is more common for low contact mode soot elimination [141] and the uncatalyzed combustion process. Taking into consideration these calculated values of activation energy in catalytic soot removal, it is accepted that an alkaline (-earth) oxide and in particular the Pt-O-M centers or Pt-OH-M sites (where M represents Ba, K or Ba+K) are involved in some of the steps of soot elimination by oxygen (Scheme 2 and 3). The role of alkali compounds in the oxygen-transfer mechanism is ascribed to their electron-donating effect that increases the local electron density of neighbouring C-sites promoting their affinity for binding with an oxygen atom. Consequently, the carbon bonds are substantially weakened, which promotes the shortening of carbon chain.



Scheme 2. Mechanism of soot combustion under O₂ atmosphere over alkaline-earth metal.



Scheme 3. Mechanism of soot combustion under O₂ atmosphere over alkaline metal.

In Figure 3.28, the function of distribution of activation energy in NO+O₂ atmosphere is shown. For the Pt-Ba/Al₂O₃, the function has a non-evident symmetrical distribution, with a similar maximum frequency value at 120 kJ·mol⁻¹, besides an additional weak contribution close to 60 kJ·mol⁻¹. However, the deconvolution of the major frequency contribution process, evidenced the contribution of two sequential reactions with a shift to lower activation energy, close to 105 and 118 kJ·mol⁻¹, with respect to those values found for the same catalyst in O₂-atmosphere. It is known that this LNT-catalyst is able to oxidize and store a high amount of NO_x-species, in nitrite and nitrate forms. So, the shifting to lower activation energy and the higher frequency values appreciated in the distribution function were justified by the intervention of more reactive oxidant species as the NO_x-adsorbed onto the catalyst and by the greater oxidant atmosphere.

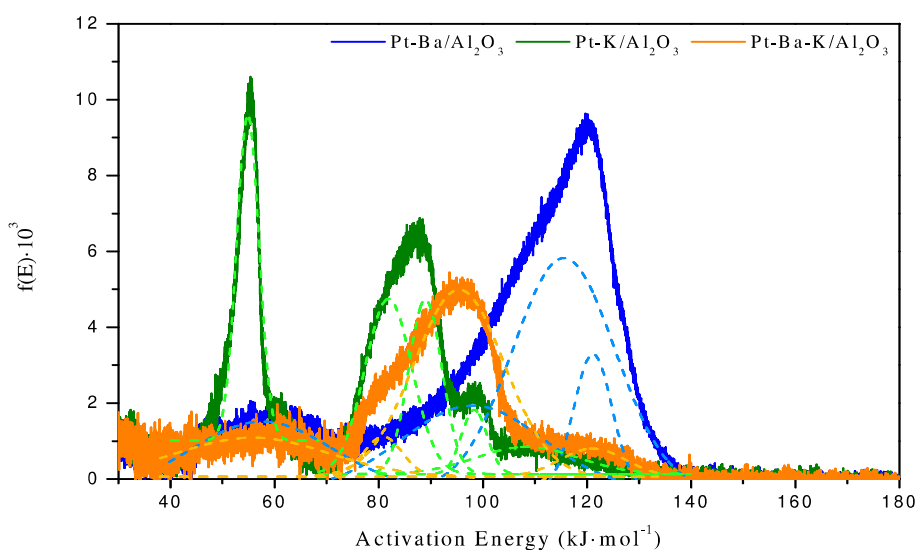


Figure 3.28. Distribution functions of activation energy and deconvolution of signals for the catalysed soot removal process in the presence of 1000ppm of NO and 3% of O₂ in He.

Over the Pt-K/Al₂O₃ catalyst it was also possible to appreciate a significant change in the symmetry of signals and the occurrence of different reactions for the distribution function when soot elimination was performed in NO+O₂ atmosphere. The maximum frequency value $f(E)$ was found for an activation energy value close to 56 kJ·mol⁻¹ and the minimal at 108 kJ·mol⁻¹. Besides, a complex signal was observed whose deconvolution resulted in kinetic parameter values of 78, 90 and 98 kJ·mol⁻¹. In NO+O₂ atmosphere over K-containing catalysts, it was clearly evidenced that soot removal is faster than in the case of Ba-containing catalysts. This might be associated with more effective surface species that should be involved during the soot elimination process compared to the Pt-Ba/Al₂O₃ catalyst. Since water production was higher than the production of CO₂ during the removal of soot with this catalyst, the involved reactions, having different values of activation energies, should be related to the intervention of the potassium surface OH-groups, the stored nitrate species and the surface oxide species in the oxidation of soot, respectively.

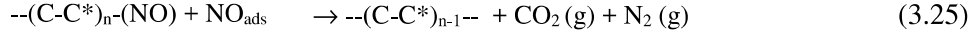
For the Pt-Ba-K/Al₂O₃ catalyst, the maximum frequency value was evidenced by the very broad and non-symmetrical distribution curve obtained, with a relative activation energy value centered at 98 kJ·mol⁻¹, in addition to the other two reactions which had a lower number of occurrences at 60 and 120 kJ·mol⁻¹. These were associated with water release and the participation of the NO_x in the gas-phase in soot removal by assisted

combustion, respectively. The deconvolution of the main contribution evidenced the participation of two parallel reactions with a shift to lower activation energies close to 82 and 95 $\text{kJ}\cdot\text{mol}^{-1}$, which would be related to the participation of the nitrate-stored species and the O_{ads} centers in the soot elimination process at lower temperatures.

The reactivity of the LNT-catalysts towards soot oxidation, under non-isothermal conditions and in different environments, points out that the alkaline and alkaline-earth-containing catalysts exhibit a significantly higher activity in soot removal than the Pt/ Al_2O_3 catalyst or even than themselves when Pt-free using the same alumina support. Besides, a more oxidizing ($\text{NO}+\text{O}_2$) atmosphere such as the diesel gas-off combustion environment with the presence of NO_2 which is dominant at temperatures in the range of 150-400°C, as was proposed by *Jelles et al.* [143], facilitates soot oxidation to CO_2 at lower temperatures [11,150] and subsequently the lowering of the activation energy values, even for the uncatalyzed process.

Unlike what occurs for the Pt-Ba/ Al_2O_3 catalyst, the presence of a more hydrated and higher hydroxylated surface was observed over Pt-K/ Al_2O_3 and also, although less-evident, for Pt-Ba-K/ Al_2O_3 catalysts. For the Pt-Ba catalyst, an O_2 -atmosphere promotes soot elimination at lower temperatures with CO_2 as the main product. The water formation that takes place at temperatures close to 150°C and with an activation energy value of between 57-60 $\text{kJ}\cdot\text{mol}^{-1}$ is due to released physisorbed water from LNT-catalysts. For the K-containing catalysts, the second water contribution evidenced at temperatures below 330°C with an estimated activation energy value close to 80 $\text{kJ}\cdot\text{mol}^{-1}$ in both atmospheres and with CO_2 production is associated with soot elimination by intervention of OH groups. A parallel and additional way, imperceptible in the absence of NO, has been noted as a further reaction in the soot elimination process; which depends on the formulation of catalysts, with activation energy values close to 85, 95 and 105 $\text{kJ}\cdot\text{mol}^{-1}$ for Pt-K, Pt-Ba-K and Pt-Ba catalysts, respectively. The differences between these values were associated with the stability of the different nitrate species stored onto the catalysts. The signals in the distribution function are justified in agreement with the products registered by mass spectrometry. Additional experiments were performed (data not shown) in which the decomposition of different types of nitrates was carried out in order to check the temperature and the activation energy values corresponding to the release of NO_x . So, the N_2 and CO_2 produced by the reaction between soot and the adsorbed nitrates on the catalyst surface [15,232], would

suggest that the route for the soot elimination might proceed in a manner analogous to that described by *W.F. Shangguan et al.* [4]



where the adsorbed NO_x attack the most accessible carbon producing CO_2 and nitrogen and resulting in the shortening of the carbon chain.

The kinetic data for the soot removal process have been further analyzed taking into account a network of first-order reactions represented by the activation energy and the frequency factor. So, the influence of the gas phase on reactivity and the composition of LNT-catalysts on the decoupling processes that occurred together with the kinetic parameters are summarized in the Tables 3.4 and 3.5.

Table 3.4. Summary of soot removal processes in O_2 atmosphere.

T (°C)	Ea (kJ·mol ⁻¹)	Soot	Pt-Ba/Al ₂ O ₃	Pt-K/Al ₂ O ₃	Pt-Ba-K/Al ₂ O ₃
200-400	45-70	-	Physisorbed H ₂ O desorption	Physisorbed and Chemisorbed H ₂ O desorption	
400-500	70-90	-	-	C + Pt-OH-M	
600-700	105-120	C + O ₂ (g)	C + Pt-O-M		
700-800	120-140		C + O ₂ (g)		

Table 3.5. Summary of soot removal processes in $NO+O_2$ atmosphere.

T (°C)	Ea (kJ·mol ⁻¹)	Soot	Pt-Ba/Al ₂ O ₃	Pt-K/Al ₂ O ₃	Pt-Ba-K/Al ₂ O ₃
200-400	45-70	-	Physisorbed H ₂ O desorption	Physisorbed and Chemisorbed H ₂ O desorption	
400-500	70-90	-	-	C + Pt-OH-M	
500-600	90-105	-	C + NO _x (ads)		
600-700	105-120	C + NO _x (g)	C + Pt-O-M		
700-800	120-140	C + O ₂ (g)			

Although it is well-known that the soot nanostructure which depends on the fuel and the engine performances plays an important role in the overall activity, for the soot model used, the differences in the temperature ranges and the activation energy values are reported, and these are linked with the highest frequency value of the parallel and decoupled processes. It is generally accepted that the $NO+O_2$ environment with respect

to O₂ atmosphere enhances the oxidation of soot, but the effect of induced reactivity should also be related to the characteristics and functionalization of the catalyst surfaces by the modification of the frequency values registered. Apart from the gas phase contribution on the soot oxidation by molecular O₂ and NO_x(g), the interaction of the carbon-chain with the active centers of the catalyst surface should modify the local electron density of the carbon sites with a weakening of C-C bonds in the carbon-chain as result of electro-donating, due to the electropositive nature of Pt-O-M and Pt-OH-M (M= K, Ba or Ba-K) centers, that favours the oxygen-transfer mechanism and subsequently the shortening of the carbon-chain. Thus, hydroxylated centers associated with alkalinity, promote the partial removal of carbon by a gasification process in the lowest temperature range. The O-M centers, based in the intermediate O-containing species detected, also contribute to the shortening of carbon chains but in a higher temperature range. Besides, the NO_x-adsorbed (NO_x-ads) species, whose proportion in NO_x atmosphere is very considerable for these DPNR-catalysts, improve the relative contribution of reactivity, lowering the temperature range of the overall process, and enhance the soot removal rate by oxidation.

The proposed mechanism schemes provide information about the primary products (CO, CO₂ and H₂O) and the process that occurs with a higher frequency, for both the non-catalytic and catalytic process conditions and agree with the kinetic parameters calculated throughout the function of distribution of activation energy, which permits intrinsic reactivity analysis by identification of the sequential steps that occur in the complex catalytic soot removal process.

The overall process was analyzed based on a model in which the reactions consist of many first-order reactions each of which had a different frequency factor as well as different activation energy. The difference in the activation energies was represented by a distribution curve that was obtained by analysis of the thermogravimetric curves measured at constant heating in different atmospheres, in the case of this intrinsic analysis of soot removal over LNT-catalysts. Therefore, a mathematical method has been proposed to obtain a distribution function of activation energy making the decoupling of the processes possible [223] and is expected to be applicable to the analysis of decoupled complex reactions [233]. In addition, real soot models supplied by Repsol or obtained in real conditions with a mixture of fuels were used in order to validate the method, obtaining similar results.

3.4. TRM study over NSR catalysts in quasi-real conditions

Once the effective performance in simultaneous NO_x and soot removal over the Pt-Ba-K/ Al_2O_3 had been evidenced, a deeper analysis into its behaviour in *quasi-real* NSR conditions was carried out.

The catalyst has been exposed to many cycles in NSR conditions in the operation temperature range both in dry and $\text{H}_2\text{O}+\text{CO}_2$ atmospheres. Thus, the steady state cycle at saturation point was used to compare the different conditions. In Figures 3.29, 3.30, 3.31 and 3.32 the profiles of the outlet gases for the experiments at 200 and 350°C, low and reference temperatures, respectively, over Pt-Ba-K/ Al_2O_3 are represented. In Figures 3.29 and 3.30, 1000ppm of $\text{NO} + 3\%$ of O_2 were alternated with 2000ppm of H_2 in He, whereas in Figures 3.31 and 3.32, 1.5% of H_2O and 0.3% of CO_2 were added throughout the experiment.

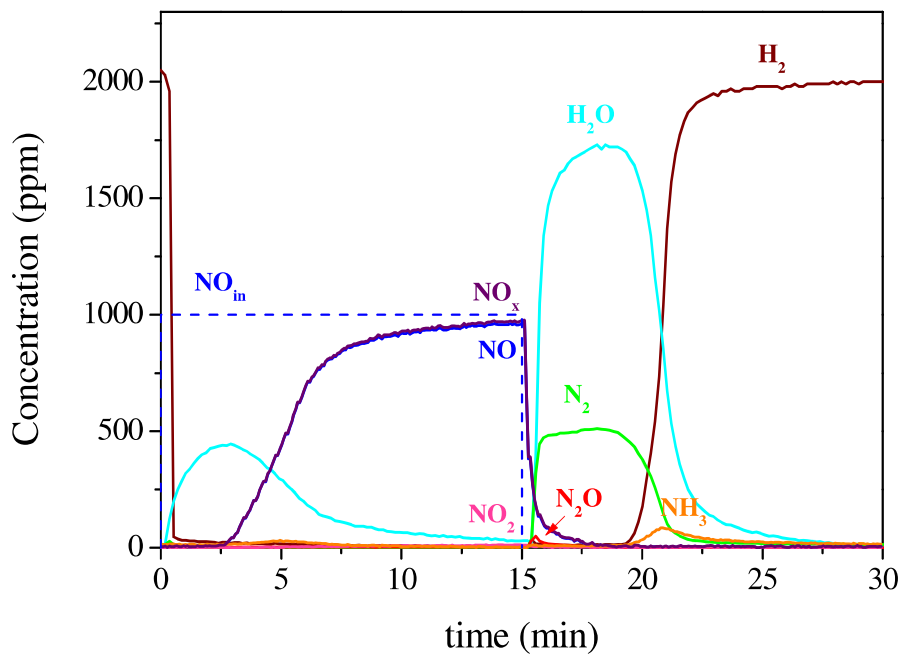


Figure 3.29. Storage–reduction stationary cycle for Pt-Ba-K/ Al_2O_3 in He at 200°C.

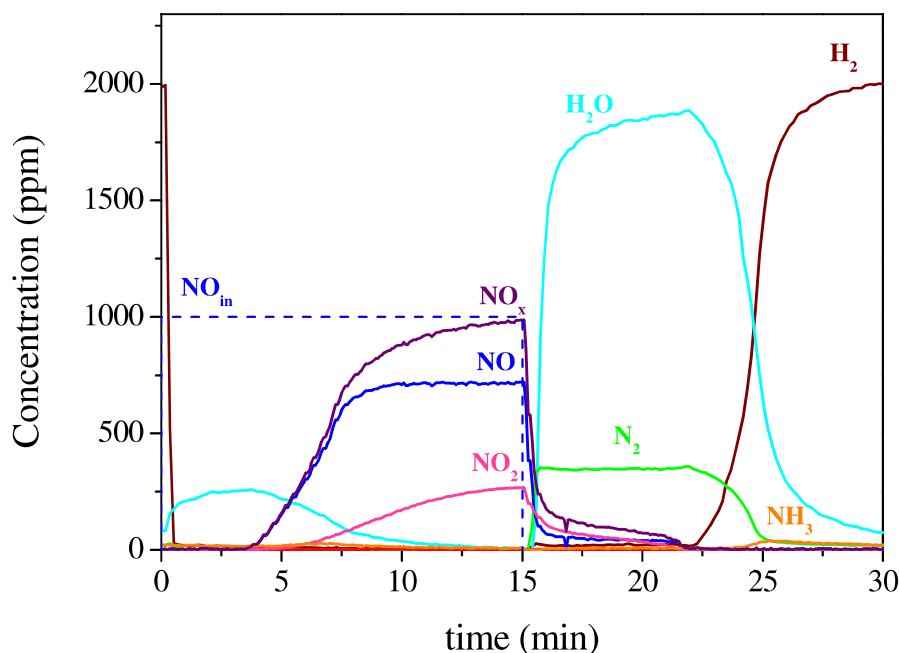


Figure 3.30. Storage–reduction stationary cycle for Pt-Ba-K/Al₂O₃ in He at 350°C.

Firstly, the influence of the temperature was addressed (Figs. 3.29-3.32). In the lean phase, the NO_x adsorption together with the oxidation of NO to NO₂ over the Pt sites took place. There was also a water formation that could be due to the uptake of NO_x on Ba(OH)₂ sites [180]. As the temperature increased, the adsorption capacity seemed to be higher, due to the increase in the breakthrough time from 2 to 4 minutes. In addition, the amount of nitrogen and water produced in the rich step was higher, as well as the time in which no hydrogen was observed because of its reaction with the adsorbed nitrates. Other undesired products were detected in the reduction phase, such as NH₃ and N₂O. These parallel reactions occur to a greater extent at lower temperatures, for example, NH₃ formation was around 100ppm at 200°C, twice the amount registered at 350°C.

The effect of water and CO₂ in the NSR process appeared to be different depending on the temperature range, although the trend in some aspects was constant. Regarding the similarities, the increase of temperature could cause an increment in the adsorption capacity and the nitrogen formation together with the reduction of undesired products and the promotion of NO oxidation, as was observed in dry conditions. However, compared at the same temperature, some differences were appreciated.

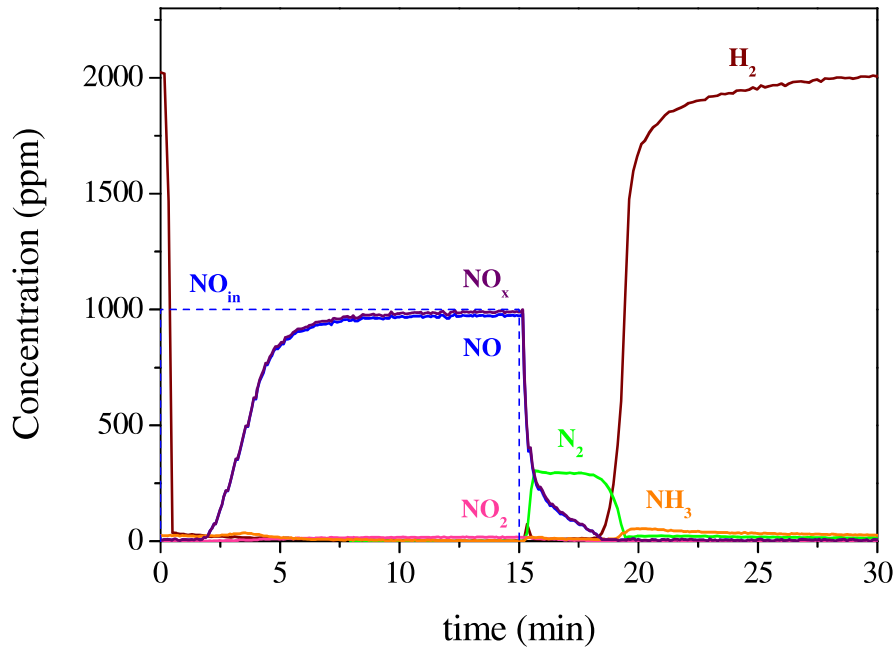


Figure 3.31. Storage–reduction stationary cycle for Pt-Ba-K/Al₂O₃ in H₂O+CO₂ at 200°C.

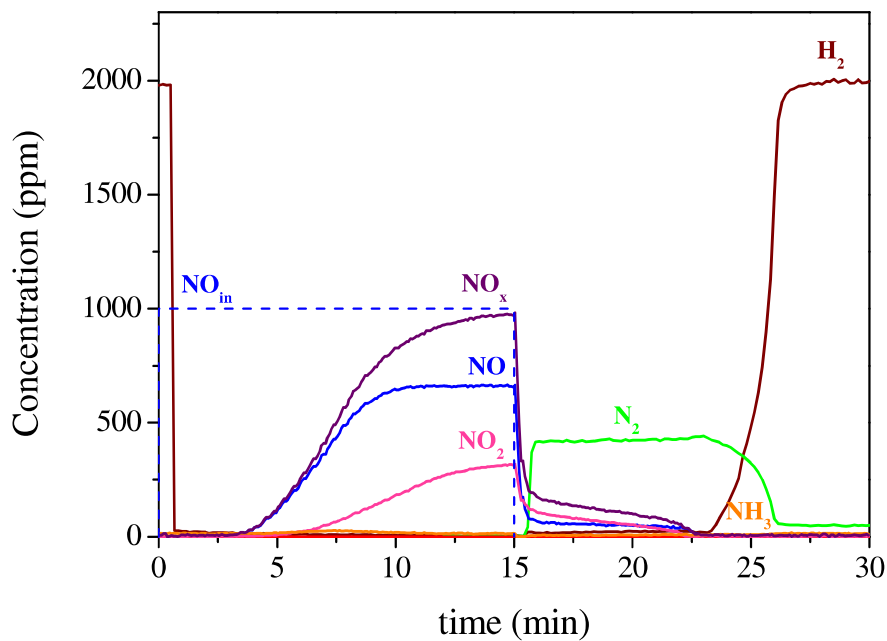


Figure 3.32. Storage–reduction stationary cycle for Pt-Ba-K/Al₂O₃ in H₂O+CO₂ at 350°C.

At low temperatures, a higher amount of ammonia was detected during the cycle and, in spite of the absence of N₂O, nitrogen selectivity could diminish, as opposed to higher temperatures, where in the presence of water and CO₂ a negligible concentration of ammonia was produced. In addition, the modification of the breakthrough point of the

NO_x saturation curve was completely different. At low temperatures, the time was reduced by 0.5 min, which represents 25%, whereas at higher temperatures a decrease of only 0.2 min was observed, without reaching a 10% reduction. This fact was strongly related to the adsorption capacity, as other authors have previously detected [234]. As a consequence, the impact of water and CO₂ on this parameter is more severe at low temperatures.

In order to clarify the effect of these factors, temperature and reaction atmosphere, a series of characteristic parameters, such as the amount of adsorbed NO_x, oxidation capacity, conversion and selectivity, were calculated and are shown in Table 3.6. These values are in keeping with the trend qualitatively observed.

Table 3.6. Reactivity data calculated during the storage-reduction of NO_x experiments from isothermal TRM profiles at 200 and 350°C.

Temperature (°C)	Atmosphere	Stored NO _x ($\cdot 10^3 \text{ mol NO}_x \text{ g}_{\text{cat}}^{-1}$)	Oxidation Capacity (%)	X _{NO_x} (%)	S _{N₂} (%)	S _{NH₃} (%)	S _{N₂O} (%)
200	He	0.39	0.9	91	94.1	5.2	0.7
200	H ₂ O+CO ₂	0.24	1.7	83	90.5	9.5	0
350	He	0.42	33	88	97	3	0
350	H ₂ O+CO ₂	0.41	47	86	100	0	0

In Helium atmosphere, the amount of adsorbed NO_x increased with the temperature, from 0.39 to 0.42 mmol·g_{cat}⁻¹, although the value was around 0.4 mmol·g_{cat}⁻¹. These values are in line with those reported in the bibliography [151,235] for this kind of materials as well as the trend. It was indicated in some of those contributions that the amounts of NO_x adsorbed at steady state are in thermodynamic equilibrium with the gas-phase NO₂ concentration, which presents a kinetically controlled formation and, thus, increases with temperature. As has been previously mentioned, this parameter was modified in a different way by the presence of water and CO₂ depending on the temperature range. So, at high temperatures, there was a minimum change in the parameter indicating that the atmosphere influence was almost nonexistent, whereas a noticeable reduction of the adsorbed nitrates was detected at low temperatures. Different authors have tried to explain the decrease in the adsorption capacity when water and CO₂ are both present in the feed stream. There are several possible reasons for the reduction in the adsorption capacity. One of them is the immediate adsorption of CO₂ forming carbonates that compete with the NO for the active sites, decreasing the amount of nitrite that could be adsorbed and hindering the "nitrite route" as has been previously reported [236]. Another similar explanation was also proposed [234] whereby the lower

storage capacity was assigned to the more difficult storage of NO_x on BaCO_3 and Ba(OH)_2 than on BaO species; furthermore, it is more complicated to form nitrites and nitrates from BaCO_3 than from Ba(OH)_2 . Some authors [115,201,234,235,237] coincided in that water has no influence on the NO_x adsorption capacity, whereas CO_2 inhibits the “nitrite route” reducing the global amount of adsorbed NO_x . The obtained data are in agreement with these observations, and it is possible to assume that water does not have a strong effect on the adsorption capacity, at least, in concentrations lower than 2%. In addition, CO_2 negatively influences the adsorption capacity of NO_x due to the formation of carbonates, causing a competition with the nitrite/nitrate species and this effect decreases when the temperature is increased, since the oxidation of NO to NO_2 is faster.

The oxidation capacity was considerably higher when the temperature was increased, with an increment in NO_2 formation being detected. Moreover, the oxidation capacity was higher when water was present in the gas phase, due to its greater oxidizing power. Other authors [238] have also observed the increment in the NO_2/NO ratio as the temperature was increased, although they have demonstrated that water presence decreases the oxidation of NO on the Pt sites.

In terms of conversion, it should be pointed out that high values, close to 90%, were observed. Nevertheless, a decrease in the value was appreciated when water and CO_2 were in the reaction atmosphere, indicating that these reactants are somehow involved in the regeneration step and could prevent the full recovery of the active centers. As has been observed [239], water hinders the release of NO_2 . In addition, *Lietti et al.* [120] analyzed the reduction step and confirmed that there is a negative effect in the regeneration of the catalyst when water and CO_2 are fed, since CO_2 is able to poison the Pt sites by CO formation due to the reverse of water gas shift.

As far as selectivity was concerned, it is noteworthy to appreciate that high values of nitrogen were observed in the whole range of operation temperatures. However, the nitrogen selectivity was not complete because of the formation of small amounts of ammonia and N_2O , as other authors have detected [234,238], the amount varying depending on the operation conditions. Once again, the effect of the reaction atmosphere depends on the temperature range. At higher temperatures, the presence of water and CO_2 caused a reduction of any undesired products, whereas at lower

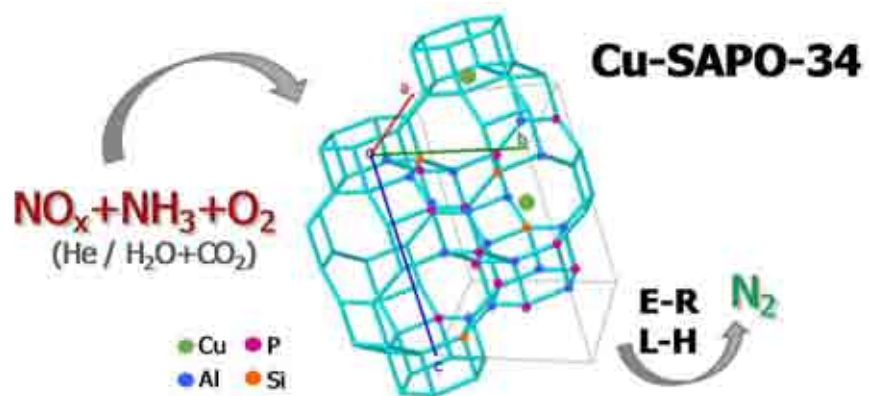
temperatures, although N₂O formation was hindered, ammonia production was slightly increased with the consequent decrease in nitrogen selectivity. N₂O was not formed when the same feed conditions were used with a similar catalyst [120] and an increase in the nitrogen selectivity was also observed. The most plausible reason for the increase in the ammonia formation at low temperatures is related to the reduction mechanism, which is composed of a series of two-step pathway where ammonia is quickly produced and, then slowly reacts with the adsorbed NO_x producing nitrogen. At low temperatures, the fast formation of ammonia makes the reaction with the nitrates impossible. In addition, -NCO species that could be formed, mainly at low temperatures where the CO₂ present in the stream has the greater influence, could be quickly hydrolyzed in the presence of water, producing ammonia.

3.5. Conclusions

To summarize, the Pt-Ba-K/Al₂O₃ with a Ba/K atomic ratio of 3.5/1.5 and the same surface species as the model catalysts, shows an excellent performance in NO_x removal as the Pt-Ba/Al₂O₃ model catalyst, without mechanism modification, improving the soot removal process by intervention of OH groups, increasing the nitrogen selectivity, reducing the formation of undesired products and maintaining the activity even in the presence of water and CO₂. Nevertheless, a slip of ammonia is produced, mainly at low temperatures, which is not admissible and must be removed. Therefore, placing a SCR bed downstream was proposed as a suitable solution in order to achieve zero emissions in the exhaust gas outlet.

4. Results and Discussion.

SCR technology





UNIVERSIDAD
DE MÁLAGA

4. Results and discussion. SCR technology

SAPO-34 materials were synthesized as has been explained in the Experimental Chapter. The most significant results of characterization and reactivity are well detailed herein.

4.1. Zeolitic material synthesis for SCR applications

4.1.1. SAPO-34

Materials with a chabazite structure have been proposed as appropriate catalysts for SCR of NO_x with ammonia, such as SSZ-13 or SAPO-34. So, SAPO-34 materials were synthesized in order to obtain a crystalline material with suitable features for the process. Hence, several synthesis parameters, such as temperature and time in the autoclave, phosphorous content or the use of ultrasound were varied. Representative materials are described below to delve into the influence of these parameters and compare them with the commercial one, supported by Albemarle (denoted as SAPO-c).

In general, the synthesis procedure consisted of the preparation of a gel by mixing the precursors of Al, Si and P, which was then introduced in an autoclave. Later, it was washed and finally calcinated. Sonochemical energy has been used by several authors [240–243] in the synthesis of materials with SAPO-34 type structure in order to obtain nanoparticles or nanostructured catalysts. So, the influence of using ultrasound in the synthesis procedure was studied. For this, the gel was sonicated before being introduced in the autoclave. In all cases, the solid yield, calculated as the ratio between the obtained weight and the expected mass was higher than 96%.

In Figure 4.1, the XRD patterns of all the samples are shown. All materials exhibited the typical diffraction patterns of the chabazite structure (JCPDS 01-087-1527) indicated by diffraction peaks at $2\theta = 9.4, 12.9, 16.15, 20.5, 26.1$ and 30.5° characteristic of SAPO-34 samples.

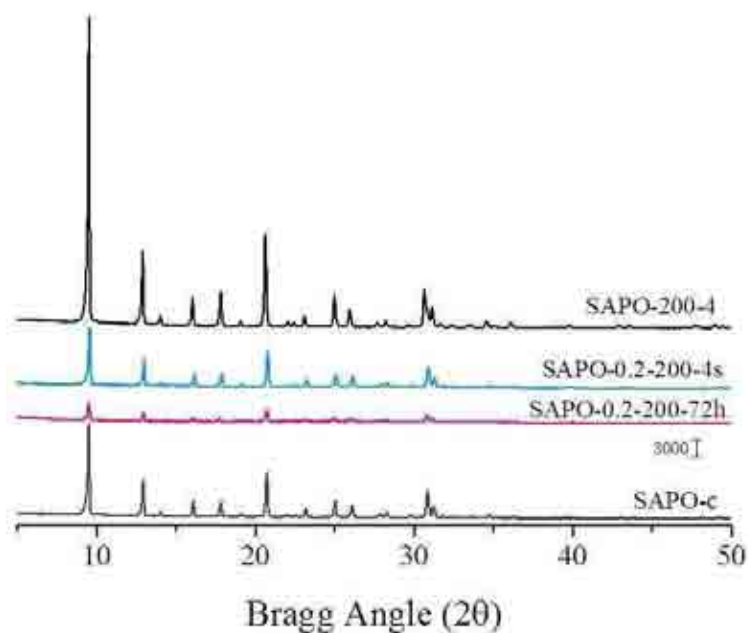


Figure 4.1. X-ray diffraction patterns of SAPO-c, SAPO-0.2-200-72h, SAPO-0.2-200-4s and SAPO-200-4.

SAPO-0.2-200-72h, which was obtained by the traditional hydrothermal method, showed crystallinity similar to that obtained for SAPO-34 synthesized by the conventional method [244–246] at 200°C, using other precursors or structure directing agents and requiring autoclaved times of between 48–120 hours, although always lower than the commercial material, SAPO-c. A higher crystallinity in SAPO-0.2-200-4s compared with SAPO-0.2-200-72h can be confirmed, using the same procedure and reducing the autoclaved time to 4 hours. The crystallization is a kinetic effect that is favoured by the use of ultrasound due to an increase in the contact between the particles and the reduction of the induction period corresponding to the nucleation. The same effect has been recently described by *F. Marzpour Shalmani et al.* [247] who reported kinetic data concerning the enhancement of sonochemically assisted synthesis with temperature modification. The SAPO-200-4 material, with a P/Al ratio of 0.8, showed the most intense peaks, indicating that higher phosphorous content causes an increment in the crystallinity.

In spite of having the same structure, several differences in the morphology could be seen due to the synthesis method. To clarify this point, Rietveld refinement of the samples was carried out, obtaining the unit cell parameters *a*, *b*, and *c*, and the volume, which is displayed in Table 4.1. The SAPO-0.2-200-72h catalyst has a slightly lower

unit cell volume than the commercial material. However, this parameter was not changed by the use of ultrasound nor the phosphorous content.

Table 4.1. Unit cell volume, surface area and pore volume of SAPO-c, SAPO-0.2-200-72h, SAPO-0.2-200-4s and SAPO-200-4.

	V* (Å ³)	Surface area (m ² ·g ⁻¹)			Pore volume (cm ³ ·g ⁻¹)	
		S _μ	S _{ext}	S _{BET}	V _{μpore}	V _{total}
SAPO-c	2389	520	10	530	0.233	0.246
SAPO-0.2-200-72h	2369	237	267	504	0.104	0.581
SAPO-0.2-200-4s	2373	185	254	439	0.081	0.509
SAPO-200-4	2375	534	25	559	0.238	0.290

*By Rietveld analysis

Some changes in the morphology of the homemade materials in relation to the commercial ones and samples synthesized by other authors have also been detected. In Table 4.1, the calculated values of specific surface areas and total pore volumes are shown. Surface area and total pore volume values of 530 m²·g⁻¹ and 0.25 cm³·g⁻¹, respectively, obtained for the SAPO-c are similar to those obtained with other synthesis methods [244,248] and materials with high phosphorous content, mainly indicating microporosity. When the phosphorous content was low, the synthesis procedure caused a modification in the porous distribution as regards the commercial material, providing an increase in the mesoporosity, in line with those reported by other authors [249], who prepared micro and meso SAPO-34 using different surfactants. While the surface area (S_{BET}) was similar, for SAPO-0.2-200-72h, the ratio between microporous surface (S_μ) and external surface (S_{ext}) was considerably lower than for SAPO-c, as well as the ratio between micropore volume and total pore volume, whose value changed from 0.95 to 0.17, indicating a higher mesopore volume. SAPO-0.2-200-4s displayed values close to the SAPO-0.2-200-72h data, maintaining a mesoporous structure: S_μ/S_{BET}=0.42 and 0.47 for SAPO-0.2-200-4s and SAPO-0.2-200-72h, respectively, and V_μ/V_t =0.16. Nevertheless, SAPO-200-4, with a V_μ/V_t ratio of 0.82, was similar to the commercial value suggesting that the structure is mainly microporous. This fact is of great relevance because it indicates that by modifying the synthesis route with a reduction in the phosphorous content, a material with the same structure but a bi-modal pore distribution can be obtained, and the process is not affected by the use of ultrasound.

The SEM images for the presented SAPO-34 materials are shown in Figure 4.2. Cubic crystals with sizes between 5 and 10 μm can be observed, which is in consonance with the literature [64,105,250], where similar particles are observed but slight differences were detected depending on the synthesis method and the autoclaved temperature. For samples with low P/Al ratio, a kind of non-crystalline structure can be observed as if some part of the precursor gel had not been completely removed in the washing process or had not reacted and, therefore, remains of aluminium were detected. Comparing these materials (Figs. 4.2. a and b), it seems that the ultrasonic assisted synthesized sample showed higher amount of crystallized cubes, due to a better crystallization process, as discussed above. On the other hand, high phosphorous contents produce better defined crystals (Fig. 4.2.d), similar to the commercial materials and in line with other characterization techniques.

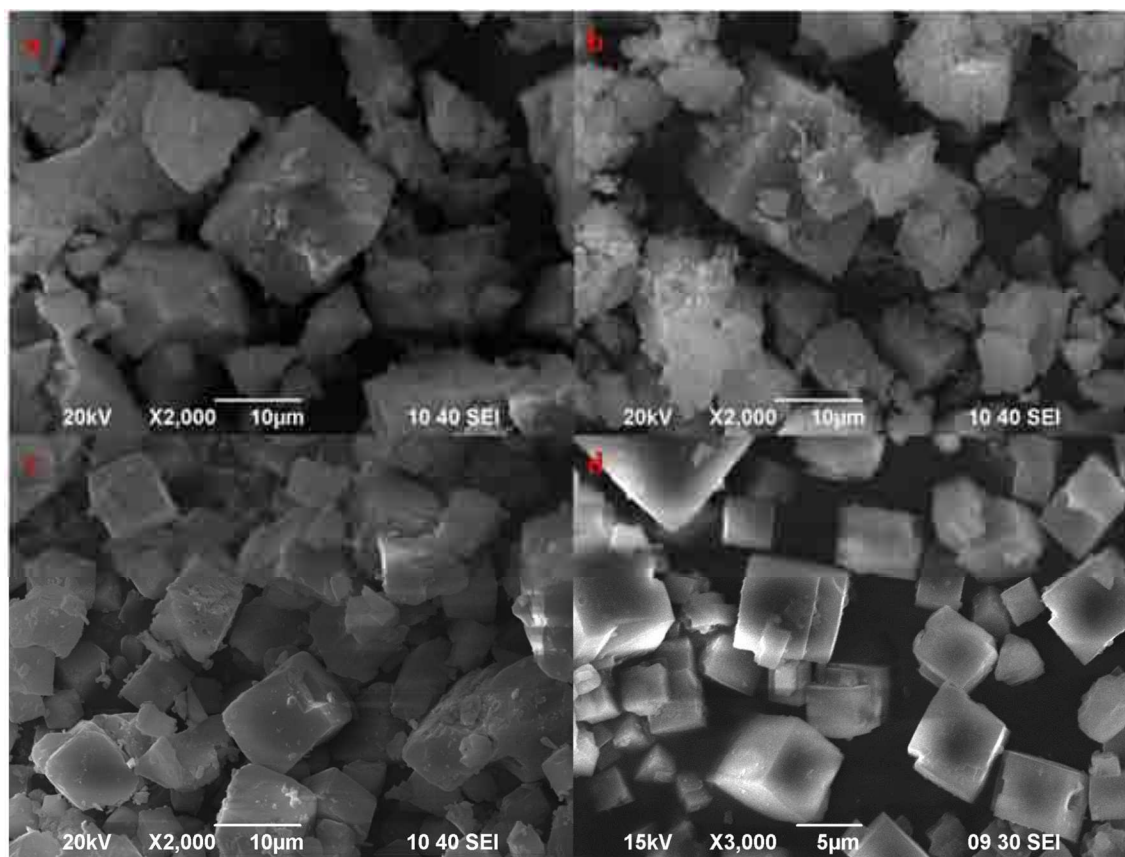


Figure 4.2. SEM images of a) SAPO-0.2-200-72h, b) SAPO-0.2-200-4s, c) SAPO-c and d) SAPO-200-4.

The behaviour of these materials in the presence of ammonia and NO is relevant in the SCR process. Therefore, different experiments involving these species were carried out in order to understand the influence of the synthesis method on the interaction between the samples and the reactant elements for the SCR reaction.

The adsorption/desorption of ammonia was performed in a thermobalance, feeding 750ppm of NH_3 up to the saturation of the sample at 100°C . Then, a purge of Helium allowed the removal of physisorbed ammonia. The obtained profiles are represented in Figure 4.3.

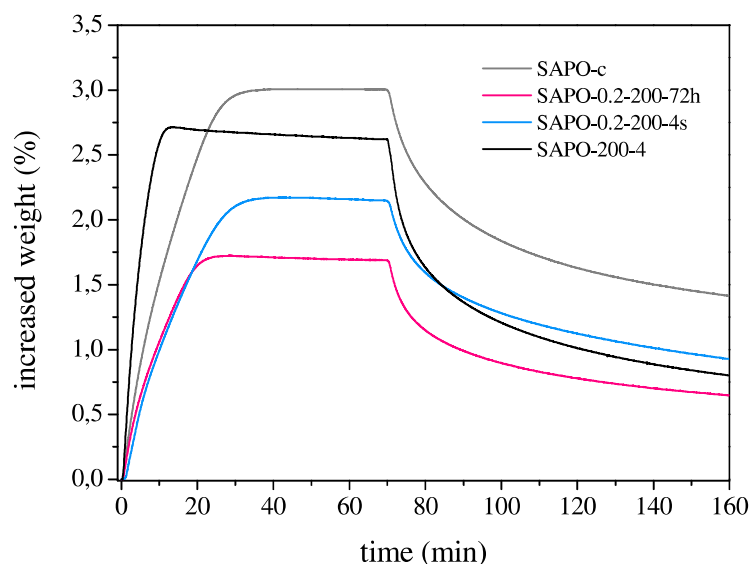


Figure 4.3. Increase of weight according to time in NH_3 saturation (750ppm) experiments at 100°C for SAPO-c, SAPO-0.2-200-72h, SAPO-0.2-200-4s and SAPO-200-4.

As can be observed, the adsorption rate depends on the characteristics of the materials and the synthesis gel composition. The ammonia adsorption-desorption reaction has been simulated by several authors [251], obtaining the rate constants and adsorption theoretical curves that reproduce the experimental data when a dual site ammonia adsorption model is supposed. The initial adsorption rate value was 0.01682 , 0.0213 , 0.02702 and $0.05401 \text{ mg}\cdot\text{min}^{-1}$ for SAPO-0.200-72h, SAPO-0.2-200-4s, SAPO-c and SAPO-200-4, respectively. There is an obvious relationship between the amount of ammonia adsorbed per minute and the crystallinity of the sample; as the crystallinity increases, the rate becomes higher. Nevertheless, the net adsorption capacities of the synthesized materials are similar and slightly lower than that of the commercial one.

In order to examine the species involved in the interaction between the SAPO-34 and both the ammonia and the NO, FTIR experiments were carried out, adsorbing the species at room temperature and registering spectra at different temperatures in evacuation. The spectra obtained after the subtraction of the activated surface spectrum, for the four catalysts mentioned above, are represented in Figure 4.4.

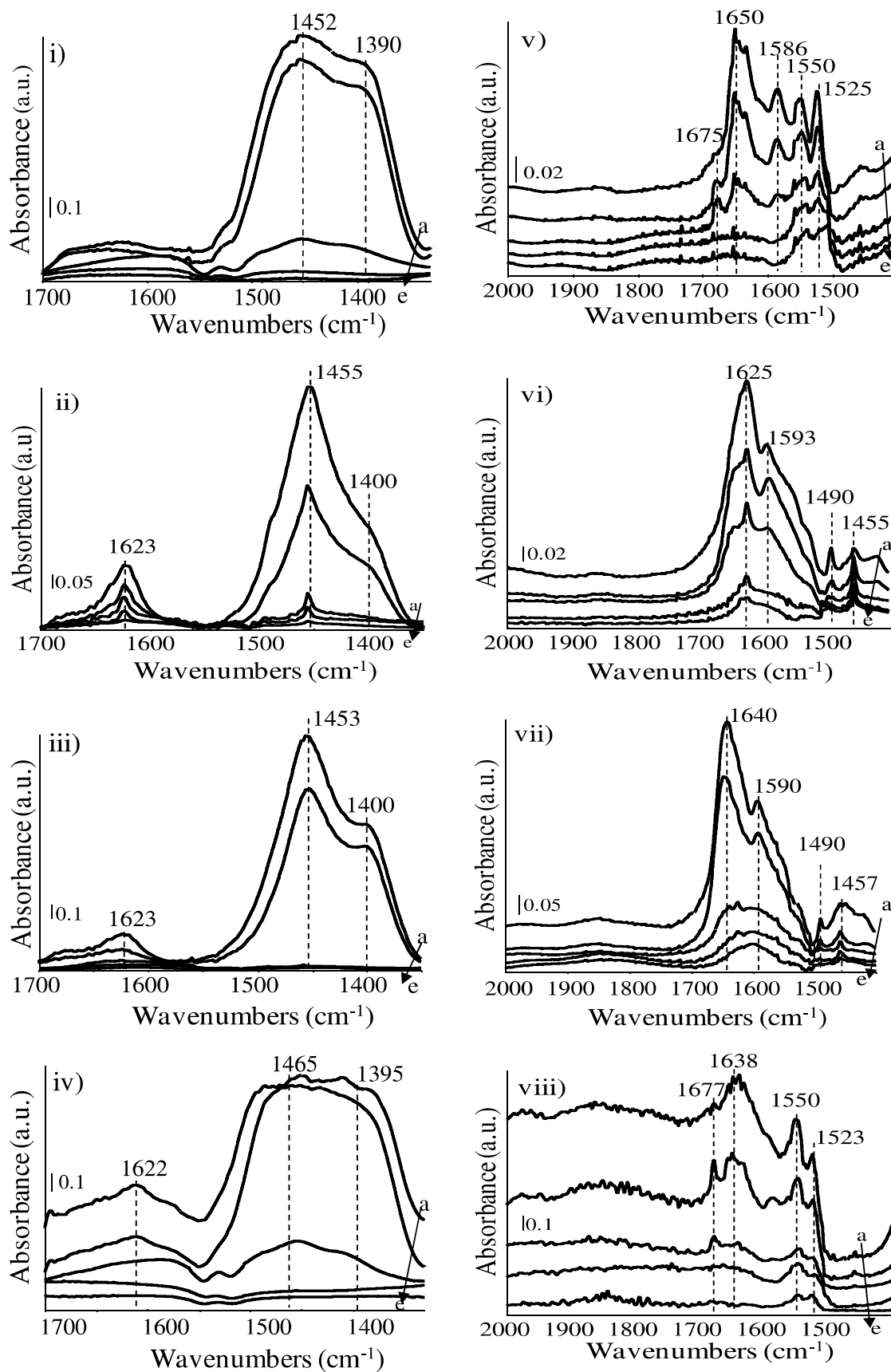


Figure 4.4. FTIR spectra of 10 torr of NH_3 i, ii, iii and iv) and NO v, vi, vii, and viii) adsorbed on SAPO-c, SAPO-0.2-200-72h, SAPO-0.2-200-4s and SAPO-200-4, respectively.

As far as ammonia adsorption is concerned, an intense band around 1450 cm^{-1} with a shoulder close to 1400 cm^{-1} was detected for all SAPO-34 materials. This signal is associated with Brønsted acid sites and characteristic of these kinds of material, as has been reported by other authors [106,252]. A weak signal ca. 1622 cm^{-1} was also observed for the synthesized materials and corresponds to the adsorption on Lewis acid sites [66,253–255]. It is noteworthy that when the phosphorous content was low, the dispersion of the formed species was narrower, indicating a lower number of species on which adsorption could take place. The use of ultrasound in the synthesis barely produced modification of the species. There was a small reduction in the Lewis acid sites, due to the increase of particle contact in the preparation. In all cases, the signals remained up to 300°C .

For NO-FTIR adsorption experiments, the resulting spectra are represented in Figures 4.4.v-viii. The region between 1400 and 1700 cm^{-1} was highly perturbed by the interaction of the support and the NO as nitrates or nitrites of different natures. The study of this region is complex due to the very high quantity of possible species at similar wavenumbers. Nevertheless, it was clearly observed that the SAPO-34 material interacted with NO in a different way, depending on the synthesis and the characteristics of the sample. So, a detailed study of the species is worthy of mention. NO adsorption onto 2Cu-SAPO-0.2-200-4s is similar to 2Cu-SAPO-0.2-200-72h and showed a band of around 1630 cm^{-1} associated with the presence of bridged nitrate groups and a less intense signal at 1590 cm^{-1} related to bidentate nitrate groups was detected. In addition, a broad weak band of around 1480 cm^{-1} corresponding to nitrites was also evidenced. For materials with higher crystallinity and phosphorous content less clearly defined signals were observed and were associated with the presence of different types of nitrates and NO_2 adsorbed onto the catalyst surface. In the absence of oxygen, the accumulation of NO over these catalysts makes the formation of these species possible, which are stable even at high temperatures and, consequently, are not active for the reaction and act as spectators.

SAPO-34 materials were synthesized for their use in the Selective Catalytic Reduction process; so, the SCR activity was studied in a fix-bed reactor, with 750ppm of NO, 750ppm of NH_3 and 3% of O_2 being fed. The conversion and selectivity values were

calculated when stationary conditions were achieved. As is well-known, the absence of a metal with redox capacity makes these materials unsuitable for the process. Therefore, only two of them are shown in Figure 4.5 in order to understand the behaviour of the support.

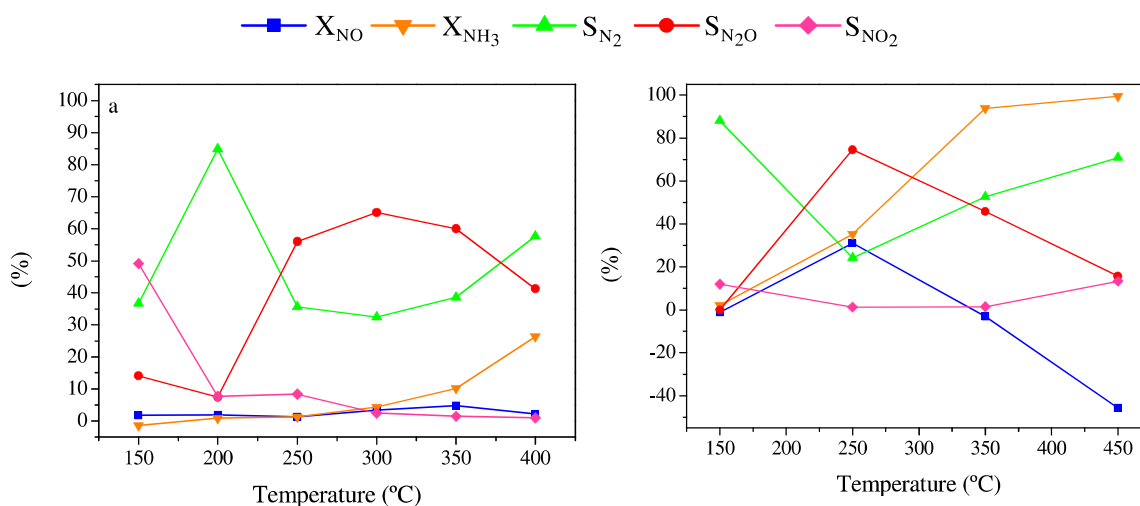


Figure 4.5. SCR conversion and selectivity values according to temperature for SAPO-0.2-200-4s and SAPO-200-4.

For SAPO-34 with low phosphorous content and crystallinity, the conversion values of NO and NH₃ were almost insignificant and were not noteworthy. The selectivity values should be understood as production and not selectivity per se. The increase in the phosphorous content in the formulation makes the material more active in the ammonia oxidation process, with NO selectivity values below zero, due to NO formation by oxidation of ammonia in gas phase. In addition, N₂O production can be caused by nitrate decomposition.

Hence, this material is suitable as an ammonia trap, although the incorporation of a metal in the structure is needed in order to use the material for NO_x removal. Nevertheless, throughout this PhD Thesis, this material has also been tested in the methanol-to-olefin (MTO) reaction and in the reforming of methanol and DME (dimethyl ether) displaying an excellent performance in these processes.

The benefits of using ultrasound-assisted synthesis have been confirmed by the use of different techniques which confirm that crystallinity increases and autoclave time is reduced, maintaining the structure of the chabazite. Nevertheless, the purpose of the

preparation of this type of material is its use in the SCR process and although the synthesized SAPO-34 materials are highly active as ammonia traps, the incorporation of a metal is completely necessary.

4.1.2. Copper incorporation in SAPO-34 materials

In the search for a suitable metal for the SCR process, different elements were considered. Among them, copper, together with iron, have been presented as the most active metals to be exchanged in the zeolite. Copper, in particular, has shown a higher activity in the SCR process and, consequently, was used as active phase in the synthesized catalysts. The synthesis method also influences the structural and activity properties and is another key point to be considered. Traditionally, zeolitic materials have been synthesized by hydrothermal methods and the metal has then been incorporated by post-synthesis ion exchange procedures, such as wet ion exchange [187] or chemical vapor deposition [86], that do not ensure a good metal distribution inside the structure. The incorporation of copper in one-pot has been studied by several authors [64,90,105,256] and is presented as a promising solution for the control of the copper location and the formed species.

The one-pot synthesis of Cu-SAPO-34 materials was carried out varying the amount of copper, the phosphorous content, the use of ultrasound or the temperature and the time in the autoclave. In all cases, the solid yield was kept above 96%. The results of the most representative catalysts are represented herein in order to better understand the influence of the synthesis parameters and the structure and SCR activity. In Figure 4.6 the diffractograms of several samples with different synthesis parameters are displayed.

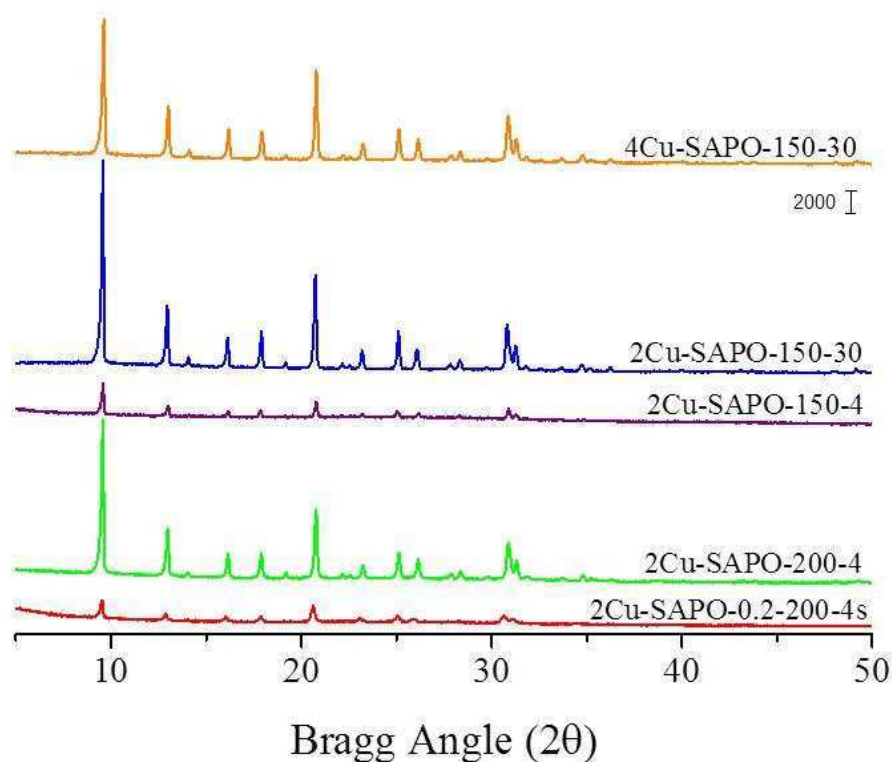


Figure 4.6. X-ray diffraction patterns of 2CuSAPO-0.2-200-4s, 2Cu-SAPO-200-4, 2Cu-SAPO-150-4, 2Cu-SAPO-150-30 and 4Cu-SAPO-150-30.

For all Cu-SAPO-34 catalysts, compared with their corresponding SAPO-34 support (some of them represented in Figure 4.1), the chabazite structure was maintained, but the presence of copper caused a reduction in the degree of crystallization. X-Ray diffractograms of Cu-containing samples do not show peaks at 35.4 and 38.0° attributable to CuO or any other feature assignable to CuO_x species, suggesting that copper ions can be effectively integrated into the lattice of the SAPO structure or highly dispersed. *R. Martínez-Franco et al.* [64,256] indicated that the incorporation of copper in one step using unassisted conventional methods strongly depends on the gel composition but, in any case, more than 7 days are necessary to obtain a non-amorphous material. On the other hand, *F. Gao et al.* [105] synthesized Cu-SAPO-34 by one-pot synthesis and solid state ion exchange and have reported that the one step process allows the incorporation of higher amounts of Cu²⁺ species to the structure, instead of CuO clusters.

The comparison between 2Cu-SAPO-0.2-200-4s and 2Cu-SAPO-200-4, which are only different in their phosphorus content, shows that an increase in the phosphorous amount causes an increase in the crystallinity. The differences between 2Cu-SAPO-200-4 and

2Cu-SAPO-150-4, highlight the influence of temperature in the autoclave, detecting a decrease in the intensity of the signals, meaning that a kinetic process takes place and that, as was observed in the diffraction pattern of 2Cu-SAPO-150-30, the increase in the time in the autoclave, caused an increment in the crystallinity of the sample. An increase in the amount of copper, of up to 4%, causes a slight decrease in crystallinity.

In terms of composition, X-ray fluorescence was used in order to obtain information about the real composition of the samples. Some of the results are displayed in Table 4.2.

Table 4.2. Composition of some samples obtained by XRF.

Catalyst	Al (%)	P (%)	Si (%)	Cu (%)	O (%)
SAPO-0.2-200-4s	31.71	10.72	5.92	0	48.85
SAPO-200-4	21.38	19.64	5.31	0	50.48
2Cu-SAPO-0.2-200-4s	33.17	5.69	8.89	2.39	47.64
2Cu-SAPO-200-4	22.61	17.91	4.82	2.46	49.38
2Cu-SAPO-150-4	29.54	14.93	1.41	3.43	48.07
2Cu-SAPO-150-30	21.9	17.65	5.79	2.27	49.47
4Cu-SAPO-150-30	22.01	16.77	5.47	4.16	48.56

As can be observed, there was a noticeable difference in the values depending on the phosphorous content. The percentage of aluminium and phosphorous was around 30 and 7%, respectively, for low phosphorous content and close to 21.5 and 19.7% for high phosphorous content, which are the theoretical values. There were several noticeable aspects. The amount of copper was similar to that introduced in the initial gel, except for 2Cu-SAPO-150-4, where it was considerably higher together with the aluminium content, whereas the silicon was minimum. This fact is in consonance with that observed in XRD patterns; 4 hours were not sufficient for a crystalline material to be obtained, so the elements had not interacted in suitable proportions. For 2Cu-SAPO-0.2-200-4s material, which also exhibited low crystallinity, the Si/P ratio was modified from lower to higher than 1 due to the copper incorporation. So, this material must present silicon excess in the structure. In all other cases, the materials showed similar values to the calculated composition, within the margins of error.

Not only is the crystallinity an important factor, but the parameters associated with the structure are also relevant, some of them are represented in Table 4.3.

Table 4.3. Unit cell volume, surface area and pore volume of the Cu-containing samples.

Catalyst	Cell unit parameters*			Surface area			Pore volume	
	V (Å ³)	a=b (Å)	c (Å)	S _μ	S _{ext}	S _{BET}	V _{μpore}	V _{total}
2Cu-SAPO-0.2-200-4s	2429	13.713	14.915	18	438	456	0.004	0.627
2Cu-SAPO-200-4	2379	13.598	14.855	479	77	556	0.215	0.431
2Cu-SAPO-150-4	2375	13.583	14.863	39	351	390	0.012	0.777
2Cu-SAPO-150-30	2386	13.604	14.886	518	24	542	0.241	0.305
4Cu-SAPO-150-30	2389	13.614	14.880	454	43	497	0.206	0.353

*by Rietveld refinement

The Rietveld refinement of the samples allowed the study of the unit cell. The 2Cu-SAPO-0.2-200-4s material exhibited these unit cell parameters: $a = b = 13.713 \text{ \AA}$, $c = 14.915 \text{ \AA}$ and unit cell volume = 2429 \AA^3 ; similar to those estimated by A. Turrina *et al.* [257] for the Cu-SAPO-34 synthesized with another gel composition ($a = b = 13.7583 \text{ \AA}$, $c = 14.9324 \text{ \AA}$ and volume = 2448 \AA^3). The incorporation of copper caused a decrease in crystallinity associated with an increase in the unit cell volume that represents 2.37% of SAPO-0.2-200-4s, suggesting that copper could be located inside the structure and causing a 3D volume expansion in consonance with the increase of $a = b$ and c distance values detected while the angles are constant, $\alpha = \beta = 90^\circ$ and $\gamma = 120^\circ$. For the samples with higher phosphorus contents, similar values were detected, with a slight decrease in the parameters as a consequence of the more compact structures. Nevertheless, in comparison with the samples without copper in the structure, an increase in the parameters was detected, mainly in a and b axis, indicating a widening of the structure due to the introduction of copper. Therefore, it could appear that in any case copper was incorporated inside the structure.

The mathematical treatment of the N₂ adsorption isotherms provided the data of the surface area and pore volume. As can be observed in Table 4.3, BET surface area values around $500 \text{ m}^2 \cdot \text{g}^{-1}$ were obtained in all cases, similar to those reported in the bibliography [102,109,258–260]. However, there was a remarkable difference depending on the synthesis process and related to the crystallinity of the samples. The materials with low crystallinity, 2Cu-SAPO-0.2-200-4s and 2Cu-SAPO-150-4 of those represented, exhibited high external surface area values and minimum micropore volume, in spite of the elevated total pore volume. The reason could be the occupancy in the micropores of the copper without the structure being completely blocked. On the

other hand, the highly crystalline materials showed high micropore area and volume values, as a consequence of a more organised structure and in consonance with those reported by other authors [108]. The increase in the copper concentration caused a decrease in the micropore volume, due to the probable micropore occupancy. Approximate calculations of the theoretical atomic density of the maximum copper load per unit cell, considering 36 atoms per cell, indicated that for 2Cu-SAPO-34 materials there would be 2 copper every 3 cells whereas with 4% of copper more than 1 per cell would be detected; this limits the copper placed inside the cavities. In the samples here shown, the ratio between micropore volume and total pore volume was modified from 80 to 58% with the incorporation of double the amount of copper. Therefore, a percentage of copper of around 4 could be the limit to maintain the structure.

SEM micrographs of the samples (Fig. 4.7) show typical regular cubic SAPO-34 polycrystals with dimensions of about 2-5 μm [64]. There was a heterogeneous distribution of the particles and the low grade of crystallinity of some samples caused higher crystal sizes and a more deformed structure was observed. This effect can be noted in Figure 4.7 a and c for 2Cu-SAPO-0.2-200-4s and 2Cu-SAPO-150-4, respectively.

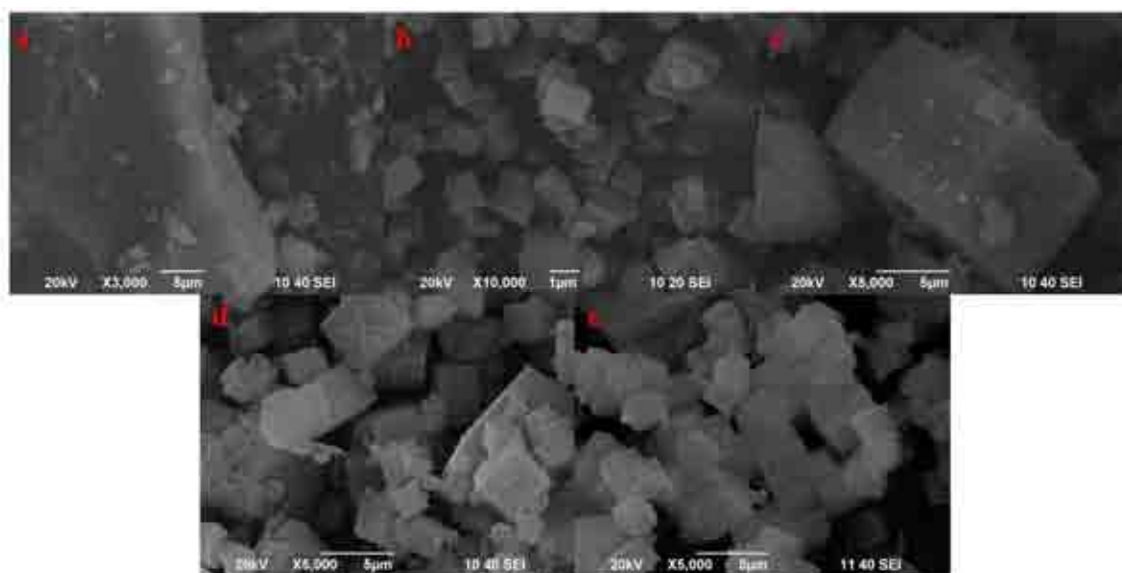


Figure 4.7. SEM images of a) 2Cu-SAPO-0.2-200-4s, b) 2Cu-SAPO-200-4, c) 2Cu-SAPO-150-4, d) 2Cu-SAPO-150-30 and e) 4Cu-SAPO-150-30.

In order to characterize the copper species that were present in the samples, different techniques were used. Here, some of the most representative results are displayed. In Figure 4.8, the UV-Vis-DR spectra are shown.

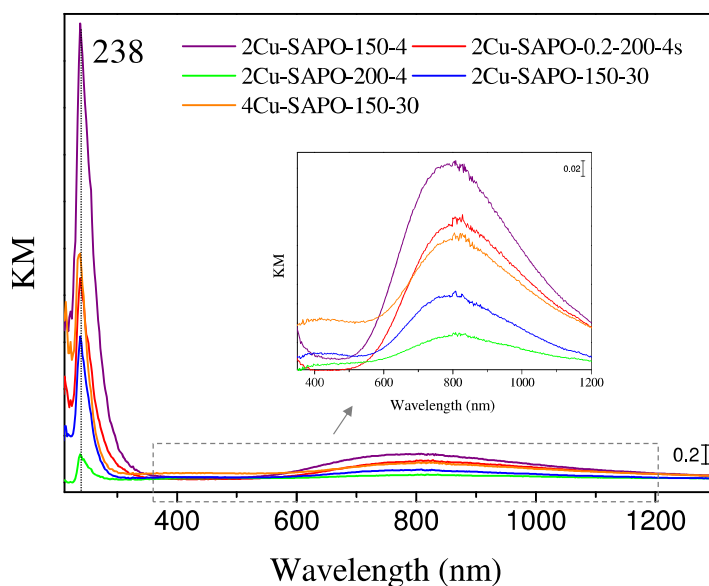


Figure 4.8. UV-Vis-DR spectra of 2CuSAPO-0.2-200-4s, 2Cu-SAPO-200-4, 2Cu-SAPO-150-4, 2Cu-SAPO-150-30 and 4Cu-SAPO-150-30.

For the SAPO-34 materials without copper (not shown), there was an absence of absorption in the whole spectra, only a weak band around 255 nm was observed and was associated with the charge transfer (CT) band of the zeolite ($O^{2-} \rightarrow Al^{3+}$) as has been reported by other authors [261] for other aluminophosphates. In the case of copper-containing materials, an intense band centered at 238 nm and a broad band extended around a maximum localized at 810 nm were registered. The intensity of the signal depended on the samples and increased with the copper content. In addition, a weak signal close to 425 nm was also detected for samples with high phosphorous content, which did not further grow with Cu content. The overall spectra are similar to those reported for Cu-zeolites such as Cu-MOR [262] and Cu-SSZ-13 (isostructural with Cu-SAPO-34 [263]), as well as for other samples of Cu-SAPO-34 [64]. The most energetic signal is attributed to $O^{2-} \rightarrow Cu^{2+}$ ligand to metal charge transfer transition of isolated Cu^{2+} species as *M. Turco et al.* [264] previously reported in the study of a hydrocalcite with copper, and the second is assigned to electron d-d transitions of Cu^{2+} ions in distorted octahedral symmetry. The absorption at *ca.* 425 nm is possibly associated with transitions involving bis(μ -oxo)dicopper species as reported by *Smeets et al.* [265] or Cu-O-Cu complexes as other authors have observed [102,103] when

Cu/SAPO-34 is obtained by ion exchange or precipitation methods. There were no bands detected at 355 nm, which are associated with the CT bands of O–Cu–O complexes, which confirms the absence of these types of species with one-pot ultrasound assisted synthesis. The overall spectrum indicated the presence of Cu²⁺ species under these conditions in the fresh catalysts.

XPS measurements were carried out to examine the effect of Cu loaded and the preparation procedure on the distribution of copper species. The Cu/Si atomic ratios on the surface obtained by XPS and the theoretical Cu/Si were also compared. The binding energy of the Cu2p_{3/2} provides information on the state of Cu species on the surface and it has been reported that Cu2p_{3/2} transition appears at energy levels lower than 933 eV. for metallic copper and Cu⁺, while it shifts to values higher than 933 eV. for Cu²⁺ species [41]. Additionally, the presence of a satellite around 942 eV. indicates the presence of Cu²⁺ in the form of CuO and this feature has been used to distinguish between Cu²⁺ and Cu⁺ [103].

Table 4.4. XPS data of copper species for Cu-SAPO-34 materials.

Catalyst	Cu/Si _{XPS}	Cu/Si _t	Cu ⁺	Cu ²⁺	Cu ⁺ /Cu ²⁺
2Cu-SAPO-0.2-200-4s	0.026	0.13	14.3	85.7	0.16
2Cu-SAPO-200-4	0.023	0.13	53.9	46.1	1.16
2Cu-SAPO-150-4	0.365	0.13	43.5	56.5	0.76
2Cu-SAPO-150-30	0.016	0.13	49.4	50.6	0.97
4Cu-SAPO-150-30	0.140	0.27	12.5	87.5	0.14

For the Cu samples presented, two main peaks can be found after Cu2p_{3/2} band deconvolution, the first at ca. 932.7 eV assigned to Cu⁺ and the second at around 934.8 eV related to Cu²⁺. The Cu²⁺ satellite was observed between 942 and 943 eV. and its intensity was related to a high Cu²⁺ proportion. In general, for 2Cu-SAPO-34 materials, Cu/Si ratios obtained by XPS were lower than theoretical Cu/Si which indicated that Cu ions were predominantly at the exchanged sites inside the SAPO-34 pores and migrated on the inside rather than dispersing onto the external surface, except for 2Cu-SAPO-150-4 which presents an opposite trend and the high Cu/Si ratio observed may be caused by the formation of CuO clusters on the external sites. In 2Cu-SAPO-34 materials, Cu⁺ and Cu²⁺ species coexist and the Cu⁺/Cu²⁺ ratio depends on the content of P in the SAPO-34 since the main difference was detected in 2Cu-SAPO-0.2-200-4s, which is the one with the lowest theoretical P/Al ratio (0.2 instead of 0.8) presenting lower Cu⁺/Cu²⁺ ratio that indicates a higher proportion of Cu²⁺. The other 2Cu-SAPO-

34 samples present a quite similar trend, with Cu^{2+} proportion that varies from 46 to 56% and gives $\text{Cu}^+/\text{Cu}^{2+}$ ratios from 0.76 to 1.16. These samples showed an intense satellite signal at ca. 942 eV. 4Cu-SAPO-34 presented a Cu/Si ratio that represents half of the theoretical Cu/Si which indicates that even at higher Cu loading, Cu ions migrate into the internal structure of the SAPO-34 and Cu^{2+} is the predominant Cu species.

It is important to note that Cu^{2+} species are prone to reduction upon exposure to X-rays. Reduction of Cu^{2+} species due to X-ray irradiation has been reported in former studies [266,267] associated with Cu-based catalytic systems. In the current XPS measurements, Cu $2p_{3/2}$ XP spectra were obtained after a 10 min X-ray exposure.

Different techniques have therefore confirmed that CuO segregates or clusters were not detected and indeed, the copper was highly dispersed and a combination of isolated Cu^{2+} and Cu^+ species were observed. So, in contrast to Cu-SAPO-34 post-synthesis incorporation methods, such as impregnation or ion exchange, it seems that the current one-pot synthesis process produces a material with uniformly distributed copper as Cu^{2+} species.

The interaction of Cu-containing samples with ammonia and NO was also studied with different tests. The adsorption of ammonia was performed in the thermobalance, and the profiles of the increase in weight according to time, when 750ppm of NH_3 was adsorbed at 100°C , are represented in Figure 4.9.

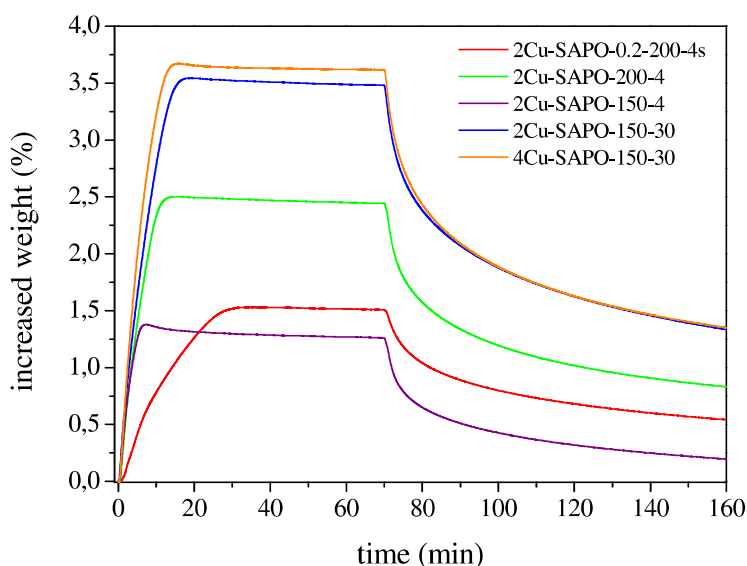


Figure 4.9. Increase of weight according to time in NH_3 saturation (750ppm) at 100°C for 2Cu-SAPO-200-4s, 2Cu-SAPO-200-4, 2Cu-SAPO-150-4, 2Cu-SAPO-150-30 and 4Cu-SAPO-150-30.

The ammonia adsorption rate and the retention capacity were dependent on the sample and were influenced by the crystallinity and phosphorous content. The initial adsorption rate was 0.01634, 0.04969, 0.05326, 0.05357 and 0.6331 $\text{mg}\cdot\text{min}^{-1}$ for 2Cu-SAPO-200-4s, 2Cu-SAPO-200-4, 2Cu-SAPO-150-4, 2Cu-SAPO-150-30 and 4Cu-SAPO-150-30, respectively. All the samples with identical initial gel composition presented similar adsorption rate values. However their adsorption capacities were different and depended on their structure. The increase in crystallinity produces an increase in the ammonia adsorption net capacity. Therefore, the adsorption rate depends on composition whereas the adsorption capacity is influenced by crystallinity.

As is well-known and previously reported [268,269], both the copper sites and the acidity are the main factors for the NH_3 -SCR reaction on Cu-CHA catalysts. In fact, it is recognized that Brønsted acid sites are most likely the active sites for the SCR process. So, to study the interaction between catalysts and the feeding of N-containing gases of the SCR process, FTIR spectra of self-supporting catalyst disks were recorded. The subtraction of the activated material spectrum to NH_3 adsorption spectra are displayed in Figure 4.10 for two of the samples, since similar signals were detected for all the synthesized copper-containing catalysts.

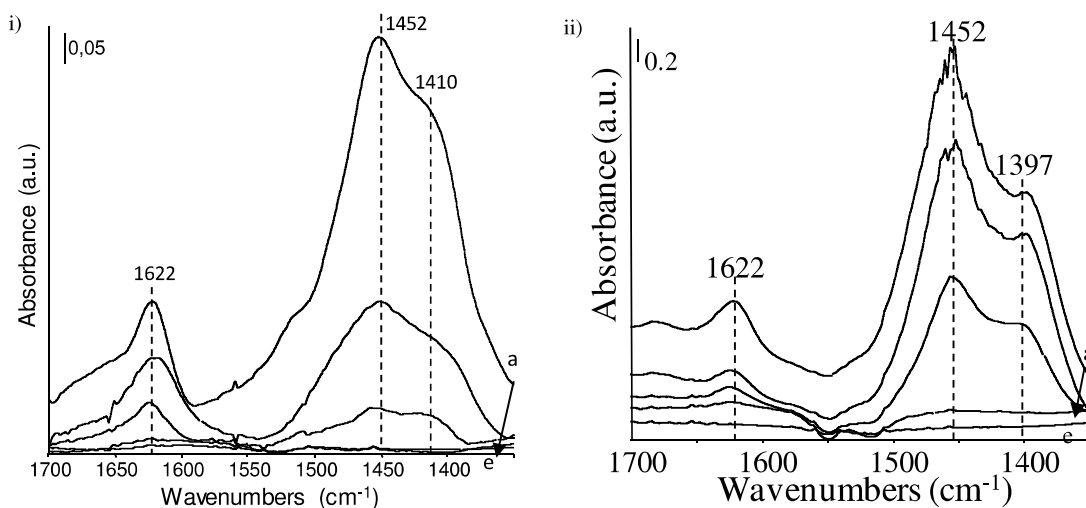


Figure 4.10. FTIR spectra of 10 torr of NH_3 adsorbed on i) 2Cu-SAPO-0.2-200-4s and ii) 2Cu-SAPO-150-30 from a) 100°C to e) 500°C.

For 2Cu-SAPO-0.2-200-4s, after evacuation at 100°C, modes centered at 1452, 1410 (sh) cm^{-1} associated with different P, Al and Si species, as other authors have observed [84], and a more intense signal at 1622 cm^{-1} (Fig. 4.10.i) related to residual ammonia coordinated over Lewis Acid Sites (LAS) were registered. The modes associated with

Brönsted Acid Sites (BAS) remained up to 300°C, as well as the additional LAS provided by the presence of copper. The variation of the synthesis route does not influence the type of species present in ammonia adsorption, although the relative intensities between them were modified. The increase in crystallinity, together with the experimental synthesis conditions, caused the identification of more precise species and the decrease in the Lewis Acid sites, as a consequence of the material being better structured and copper less accessible.

Additionally, isothermal NH₃ adsorption runs were performed in a fix bed reactor (pulse of 800ppm of NH₃ in He, 20 min/35 min of He purge) to calculate the net ammonia adsorption capacity at different temperatures, with that for SAPO-0.2-200-4s being obtained in the low temperature of the SCR range (200°C) the adsorption capacity was around 70 μmol·g⁻¹ while for 2Cu- SAPO-0.2-200-4s, 84 μmol·of adsorbed ammonia per gram of catalyst was obtained, which represents an increase of 20wt% over the total acidity of the materials; as a result, 2Cu-SAPO-0.2-200-4s can also be used as an effective NH₃-trap. Nevertheless, at high phosphorous concentrations, the adsorption of ammonia was slightly higher for the SAPO-34 material than for the copper containing zeolites and it is likely because the support is the main responsible for NH₃ adsorption.

NO adsorption was studied in the same conditions as ammonia probe molecule adsorption at different temperatures. As the copper species of the samples are very similar, slight differences in the types of nitrate were detected, since their formation depends on the support and, as has been explained above, only one of all the materials is represented in Figure 4.11.

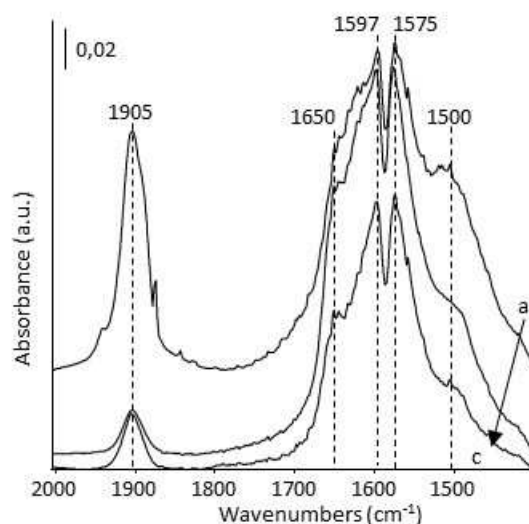


Figure 4.11. FTIR spectra of 10 torr of NO adsorbed on 2Cu-SAPO-0.2-200-4s from a) 100°C to c) 300°C.

For 2Cu-SAPO-0.2-200-4s, intense modes appeared below 1800 cm^{-1} , at 1650, 1597 and 1575 cm^{-1} . An additional strong signal was observed at 1905 cm^{-1} , characteristic of isolated Cu^{2+} ions in square pyramidal configuration. In comparison with the materials without metal, the chemical environment modified by the copper incorporation and localization causes several effects: a) splitting of the signal at 1590 cm^{-1} into two modes at 1597 and 1575 cm^{-1} associated with bidentate nitrate groups over different species, b) shifting of the band at 1630 to 1650 cm^{-1} , indicating the presence of bridged nitrate groups more strongly anchored to the catalyst and c) the shoulder below 1500 cm^{-1} related to nitrite groups is modified to higher energy. At 100°C it is possible to detect a band at 1940 cm^{-1} , assigned to Cu^{2+} sites and a shoulder of around 1890 cm^{-1} related to NO interacting with the OH group of $[\text{Cu-OH}]^+$ sites (modes at 1898-1880 cm^{-1}). It should be noted that other species such as Cu^+ mononitrosyl complex $[\text{Cu}^+(\text{NO})]$ (band at 1755 cm^{-1}) or NO adsorbed on other types of Cu^{2+} sites, such as Cu_xO_y clusters (band at 1897 cm^{-1}) were not detected. When the sample was heated at 200°C, the main signals remained even at temperatures above 300°C. It is well-known that isolated Cu^{2+} species on Cu-SAPO-34 are the active sites for the NH_3 -SCR reaction [67,86,268] and are very stable when harsh hydrothermal treatments are performed with similar catalysts as *R. Martínez-Franco et al.* [256] have reported.

At this point, the presence of Cu^{2+} species, active in NO adsorption, has been confirmed, together with Brönsted and Lewis acidic sites. In atmosphere of NO, copper

containing zeolites allow the retention of nitrate species and mononitrosyl [$\text{Cu}^{2+}(\text{NO})$] species; nitrates are mainly related to the interaction with the support, although can be energetically modified by the presence of copper and, mononitrosyl species are the most likely intermediates in the SCR mechanism.

In order to study the behaviour of these materials as an SCR catalyst and better understand the necessity of the metal in the formulation, co-adsorption experiments of NH_3 and $\text{NO}+\text{O}_2$ were carried out at different temperatures and here the results for two SAPO-34 both with and without being synthesized in the same conditions are represented. For this, once the catalyst was activated in He at 500°C , 800 ppm of NH_3 was adsorbed on the catalysts for 20 min. Afterwards, Helium was circulated for 40 min in order to remove the physisorbed ammonia. Then, 1000ppm of $\text{NO} + 3\%$ of O_2 were fed for 20 min and, finally, 40 min of Helium flow passed through the catalyst. The process was repeated for several cycles. The profiles obtained at 200 and 300°C for two cycles over SAPO-0.2-200-4s are represented in Figure 4.12.

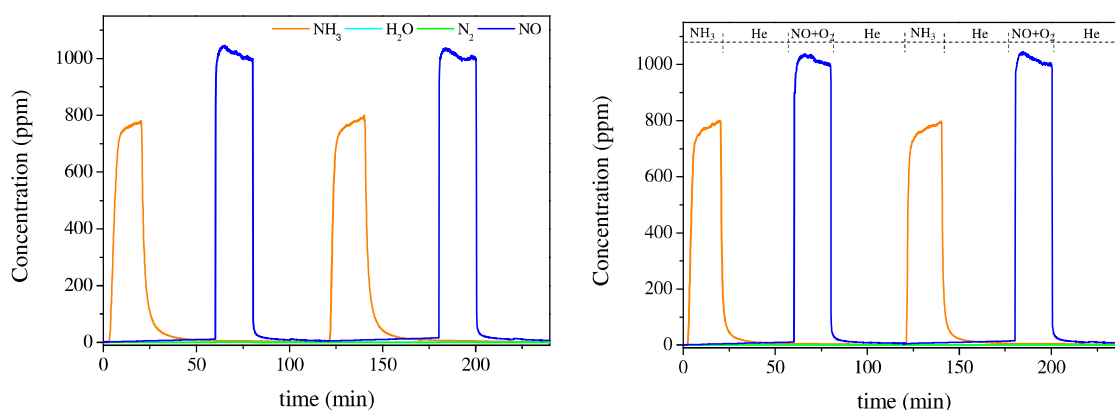


Figure 4.12. Co-adsorption flow experiments of 800ppm of NH_3 and 1000ppm of $\text{NO} + 3\%$ of O_2 over SAPO-0.2-200-4s at a) 200°C and b) 300°C .

From the figure, it can be observed that a certain amount of ammonia was retained since the rectangular pulse provided a saturation curve. The adsorption capacity seemed to decrease with temperature and the number of cycles. The introduction of the $\text{NO}+\text{O}_2$ atmosphere did not cause any reaction and neither water nor nitrogen were detected. In addition, the NO at the outlet was almost identical to the input. However, the amount of ammonia that was able to be adsorbed was considerable. In particular, the initial mmol amount of ammonia per gram of catalyst was around 30 and the value decreased to a

third. On the other hand, the profiles obtained for the catalyst with copper are presented in Figure 4.13.

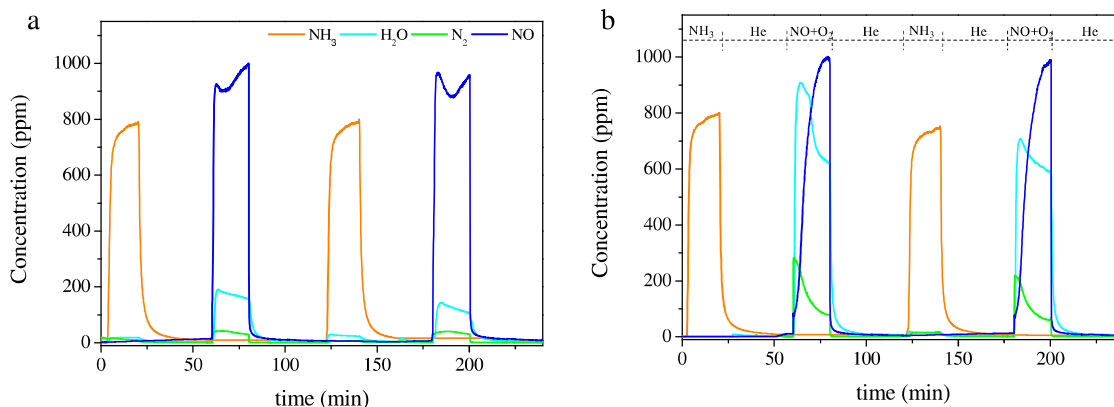


Figure 4.13. Co-adsorption flow experiments of 800ppm of NH_3 and 1000ppm of $\text{NO} + 3\%$ of O_2 over 2Cu-SAPO-0.2-200-4s at a) 200°C and b) 300°C.

As can be seen above, in addition to ammonia adsorption, the introduction of a pulse of $\text{NO} + \text{O}_2$ when the catalyst is saturated produces a reaction with nitrogen and water and, the subsequent catalyst regeneration. So that, the ammonia adsorption capacity was maintained at values of around 20mmol per gram of catalyst. In addition, the conversion of the process increased with the temperature, since the formation of nitrogen and water was greater.

Tests performed in SCR atmosphere (750ppm $\text{NO} + 750\text{ppm NH}_3 + 3\% \text{O}_2$ in He) were carried out and NO and NH_3 conversion and N_2 , N_2O and NO_2 selectivity values at different temperatures were calculated when stationary conditions were achieved. In Figure 4.14, these parameters are represented according to temperature for several of the catalysts.

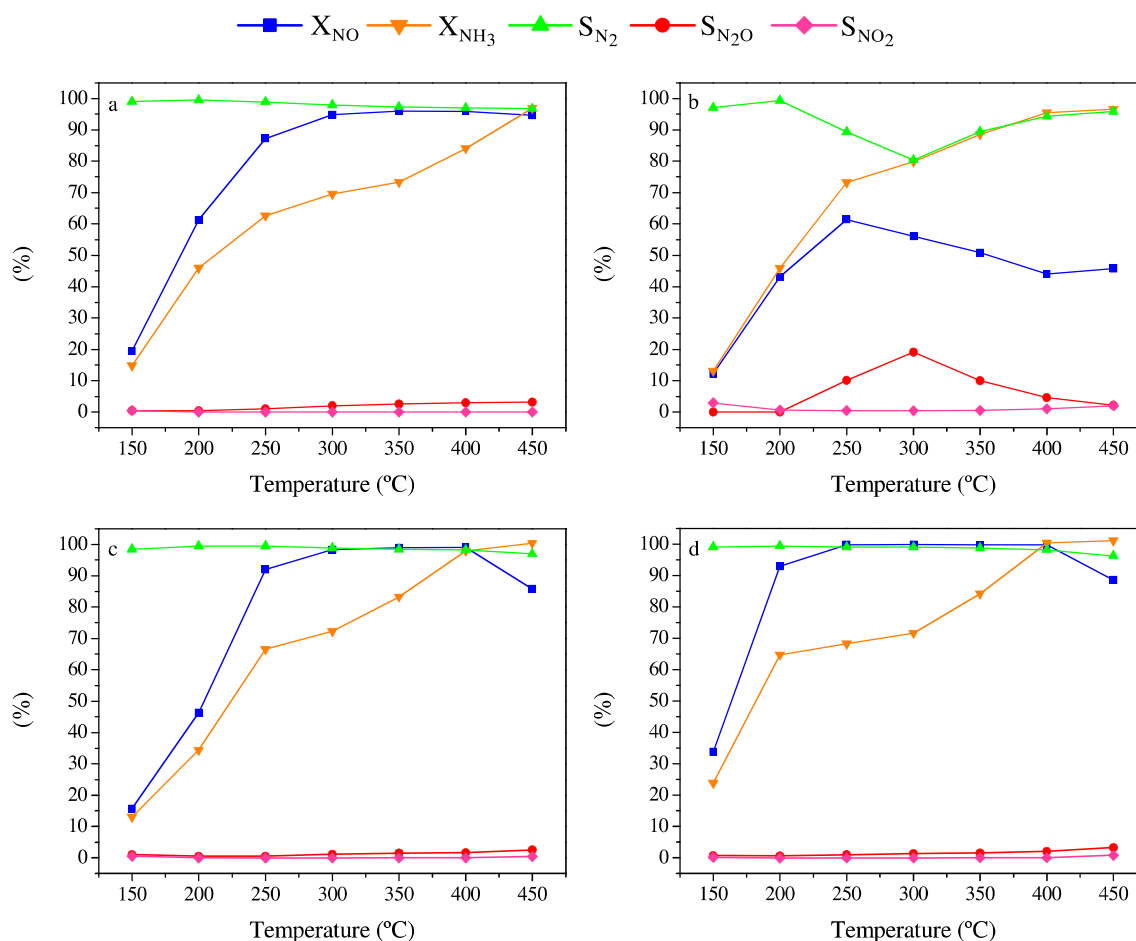


Figure 4.14. SCR conversion and selectivity values according to temperature for a) 2Cu-SAPO-0.2-200-4s, b) 2Cu-SAPO-200-4, c) 2Cu-SAPO-150-30 and d) 4Cu-SAPO-150-30. Feeding conditions: 750ppm NO+750ppmNH₃+3%O₂ in He.

The SCR activity for 2Cu-SAPO-0.2-200-4s (Fig. 4.14.a), showed high NO conversion values in the whole SCR range, similar to those obtained by other authors who, despite preparing the materials by post-synthesis methods, have observed the same behavior [241,246]. NH₃ conversion increased with temperature and was slightly lower than NO conversion at low temperatures. This fact could be explained in terms of the amount of adsorbed nitrates is higher than the ammonia retention, so this catalyst structure favours NO conversion due to its reaction with ammonia in addition to the nitrate formation. Another plausible explanation could be the direct NO decomposition by the active species of copper, which act as dimmers such as the bis(μ -oxo)dicopper that have been proposed as the active species in NO decomposition over Cu-ZSM5 catalysts [51,99,100,270]. Around 350°C, the conversions values are higher but still different, due to the coupling of the standard SCR reaction with the nitrate decomposition that takes place, close to this temperature, with nitrogen formation. At high temperatures only the

standard SCR reaction occurs, in consonance with the stoichiometric consumption of the reagents. It should be pointed out that the selectivity to N_2 is complete in the whole SCR range, with negligible detection of other undesired products, such as N_2O .

The 2Cu-SAPO-200-4 showed a completely different behaviour; although at low temperatures the standard SCR took place because of the stoichiometric consumption of the reagents, after 200°C the conversion of ammonia increased above that for the NO, and the selectivity to nitrogen decreased due to N_2O formation, indicating the occurrence of co-side reactions. This sample displayed the lowest amount of Cu^{2+} species, as has been observed by XPS and UV and the absence of these active species could favour ammonia oxidation and nitrate formation with N_2O production by decomposition and could inhibit direct NO decomposition.

For 2Cu-SAPO-150-30, NO conversion values above 60% were detected in the range between 200 and 400°C. Although the trend of conversion vs. temperature is similar to that obtained by other authors in dry conditions with slightly lower amounts of copper and a different synthesis procedure [109,271], the values are higher, probably because of the increase in the amount of effective copper present in the material. NH_3 conversion values are almost identical to the NO ones, confirming that the standard SCR reaction is taking place. The catalytic activity clearly depends on the amount of copper as noted by other authors that have observed a similar trend for Cu-exchanged zeolites [41]. The increase in the copper percentage, as well as the increment of oxygen content, caused a rise in the conversion values at low temperatures and, consequently, a widening of the operation temperature window. In contrast to other authors [80] that have prepared the samples by ion-exchange and, at high temperatures, a decrease in the conversion has been observed. In terms of selectivity, it should be pointed out that these materials are highly selective to nitrogen in the whole operation range, with a negligible production of NO_2 and a small formation of N_2O .

So, it can be confirmed that the incorporation of copper into the SAPO-34 structure is necessary to have active species for the SCR process and, moreover, the preparation route in one-pot here explained allows the location of copper as isolated Cu^{2+} being the main possible species, which are the active sites in the reaction, depending on the synthesis conditions.

4.2. Copper species differentiation and location for a model Cu-SAPO-34

The influence of the species over the SCR catalytic activity, the location of the copper, inside or outside the framework and the type of species present in the formulation, such as Cu^+ , Cu^{2+} or dimers, are key parameters in the SCR process. Therefore, a detailed study should be performed in order to better understand all these points.

As an initial approach, a study of the modification of the skeletal structure and hydroxyl groups by the introduction of copper was carried out, with the presupposing that 4% is the maximum amount of OH that can be exchange without the formation of clusters or aggregates.

FTIR skeletal spectra of the catalysts (Fig. 4.15) showed a strong and broad absorption centered at about 1090 cm^{-1} , with a shoulder at higher frequencies, characterizing the chabazite-like structure (ν_1 mode, mainly asymmetric stretching of the T-O-T units), further broadened and shifted as a consequence of the different framework composition. The corresponding T-O-T symmetric stretching mode, mixed with a bending mode (ν_2 mode), was detected at 725 cm^{-1} . Additional broader and weaker components were detected at 630 cm^{-1} (D6 rings vibrational mode) and 475 cm^{-1} (ν_3 , T-O-T out of plane deformation mode) [272]. Wang *et al.* [80] assigned two weak bands at 891 and 844 cm^{-1} to framework vibrations perturbed by copper cations in Cu-SAPO-34 spectra and presumed the detection of such bands in DRIFT spectra as direct evidence of Cu in exchange sites inside the pores. The spectra here reported substantially agree with those reported by several authors [272] recorded by transmission IR of KBr pressed disks. They differ strongly from those recorded using a diffuse reflectance technique (DRIFTS) reported by other authors [80,84,108,273], which do not essentially correspond to those expected for these zeolite-like framework structures based on tetrahedral units. DRIFT spectra reported [108,273] showed a strong band at 1362 cm^{-1} , not found in the transmission spectra. It is an artefact that appears in the DRIFT spectra, due to the superimposition of "positive" diffuse reflectance absorption and "negative" specular reflectance.

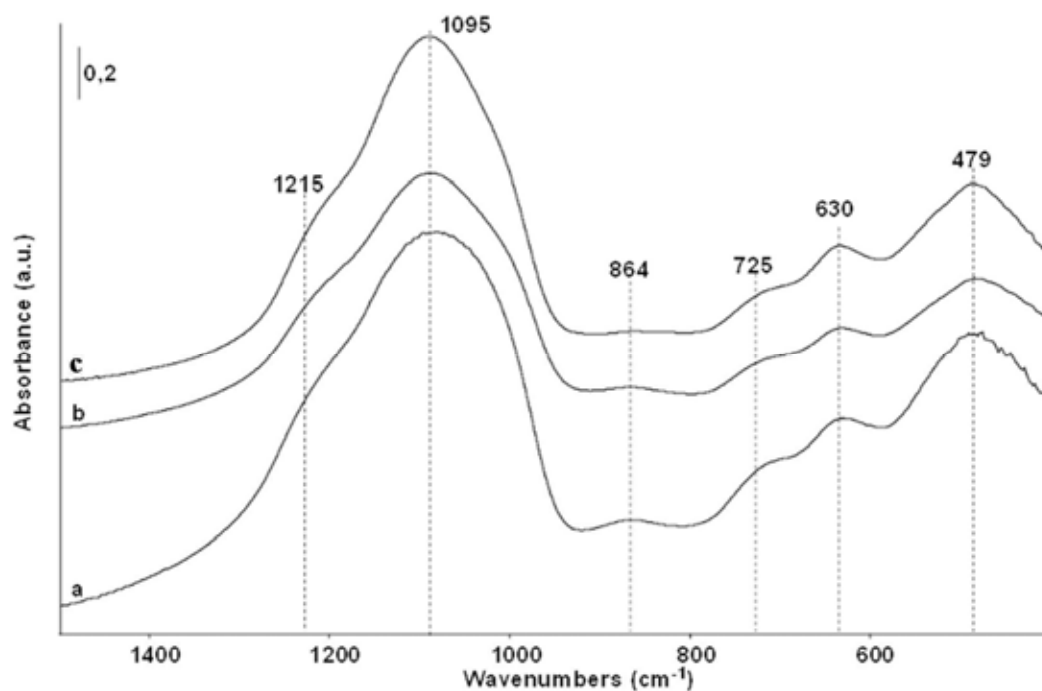


Figure 4.15. FT-IR skeletal spectra of a) SAPO-200-4, b) 2Cu-SAPO-150-30 and c) 4Cu-SAPO-150-30.

Pure powder pressed disks of the catalysts were activated by outgassing at 500°C for one hour, and IR spectra of the surface species were recorded after cooling at room temperature. The overall spectrum of the pressed disk of SAPO-200-4 (Fig. 4.16) showed complex features. As is typical of the spectra of pure powder pressed disks, the spectrum showed a cut-off limit in the region of the highest energy vibrational modes of the bulk structure. In this case, cut-off is observed near 1300 cm^{-1} , at the higher energy limit of Si-O-Si asymmetric stretching and P-O stretching modes, detected in the skeletal spectrum (Fig. 4.15). At higher energy other broad absorptions are observed. In particular, a broad absorption in the range 2400-2050 cm^{-1} is due the first overtones of T-O-T asymmetric stretching modes, while other maxima centered near 1840 and 1640 cm^{-1} are due to combinations of bulk vibrations.

At higher energies the spectrum showed a broad absorption extending from near 3800 cm^{-1} down to ca 2000 cm^{-1} over which a sharper band barely split at 3625 and 3600 cm^{-1} was superimposed, in the region of the OH stretching modes of hydroxyl groups. The presence of bands, in these or similar positions, has been reported by several authors, for different H-SAPO-34 samples [273–277]. The complex band in the region near 3600 cm^{-1} falls into the typical region for the OH stretching of Si-(OH)-Al bridging groups of zeolites, and is also present in the spectra of all SAPOs. Consequently, it should be related to bridging hydroxyl groups in SAPO-34 cavities. Its multiplicity can be related

to that of the oxygen positions in the CHA structure. In fact, this structure is characterized by the presence of a single crystallographic position for the tetrahedrally coordinated atom, but with the presence of four different crystallographic positions for oxygen. According to previous studies [274,275] the group absorbing at $\sim 3600\text{ cm}^{-1}$ is presumed to be localized in the hexagonal prism, maybe forming a weak H-bond with adjacent oxygen atoms in the framework, whereas the isolated bridging OH groups pointing toward the center of the elliptical cage would give rise to the band at $\sim 3625\text{ cm}^{-1}$.

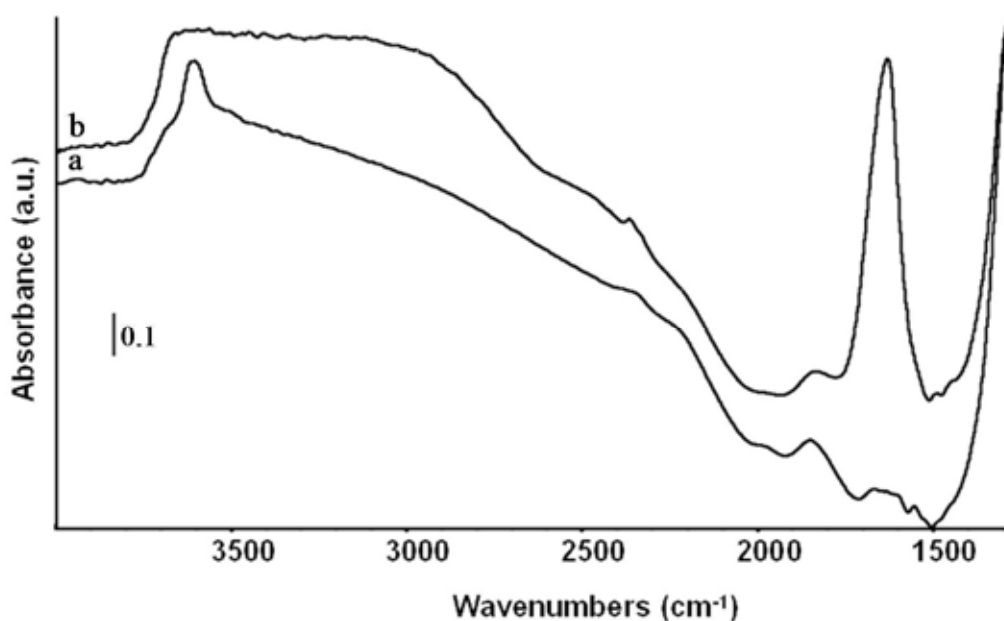


Figure 4.16. FTIR spectra of a) SAPO-200-4 after activation at 500°C and b) after further adsorption of water and brief outgassing at r.T.

The spectrum resulting from water absorption on H-SAPO-34 is also reported in Figure 4.16. The so-called ABC pattern is clearly recognizable, with maxima at 2900 , 2475 and 1630 cm^{-1} , the latter being superimposed to the peak due to the scissoring deformation mode of adsorbed water. The ABC spectrum is indicative of a strong hydrogen bond between water molecules and at least some part of the hydroxyl groups of the solid. After outgassing at sufficiently high temperatures the original spectrum of SAPO-34 was restored. This supports the idea that the strong absorption in the SAPO-34 spectrum extending from 3800 to ca 2000 cm^{-1} with continuous outgassing at 500°C is due to H-bonding between internal OH groups. According to the stoichiometry calculated for the synthesized sample, several protons are expected to be present in the same cavities, and a large part of them can H-bond with each other or with framework oxygen atoms.

Indeed it has been remarked [277,278] that several Al-rich (and proton-rich) zeolites show broad absorptions centered in the region $3500\text{-}3300\text{ cm}^{-1}$, which must be assigned to H-bonded bridging hydroxyl groups.

Remarkably, the spectra of 2Cu-SAPO-150-30 and 4Cu-SAPO-150-30 samples show similar overall spectra and the same sharp components in the OH stretching region were almost unaffected, or even enhanced in intensity (Fig. 4.17). This agrees with the spectra reported by Wang *et al.* [108] for samples prepared with a “one pot” method. This means that the number of Brönsted acid sites of the SAPO-34 is not significantly changed by Cu introduction. On the other hand, looking at the stoichiometries of the solids that were measured, the addition of copper in the preparation mixture (assuming copper did not enter the framework) causes an increased Al/P ratio and thus an increased charge unbalance of the framework. Even supposing Cu participates in balancing the framework charge defect as Cu^{2+} , the number of protons also balancing this charge defect does not decrease.

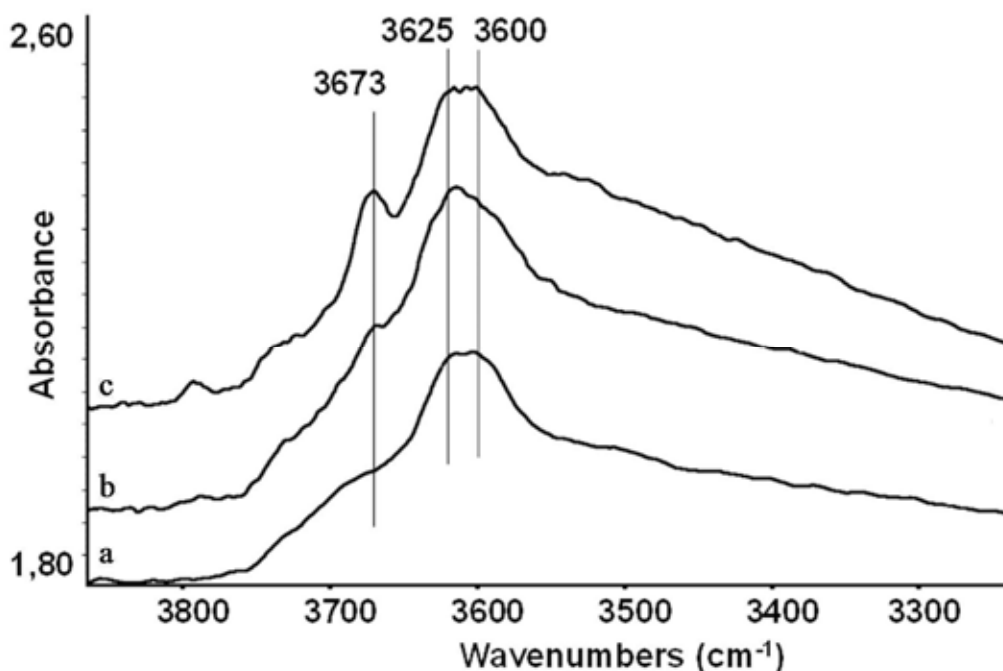


Figure 4.17. FTIR spectra of pure powders after activation at 500°C of a) SAPO-200-4, b) 2Cu-SAPO-150-30 and c) 4Cu-SAPO-150-30.

An additional band at 3673 cm^{-1} increases in intensity upon increasing copper content, in particular for the 4Cu-SAPO-150-30 sample. Indeed, a weak band is found at 3670-

3680 cm^{-1} in the spectra of protonic SAPO-34 reported by several authors: [64,274,275,279] it has been assigned either to POH groups [80,274,275] located on the surface or in defect, or, alternatively, to extra lattice or partially extra lattice Al–OH vibrations [274]. In a recent paper *Halasz et al.* [279] discussed the assignments given in the literature and provided new data arising from DRIFT and transmission IR experiments performed on both H-SAPO-34 and H-CHA. Indeed the comparison of data taken in the transmission mode and in the diffuse reflectance mode provides a good support for the assignment of the band at 3680-3670 cm^{-1} , much stronger in the DRIFT than in the transmission IR spectrum, due to a species located on the surface. Based on DFT (Density Functional Theory) calculations, these authors support the assignment of this band to Al-OH more than POH groups. On the other hand, the vibrational stretching mode of residual Cu^{2+} -OH species was reported to fall in this frequency range too, for microporous Cu-SSZ-13 materials (i.e. 3665 cm^{-1}). The contribution of these species, although masked by the stronger bands due to the support absorption, could explain the increase in intensity of the OH stretching band with increased Cu content [280]. However, as will be discussed further, the presence of Cu^{2+} ions on the surface of our samples is strongly limited due to the $\text{Cu}^{2+}/\text{Cu}^+$ reduction after the pretreatment at 500°C in high vacuum.

Another very weak absorption can be detected at higher frequencies around 3745-3700 cm^{-1} , possibly assigned to another Al-OH stretching mode of extraframework material, most likely present in very small amounts.

Therefore, the hydroxyls groups that are exchanged with the copper are inside the framework and the speciation of copper sites causes the functionalization of centers that did not previously have any redox capacity.

By different characterization techniques, such as XRD or FTIR, it can be ensured that the presence of copper oxides or aggregates was not found in the samples. However, in order to study the dispersion of the copper in the sample, HRTEM images and EDX mapping was performed in order to better understand the distribution of the copper in the particles and the obtained images for 2Cu-SAPO-150-30 and 4Cu-SAPO-150-30 are represented in Figures 4.18 and 4.19, respectively, where all the elements present in a particle were analyzed.

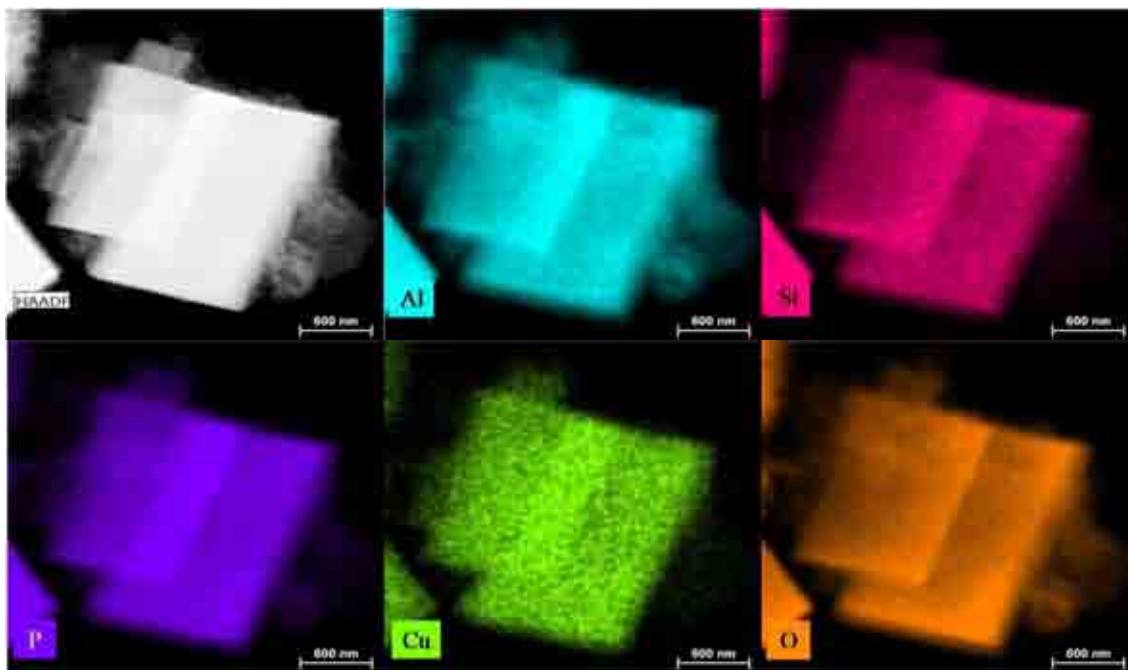


Figure 4.18. EDX mapping of HRTEM for 2Cu-SAPO-150-30.

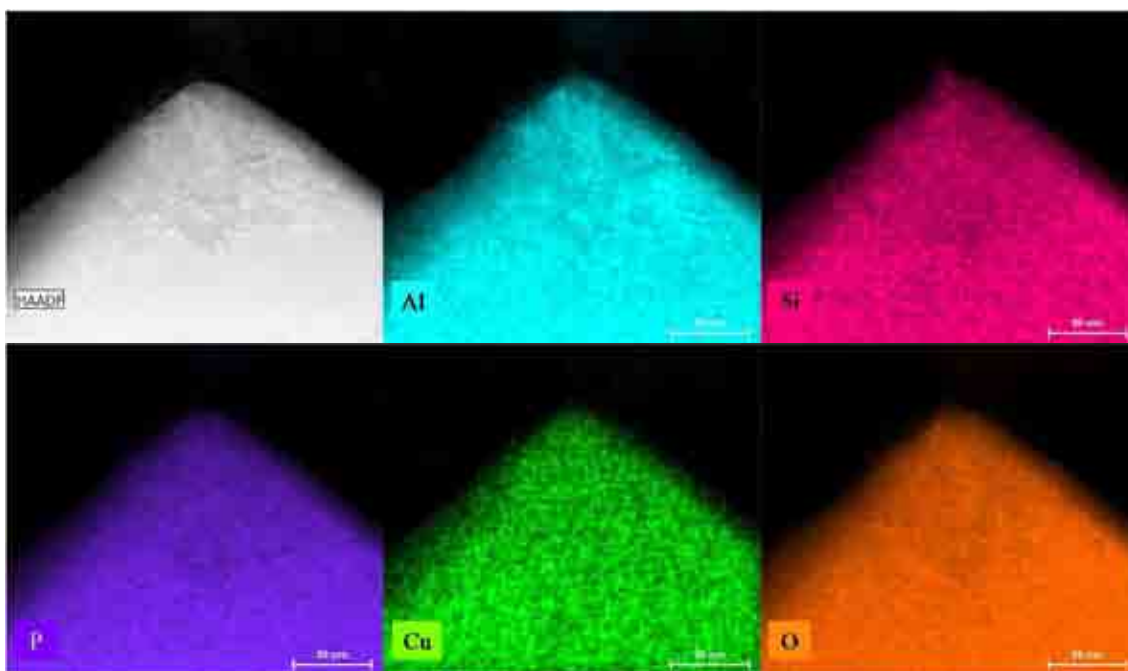


Figure 4.19. EDX mapping of HRTEM for 4Cu-SAPO-150-30.

In all the samples, there was a homogeneous distribution of silicon, aluminum and phosphorus and the weight percentage of each element was in consonance with gel composition and X-ray fluorescence data. In particular, the copper detected showed an extremely high dispersion of itself element along the whole particle and clusters were not clearly evidenced.

The homogeneous distribution of copper has been proved; however, the identification of the copper species is a key point in SCR activity. By UV, Cu^{2+} species were detected and these can be associated with two different species, tetrahedral and octahedral that were located in the 6 and 8 member rings, respectively. Based on the chabazite structure, the ratio 6-rings/8-rings would be 2, so there should be a higher probability of localization of isolated tetrahedral species in the 6-membered rings, whereas the octahedral species due to their environment should preferably be located in the cavities of 8 rings. C. Tyrsted *et al.* [281] indicated that under hydrated conditions a higher population of octahedral species in the 8-rings was detected. This would have an almost direct relationship with the intensity of the UV signals of those species. The Rietveld analysis provided information about the modification of the structure by the copper incorporation. Other authors [282] have also detected species Cu^+ and Cu^{2+} using XANES as seen in the data of XPS, UV and the IR spectra in vacuum. It seems that becomes more sensitive to the surface depending on the analysis conditions and the gas phase present. CO adsorption was carried out in order to go examine the copper species. Previous studies reported carbon monoxide entering the SAPO-34 cavities, in spite of its critical radius (kinetic diameter 0.376 nm) being precisely at the limit of the cavity dimension. Low temperature CO adsorption over SAPO-34 gives rise to the spectra reported in Figure 4.20 recorded in the presence of CO at liquid nitrogen temperature and after outgassing upon warming. Maximum CO coverage results in a main band at 2141 cm^{-1} assigned to liquid-like CO, i.e. not interacting specifically with OH groups. This component quickly disappears at low coverage, where two additional features can be detected at 2162 and 2169 cm^{-1} , first as shoulders of the main CO band, then as separate components resisting outgassing almost to room temperature. These bands are indeed associated with CO interacting with the two families of structural bridging OH groups having slightly different acidic strengths. The first band is due to CO molecules interacting with OHs and has the highest acidic nature, whereas the latter band is due to CO interacting with the lower acidic OHs, which seems to be present in higher concentrations at the support surface. The position of the bands is at a slightly lower frequency than that observed typically with protonic zeolites ($2180\text{-}2170\text{ cm}^{-1}$), thus showing that the interaction with the OH groups is slightly weaker than that observed with most zeolites, either because of the lower Brönsted acidity or because the cavity size is too small to allow strong interaction. The data virtually coincide with those published by Bordiga *et al.* [274].

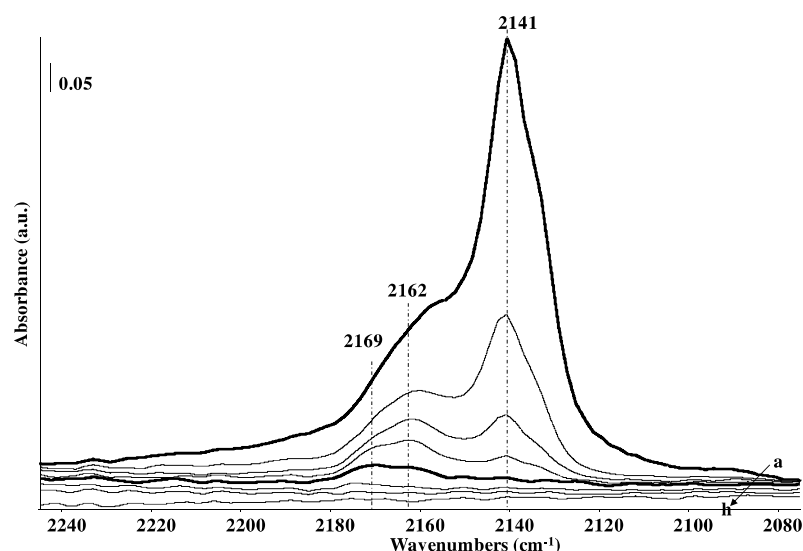


Figure 4.20. FTIR spectra of surface species arising from low temperature CO adsorption over SAPO-200-4 sample: a) CO adsorbed at -140°C , (b-h) outgassing from -140°C to room temperature. The activated surface has been subtracted.

CO adsorption over the 2Cu-SAPO-150-30 catalyst resulted in a quite complex band pattern (Fig. 4.21), undeniably more complex than those reported by other authors for similar catalysts [83,84,256,259,280]. At the highest coverage (-140°C) two main bands were evident at 2141 and 2168 cm^{-1} , the latter stronger, with two shoulders at 2192 and 2220 cm^{-1} . The band at 2141 cm^{-1} decreased in intensity more rapidly by outgassing with total disappearance occurring when the sample was warmed to -100°C . As previously discussed, this band (2141 cm^{-1}) is assigned to liquid-like CO. After this treatment, the higher frequency band is the strongest one; now being shifted a little upwards (2171 cm^{-1}). Together a new weaker band is now apparent at 2148 cm^{-1} .

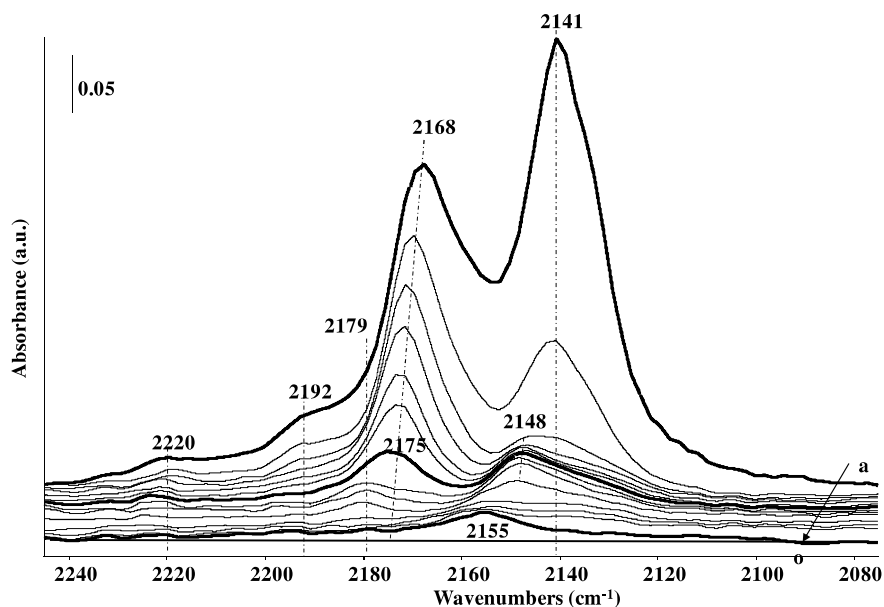


Figure 4.21. FTIR spectra of surface species arising from low temperature CO adsorption over 2Cu-SAPO-150-30 sample: a) CO adsorbed at -140°C , (b-o) outgassing from -140°C to 150°C . The activated surface has been subtracted.

Further outgassing upon warming caused the band at 2171 cm^{-1} to decrease faster together with the component at 2192 cm^{-1} , until essentially disappearing at -50°C , being shifted up to 2175 and 2196 cm^{-1} , respectively. After this treatment, a doublet was still present at 2148 and 2180 cm^{-1} . Further outgassing upon warming also caused the disappearance of this doublet. At 0°C a single band is observed at 2155 cm^{-1} , but a broad feature was also observed centered at 2135 cm^{-1} . The latter disappeared at 90°C while the former did so at 100°C . The permanently weak feature at ca 2220 cm^{-1} , disappears progressively and at -40°C was no longer observed. Interestingly, through the experiments CO_2 formation on the surface was not observed. While the band at 2141 cm^{-1} was assigned to liquid-like CO and that at 2220 cm^{-1} was most likely due to CO on Al^{3+} either surface or extraframework or on Cu^{2+} species, at least four different features must be attributed to CO interacting with copper centers. All these species can be assigned to CO interacting with monovalent copper.

Even more complex are the spectra of CO adsorbed on the 4Cu-SAPO-150-30 sample (Fig. 4.22). However, the species observed are similar, with some additional features.

A complex envelope of overlapped bands can be detected, showing several maxima shifting and disappearing depending on the surface CO coverage. At the highest CO coverage (i.e. -140°C) the main band is still due to liquid-like CO (2141 cm^{-1}), with a shoulder at lower frequencies also completely disappearing at low temperatures most

likely due to a second liquid like species. The doublet at 2168 and 2192 cm^{-1} was again observed but in this case a second doublet due to an even more weakly bonded species was also found at 2159, 2183 cm^{-1} . Both these doublets disappeared by outgassing in the range of $-140/90^\circ\text{C}$. The doublet at ca 2150 and 2180 cm^{-1} still present at 90°C is due to a more stable species and disappeared progressively in the $-50/10^\circ\text{C}$ range. In this case, two bands were formed from the previous doublet, at 2155 and 2133 cm^{-1} , respectively.

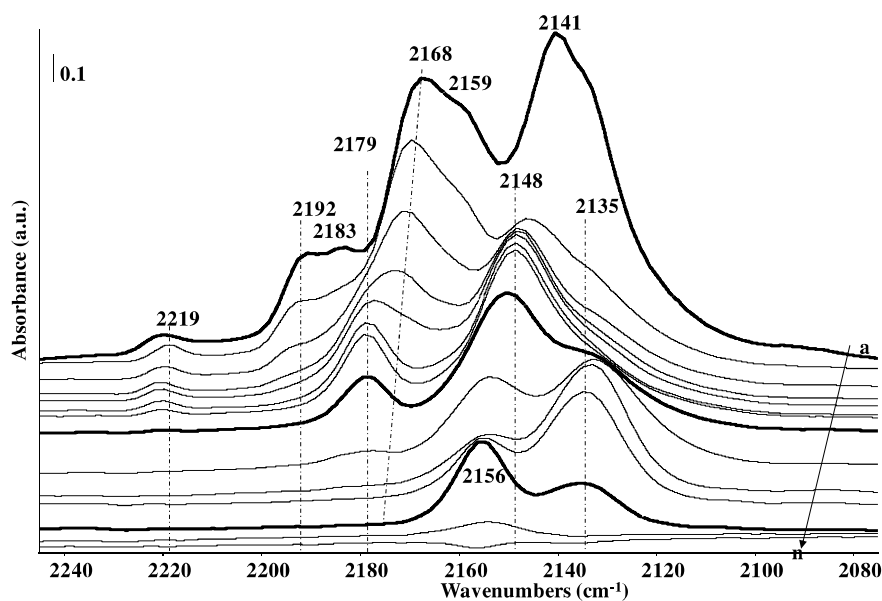


Figure 4.22. FTIR spectra of surface species arising from low temperature CO adsorption over 4Cu-SAPO-150-30 sample: a) CO adsorbed at -140°C , (b-n) outgassing from -140°C to 200°C . The activated surface has been subtracted.

By further warming it was evident that the species responsible for the band at 2133 cm^{-1} became the species responsible for the band at 2155 cm^{-1} . The weak band at 2219 cm^{-1} was again observed, most likely due to CO interacting with Al^{3+} .

Taking into account that UV-vis data indicate that most of the copper in the fresh catalysts is in the form of Cu^{2+} , while IR studies of adsorption of CO indicate the presence of Cu^+ almost exclusively, it is concluded that Cu^{2+} on Cu-SAPO-34 are very easily reduced into Cu^+ by outgassing in the IR cell.

In order to know the location of the copper, the adsorption of molecules with different sizes was carried out. AN (acetonitrile) adsorption has been tested to analyze the acidity and accessibility of acidic groups of SAPO-34. The kinetic diameter reported is in the

range 0.38-0.42 nm [276] and the molecule is linear and quite flexible, thus can actually access the small SAPO-34 pores. The spectrum of SAPO-34 support in the presence of acetonitrile (AN) vapour typically displays a doublet at 2300 and 2268 cm^{-1} , with frequencies that are slightly shifted to a higher frequencies compared to those of liquid AN (2294 and 2254 cm^{-1} , Fermi resonance between the CN stretching and the $\delta\text{CH}_3+\nu\text{CC}$ combination). These features are due to AN interacting with moderate electron withdrawing sites, i.e. acidic OHs (Figure 4.23.a). Another very weak component around 2320 cm^{-1} could be due to the higher frequency component of the Fermi resonance doublet of AN interacting with Lewis sites, such as extraframework Al ions, via the coordination of the electron lone pair on the N-atom. The other component of this doublet is overlapped with the band at 2300 cm^{-1} . Evacuation at room temperature and up to 300°C reduces the intensity of the main bands, which are however still detectable.

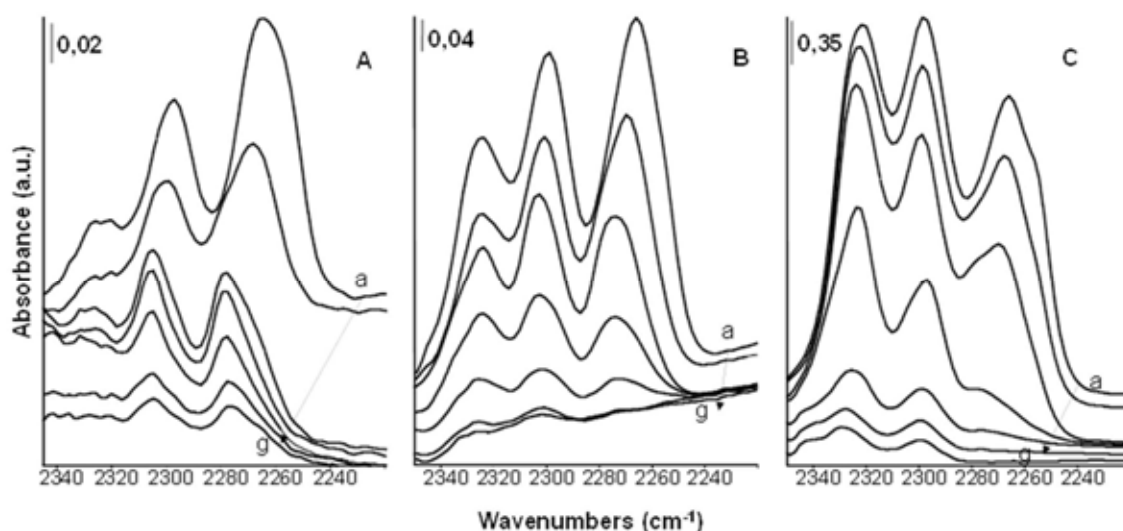


Figure 4.23. FTIR spectra of surface species arising from AN adsorption over sample (A) SAPO-200-4, (B) 2Cu-SAPO-150-30 (C) 4Cu-SAPO-150-30. a) In the presence of AN vapor, b) after outgassing at room temperature, c) at 100°C, d) at 150°C, e) at 200°C, f) at 250°C, g) at 300°C. The activated surface spectrum has been subtracted.

Figure 4.23 also presents the FT-IR spectra of AN adsorption on 2Cu-SAPO-150-30 and 4Cu-SAPO-150-30 catalysts followed by outgassing at temperatures up to 300°C. In these spectra, a triplet band at 2327-29, 2300 and 2269-70 cm^{-1} , respectively, is strongly observed, before and after outgassing AN vapour. The triplet actually corresponds to the superimposition of two doublets due to AN coordinated over Lewis acidic sites and interacting with OH groups. In detail, the highest frequency band is

assigned to AN coordinated over Cu ions, behaving as medium strength Lewis sites and is still detectable, although very weak, up to 300°C. High Cu loading corresponds to an increased intensity of this band, which is the most evident in the spectra of sample 4Cu-SAPO (Figure 4.23, C).

The interaction of a bulkier basic probe such as Pivalonitrile, whose kinetic diameter is reported to be about 0.6 nm [276] was also tested. The corresponding spectra in the region of CN stretching are reported in Figure 4.24. Spectra of 2Cu-SAPO-150-30 and 4Cu-SAPO-150-30 samples, as well as the band at ca. 2250 cm⁻¹ due to PN interacting with acidic OHs, show an additional band centered just below 2300 cm⁻¹. This band is more evident at increased Cu loading and can be assigned to PN coordinated with Cu ions behaving as medium strength Lewis sites. All these bands are barely detectable, in agreement with the small exposed external surface of the zeolite and this effect can indeed be taken as a further indication that the PN branched molecule cannot enter the pores of SAPO-34. Consequently, there are a number of copper ions coordinating PN molecules that are mainly located at the external surface.

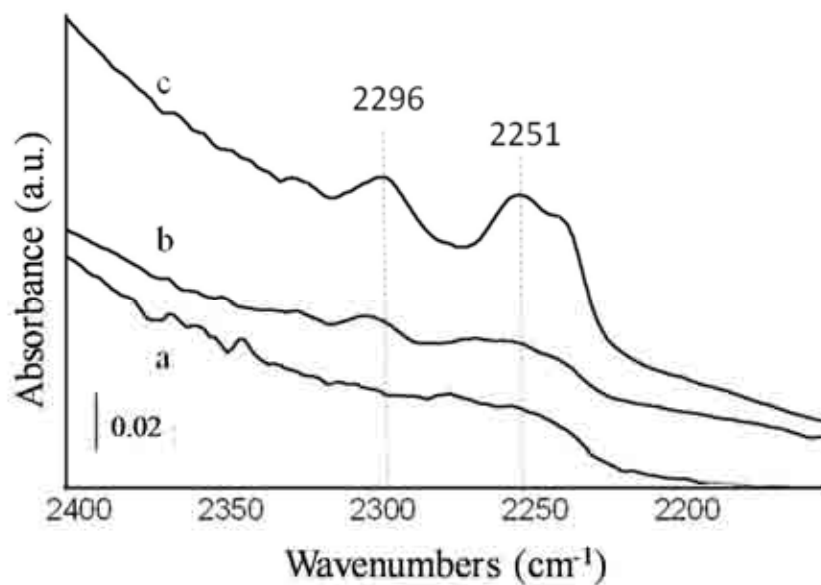


Figure 4.24. FTIR spectra of surface species arising from PN adsorption at room temperature over sample a) SAPO-200-4, b) 2Cu-SAPO-150-30 and c) 4Cu-SAPO-150-30. The activated surface spectrum has been subtracted.

The comparison of the spectra obtained using AN and PN as the probes, shows a much higher relative amount of nitrile interacting with Lewis acid sites revealed by AN (that should enter the cavities) than by PN (that does not enter the cavities) on both 2Cu-

SAPO-150-30 and 4Cu-SAPO-150-30. Thus, it is confirmed that a significant amount of Copper penetrated the cavities, even if it did not significantly exchange the protons. The speciation of copper introduces Lewis character, which could be involved in the mechanism, and the strength depends on whether the copper species is Cu^+ or Cu^{2+} .

The one-pot synthesis allows the introduction of 2wt% of copper inside the framework without the formation of clusters or dimmers but, even with 4% of Cu, they are not clearly evident. The formation of Cu-dimers could be hindered by the size of the pores, although as direct decomposition of NO has been observed, a possible explanation could be that near copper species act as dimmers without being them.

4.3. Insights into the SCR mechanism

In order to delve into the SCR mechanism, IR and DRIFTS-MS experiments were carried out. As has been previously explained, copper species play an important role in the SCR mechanism. Thus, adsorption of 10 torr of pure NO in a vacuum cell with the sample previously activated was carried out at different temperatures in order to study the copper environment at the reaction temperature. In Figure 4.25, the spectra recorded at different temperatures for 2Cu-SAPO-150-30 are presented.

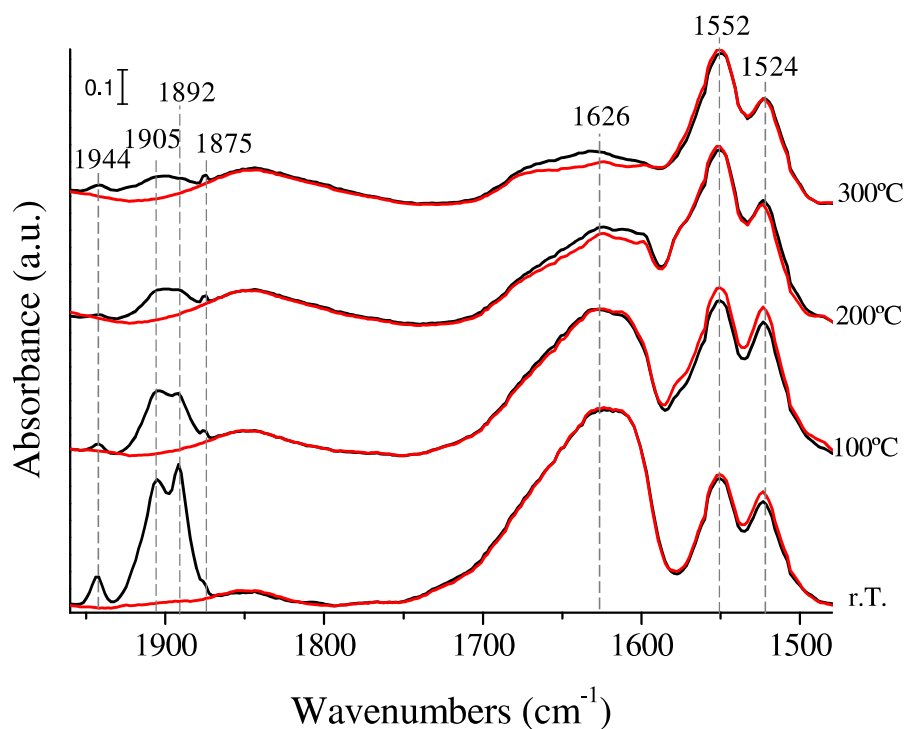


Figure 4.25. FTIR spectra of 10 torr of NO adsorbed on 2Cu-SAPO-0.2-200-4s from r.T. to 300°C without evacuation (black line) and in evacuation (red line).

The nitrate region was highly perturbed with different nitrates, with signals between 1500-1700 cm^{-1} as has been before explained, which are not involved in the reaction and are stable in evacuation,. The region corresponding to the copper species, around 1900 cm^{-1} showed intense signals associated with the presence of Cu^{2+} in different coordination, in agreement with the characterization data. A strong signal was observed at 1905 cm^{-1} , characteristic of isolated Cu^{2+} ions in square pyramidal configuration. At higher wavenumbers, around 1940 cm^{-1} , other species of Cu^{2+} were observed, which could be due to the copper in octahedral positions. The signal around 1890 cm^{-1} is related to NO interacting with the OH group of $[\text{Cu-OH}]^+$ sites (modes at 1898-1880 cm^{-1}) caused by the high capacity of water adsorption that is present in the zeolite.

To study the species involved into the SCR mechanism, co-adsorption of NH_3 , NO and O_2 was carried out and was analyzed by FTIR. A minimum amount of reagents gas was used in order to identify the species involved, decreasing the reaction rate. In Figure 4.26 the FTIR spectra in $\text{NO}+\text{O}_2$ atmosphere with the time evolution after NH_3 adsorption and evacuation are represented for 2Cu-SAPO-150-30. After NH_3 adsorption and evacuation in the N-H bending vibration region, several bands can be observed. The bands at 1400 and 1456 cm^{-1} are due to bending vibration of NH_4^+ on the Brønsted acid sites, while the less intense band at 1620 cm^{-1} can be assigned to the vibration of the N-N bond in the NH_3 coordinated with Lewis acid sites (copper ion sites) [66,253–255]. Any nitrates formed would quickly build up with signals in the same range, and no additional signals can be observed. The peaks for the Lewis acid bound ammonia might be obscured by the broad IR bands for nitrate/ NO_2 formation in this region. At any given exposure time, the intensity of this group of bands is always essentially the same [66]. After evacuation a very weak signal is only detected in the region assigned to acidity Brønsted and/or nitrate species.

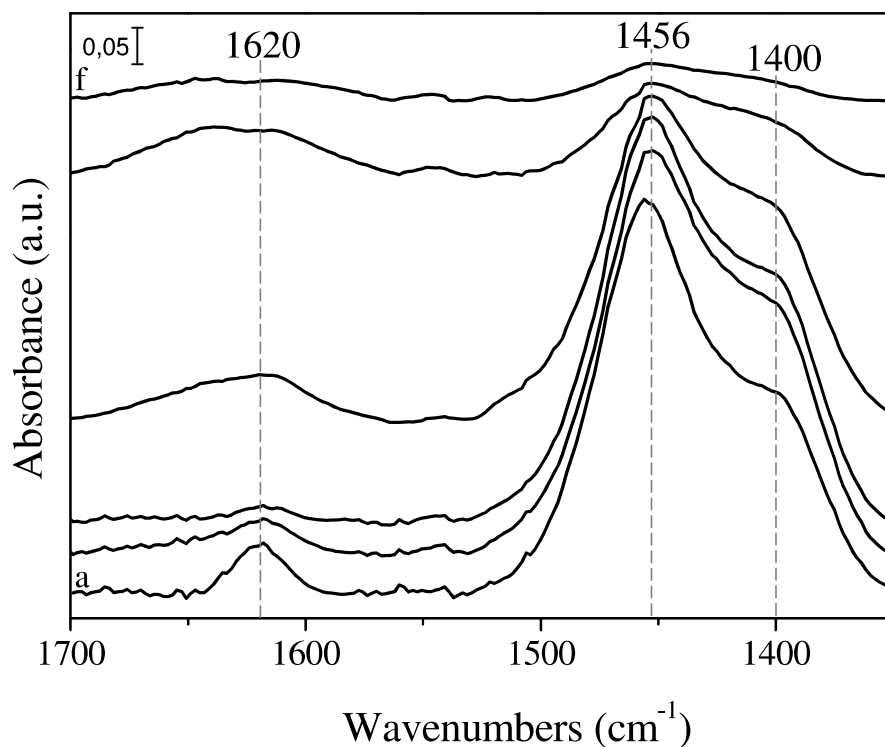


Figure 4.26. FTIR co-adsorption spectra over 2Cu-SAPO-150-30 at 300°C after: a) NH_3 adsorption and evacuation, b-e) in $\text{NO} + \text{O}_2$ atmosphere and f) the evacuation of all the gas phase.

So, it seems that the mechanism could involve the fast consumption of Lewis acid sites with NO_x in gas phase with an Eley-Rideal (E-R) mechanism that has been proposed by many researchers [101], where ammonia is adsorbed on the Lewis acid center and then reacts directly or via an intermediate with NO or NO_2 in gas phase. In addition, the high amount of Brönsted acid sites that were adsorbed onto the zeolite could provide the Lewis centers with the necessary ammonia, acting as a store, or the ammonia adsorb could also react with the NO adsorbed as nitrates or nitrites depending on the species [281] via a Langmuir-Hinshelwood (L-H) mechanism. Moreover, this mechanism could also be observed with ammonia and NO_x adsorbed in near copper species. In Figure 4.27, a possible pathway for the reaction is shown, where OZ corresponds to the zeolite framework oxygen.

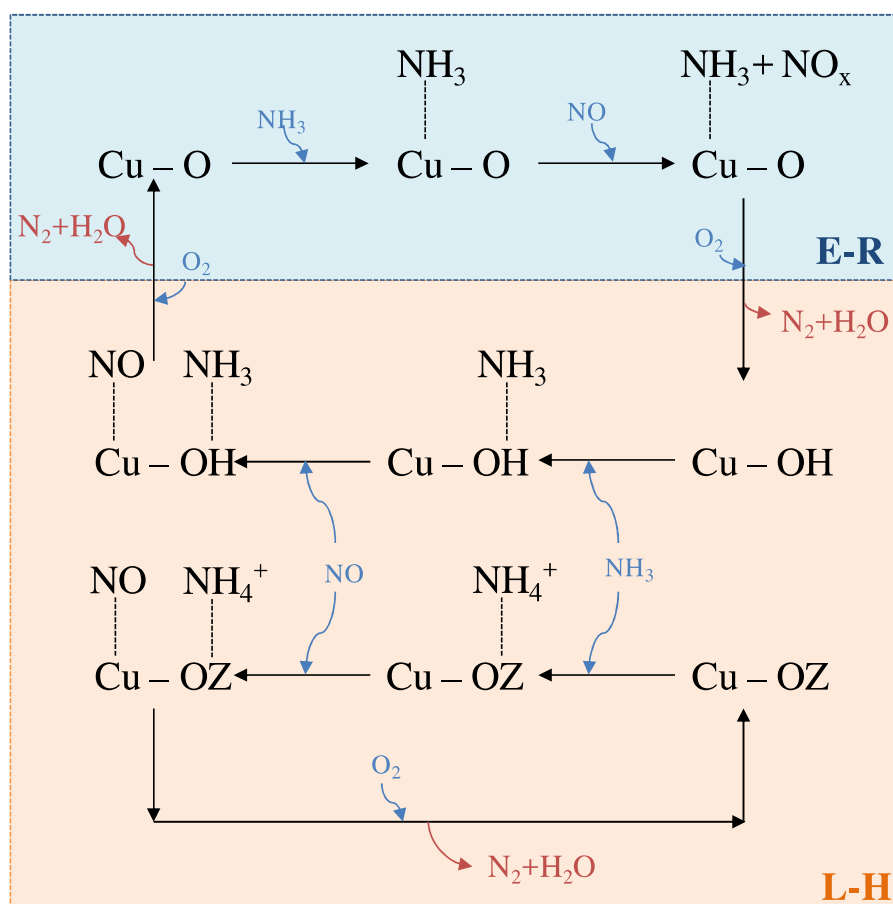


Figure 4.27. Pathways of the SCR reaction over Copper-zeolites.

The increase in the concentration of the species to be studied by FTIR was also considered, since it is more similar to real conditions where high amounts of the compounds are in contact with the catalyst. For this, NH_3 , NO and O_2 with concentrations 10 times higher, were used and the spectra are presented. In Figure 4.28a, the spectrum after ammonia adsorption at 300°C is represented. Modes around 1621 and 1452 cm^{-1} were observed that are associated with Lewis and Brønsted acid sites, respectively, and are in keeping with the NH_3 adsorption spectra explained above. At this temperature, the number of more stable Lewis acid sites related to the presence of copper increased. In all spectra, a signal at 1350 cm^{-1} can be observed and it corresponds to the potassium nitrate formed in the KBr cell window. After the introduction of NO and oxygen, a prompt nitrogen formation was monitored by MS, and a broad band between 1500 and 1700 cm^{-1} was observed in the spectrum (Fig. 4.28b). The SCR reaction with the retained ammonia is responsible for the production of nitrogen, and the excess NO and O_2 causes the accumulation of different nitrate species. A less intense band around 1750 cm^{-1} was also detected and can be related to

the interaction of NO with Cu⁺ or NO dimmers. In any case, all these species act as spectators in the reaction. At the end of the process, only a slow number of nitrates remained over the surface, indicating the complete removal of the adsorbed ammonia and the almost total regeneration of the catalyst.

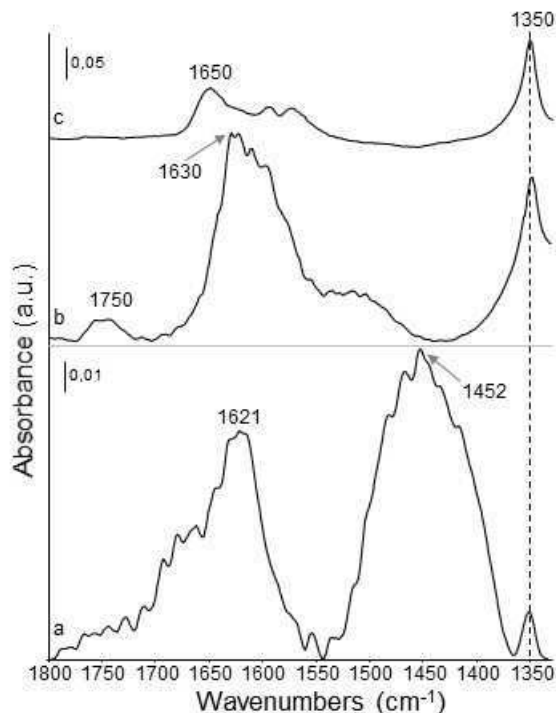


Figure 4.28. FTIR co-adsorption spectra over 2Cu-SAPO-150-30 at 300°C after: a) NH₃ adsorption and evacuation, b) 15 min in NO + O₂ atmosphere and c) the evacuation of all the gas phase.

Similar experiments, in flow conditions were carried out by DRIFTS-MS, feeding 750ppm of NH₃+750ppm of NO + 3% of O₂ at low temperatures, in order to decrease the rate of the reaction and be able to identify the routes. Figures 4.29, 4.30 and 4.31 A and B show the DRIFT spectra collected during the simultaneous exposure to these conditions with an increase in time over 2Cu-SAPO-150-30 at 40, 100 and 200°C, respectively, in the 1500-2200 cm⁻¹ region (Figures A) and 1120-1300 cm⁻¹ (Figures B). DRIFT spectra of the surface complex adsorption on the Cu-SAPO-34 samples are very similar for all temperatures. Two major bands at 1454 and 1625 cm⁻¹ were detected after introducing the mixture of ammonia, NO and O₂; these signals are associated with NH₄⁺ species resulting from NH₃ adsorbed on Brönsted acid sites and molecularly adsorbed NH₃ on Lewis acid sites, respectively [66,253–255]. Furthermore, the intensities of these bands increase as the time increases and the 1450-1600 cm⁻¹ region is wider with a peak centered at 1486 cm⁻¹ (1471 cm⁻¹ for the higher temperature, 200°C). This region is

very complex and involves different surface nitrate groups or nitro species adsorbed onto the transition metal active sites of catalysts for $\text{NO} + \text{O}_2$ atmosphere [221,254]. However, accurate identification of these bands is not straightforward because of different structures having similar vibration modes (monodentate, bridging monodentate, chelating bidentate and bridging bidentate species) [221,254]. Nitrate species were produced in the full temperature window when 750ppm of $\text{NO} + 3\%$ of O_2 were introduced over the Cu-SAPO-34 catalyst. These nitrate species were relatively stable as all these bands maintained their intensities during the exposure time for all temperatures.

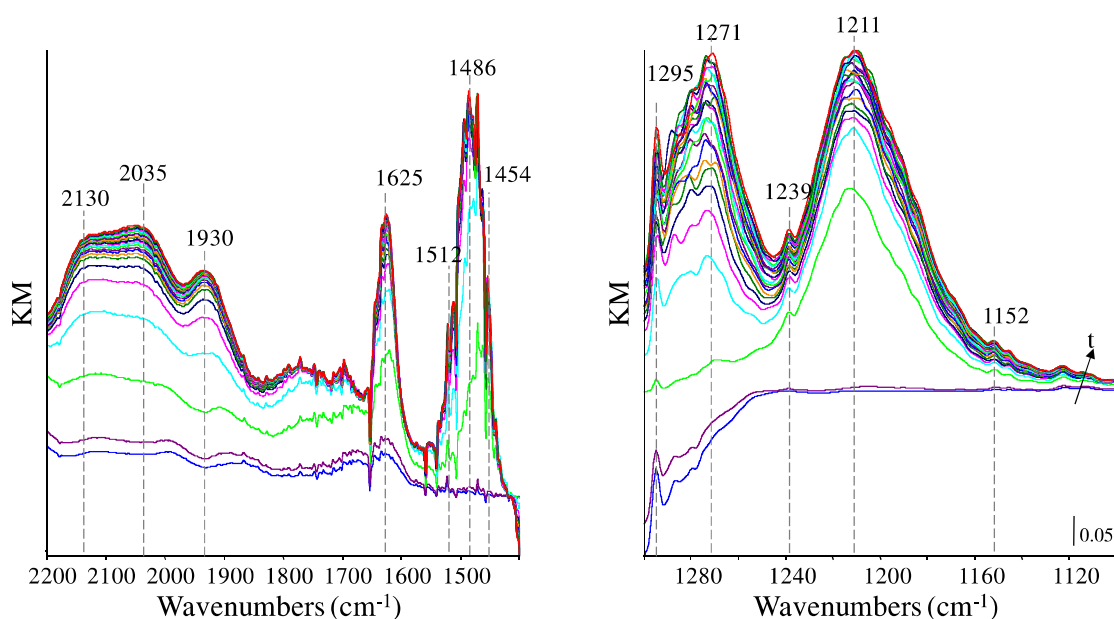


Figure 4.29. DRIFT spectra of the simultaneous adsorption of 750ppm of $\text{NH}_3 + 750\text{ppm}$ of $\text{NO} + 3\%$ of O_2 as the time increases over 2Cu-SAPO-150-30 at 40°C .

The main difference is found in the intensity of the signal with the temperature. The intensity decreases with the increase of temperature. For the three temperatures, another important difference can be seen. For the lowest temperature (40°C), the bands are not immediately formed by the contact between the catalyst and the mixture and some time is necessary the presence of peaks to be detected. For the higher temperatures (100 and 200°C) the signal at 1454 cm^{-1} was not immediately apparent however the signals were detected at 1486 cm^{-1} or 1471 cm^{-1} , respectively

The $1120\text{-}1300\text{ cm}^{-1}$ region (right hand side of the figures 4.29-4.31) is very similar for different temperatures and the difference showed can be detected with the temperature

in the range 1500-2200 cm^{-1} . Overlapping bands of nitrates and nitrites species are expected upon adsorption in this region. At 1239 cm^{-1} , weak peaks can be observed that could be assigned to ammonia coordinated over Me^{+2} species [264]. The most prominent features are two broad bands centered around 1211 and 1271 cm^{-1} both of which are associated with to adsorbed nitrite species [283].

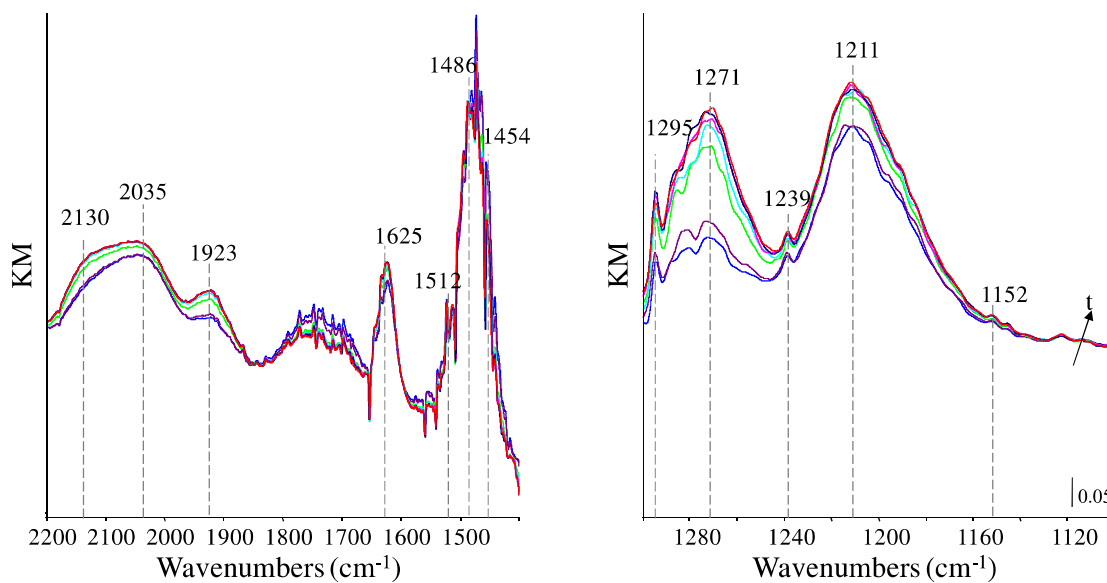


Figure 4.30. DRIFT spectra of the simultaneous adsorption of 750ppm of NH_3 + 750ppm of NO + 3% of O_2 as the time increases over 2Cu-SAPO-150-30 at 100°C.

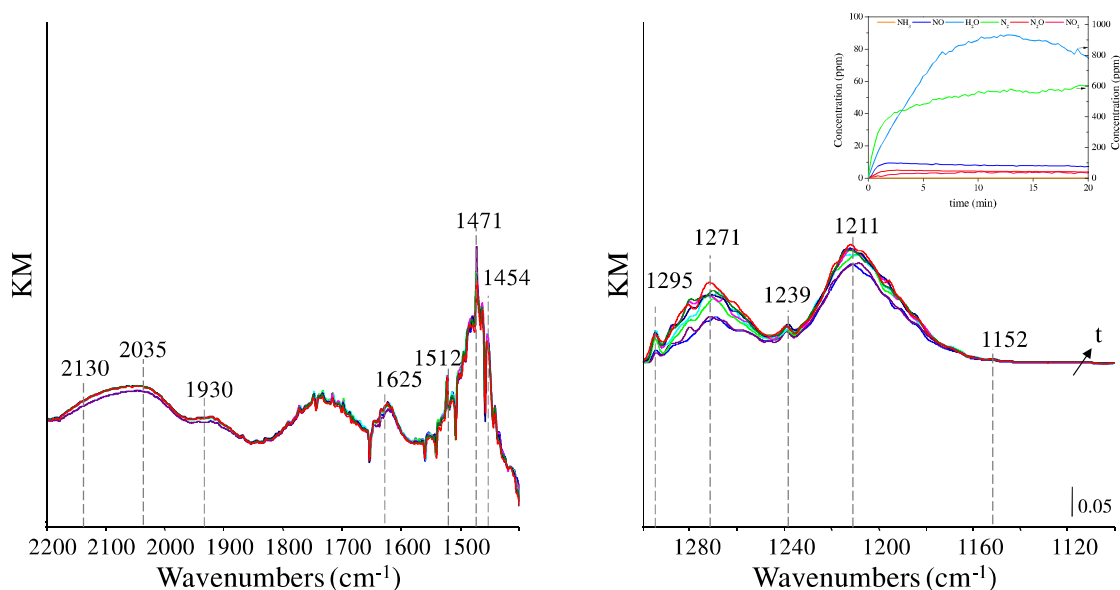


Figure 4.31. DRIFT spectra of the simultaneous adsorption of 750ppm of NH_3 + 750ppm of NO + 3% of O_2 as the time increases over 2Cu-SAPO-150-30 at 200°C.

DRIFTS experiments allow the study of the mechanism *in situ*; however, due to the high reagent concentration and the low value of the temperatures, the situation that could be observed is similar to final equilibrium conditions, as occurs in the adsorption of pulses with high concentration.

Therefore, the proposed mechanism that is in agreement with other authors justifies the activity data in dry conditions where the ammonia nitrate or nitrite is needed for the reaction. DRIFTS experiments provide information about the spectator species, which are the same as the final surface obtained by FTIR with high concentration pulses.

The influence of some external elements that are present in exhaust, such as the behaviour of the catalysts in the presence of soot or oxygenated compounds, their hydrothermal aging or their SCR activity in the presence of water and CO₂ has also been addressed.

It has been tested that hydrocarbon molecules with a greater size than propylene, only can modify the catalyst surface, with cracking or carbon formation and its retention inside the cavities. Oxygenated compounds below C₂, e.g. methanol, accede to the pores and produce oligomerization by interaction with copper and cracking inside the zeolite, which would cause the decay of the activity by the deactivation of the copper. Other molecules with greater sizes cannot access the pores and can only produce surface dehydration. The influence of the presence of soot in contact with the zeolite was analyzed as in Chapter 3 with the NSR catalysts. Experiments with Cu-SAPO-34 + soot (10wt%) mixtures were carried out in the thermobalance in different oxidant atmospheres (NO+O₂/O₂). In addition, the distribution function of activation energy was also obtained, as was previously explained, in order to identify the processes involved in the removal of soot in the presence of Cu-SAPO-34. In Figure 4.32, the TG profile and the distribution function of activation energy is shown.

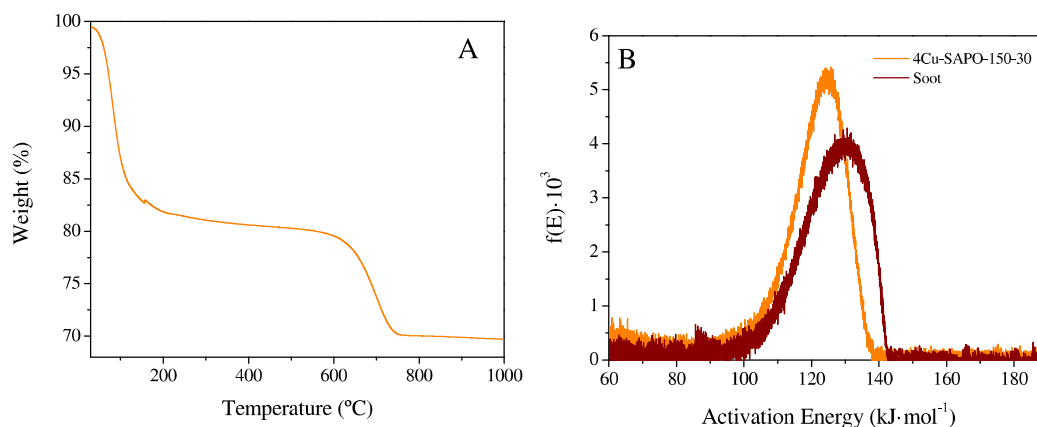


Figure 4.32. A) Weight loss vs. temperature in the presence of 1000ppm of NO + 3% of O₂ in He for 4Cu-SAPO-150-30. B) Distribution functions of activation energy for 4Cu-SAPO-150-30 and uncatylyzed soot in NO+O₂ atmosphere.

In the weight profiles two intense weight losses can be observed, one of them around 100°C associated with the high amount of water desorbed by the catalyst and the other, between 600 and 800°C, with high CO₂ production corresponding to the soot removal process that presents an activation energy value close to the uncatylyzed process [284]. The size of the particulate matter is around 2.5 μm and in consequence it does not penetrate the pores. The zeolite is not active for soot removal and the absence of interaction with the copper produces a behaviour similar to the process of soot combustion with the gas phase. The catalyst is able to resist these conditions and the core of the zeolite is not modified by the presence of soot. The regeneration of the zeolite is obtained by increasing the temperature and the thermal resistance of the materials was also tested.

The hydrothermal stability of the samples was analyzed by thermogravimetric experiments (TGA-MS). The sample (20 mg) was warmed to 750°C in (1%) water stream simulating hydrothermal aging and was kept at this temperature for 5 h. The same experiment in the absence of water was performed in order to clarify the effect of the water. In Figure 4.33, the evolution of the weight profile and the specific heat flow with the time and the temperature for the 2Cu-SAPO-200-4 are shown. The full time at constant temperature has not been represented since it was almost invariable.

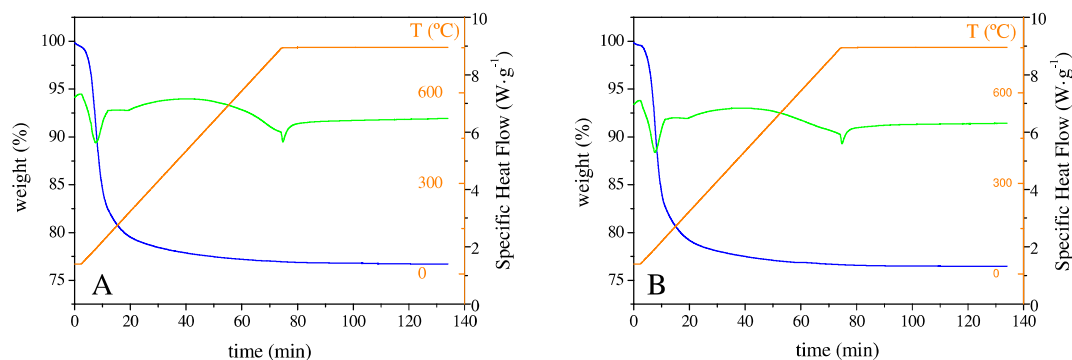


Figure 4.33. Weight and heat flow profiles for 2Cu-SAPO-200-4 during thermal aging in A) He and B) H₂O.

As can be observed, there is no significant difference between the reaction atmospheres. In both cases, there is a loss of weight between room temperature and 200°C, due to the removal of a high quantity of structural water, as well as other species, such as labile carbonate species. The desorption of quimisorbed water is an endothermic process and, accordingly, it occurs accompanied by a downward peak in the heat flow signal. After the water loss, the weight of the samples was constant and the heat flow was slightly modified; the only detectable peak was observed at maximum temperature, so this must be due to the operation of the equipment.

In view of the results, it seems that regarding the weight and the heat flow, the result reaction is identical regardless of whether there is water in the atmosphere. Moreover, no severe changes in the sample were detected as a consequence of thermal aging. However, other techniques such as XRD with Rietveld refinement were carried out in order to study the modification of the structure of the chabazite. In Figure 4.34, the XRD patterns and unit cell parameters obtained by Rietveld refinement for both the fresh 2Cu-SAPO-200-4 and the hydrothermally aged sample are shown in the inset table.

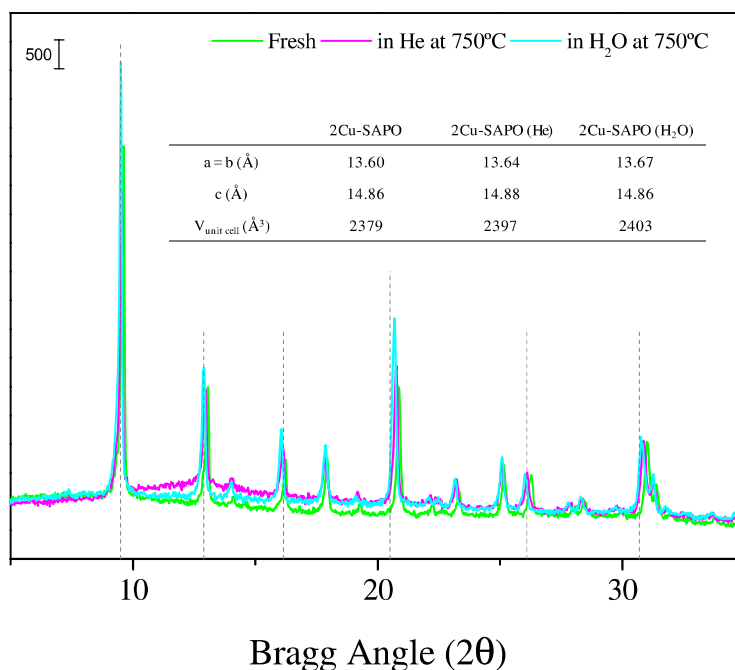


Figure 4.34. X-ray diffraction patterns of 2Cu-SAPO-200-4 (fresh and hydrothermally aged in He and in H₂O) and unit cell values (inset table).

In all cases, the XRD patterns coincide with those corresponding to the SAPO-34 structure. The comparison between the fresh sample and the thermally or hydrothermally aged sample did not reveal an apparent difference in structure and it might even seem that hydrothermal aging slightly increases crystallinity. No other copper phases, such as Cu, Cu₂O or CuO, were detected. This is similar to that reported by *D. Wang et al.* [67] for a Cu-SAPO-34 synthesized by ion-exchange of a commercial material with 4% of copper or as discussed by *J. Wang et al.* [82] with the same procedure but with a lower copper percentage (1%). Unit cell parameters were calculated by Rietveld refinement and an increase in the unit cell volume caused by the hydrothermal treatment could be observed. In spite of the distances, the parameter “c” did not suffer any modification, whereas “a” and “b” distances increased, indicating that the cell widens. Other authors have also observed a lattice expansion of the SAPO-34 support after the hydrothermal aging when 0.9% of copper was incorporated by ion-exchange [103]. Although it is possible to find some works [258] that indicate a significant decrease of crystallinity over a Cu-SAPO-34 synthesized by wetness impregnation, it is generally accepted that the ion exchange method [94,259,285], or even the one-pot synthesis with different precursors and protocols [105], produce

materials with high hydrothermal stability and the copper is well dispersed or may migrate into the SAPO-34 cavity, next to the 8-membered rings.

In order to study the influence of water and CO₂ presence in the ammonia adsorption capacity, NH₃-TPD of the different samples was performed in He and in H₂O+CO₂ atmospheres, adsorbing 750ppm of NH₃ up to saturation (around 2 hours) at several operation range temperatures. In Figure 4.35, the ammonia profiles during the tests are represented. In all cases, an hour is needed to obtain complete saturation of the catalyst; however, the breakthrough time and the adsorption rate depend on the temperature and the reaction atmosphere. The latter decreases with the increase of temperature and, therefore, the adsorption capacity is lower, as other authors have reported [94], indicating that the number of NH₃ adsorption sites decrease.

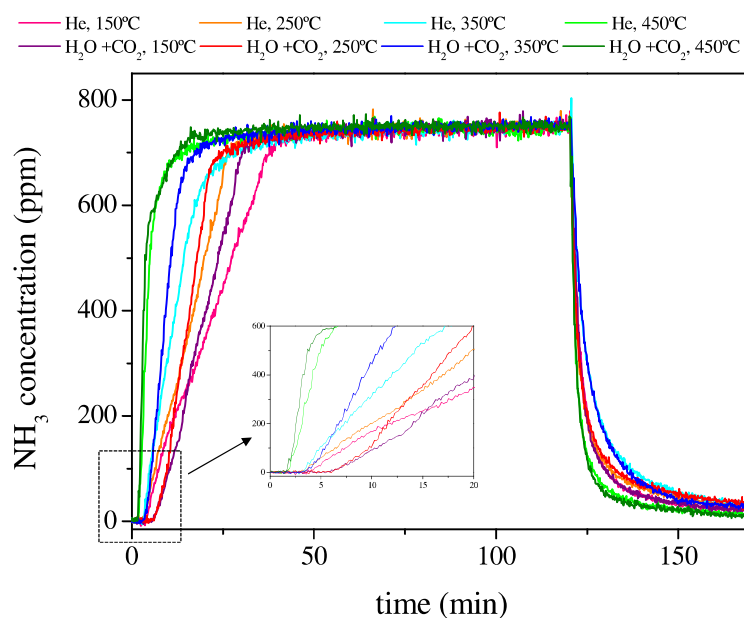


Figure 4.35. NH₃ profiles for NH₃-TPD experiments (750ppm of NH₃) in He and in 1.5% H₂O and 0.3% CO₂ at different temperatures.

Regarding the breakthrough time, it is noteworthy that higher values were detected in the presence of water and CO₂, and afterwards saturation was faster, with the rate increasing with respect to the experiments in Helium (dry conditions). In view of these results, it could be suggested that different species or processes are somehow involved in ammonia adsorption. In He atmosphere, only the adsorption of ammonia mainly onto the Brønsted acid sites occurs, as previous experiments in FTIR have shown [286]. In the presence of water and CO₂, which compete for the same active sites, these reagents could react with ammonia, with the formation of ammonium hydrated carbonate,

initially increasing the adsorption time, although saturation is then reached faster, due to the active sites being blocked.

In order to better understand the adsorption, values of adsorbed NH_3 ($\text{mmol NH}_3/\text{g}_{\text{cat}}^{-1}$) were calculated subtracting the ammonia desorbed in the purge by mathematical treatment of the curves and are shown in Table 4.5. The results are similar to those previously reported [94].

Table 4.5. Amount of ammonia adsorbed per gram of 2Cu-SAPO-200-4 or SAPO-200-4 at different temperatures and atmospheres.

Temperature (°C)	150	250	350	450
SAPO-34 (He)	0.87	0.55	0.20	0.16
SAPO-34 (H_2O)	0.82	0.51	0.18	0.14
2Cu-SAPO-34 (He)	0.87	0.53	0.18	0.11
2Cu-SAPO-34 (H_2O)	0.76	0.43	0.11	0.05

As a general trend, it was observed that the ammonia adsorption capacity decreases with the increase of temperature, as expected, irrespective of the material or the reaction atmosphere. The retention when copper is in the structure, although was not greatly affected, was slightly lower, indicating that it is the support that is mainly responsible for the ammonia adsorption capacity. Although some authors have observed the opposite effect [94], the reduction of the acid sites of SAPO-34 with the loading of copper can be justified due to the substitution of the proton (-Si-OH-Al-) by Cu^{2+} species in the support [82]. In any case, the combination of water and CO_2 caused a decrease in the ammonia adsorption capacity at all temperatures, being more evident for the copper containing catalysts. The reason could be the competition between ammonia and water and/or CO_2 for the same active centers. However, it has been reported that CO_2 has an insignificant effect on the adsorption capacity. There is controversy about the influence of water on the ammonia adsorption capacity. Some authors [109] have observed an increase in the adsorbed NH_3 contents and the acid density, whereas in general, a decrease in ammonia storage in the presence of water has been justified due to the competitive adsorption on the same sites [102]. The reduction in the number of acid sites was more noticeable in the Cu-SAPO-34, so the interaction between copper and water and/or CO_2 could block the support centers used for adsorption.

The species formed during the SCR process were also studied by the co-adsorption of low concentrations of gas probe molecules by FTIR, such as has been explained previously. In Figure 4.36, the spectra obtained by the subtraction of the activated sample are shown.

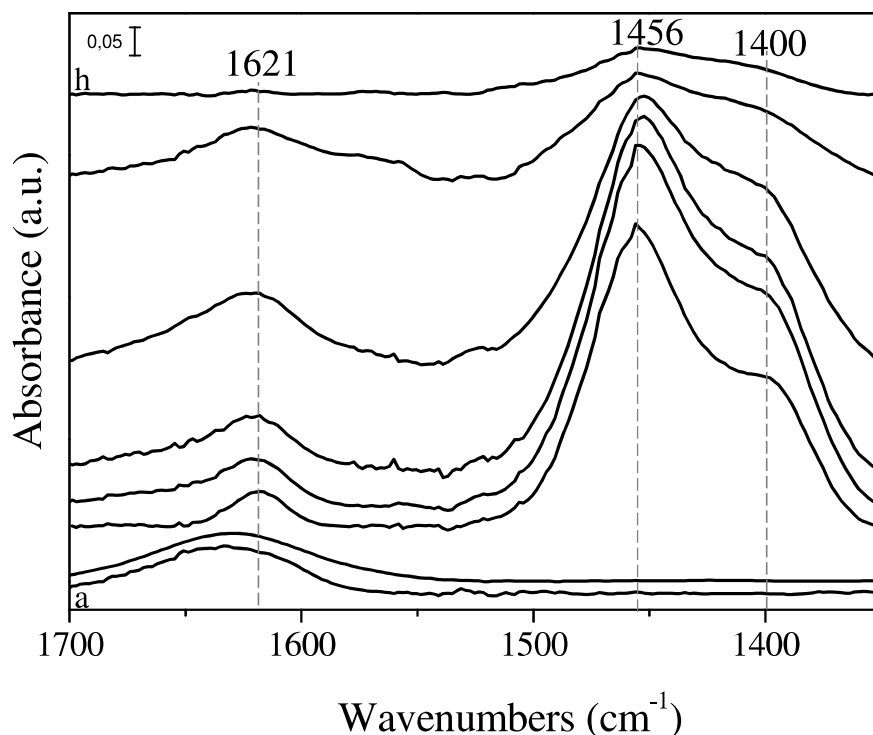


Figure 4.36. FTIR co-adsorption spectra over 2Cu-SAPO-150-30 at 200°C after: a) H₂O adsorption, b) CO₂ adsorption, c) NH₃ adsorption in evacuation, d-g) in NO + O₂ atmosphere and h) evacuation of all the gas phase.

In the Figure, the spectrum of the hydrated material showed a wide band around 1620 cm⁻¹ characteristic of water adsorption. The presence of CO₂ (b) barely modified the spectra; although the presence of carbohydrated species cannot be discarded. After NH₃ adsorption and evacuation in the N-H bending vibration region, several bands very similar to those detected in dry conditions can be observed. The bands at 1400 and 1456 cm⁻¹ are due to bending vibration of NH₄⁺ on the Brönsted acid sites, while the less intense band at 1620 cm⁻¹ can be assigned to the vibration of the N-N bond in the NH₃ coordinated to Lewis acid sites (copper ion sites) [66,253–255]. The profiles are also very similar in NO+O₂ atmosphere and time does not modify the signals. Nitrate formation could seem faster as a consequence of the more active species available in the presence of water and CO₂. The co-adsorption of H₂O and CO₂ modified the intensity of the peak at 1620 cm⁻¹ assigned to coordinated NH₃. After hydrothermal aging, the band

intensities in the Lewis region were higher than those observed on the sample analyzed in dry conditions (Figure 4.26). After evacuation only a very weak signal in the region assigned to Brønsted acidity and/or nitrates species is detected.

In order to better understand the species involved in the SCR process in the presence of water, its adsorption was analyzed at different temperatures by FTIR. In Figure 4.37, the adsorption spectra in evacuation at 100°C are represented for SAPO-200-4 and 2Cu-SAPO-200-4 in order to detect the difference caused by the presence of copper.

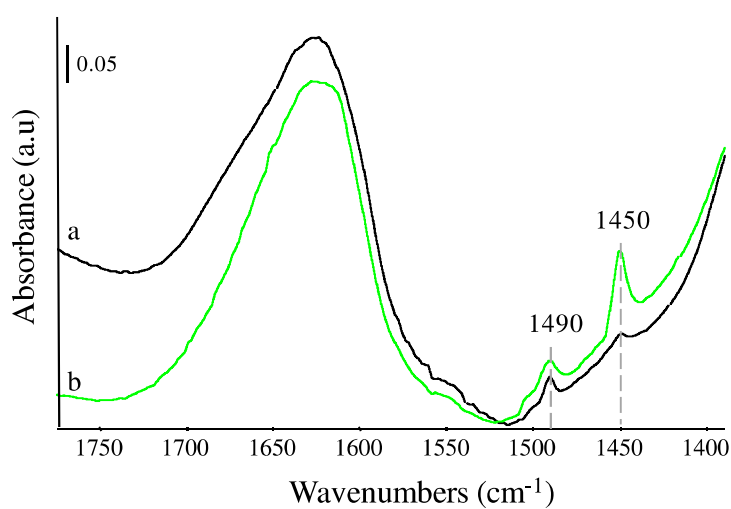


Figure 4.37. FTIR spectra after water adsorption and outgassing at 100°C of a) SAPO-200-4 and b) 2Cu-SAPO-200-4.

For both samples, the main signal was broad and detected in the region between 1800 and 1500 cm^{-1} , with a maximum at 1640 cm^{-1} . In presence of copper, a symmetric signal located at 1450 cm^{-1} was evident and associated with highly hydrated Cu^{2+} species in octahedral coordination, as a result of hydration of isolated Cu species [97]. This signal remained until evacuation of around 300°C.

SCR activity was studied in a flow reactor, feeding 750ppm of NH_3 , 750ppm of NO and 3% of O_2 in He or 1.5% of H_2O and 0.3% of CO_2 , reaching stationary state at any temperature. In Figure 4.38, the SCR activity parameters, such as ammonia and NO conversion and N_2 , N_2O and NO_2 selectivity, both in He and $\text{H}_2\text{O}+\text{CO}_2$ atmospheres are displayed in all the temperature ranges for the SAPO-200-4 with and without copper.

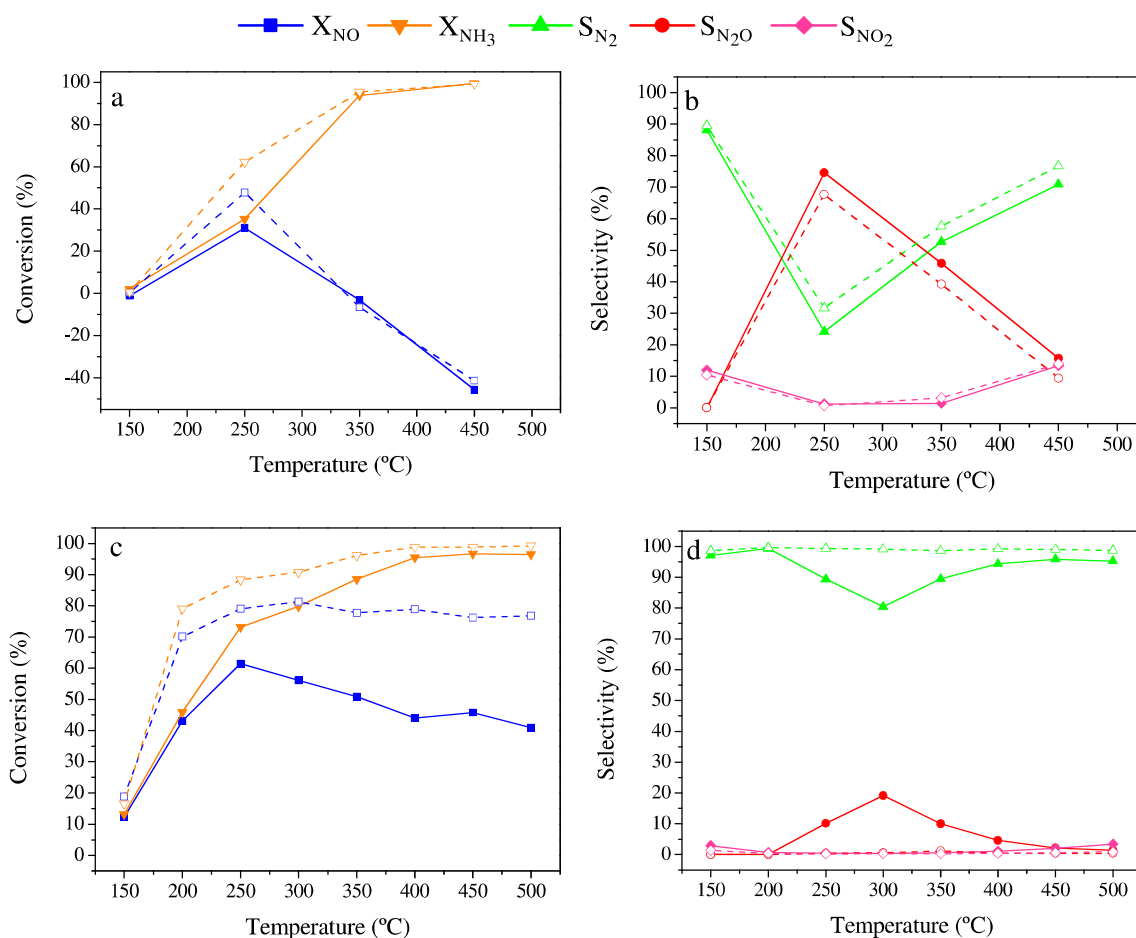


Figure 4.38. SCR conversion and selectivity values according to the temperature for a and b) SAPO-200-4 and c and d) 2Cu-SAPO-200-4. Feeding conditions: 750ppm NO+750ppmNH₃+3%O₂ in He. Dotted lines (H₂O+CO₂), solid lines (He).

Regarding SAPO-200-4 behavior, the conversion of NO was almost absent, with a maximum of around 30% at 250°C. Then, the conversion decreased below zero, indicating that a process with NO production was taking place. However, NH₃ conversion increased with temperature up to 100% of conversion above 300°C. So, the ammonia must have been reacting with the oxygen, via ammonia oxidation, and producing not only nitrogen, but also NO and other N-compounds. It should also be noted that around 250°C a process was detected with high levels of N₂O formation, the least desired product, due to its strong effect as a greenhouse gas. There has to be a process involving the NO reaction and production of N₂O, associated with the support. *T. Yu et al.* [109] have also reported similar data for a SAPO-200-4 material synthesized by hydrothermal method using morpholine and boehmite as precursors; they observed low NO conversion values, ammonia oxidation from 300°C and N₂O generation with a maximum at 320°C.

The profiles of conversion and selectivity in dry conditions for the 2Cu-SAPO-200-4 (Fig. 4.38c and d, solid lines) indicated that there are several processes taking place. At low temperatures (up to 200°C), the conversion of NH₃ and NO was stoichiometric producing nitrogen and water, which means that standard SCR was occurring. In the SCR temperature range, between 200 and 400°C, and up to 500°C, NH₃ conversion values were higher than NO conversion, so there has to be a process where ammonia is consumed without NO intervention, such as the ammonia oxidation. Furthermore, there was significant N₂O formation with a maximum at 300°C, similar to that detected in the SAPO-34 study. A possible route for the N₂O is related to the direct nitrate decomposition, which occurs in this temperature range. As has been explained in a previous work [286] nitrates are formed on the surface of the zeolites when NO is adsorbed and remain even in evacuation. The decomposition of nitrates can produce N₂O since it is one of the possible parallel reactions [93]. Cu-SAPO-34 materials show higher NO conversion compared to SAPO-34, due to the promotion role of copper on the redox activity necessary for the SCR process. The oxidation of NH₃ together with a decrease in NO conversion was also observed [254] at temperature higher than 200°C over a commercial material.

The presence of water and CO₂ in the reaction atmosphere caused a modification in the processes that take place, as can be deduced from the activity data. At low temperatures, the conversions of NO and NH₃ were almost identical with total nitrogen production, so the standard SCR was taking place with a conversion of the reagents around 75% and 100% selective to N₂. No N₂O formation was detected in the whole range, involving parallel reactions with undesired compounds production. Water and CO₂ presence, in some way, inhibit nitrate formation and, consequently, the nitrate decomposition. Nevertheless, between 200 and 500°C, NH₃ conversion remained higher than that of NO, indicating that ammonia oxidation occurs to some extent, even so, both the standard SCR and the ammonia oxidation led to nitrogen production. So, it would appear that the presence of water and CO₂ inhibits ammonia oxidation and nitrate formation/decomposition by the formation of species associated with copper; although some authors have reported that the presence of CO₂ did not influence SCR activity for a material prepared in two steps by ion-exchange [109], whereas the water improved the NH₃-SCR activity and the NO₂ and N₂O formation decreased. The SCR activity is usually studied in the presence of water and compared to dry conditions in almost all

cases the performance is higher and the selectivity to nitrogen increases due to the inhibition of N_2O formation [88]. At low temperatures, water improves the reducibility of the Cu^{2+} species, probably due to the migration of copper species probably to octahedral positions, which modifies the bond strength between Cu^{2+} species and the oxygen atoms of the SAPO-34 skeleton and makes the reduction of the adsorbed species faster. Similar effects have been observed over Cu-SSZ-13 synthesized by ion-exchange [287], with the same CHA structure, where it was confirmed that the movement of the copper ions inside the zeolite, as a result of water adsorption, produced Cu^{2+} ions that were easier to reduce and, as a result, the activity of the SCR improved. Although it has not been detected in the NH_3 -TPD experiments, an increment of acid sites or the modification of the types of adsorption sites as other authors have observed [82,88,104,109] cannot be rejected and could benefit the first step in the NH_3 -SCR process. Although the improvement of SCR activity due to the presence of water can be justified, the decrease in N_2O formation has not been explained. Some authors [110] have observed an increase in N_2O production at intermediate temperatures after hydrothermal aging and have related it to the partial loss of acidity and the micropore volume of the catalysts. In this case, the opposite effect was observed and, thus, the presence of water and CO_2 improved the Cu-environment of the samples; although, the influence of the ammonia oxidation cannot be discarded, as has been observed [254] for commercial materials with around 1% of copper at temperatures higher than 200°C .

In order to confirm the cooperative effect of these components ($\text{H}_2\text{O}+\text{CO}_2$) in ammonia oxidation and ensure that the process is totally selective to nitrogen, NH_3 oxidation was also studied, feeding 750ppm of NH_3 + 3% of O_2 and the results are shown in Figure 4.39.

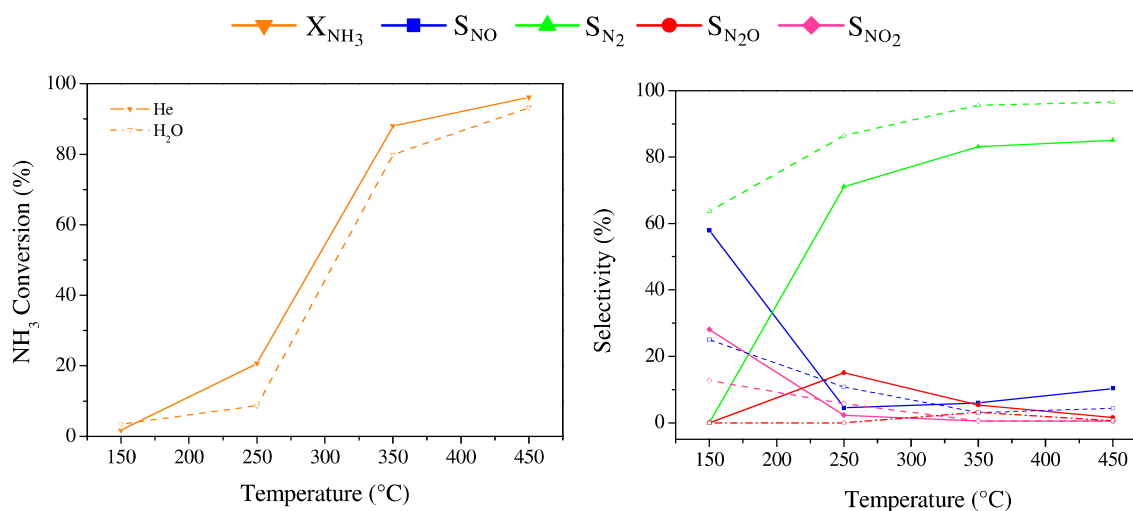


Figure 4.39. Conversion and selectivity values for NH₃ oxidation over 2Cu-SAPO-200-4 in the presence of He (solid lines) and water and CO₂ (dotted lines).

NH₃ conversion increased with temperature regardless the atmosphere, with values higher than 90% at temperatures above 300°C in dry conditions. At low temperatures, the conversion values were insignificant and, therefore, the selectivity values cannot be considered as representative, due to the small concentrations of the products. Around 250°C, there was a slight formation of N₂O, which could contribute to the N₂O production detected in the SCR experiments. However, the increase in temperature did not produce a higher concentration of this component, and the maximum detected in the previous experiments therefore has to involve another process. The presence of water and CO₂, not only inhibits ammonia oxidation, but also increases nitrogen selectivity, as observed in the SCR experiments. In addition, there was no production of N₂O in the whole temperature range. Regarding the inhibition of ammonia oxidation in the presence of water, these data are in consonance with those reported by other authors [80,109,259], due to the fact that water interaction reduces the Cu_xO_y clusters or Cu⁺ species that are responsible for ammonia oxidation. Nevertheless, it is noteworthy that several authors have detected NO as the main product of oxidation, because of its formation in CuO species, whereas for this one-pot synthesized material the principal product was nitrogen in the high ammonia conversion range.

According to the observations in the SCR and NH₃ oxidation experiments and in agreement with the bibliography [288], N₂O formation has to be caused by the decomposition of surface nitrates, which, in the presence of water and CO₂, increase

their stability or reduce their formation by the action of $[\text{Cu}^{2+}-(\text{H}_2\text{O})-(\text{CO}_2)]$ species, inhibiting their decomposition and reducing the formation of undesired products.

Therefore, at lower temperatures standard NH_3 -SCR reaction is much faster than ammonia oxidation and was the main reaction in any atmosphere, with conversion values increasing in the presence of water and CO_2 . At higher temperatures, in dry conditions, N_2O formation was observed due to nitrate decomposition, and ammonia oxidation took place to a great extent. The presence of water and CO_2 inhibited these two latter processes, as a result of the copper species environment modification, being completely selective to nitrogen in the whole SCR range.

Taking all the information into account and in addition to the SCR proposed mechanism, the behavior of the copper species is summarized. Cu^{2+} species are the main species involved in the SCR process, whereas ammonia oxidation and nitrate decomposition take place in presence of Cu^+ species. The most reactive species are Cu^{2+} located in the six member rings, with tetrahedral symmetry, which in presence of water and CO_2 would be somehow hydrated, hindering their reduction to Cu^+ and inhibiting the nitrate decomposition and the ammonia oxidation. In addition, Cu^{2+} species placed in the 8 member rings that are highly hydrated would be formed in octahedral coordination and, in presence of water and CO_2 , would be the responsible for the hydrated carbonate species formation that are highly active in the SCR process. Finally, the possible location of the species inside the structure is proposed and represented in Figure 4.40.

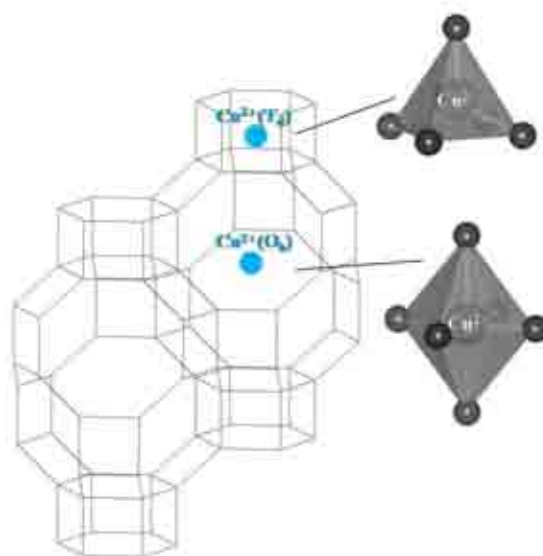


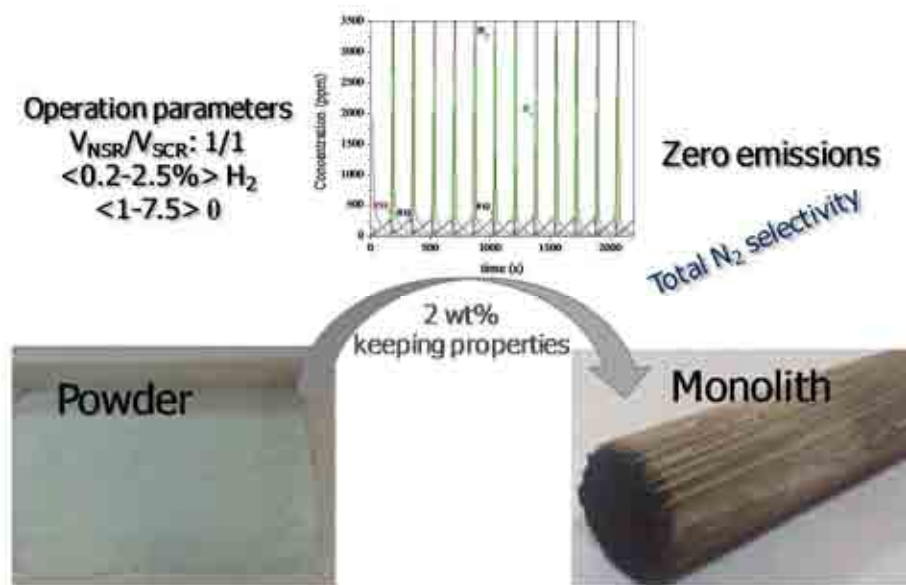
Figure 4.40. Scheme of possible copper location inside the SAPO-34 structure.

4.4. Conclusions

The synthesis of small pore zeolites has been considered in order to obtain the most suitable conditions for maximizing copper content, ensuring its location inside the structure. In addition, in dry atmosphere the equilibrium conditions and the reaction pathway have been proposed, identifying the active copper species. Moreover, the resistance of the catalyst to the external compounds present in exhaust gas was addressed together with the improvement of the catalytic activity in the presence of water and CO₂.

5. Results and Discussion.

NSR-SCR coupled technologies





UNIVERSIDAD
DE MÁLAGA

5. Results and discussion. NSR-SCR coupled technologies

As has been detailed in the previous chapters, the NSR catalysts efficiently remove NO_x and soot simultaneously; however, in particular operation conditions some ammonia is also produced during the rich phase. The ammonia formed can be utilized by the downstream SCR catalyst to further reduce NO_x in the exhaust gas. Although the implementation of the hybrid system could be complicated, it may provide a way of lowering the NO_x emissions without NH_3 slip. Therefore, this section is focused on the study of the behaviour and the operation conditions of the sequential LNT-catalyst and SCR material in powder and monolithic form.

First, the most suitable combination of volume ratio between NSR and SCR fixed beds must be proposed in order to obtain the higher De- NO_x performance and eliminate the N_2O and NH_3 emissions. For this purpose, experiments in powder were carried out, varying the ratio between the amounts of each catalytic bed. It should be noted that $V_{\text{NSR}}/V_{\text{SCR}}$ ratio under one were not included, since as was detailed in Chapter 3, the levels of ammonia produced in the Pt-Ba-K/ Al_2O_3 were not very high and the excessive amount of SCR catalyst would be completely unnecessary. The optimization of the ratio between both catalytic beds was performed in Helium atmosphere, instead of in $\text{H}_2\text{O} + \text{CO}_2$, because it is a more unfavourable condition in product distribution, with an N_2O formation at low temperatures that was not detected in the presence of water, and higher ammonia selectivity (3%) at high temperatures under dry conditions.

Pt-Ba-K/ Al_2O_3 was employed as NSR catalyst due to its excellent properties in NO_x and soot removal, and 2Cu-SAPO-150-30 was used as SCR catalytic bed because of the combination of its catalytic activity and structural properties. Both catalysts presented the highest performance in the individualized processes as has been widely detailed in Chapters 3 and 4. The zeolite was placed downstream in the reactor and both catalytic beds were separated by a quartz wool layer, as can be observed in Figure 5.1, together with the experimental conditions of this experimental series. Experiments were carried out alternating lean-rich cycles in identical conditions to the TRM experiments, with 1000ppm of $\text{NO} + 3\%$ of O_2 and 2000ppm of hydrogen as reductant up to saturation and complete regeneration, i.e. 15 min for each phase. The hydrogen concentration is almost the stoichiometric value. The GHSV was $3 \cdot 10^4 \text{ h}^{-1}$ with respect to each catalytic bed in order to obtain data that were comparable to those reported for the single bed.

Table 5.1. Experimental parameters of the double catalytic bed configurations.

		1NSR:0SCR	1NSR:1SCR	1NSR:0.5SCR
NSR	Pt-Ba-K/Al ₂ O ₃	1	1	1
SCR	2Cu-SAPO-150-30	0	1	0.5



Figure 5.1. Double bed configuration.

Table 5.2. Experimental conditions for the study of different NSR/SCR catalytic beds.

	Lean	Rich
NO (ppm)	1000	-
O ₂ (%)	3	-
H ₂ (ppm)	-	2000
He	balance	balance
GHSV (h ⁻¹)	30000	30000
time (min)	15	15

The cyclic experiments were carried out at different temperatures up to the stabilization of the catalysts. In Figure 5.2, the results of the study of the most representative NSR-SCR volume ratios, in terms of NO_x conversion and nitrogen, ammonia and N₂O selectivity values are represented for two characteristic temperatures, 200°C as low temperature of the SCR range and 350°C, typical of the standard NSR experiments.

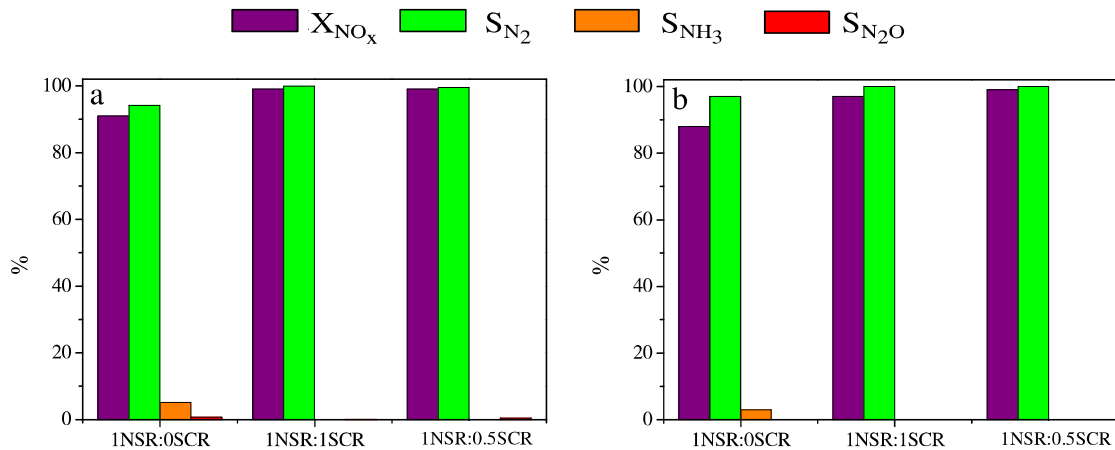


Figure 5.2. Conversion and selectivity values for different NSR/SCR volume ratios in experiments with NSR conditions (1000ppm NO+3%O₂/2000ppm H₂ in He, 15-15 min) at a) 200°C and b) 350°C.

The coupling of the technologies, regardless of the catalysts, always increases the conversion of nitrogen oxides and the amount of NO_x removed per gram of catalyst, due to the storage and reduction by the NSR technology together with the reaction with the stored ammonia by the SCR process, as reported by other authors for both Pt-(Rh)-Ba/Al₂O₃ catalysts and Cu-zeolites, such as ZSM5, BETA or CHA [110,175,183]. For Pt-Ba-K/Al₂O₃, the configuration 1NSR:0SCR, with only the NSR catalytic bed,

presents a high performance and low ammonia emissions; in addition, a slight amount of N_2O is detected only at low temperatures in dry conditions. The placing of the SCR catalyst after the NSR catalytic bed completely removes the ammonia production in all the possible configurations. The volume ratio equal to 1, 1NSR:1SCR, besides the improvement in the NO_x and ammonia reduction, causes a decrease in the N_2O emission, a highly polluting greenhouse gas, which could be removed by decomposition over the copper zeolite. Nevertheless, the increase of the weight of the NSR catalyst, 1NSR:0.5SCR, in spite of reducing the NO_x and NH_3 production, negatively affects the N_2O decrease, as other authors have observed for the coupling of an NSR catalyst based on noble metals and an Fe-zeolite [289]. A plausible explanation of this effect is that the increase in the NSR weight produces a higher amount of N_2O and the SCR in this condition is not able to reduce all the gas produced.

Considering the NO_x conversion, NH_3 slip and N_2O production, which were evaluated for three differently NSR-SCR systems in dry conditions, the most suitable volume ratio of catalysts was selected 1:1 for the NSR-SCR hybrid system, in agreement with other authors, since it keeps the NO_x conversion, prevents the ammonia slip and reduces the N_2O emission by decomposition over the zeolite.

5.1. Influence of quasi-real conditions over NSR-SCR systems with volume ratio 1:1

The double bed system was also studied in water and CO_2 atmosphere, and although the NSR catalyst presents higher selectivity values, this is a more realistic condition and influences the NO_x removal. In addition, the Cu-SAPO-34 materials synthesized and well-characterized in the previous Chapter, have demonstrated excellent hydrothermal resistance, so, at least initially, the proposed system with 1:1 in volume ratio could improve the performance of the process. The feed stream consisted of 1000ppm of NO + 3% of O_2 and 2000ppm of hydrogen for the lean and rich phases, respectively, in a He or 1.5% of H_2O + 0.3% of CO_2 atmosphere. The cycle duration was 30 min, 15 min per phase, in order to achieve complete saturation and, then, the total regeneration of the catalysts with these concentrations of feeding. In Figure 5.3, the profiles of the product distribution at 350°C are represented for a cycle in which the catalysts are working in stable way, in helium and water + CO_2 atmospheres.

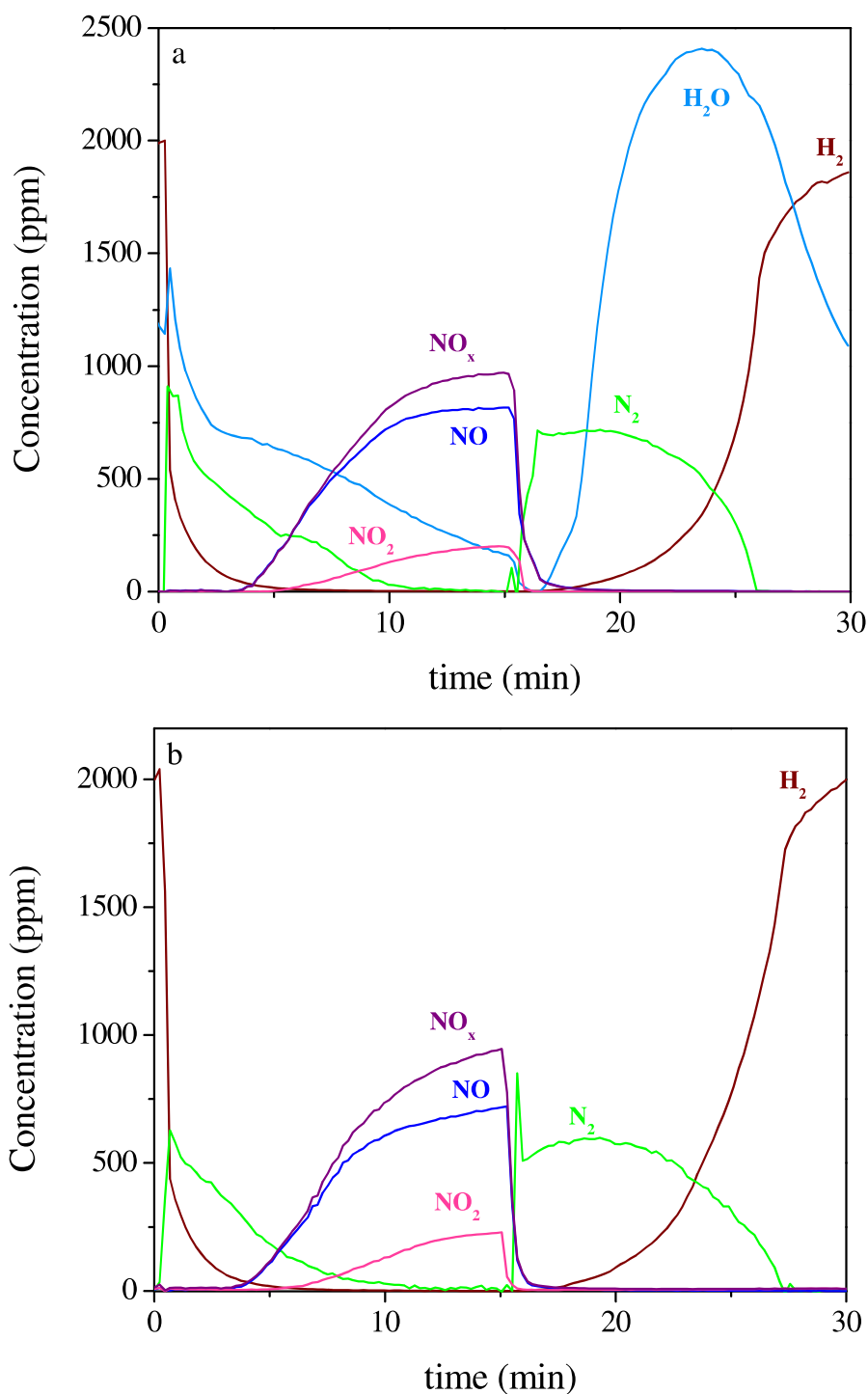


Figure 5.3. Storage–reduction stationary cycle (15-15 min) for Pt-Ba-K/Al₂O₃ + 2Cu-SAPO-150-30 at 350°C in (a) He and (b) H₂O+CO₂.

As can be observed in Figure 5.3, the shape of the product distribution throughout the cycles is similar to the TRM-experiments with the single Pt-Ba-K/Al₂O₃ catalyst (Fig. 3.30 and 3.32). In the lean phase, the typical NO_x saturation curve was appreciated, as consequence of the storage of nitrites/nitrates, and the reaction with the adsorbed

ammonia producing nitrogen and water as is shown. In the rich phase, the profile of hydrogen is representative of the consumption by the reduction of the NO_x adsorbed on the catalyst surface up to the entire regeneration of the catalyst with the corresponding nitrogen and water formation. However, in this phase, ammonia presence was undetectable, in all the conditions that have been studied, due to the storage of the produced amount in the SCR catalyst placed downstream. Moreover, the formation of N_2O that was observed in dry conditions at low temperatures is almost insignificant, due to the capacity of the zeolite for the N_2O decomposition, as was explained in Chapter 4. In addition, in the presence of water and CO_2 , a consumption of the latter was detected with CO formation (data not shown) due to the reverse reaction of Water Gas Shift as other authors have reported [178]. The obtained profiles both in Helium and $\text{H}_2\text{O} + \text{CO}_2$ presence are similar to those observed by other authors [180] when the Pt-Ba model catalyst and Fe-ZSM5 are coupled, in terms of nitrogen and water production and the shape of the NO_x and H_2 saturation curves.

From the mathematical treatment of the product distribution, a series of representative parameters can be calculated and compared with those obtained for the single NSR catalytic bed. In Table 5.3, the most characteristic are shown.

Table 5.3. Reactivity data calculated during the storage-reduction of NO_x experiments from isothermal TRM profiles at 200 and 350°C for Pt-Ba-K/ Al_2O_3 and Pt-Ba-K/ $\text{Al}_2\text{O}_3+2\text{Cu-SAPO-150-30}$ systems.

Temperature (°C)	Atmosphere	System	Removed NO_x ($\cdot 10^3 \text{mol NO}_x \text{ g}_{\text{NSR}}^{-1}$)	X_{NO_x} (%)	S_{N_2} (%)	S_{NH_3} (%)	$S_{\text{N}_2\text{O}}$ (%)
200	He	NSR	0.39	91	94.1	5.2	0.7
		NSR-SCR	0.51	99	99.9	0	0.1
	$\text{H}_2\text{O}+\text{CO}_2$	NSR	0.24	83	90.5	9.5	0
		NSR-SCR	0.35	84	100	0	0
350	He	NSR	0.42	88	97	3	0
		NSR-SCR	0.53	91	100	0	0
	$\text{H}_2\text{O}+\text{CO}_2$	NSR	0.41	86	100	0	0
		NSR-SCR	0.52	92	100	0	0

Similar trends were observed for both systems; however the difference between the analyzed parameters should be pointed out. For this type of experiments, the parameter stored NO_x has been modified to removed NO_x , since the nitrogen oxides are not only adsorbed on the surface but also react with the ammonia stored in the zeolite. For all the experiments, as was to be expected, the amount of NO_x removed increased with the incorporation of an SCR bed downstream, with increased values similar to those

previously reported [177,180,181]. Nevertheless, the effect depended on the temperature and the reaction atmosphere. At low temperatures, the impact was more noticeable, because of the higher ammonia production that can be used in the SCR process and the initially more unfavourable conditions. The higher the amount of ammonia adsorbed the more efficient the configuration, since the SCR catalyst begins to work when a considerable amount of ammonia is stored in the catalyst, as has been explained in the previous Chapter. The conversion values also increased as shown by *U. De La Torre et al.* [50] who observed an increment higher than 30% in the presence of copper zeolites. Here, the initial values are high, almost 90%, and the effect was less remarkable, with increments below 10%.

In H_2O+CO_2 at 200°C, there is a balanced effect that makes the behaviour different. On the one hand, the Pt-Ba-K/ Al_2O_3 catalyst in presence of water and CO_2 reduced the NO_x adsorption capacity and conversion, as was explained in Chapter 3 and in consonance with other authors [120,239], due to the interaction of the carbonates that compete with the nitrates for the same active sites, the difficulty in the NO_2 release in presence of water and the negative impact in the regeneration step when water and CO_2 are fed, because of the poisoning of the Pt sites by CO formation by the reverse reaction of water gas shift. On the other hand, the presence of water and CO_2 in the SCR process over the 2Cu-SAPO-150-30 zeolite improves the performance in terms of conversion and selectivity values, since it inhibits the ammonia oxidation and the nitrate decomposition and modifies the copper environment, obtaining more active species, as has been detailed in Chapter 4. Therefore, in spite of the improvement provided by the SCR catalyst in these conditions, the negative effect of the reaction atmosphere over the NSR catalyst is stronger and, in consequence, the conversion value is not considerably increased as observed by other authors [183], who detected a decrease in conversion of around 23% at 250°C and 9% at 300°C with the incorporation of 1% of water.

At high temperatures, for the single NSR catalyst, the parameters were high, with conversion and N_2 selectivity values of around 90% and higher than 95%, respectively, and the influence of placing a SCR catalyst downstream is less noteworthy. Nevertheless, conversion and the removed NO_x increased due to the reduction with the adsorbed ammonia. An increase in the conversion value, which is defined as the converted of those stored, can also be obtained because in the reduction phase the

hydrogen can react with an initial ammonia formation, as has been explained before, and this ammonia could interact with the unconverted NO_x forming nitrogen and water by selective catalytic reduction. *L. Castoldi et al.* [177] have observed the same effects caused by the presence of water and CO_2 for the coupling of Pt-Ba/ Al_2O_3 and Fe-ZSM5, with an increase in the selectivity and conversion with a rise in temperature or compared to the single NSR catalyst.

As far as selectivity is concerned, almost complete nitrogen selectivity was observed in the whole temperature range regardless of the reaction atmosphere. Thus, the double bed configuration, working up to saturation and total regeneration of the catalysts, allows the adsorption of the ammonia that is produced in the NSR catalyst and the reaction with the nitrogen oxides of the following cycle. In addition, the reduction of the low amount of N_2O , only formed at low temperatures in dry conditions, was performed by the zeolite that, as has been explained, is able to decompose the N_2O producing nitrogen.

Therefore, the coupling of the technologies in a double catalytic bed produces the reduction of the pollutant production levels to zero emissions in *quasi-real* conditions, i.e. in the presence of water and CO_2 , working up to saturation and complete regeneration.

5.2. Efficiency in dual system configuration even varying the operation parameters

The experiments up to the saturation of the samples are used to understand the behaviour of the catalysts, which have had the time required to adsorb the highest amount of NO_x and have completely regenerated their surface using almost the stoichiometric amount of reducing agent. Nevertheless, the real conditions of engine operation are far from being so. Indeed, several authors [189,290,291] have reported the importance of the control and simulation of the operation parameters. Thus, additional studies were carried out in order to analyze the influence of the operation parameters in the catalytic activity of the NSR-SCR system. For this purpose and with the intention of comparing the results with other authors, the dimensionless parameter θ has been defined as the ratio between the oxidation and reduction times and different values have been used, while the space velocity, the weight ratio between catalytic beds and the feed composition were maintained, since the optimization of lean and rich periods in order to ensure stable lean–rich cycles is essential for the engine operation [290]. In addition, the

concentration of the reducing agent was also modified. All the operation parameters are summarized in Table 5.4.

Table 5.4. Flow conditions used in the TRM experiments over NSR-SCR systems.

	Lean phase	Rich phase
NO (ppm)	1000	-
O ₂ (%)	3	-
H ₂ (%)	-	0.2, 1, 2.5
H ₂ O (%)	1.5	1.5
CO ₂ (%)	0.3	0.3
He	Balance	Balance
GHSV (h ⁻¹)	3·10 ⁴	3·10 ⁴
Temperature(°C)	200, 350	200, 350 s
θ = 1	20, 60 s	20, 60 s
θ = 3	60 s	20 s
θ = 7.5	150 s	20 s

Therefore, temperature, hydrogen concentration and θ values were modified and cycles were performed until the behaviour of the catalyst was stabilized. The most representative results of the factorial design that was carried out in order to analyze all the variables are presented in this Chapter. In Figures 5.4 and 5.5, the profiles throughout the cycles for the experiments over the hybrid system when the parameter θ is set at 7.5 at 200 and 350°C, respectively, are shown.

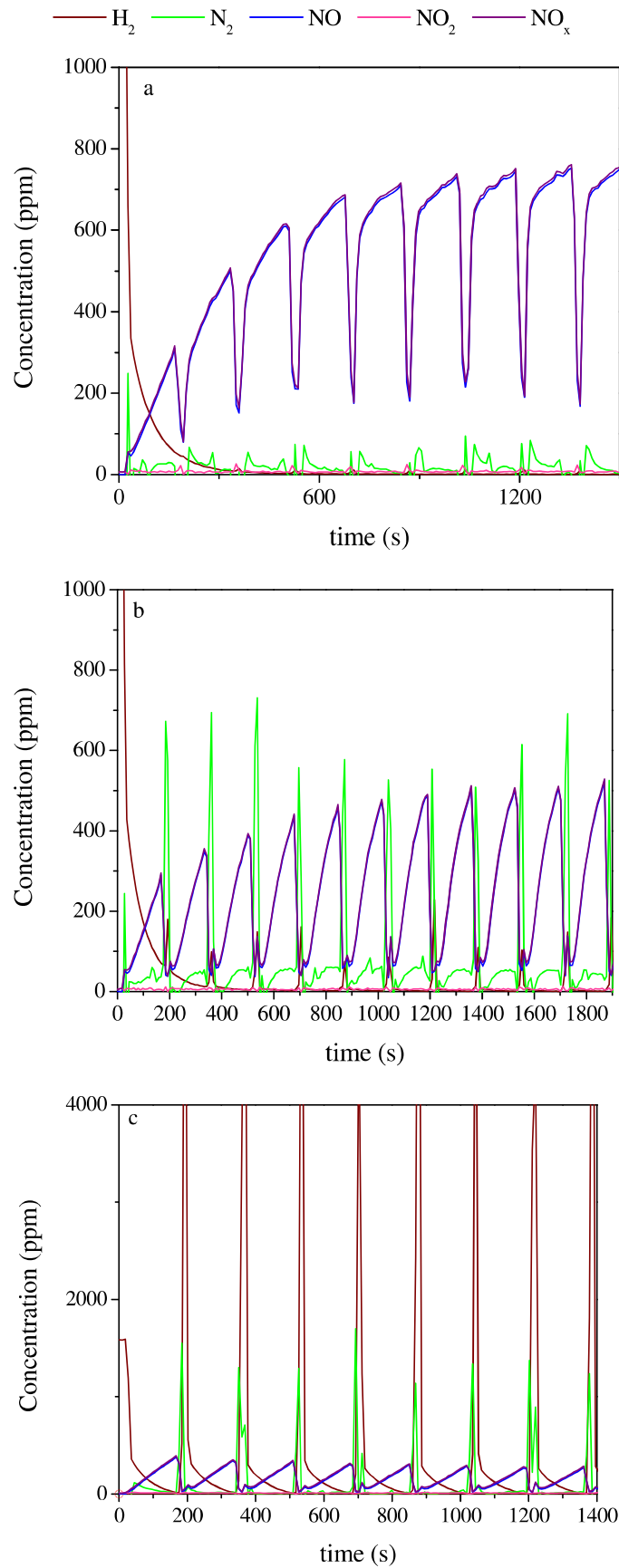


Figure 5.4. Storage-reduction cycles for Pt-Ba-K/Al₂O₃ + 2Cu-SAPO-150-30 at 200°C with lean-rich periods of 150-20 s ($\theta = 7.5$) with a hydrogen concentration of a) 0.2% b) 1% and c) 2.5% in H₂O+CO₂.

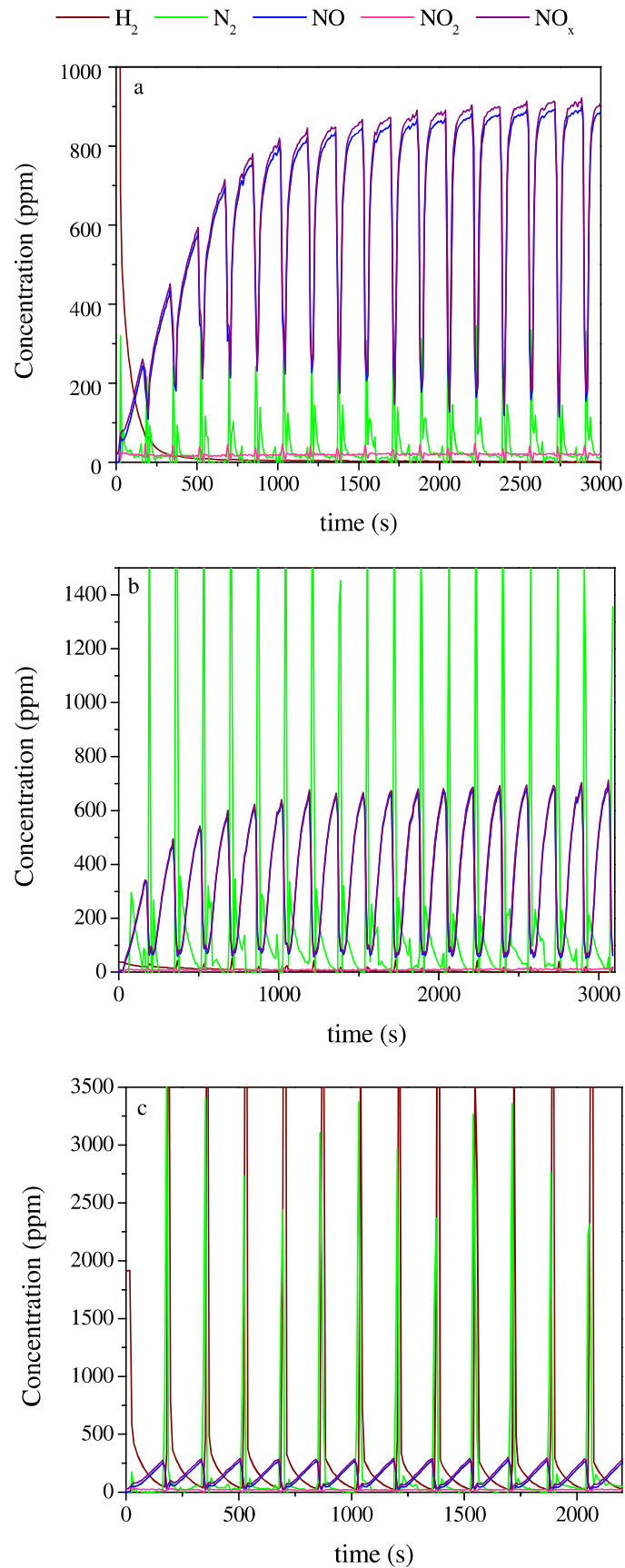


Figure 5.5. Storage-reduction cycles for Pt-Ba-K/Al₂O₃ + 2Cu-SAPO-150-30 at 350°C with lean-rich periods of 150-20 s ($\theta = 7.5$) with a hydrogen concentration of a) 0.2% b) 1% and c) 2.5% in H₂O+CO₂.

As can be observed in these two Figures, the behaviour in the storage and reduction of NO_x is completely dependent on the temperature and the reductant concentration. At hydrogen contents close to the stoichiometric value (2000ppm), the NO_x amount at the outlet increases throughout the cycles up to stabilization, indicating that the amount of the reducing agent is not enough for the complete regeneration of the catalyst. This effect is similar to that observed in the TRM experiments carried out in the thermobalance where the baseline increased due to the incomplete regeneration of the catalyst in the presence of the alkaline in the formulation (Fig. 3.7) [170]. Hydrogen was not detected during the cycles, due to the total consumption in the reaction with the adsorbed nitrates. At hydrogen content of 1%, the amount of NO_x detected was lower than in the previous experiments, although also increased with time, and hydrogen was not observed during the experiment, meaning that this concentration is not enough for the whole regeneration of the surface when the time of the oxidant phase is 7.5 times the reduction period. However, the saturation process of the catalyst is slower as the reductant content increases. For a reducing agent concentration of 2.5%, the product distribution was completely different; the profile of NO_x was identical for all the cycles, signifying that the nitrates adsorbed onto the catalyst are fully removed by their reaction with the hydrogen in each cycle. In addition, H_2 was detected during the rich step, since an excess of the reductant was being fed into the reactor in these conditions. In addition, as other authors have observed [178], if an overestimated amount of hydrogen is used, the production of ammonia would be too high and the SCR activity would decrease.

In terms of the product distribution and the selectivity of the process, nitrogen was the only compound observed at the outlet, neither ammonia nor N_2O were detected. However, the nitrogen production was higher as the hydrogen content increased, in consonance with the regeneration process above explained. Therefore, the combination of Pt-Ba-K/ Al_2O_3 and 2Cu-SAPO-150-30 is effective in the studied temperature range in order to obtain nitrogen selectivity values around 100% in presence of water and CO_2 , notwithstanding the above θ and hydrogen concentration values.

As has been reported [292], the hydrogen content has a noticeable effect on the ammonia production; the undesired nitrogen compound production increases as does the concentration of reducing agent.

The influence of the reaction temperature was less noticeable than the hydrogen concentration, since similar trends were observed when the same reductant content was used. Nevertheless, the amounts of nitrogen produced as well as the NO_x at the outlet were slightly different depending on the temperature. Higher values of the activity parameters were obtained in the experiments at high temperatures, as occurs in the single NSR catalytic bed; however, the improvement of the coupling of both technologies in the hybrid system was more remarkable at low temperatures, since the initial conditions were less favourable.

The influence of hydrogen concentration on the catalytic behaviour of the NSR and NSR-SCR configuration is noticeable. The determination of the optimum NSR operation conditions is an open point that should be treated and controlled, since the production of ammonia and the efficiency of the hybrid system depend on the parameters. High amounts of hydrogen lead to the complete regeneration of the catalyst surface and increase the ammonia production and the NO conversion to nitrogen; however, overestimated concentrations were not recommendable. In addition, the operation temperature was another parameter to control, since the amount of nitrogen oxides that can be stored on the surface depends on the temperature, as well as the product distribution. As has been reported [292], the improvement of the activity values at low temperatures is more noteworthy than at higher temperatures.

The reduction of the θ value down to 3 modifies the behaviour of the hybrid system depending on the hydrogen content as can be observed in Figures 5.6 and 5.7, for the experiments carried out at 200 and 350°C, respectively, and the effect is detailed below.

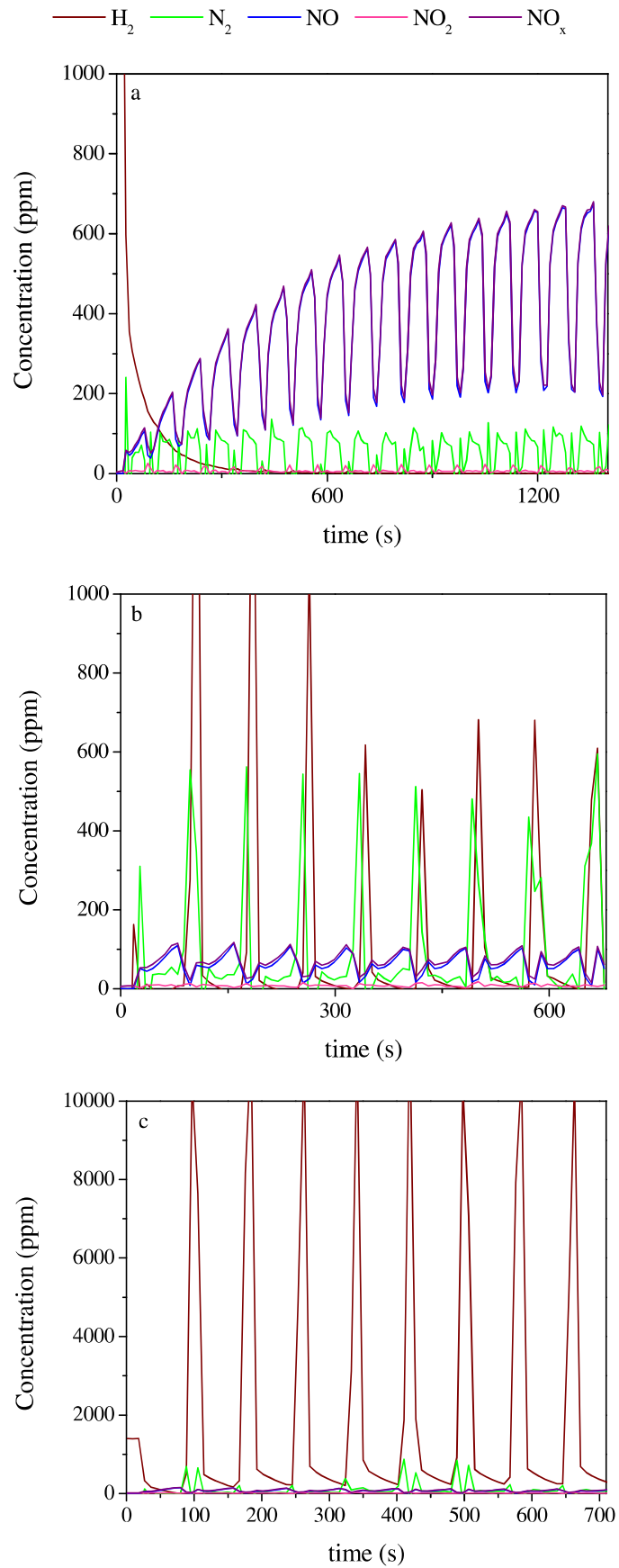


Figure 5.6. Storage-reduction cycles for Pt-Ba-K/Al₂O₃ + 2Cu-SAPO-150-30 at 200°C with lean-rich periods of 60-20 s ($\theta = 3$) with a hydrogen concentration of a) 0.2% b) 1% and c) 2.5% in H₂O+CO₂.

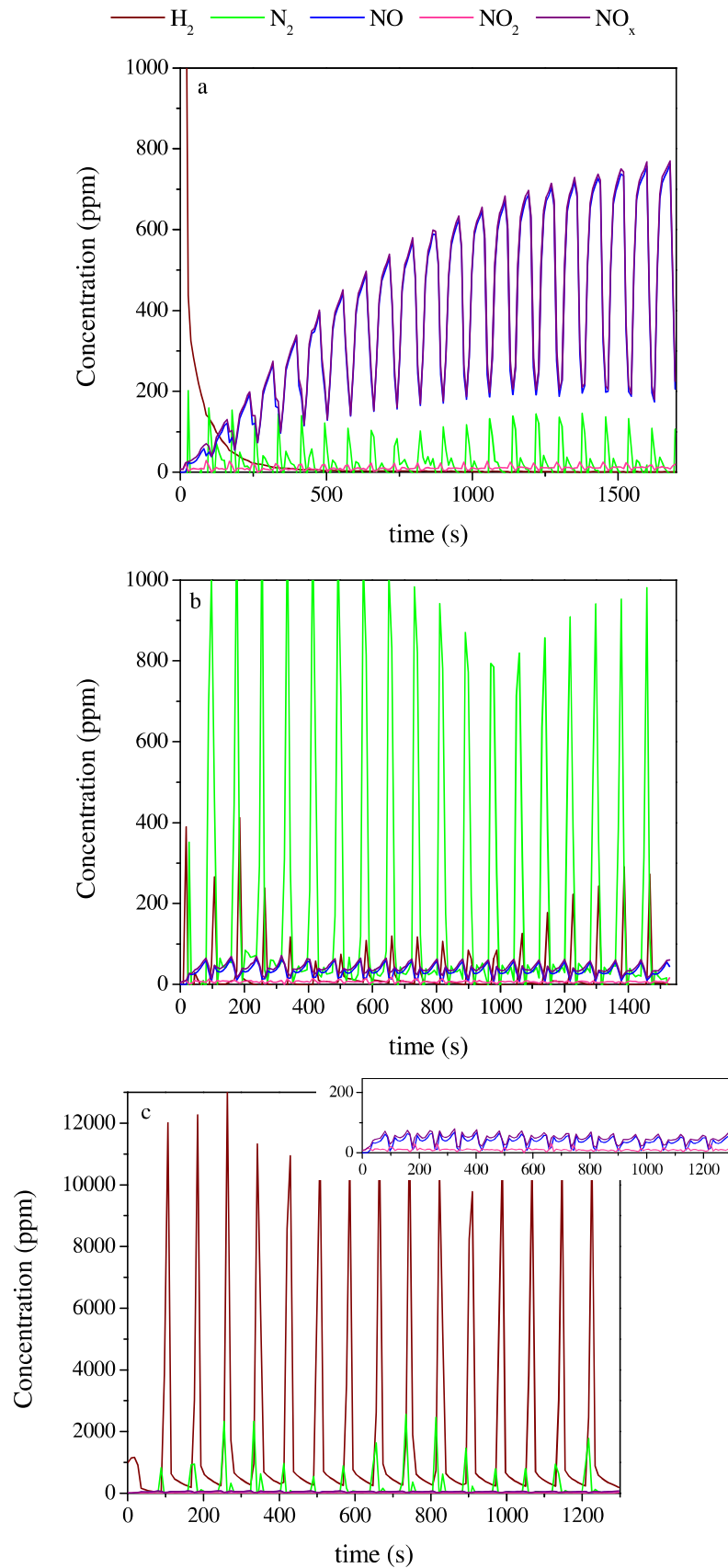


Figure 5.7. Storage-reduction cycles for Pt-Ba-K/Al₂O₃ + 2Cu-SAPO-150-30 at 350°C with lean-rich periods of 60-20 s ($\theta = 3$) with a hydrogen concentration of a) 0.2% b) 1% and c) 2.5% in H₂O+CO₂.

For the experiments with 0.2% of hydrogen, periods of three times the oxidant phase for each reducing step were not enough for the regeneration of the catalyst, and the NO_x concentration at the outlet increased throughout the cycles. The reduction of θ by half allows for the regeneration of the catalyst with less amount of hydrogen, i.e. 1% of H_2 is enough for the complete reaction with the adsorbed nitrates. The conversion values obtained in these conditions makes total regeneration possible working with reducing agent content around five times the stoichiometric value, in consonance with other authors [188]. The concentration value of hydrogen around 2.5% was overestimated for the regeneration of the catalyst and a minimum amount of NO_x was detected (as can be observed in the inset). Zero emissions of nitrogen pollutant compounds were appreciated in these conditions; however the amount of hydrogen at the outlet was high and this would imply the use of an unnecessary excess of reductant. Regarding the product distribution, nitrogen was the only product detected during the experiments, such as was observed for higher values of θ . Nevertheless, the amount of nitrogen for lower θ values was higher since the time of reduction was the same whereas the time of oxidation was lower.

The same effect regarding the temperature as working with higher θ values was observed. At low temperatures the improvement with respect to the single bed was more noticeable, although the nitrogen produced and, as consequence, the adsorbed/reduced nitrates were higher at high temperatures.

By mathematical treatment of the profiles, the activity parameters were calculated, and are represented in Table 5.5 for two values of θ , three different hydrogen contents and two values of temperature.

Table 5.5. TRM parameter values for the experiments with lean/rich time ratio variation as a function of the hydrogen percentage and the temperature.

H_2 (ppm)	T (°C)	60-20 ($\theta = 3$)		150-20 ($\theta = 7.5$)	
		$\text{mmolNO}_x \cdot \text{gNSR}^{-1}$	X_{NO_x} (%)	$\text{mmolNO}_x \cdot \text{gNSR}^{-1}$	X_{NO_x} (%)
2000	200	0.44	78.6	0.61	76.3
	350	0.46	82.5	0.62	81.3
10000	200	0.69	97.3	1.2	94.3
	350	0.71	99.3	1.3	95.6
25000	200	0.69	97.7	1.6	97.7
	350	0.71	99.4	1.6	97.9

The activity parameters were calculated in the tenth cycle and confirmed the effects observed in the profiles. In the whole operation range, the amount of nitrogen oxides removed and the conversion and nitrogen selectivity values were higher than in the experiments with the single Pt-Ba-K/Al₂O₃ catalyst. The amount of removed NO_x decreased as did the hydrogen concentration, as a consequence of the incomplete regeneration of the catalyst above explained. The increase in the oxidation phase time caused an increment of almost double the amount of removed NO_x, indicating a constant removal rate. At high temperatures, the effect of the reductant content is irrelevant provided that it is higher than the stoichiometric concentration, since the conversion values are above 90% and the nitrogen selectivity is high. This means that such high amounts of hydrogen are not necessary and the reducing agent consumption can be reduced with the corresponding economic benefit. Nevertheless, although all the conditions are highly effective, hydrogen content around the stoichiometric seems not to be suitable for the removal of NO_x in cyclic periods when the time of oxidation is higher to the reduction time. In addition, hydrogen levels below 0.8 % were not recommendable [176] to work with θ value around 7 due to the fact that the reductant supply would be in defect and, as consequence, the catalyst could not be completely regenerated, decreasing the NO_x removal efficiency. The θ decrease allows the regeneration of the catalyst, high NO_x removal and remarkable conversion values with less amount of hydrogen in the whole operation range. *M. Al-Harbi et al.* [189] have also reported that the longer times for the regeneration period allow the cleaning of the surface and the properly use in the following cycle.

Several authors [185,186] have proposed the modification of the catalyst formulation in order to incorporate elements with higher ammonia production capacity, such as ceria. The role of the ceria is the promotion of the ammonia formation due to the fact that higher ammonia contents produce an increase in the SCR activity of the catalysts. The home-made NSR-catalysts that are presented in this PhD Thesis, do not produce high amounts of ammonia and modifications of the structure or the elements in order to increase the ammonia production were not considered, since high selectivity values were detected in these conditions in the whole range.

The simultaneous influence of θ and the reducing agent content has been studied and some conclusions have been arrived at. The reduction in θ implies the decrease in the necessary content of the reducing agent for the regeneration of the catalyst and the obtaining of high conversion values preventing catalyst saturation. If the ratio between oxidant and reduction times is above 1, the amount of hydrogen used in the regeneration phase has to be higher than the stoichiometric value. Nevertheless, as has been observed in all the experiments up to saturation with the same time for both phases, the regeneration of the catalysts was complete. So, it is worth considering the influence of the period time when the value of θ is set to 1. For that, experiments with the same time period for both steps were carried out without modifying the θ value, and the profiles of the product distribution for the experiments with 60-60 s and 20-20s using 0.2 and 1% of hydrogen are represented in Figure 5.8. Data for higher amounts of hydrogen are not shown since its content is overestimated.

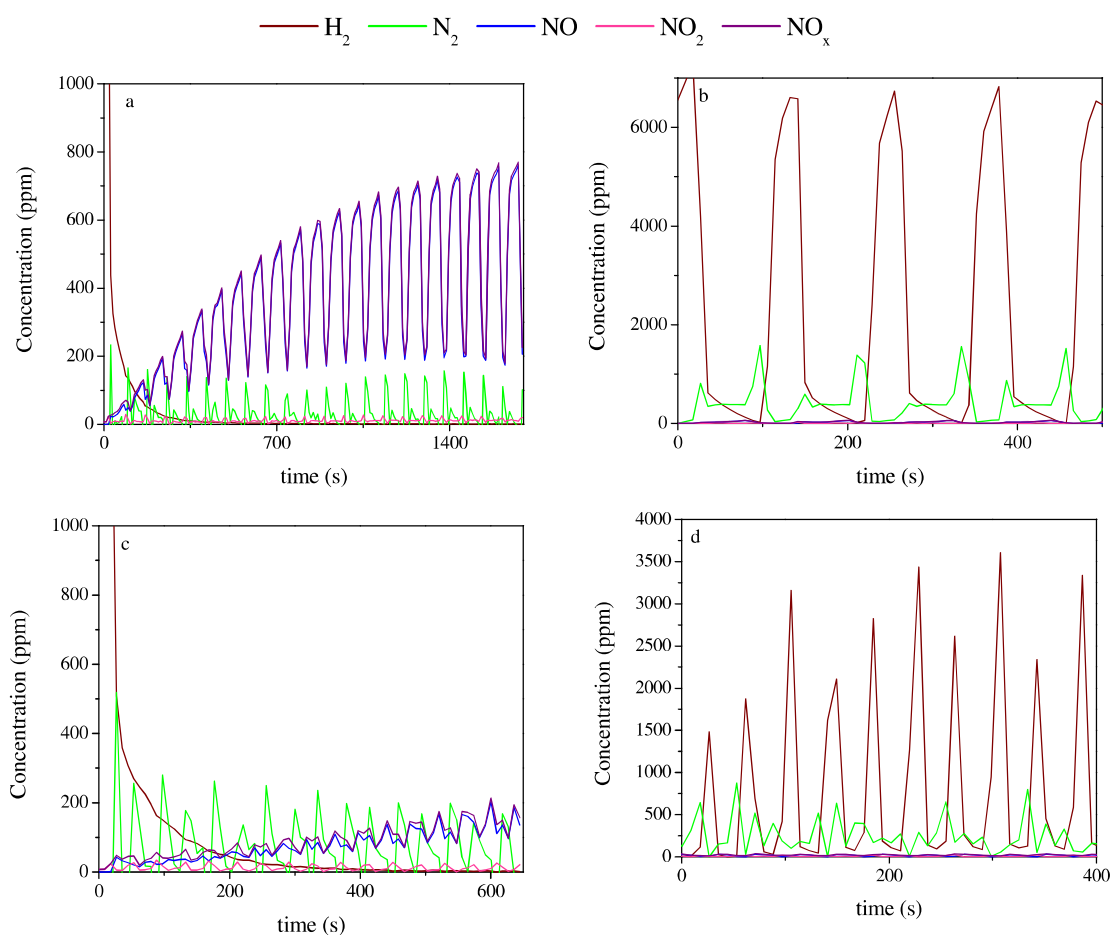


Figure 5.8. Storage-reduction cycles for Pt-Ba-K/Al₂O₃ + 2Cu-SAPO-150-30 at 350°C with lean-rich periods of 60-60 s ($\theta = 1$) with a hydrogen concentration of a) 0.2% and b) 1% and 20-20 s ($\theta = 1$) with H₂% of c) 0.2% and d) 1% in H₂O+CO₂.

As can be observed in Figure 5.8b and d, hydrogen concentrations above the stoichiometric, 1% in this case, are higher than the exact content for the reduction of the nitrates and would involve an unnecessary cost; however the total removal of the nitrogen oxides and the complete selectivity to nitrogen can be ensured. On the other hand, the use of the stoichiometric value behaved differently depending on the time of each period. In these conditions, the catalyst was being saturated slowly, although the saturation time is modified by the period time. The saturation of the catalyst is reached before when longer times are used; as can be observed in Figure 5.8, in the experiment with 60s for each step, the catalyst is saturated faster than using 20s for each phase. This is due to the fact that the regeneration rate is different from the adsorption rate. The removed amount percentage and the rate are identical in each cycle, because they depend on the temperature. The changes detected were similar to the kinetic and geometric effects observed in the TG experiments when the catalyst was not completely regenerated and, consequently, 2000ppm of hydrogen is the exact stoichiometric value and the total reduction of the adsorbed species requires much longer period times.

Therefore, stoichiometric hydrogen levels in over accumulation conditions cause the incomplete regeneration of a part of the catalyst and the saturation of the surface throughout the cycles. The operation conditions should ensure the availability of the catalyst for the following cycle. So, hydrogen concentrations above 1.1 times the stoichiometric value are needed in order to obtain zero emissions and the regeneration of the catalyst when the θ value is around 1. Nevertheless, the real operational conditions use oxidation period times longer than the reduction time; experiments up to saturation are only useful for the chemical study of the process.

The Cu-SAPO-34 material that has been synthesized with the copper inside the structure placed downstream of the Pt-Ba-K/Al₂O₃ catalyst completely reduces the ammonia emissions. High performances were observed for the single NSR catalytic bed, however, even under severe conditions, the combination is able to work efficiently with zero emissions. For the standard SCR low temperature (around 200°C), the improvement and activity parameters were maintained in contrast to other authors.

In a double catalytic bed configuration, zero emissions are obtained provided that the operational conditions, θ and hydrogen percent, are optimized. The significance or recommendations of the operation parameters in the use of the Pt-Ba-K/Al₂O₃-2Cu-

SAPO-150-30 hybrid system are: the use of a volume ratio 1:1 between the NSR and SCR catalytic beds, θ values lower than 3 and less than 1% but greater than 0.2% of hydrogen content as reducing agent. In these conditions, conversion values around 98% and total selectivity to nitrogen are ensured working in real conditions.

5.3. Synthesis and characterization of monoliths

Until now, the synthesized materials have been studied in powder form. Nevertheless, the scaling up to monolithic form has also been performed in order to understand catalytic behaviour and the problems of synthesis in a different conformation. Cordierite monoliths provided by Johnson Matthey were used as support, with 4 inches length and 1 inch diameter. The more relevant characteristics of the materials are detailed in Table 5.6.

Table 5.6. Characteristics of the monolith.

Dimensions	1x4"
Weight	25 g
Volume	50 cm ³
BET Surface Area	20 m ² ·g ⁻¹
Al ₂ O ₃ coverage	0.09 g·cm ³

These supports with surface area values of around 20 m²·g⁻¹ contained an alumina monolayer coverage with 1.5 g·in⁻³ washcoat thickness, equivalent to the 20wt% of the monolith. These monoliths were characterized by different techniques in order to better explore the structure, the surface and the coating quality.

SEM images of the channels were taken at different magnifications of the axial and cross sections. In addition, EDX analysis was performed over different points to verify the dispersion of the alumina. In Figure 5.9, some of the images together with the composition of several surface positions are represented.

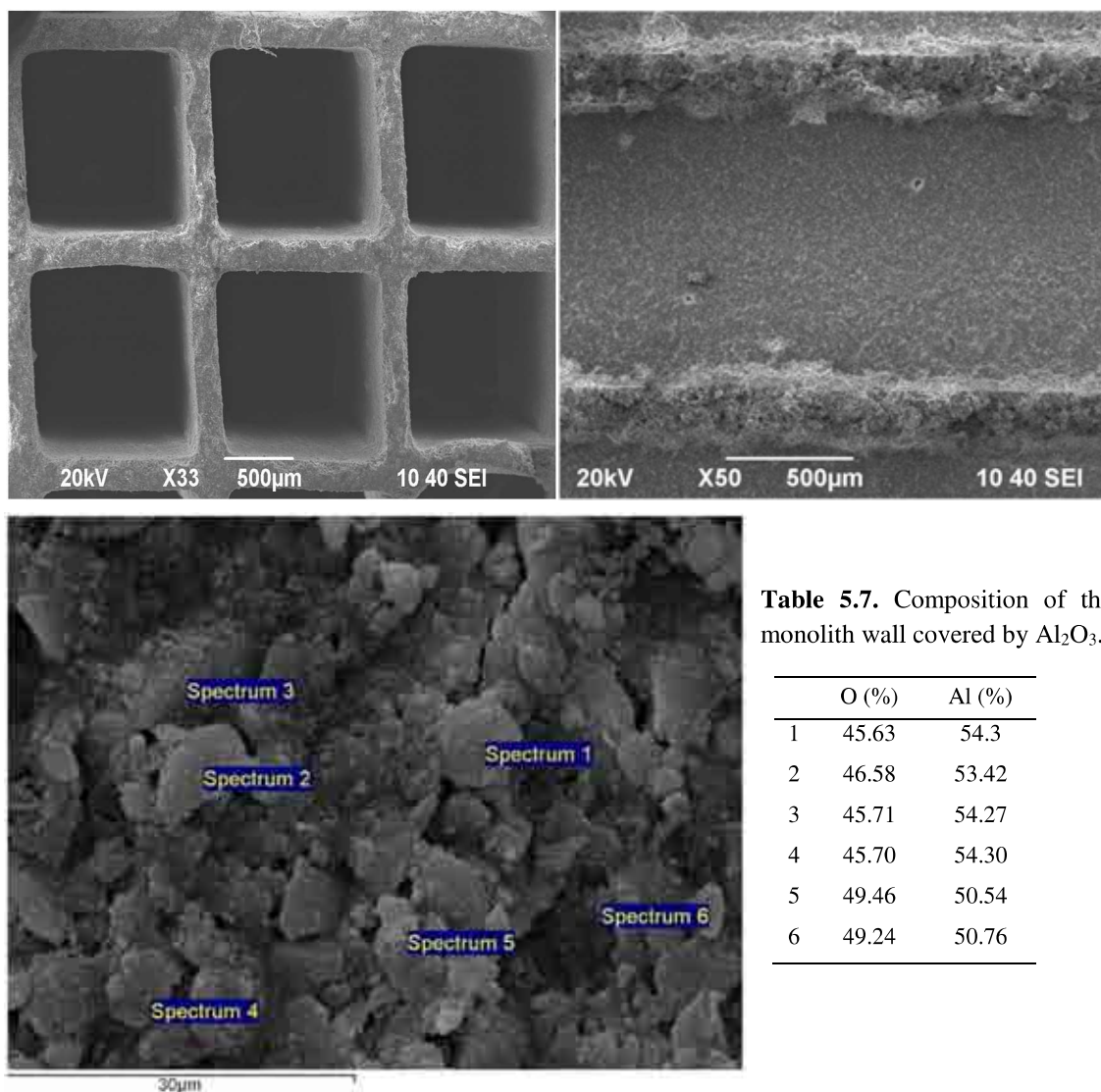


Figure 5.9. SEM images of the cross and axial sections of the cordierite monolith with Al₂O₃ coverage and the composition analyzed by EDX (inset Table 5.7).

Channels of 1 mm width were observed with a homogeneous surface. Along the wall of the channels, the surface seemed to be uniform and the analysis of the composition in different points provided similar results with the only presence of oxygen and aluminum, pointing out the well dispersion of the alumina washcoating. The synthesis procedure and the precursors used in the impregnation of the monoliths strongly influence the catalytic activity [129,174]. For the cordierite monoliths provided by Johnson Matthey, the alumina washcoating of around 20 wt% of the monolith weight completely covers the support and is well attached allowing the incorporation of active metals.

Therefore, the cordierite ($2\text{MgO}\cdot\text{Al}_2\text{O}_3\cdot 5\text{SiO}_2$) supports were modified in order to incorporate the active metals of NSR and SCR technologies. For Pt-Ba-K/ Al_2O_3 -M, the synthesis procedure was similar to the powder preparation, maintaining the times and rates of calcination and they were prepared according to the atomic density in the same way as the powder catalysts. So that, the exact amount of platinum precursor was calculated in order to obtain $0.4\text{ at}\cdot\text{nm}^{-2}$ of support, and the same process was performed to calculate the barium and potassium precursor content in order to reach 3.5 and $1.5\text{ at}\cdot\text{nm}^{-2}$, respectively. Theoretically, these values would be close to the monolayer coverage of the support. The precursor solutions were prepared and kept for 48 hours in order to ensure the stability of the aqueous solutions. The procedure of synthesis was almost identical to the powder preparation as stated above. The monolith was impregnated with the platinum solution dropwise, as can be observed in Figure 5.10. Then, it was placed in a rotation system for 24 hours and dried overnight at 90°C . After this, an intermediate calcination at 350°C was carried out for 3 hours in order to attach the noble metal to the structure and it was blown out with compressed air before and after the calcination to remove any excess liquid or particles. Next, the impregnation of the Ba-K stabilized solution was carried out in the same way and the final calcination was performed at 500°C for 5 hours and $5^\circ\text{C}\cdot\text{min}^{-1}$, as was used in the powder synthesis.

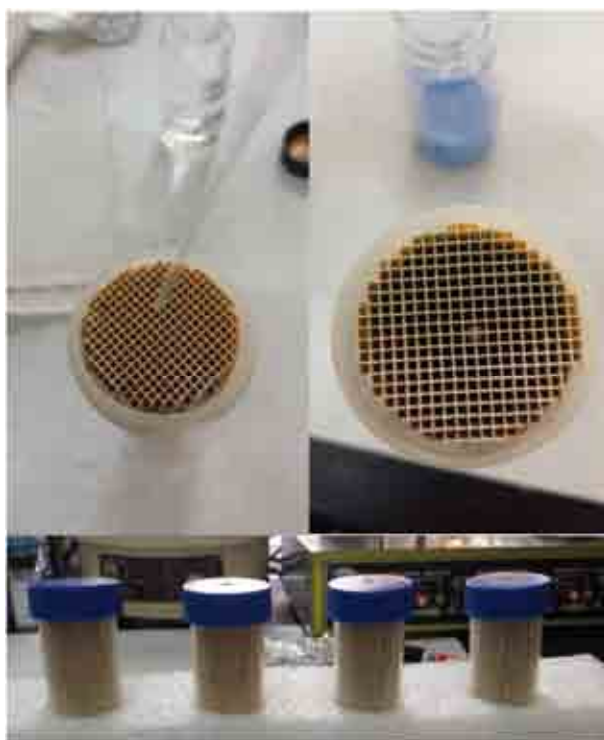


Figure 5.10. Synthesis of the NSR and SCR catalysts in the monolithic form.

From the atomic density of the active metals, the amount of active phase over the monolith can be obtained and corresponds to a 2wt% of the total weight of the support. This value allows the almost complete alumina coverage and high catalytic activity in the simultaneous NO_x and soot removal at least in powder form. As has been explained in the previous sections and coinciding with other authors, the optimal ratio between NSR and SCR catalyst volume was 1:1. Taking all this into account, a procedure in order to obtain 2wt% of zeolite spread over the monolith structure was developed. The calculation was optimized with the intention of obtaining the zeolite crystallized over the monolith keeping the structure and the properties of Cu-SAPO-34 in powder form. As *B. Pereda-Ayo et al.* have reported [293], the washcoating with the powder zeolite previously exchanged with the metal provides better results, in terms of NO_x conversion and N₂ selectivity, than the incorporation of the metal over the bare zeolite in the monolithic form. Therefore, for the synthesis, firstly, the initial gel was prepared as in the powder form, with the following composition 2 DEA: 0.6 SiO₂: 1 Al₂O₃: 0.8 P₂O₅: 50 H₂O, incorporating 2wt% of copper, using the same precursors and mixture times. Then, the gel was sonicated in pulses of 30 seconds up to 3 minutes and was introduced in the autoclave at 150°C for 30 hours; the product was then washed several times and filtered. A series of solutions were prepared varying the gel/water ratio. The amount of water was set by the total pore volume of the monolith and, as the gel also contained water that had to be removed in the calcination, the amount of gel in the solution was varied around the theoretical value in order to obtain the exact monolayer coverage and the 2wt% of weight gained after calcination. These solutions were also stabilized for 48 hours, impregnated over the monolith surface and placed in the rotation system for 24 hours. Finally, the monoliths were dried overnight at 110°C and calcined at 550°C (1.8°C·min⁻¹) in air for 5h. Other authors [185–188] have proposed the synthesis of a dual-layer monolith by washcoating of the substrate; however, the preparation of monoliths with both catalysts in different layers was discarded.

The impregnation and calcination were carried out over the full size monoliths, i.e. 1x4 inches diameter and length, after the synthesis they were cut in 1x1" cylinders. The light path modification, the morphological properties, the incorporation of the metals on the surface and the homogeneous distribution were analyzed by different techniques, such as XRD, SEM or XPS.

The SEM image of the cross section of Pt-Ba-K/Al₂O₃-M is shown in Figure 5.11. As can be observed, and compared to the cordierite monolith images shown in Figure 5.9, the incorporation of these metals into the support did not cause the blockage of the channels and the light path was not modified. The analysis of several points by EDX provided the composition of the material. Thus, the elements of the cordierite were identified on the outer walls, whereas alumina, Pt, Ba and K were detected on the interior walls of the channel, although in slightly lower concentrations than was expected.

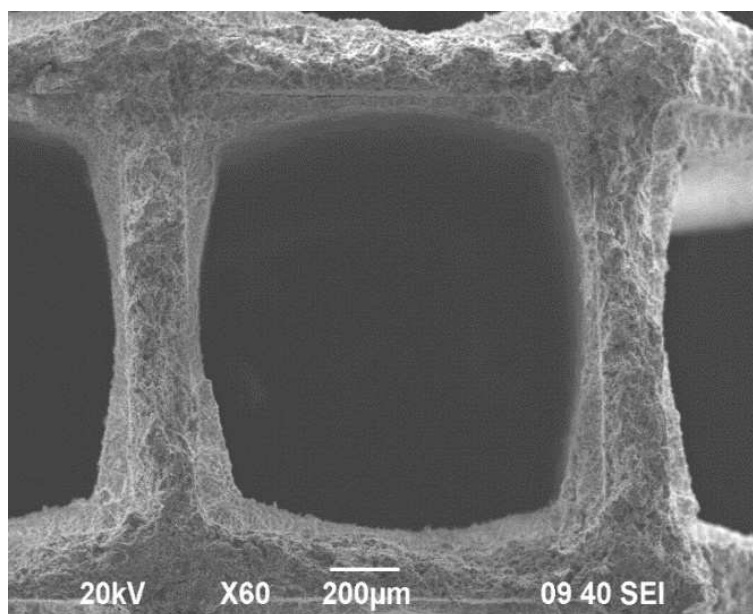


Figure 5.11. SEM images of the cross section of the Pt-Ba-K/Al₂O₃-M monolith.

For the purposes of analyzing the metal dispersion along the channels, EDX mappings of the metals present in the formulation were carried out in different channels and areas of the monolith. In Figure 5.12, one of the studied areas and its dispersion of platinum, barium and potassium are represented.

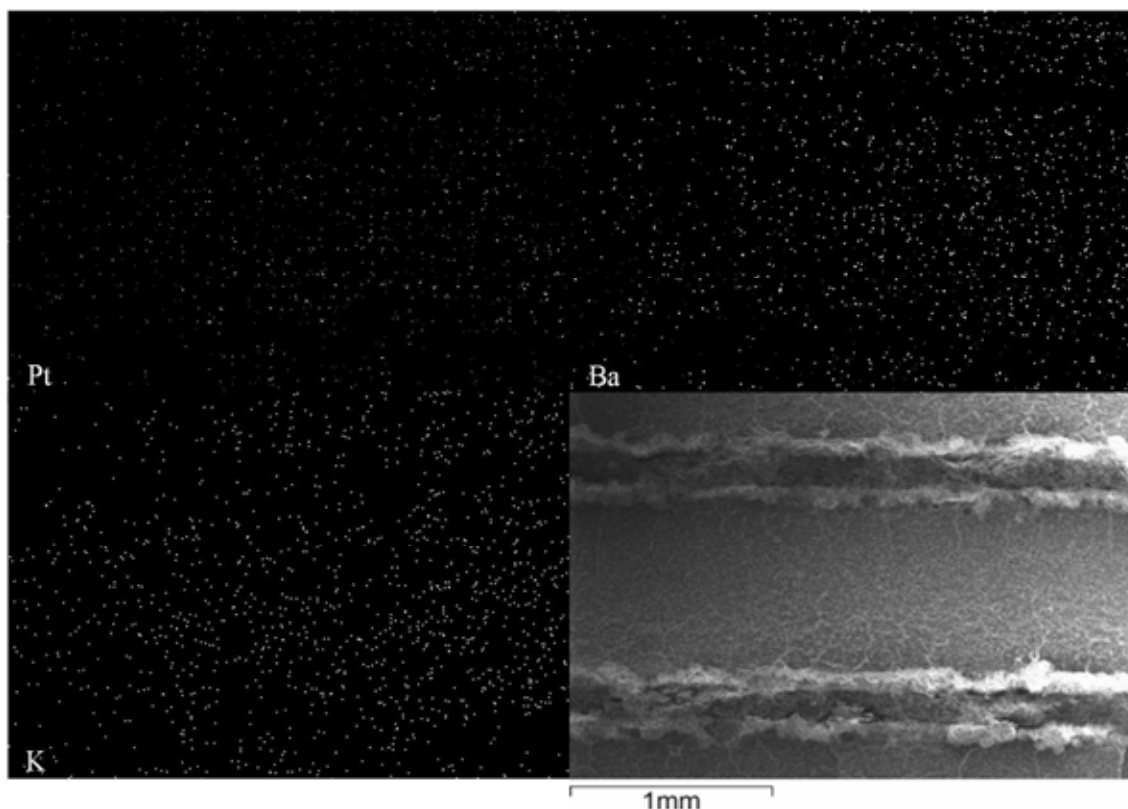


Figure 5.12. EDX mapping of SEM images of Pt-Ba-K/Al₂O₃-M sample.

Every element is presented as white dots and the scale in all cases is the same as the SEM image used as a reference. Well dispersed micropoints were observed along the channels except for the area corresponding to the walls. The number of signals associated with barium is higher than potassium and platinum due to the difference in the concentration. The composition of different areas along several channels was also analyzed by XPS and some of their compositions are represented in Table 5.8.

Table 5.8. Composition data obtained by XPS of Pt-Ba-K/Al₂O₃-M.

O (%)	Al (%)	K (%)	Ba (%)	Pt (%)
69.34	29.00	0.18	1.07	0.40
68.31	29.98	0.17	1.22	0.34
67.96	30.29	0.20	1.24	0.31
68.19	30.05	0.20	1.29	0.27
67.12	31.05	0.22	1.35	0.27
67.67	30.56	0.20	1.31	0.28

Alumina was the main species detected and concentrations lower than the theoretical values were observed for the metals of the active phase. Nevertheless, similar values were measured along the structure, meaning that the metals are homogeneously

distributed on the surface. The deconvolution of the signals provided information about the species that are present in the catalyst. So, in Table 5.9, the binding energy values and the percentage of each species are represented.

Table 5.9. Binding energies from XPS data in eV for Pt-Ba-K-Al₂O₃-M (% species concentration).

Pt	Ba	K
314.4 (69.7)	779.4 (29.0)	292.7 (30.0)
316.8 (21.1)	780.8 (70.1)	293.6 (70.0)
318.5 (9.2)		
314.5 (67.7)	779.4 (31.5)	292.7 (21.8)
316.8 (22.0)	780.8 (68.5)	293.5 (78.2)
318.4 (10.3)		
314.5 (68.9)	779.2 (26.5)	292.5 (26.6)
316.8 (20.8)	780.6 (73.5)	293.5 (73.4)
318.4 (10.3)		
314.5 (62.7)	779.3 (32.5)	292.5 (29.8)
316.8 (25.6)	780.6 (67.5)	293.4 (70.2)
318.4 (11.7)		
314.9 (63.5)	779.1 (19.2)	292.6 (16.2)
316.9 (25.8)	780.6 (80.8)	293.5 (83.8)
318.5 (10.8)		
314.5 (68.2)	779.3 (30.6)	292.6 (25.3)
316.8 (20.7)	780.6 (69.4)	293.5 (74.7)
318.5 (11.1)		

The deconvolution of the platinum signal (Pt4d_{5/2} region) provided three bands with binding energies around 314, 317 and 319, corresponding to Pt⁰, Pt²⁺ and Pt⁴⁺, respectively, similar to those detected for the catalysts in powder. As has been widely explained before, the ratio between both platinum states, metallic (Pt⁰) and oxidised (Pt_{ox}), the latter being the result of adding Pt²⁺ and Pt⁴⁺ contributions, which can be obtained from the deconvolution of the signal, was affected by the metal incorporated into the formulation and was related to the catalytic behaviour. As has been previously mentioned [171,193], the interaction between platinum and the storage element is related to the NO_x removal, and the stabilization of Pt⁰ by barium species was obtained for the Ba-model catalyst [113,140] and the Pt-Ba-K/Al₂O₃ presented in Chapter 3. Ratio values around 1.8 were obtained in the powder catalysts. For the Pt-Ba-K/Al₂O₃-M monolith, the Pt⁰/Pt_{ox} ratios calculated in different positions of the channels were found to be between 1.7 and 2.3, with the average value of all the analyzed points being around 2. This indicates that the incorporation of the metals to the monolith

conformation, with this procedure and conditions, allows the stabilization of the platinum as in the powder catalysts and, as a consequence, high NO_x removal activity can be expected.

The deconvolution of the signal associated with barium also evidenced the presence of two types of species. The band close to 780.5 eV was related to barium carbonate and represented around 70% of barium content, such as was observed for the powder catalyst. In addition, a less intense band at lower binding energy corresponding to barium oxide was also noticed. For the potassium, the same species as in powder, around 292.5 and 293.5 eV associated with the oxide phase and the hydrated hydroxycarbonate species, respectively, were detected. The ratio was approximately 75-25%, with carbonate being the main species. A slight increase in the oxide phase with respect to the powder catalyst was observed, since for those catalysts the ratio was 80-20; however, the variation was not relevant enough to influence the catalytic activity.

Therefore, the synthesis process of NSR monoliths ensures the dispersion of the metals along the surface, without blocking the channel and maintaining the same active species, in almost identical proportions, as for the powder catalyst.

The 2Cu-SAPO-150-30-M monolith was also characterized in order to have information about the zeolite crystallization onto the alumina and the dispersion of the elements. XRD patterns of the cordierite and the 2Cu-SAPO-150-30-M were registered and are represented in Figure 5.13.

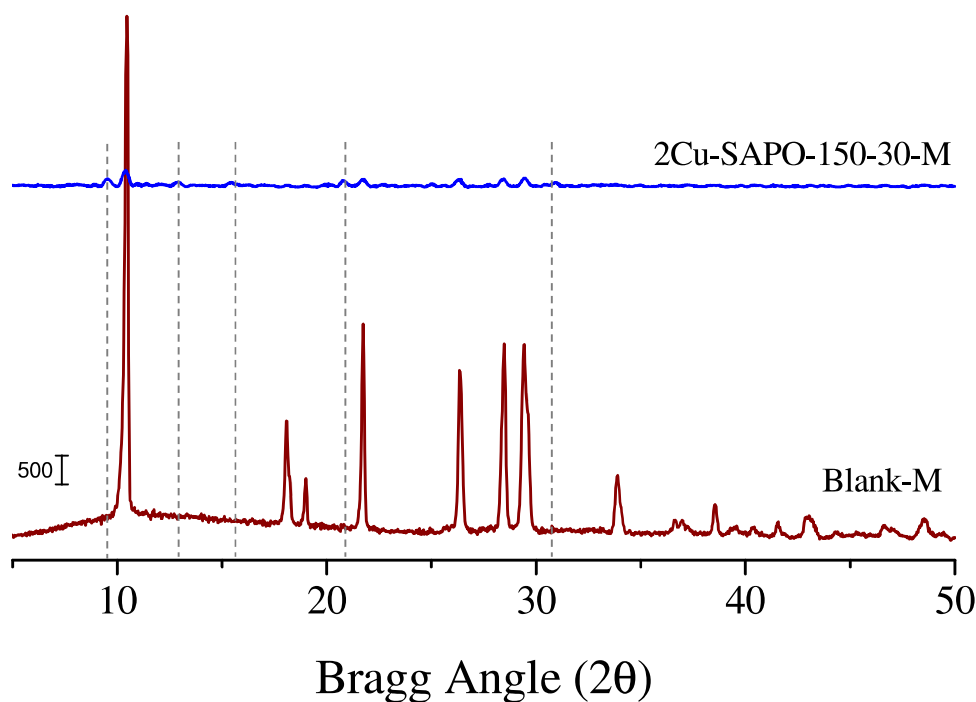


Figure 5.13. XRD patterns of the Blank-M and 2Cu-SAPO-150-30-M monoliths.

The blank-M sample is the monolith supported by Johnson Matthey with the alumina coverage and presents a high crystallinity. Bragg angle values at 10.5, 18.2, 19.1, 21.7, 26.4, 28.5, 29.5 and 33.9° were the most intense diffraction peaks and are associated with the α -cordierite [294,295]. For the monolith incorporating the zeolite, the analysis became more difficult, since the amount of zeolitic material was only 2wt% and the extraction of the sample for analysis was complex. So, the XRD pattern was obtained by consecutive subtractions and, consequently, the signals were not intense. Nevertheless, signals related to α -cordierite together with diffraction peaks at $2\theta = 9.4$, 12.9, 16.15, 20.5, 26.1 and 30.5° characteristic of SAPO-34 [244–246] can be detected.

SEM images of the 2Cu-SAPO-150-30-M monolith were taken in order to ensure the appropriate distribution and crystallization of the zeolite over the support. In Figure 5.14, some of these images are shown.

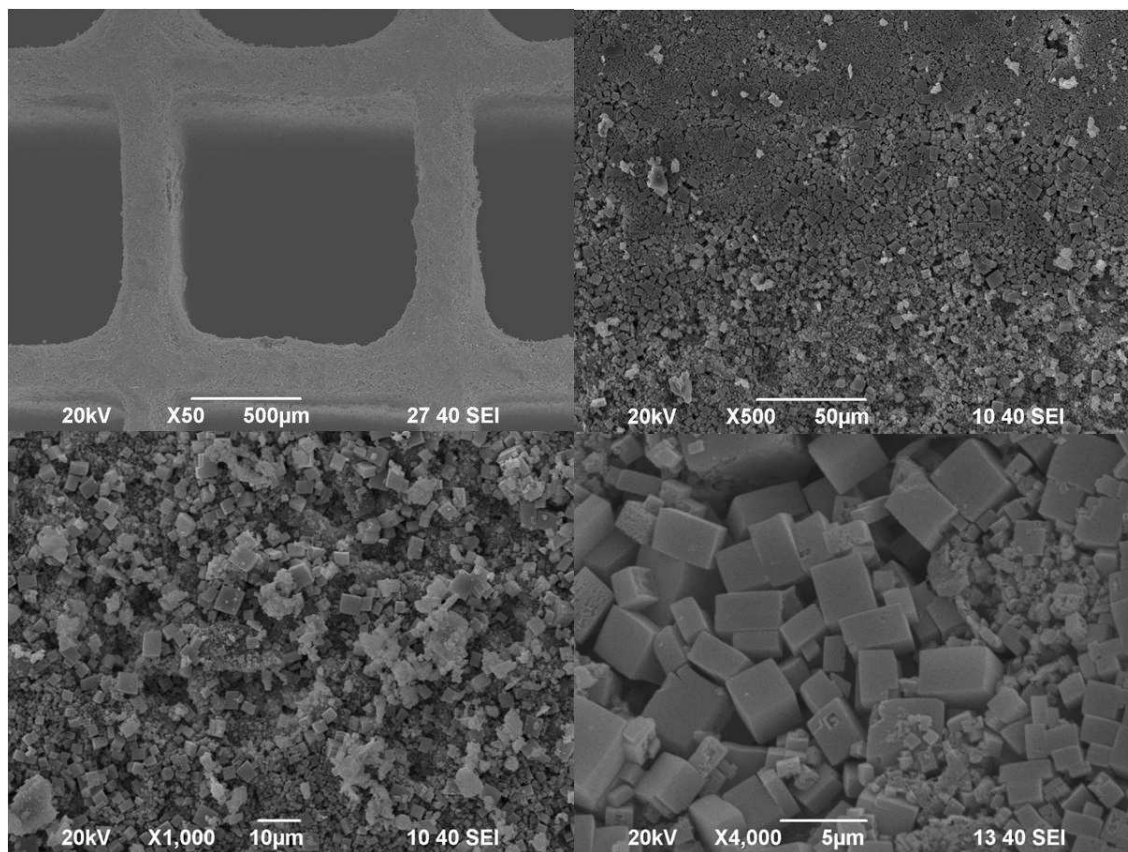


Figure 5.14. SEM images of the cross and axial sections of 2Cu-SAPO-150-30-M.

In the cross section, the width of the channel was not modified by the incorporation of the zeolite; only a slight curvature of the corners was detected. In the axial section, as the magnification was increased little cubic crystals of around 3 μm were appreciated, similar to those shown in the SEM images of the SAPO-34 materials detailed in Chapter 4 and in consonance with the bibliography [64,105,250]. The surface is completely covered by these crystals. *B. Pereda-Ayo et al.* [296] have observed small cubic crystals in the washcoating of monoliths with alumina; however, the EDX analysis over different areas to establish the composition revealed the presence of phosphorous and copper together with aluminum, oxygen and silicon, indicating zeolite incorporation in the structure. In order to delve into the dispersion of copper along the channels, EDX mapping of the sample was carried out in different areas, one of which is represented in Figure 5.15.

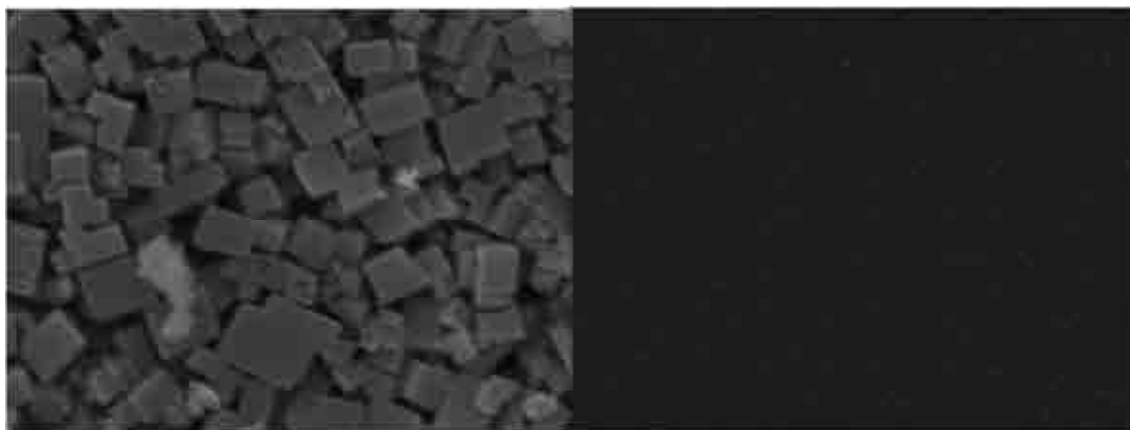


Figure 5.15. Copper EDX mapping of SEM images of 2Cu-SAPO-150-30-M sample.

In the Figure, tiny points associated with the presence of copper can be observed; the signal was not excessively intense, but a high dispersion was confirmed. The composition along the channels in different positions was also analyzed by XPS and the results of three of them are represented in Table 5.10.

Table 5.10. Composition data obtained by XPS of 2Cu-SAPO-150-30-M.

O (%)	Al (%)	Si (%)	P (%)	Cu (%)
70.36	14.99	5.27	9.21	0.17
70.83	14.15	5.29	9.61	0.13
70.88	14.42	5.27	9.30	0.13

The homogeneous distribution of the monolith surface was verified from the XPS data and was consistent in all the channels. The ratio between the elements is also representative of the Copper-containing SAPO-34. The detailed analysis of the region associated with copper ($\text{Cu}2p_{3/2}$) allows the identification of the copper species, and a combination of Cu^+ and Cu^{2+} was detected along the surface as in the powder materials [286,297].

5.4. Activity of NSR-SCR system structured in monolithic form

A series of experiments were carried out on the catalysts structured in monolithic form in order to study the catalytic activity under NSR conditions. For that, Cu-SAPO-150-30-M was placed downstream to Pt-Ba-K/ Al_2O_3 -M, both of them with the same volume (dimensions: 1x1”), weight ratio 1:1 and equally positioned to inhibit flow disturbances. The system is shown in Figure 5.16, where the reactor with a narrowing at the outlet gas

in order to increase the flow rate and prevent the modification of the product distribution can be observed.



Figure 5.16. Double bed configuration system for experiments with monoliths.

As can be seen in Figure 5.16, the inlet section and the diameter of the monoliths have the same length in order to ensure that the flow only circulates through the internal channels. Cyclic conditions were fed into the reactor, alternating oxidant phases with 1000ppm of NO + 3% of O₂ with reducing steps of different hydrogen concentrations (0.2 – 2.5 %) in atmosphere of 1.5% of H₂O + 0.3% of CO₂. The experiments were performed up to the saturation and complete regeneration of the samples, so, the time of each period was modified according to the response of the catalysts. The system was working in laminar regime, with a total flow of 100 cm³·min⁻¹ as a result of the equipment limitations and, therefore the GHSV was set at 10³ h⁻¹ with respect to each catalytic bed. The temperature was also modified between 200 and 350°C.

The profile of the product distribution obtained for a cycle using 2000ppm of hydrogen in the regeneration step is shown in Figure 5.17.

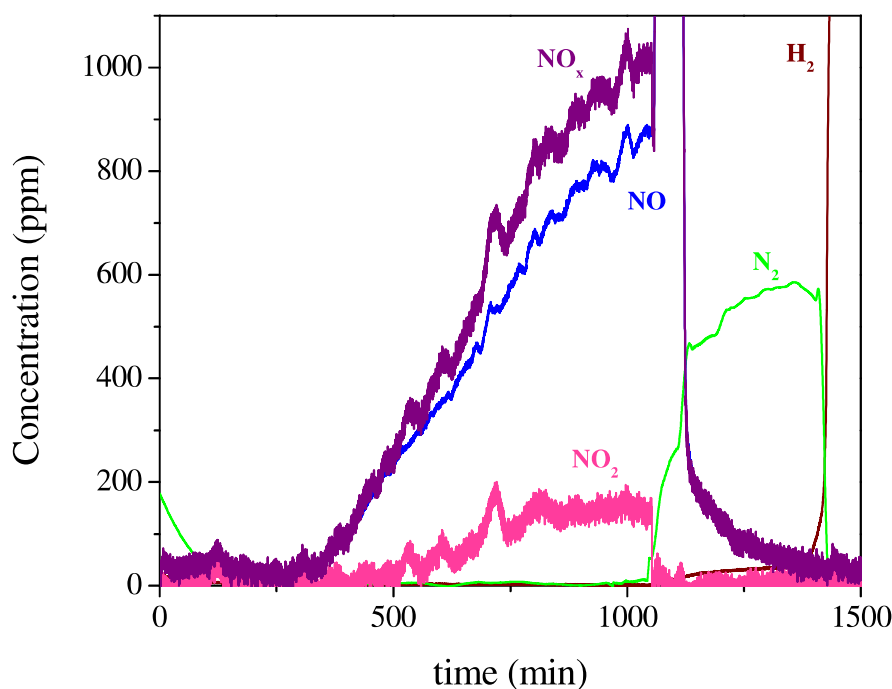


Figure 5.17. Storage-reduction cycles to saturation for Pt-Ba-K/Al₂O₃-M + Cu-SAPO-150-30-M at 350°C with lean-rich periods of 17-8h with a hydrogen concentration of 0.2% in H₂O+CO₂.

The combination of NSR-SCR monoliths was exposed to the mixture of NO+O₂ in *quasi*-real conditions (i.e. in the presence of water and CO₂) up to the saturation of the catalysts. The adsorption process is slow due to the low GHSV value and 17 hours was needed for complete saturation; the increase in space velocity implies significant differences in the behaviour as other authors have studied [298]. In the oxidant phase, nitrogen was detected as a consequence of the reaction between the NO_x and the adsorbed ammonia. Then, NO was oxidized to NO₂ and/or stored as nitrates or detected at the outlet. The breakthrough point was reached at around 5.5h, and then, a typical NO_x saturation curve was observed. In the reduction step, 2000ppm of hydrogen reacted with the adsorbed nitrates forming nitrogen and water, requiring almost 8 hours for the complete regeneration of the surface. An NO slip was detected in the change of conditions, decreasing the conversion value to 67% because the small amount of reducing agent was unable to remove the NO_x with this GHSV value. The NO slip was also detected by other authors [178] when an Fe-zeolite was used as an SCR catalyst. The system was able to remove 21 mmolNO_x per gram of theoretical active phase; however the removed NO_x amount as a function of the grams of NSR monolith was 0.42 mmol, similar value to the obtained in powder form. A similar effect was observed by other authors [110] with granular and monolithic forms of Copper-zeolites; although

these were synthesized by a different procedure. Total selectivity to nitrogen was observed during the cycles, since neither ammonia nor N_2O were detected. At low temperatures, both the detected species and the process are the same, although the amount of NO_x reduced was slightly higher with a value of $0.45 \text{ mmol} \cdot \text{g}_{\text{NSR monolith}}^{-1}$ at 200°C .

The operational parameters were also modified for the catalysts structured in monolithic form in order to study their influence on catalytic behaviour. So, hydrogen content was varied between 0.2 and 2.5% and the θ value was modified between 1 and 14. In this study, instead of analyzing the influence of θ , the minimum value of θ for the complete regeneration of the catalyst was obtained. For that, identical and shorter oxidation times were used, in particular, 7 hours was set as the lean phase time, whereas the reduction time depended on the hydrogen concentration. In Figure 5.18, the profiles registered for the experiment at 350°C with 0.2% of H_2 are shown.

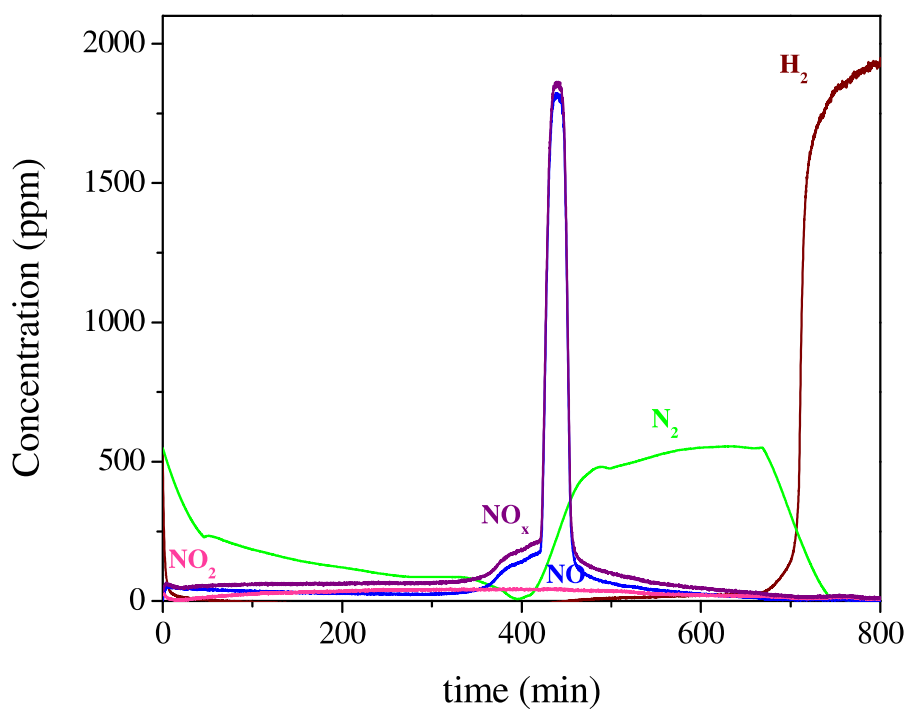


Figure 5.18. Storage-reduction cycles for Pt-Ba-K/ Al_2O_3 -M + Cu-SAPO-150-30-M at 350°C with lean-rich periods of 7-7h with a hydrogen concentration of 0.2% in H_2O+CO_2 .

As can be seen, nitrogen production as a consequence of the SCR reaction was observed, whereas ammonia and N_2O emissions were not detected during the cycles. The amount of removed NO_x for 7 hours was around 0.26 mmol per gram of NSR

monolith. In addition, the NO slip in the change from lean to rich conditions was also detected, indicating again that the stoichiometric concentration in these conditions is not enough to remove the adsorbed NO_x and the physisorbed NO or that the lightly stored nitrates are removed without a reaction and, conversion values of 80% were obtained. The time required for the complete regeneration of the catalyst with nitrogen formation was around 7 hours, i.e. θ values around 1 are needed when the reductant content is approximately the stoichiometric concentration, in agreement with the data observed in powder form.

The hydrogen content was increased up to 1% and the profile at the outlet of the reactor during one of the cycles is represented in Figure 5.19.

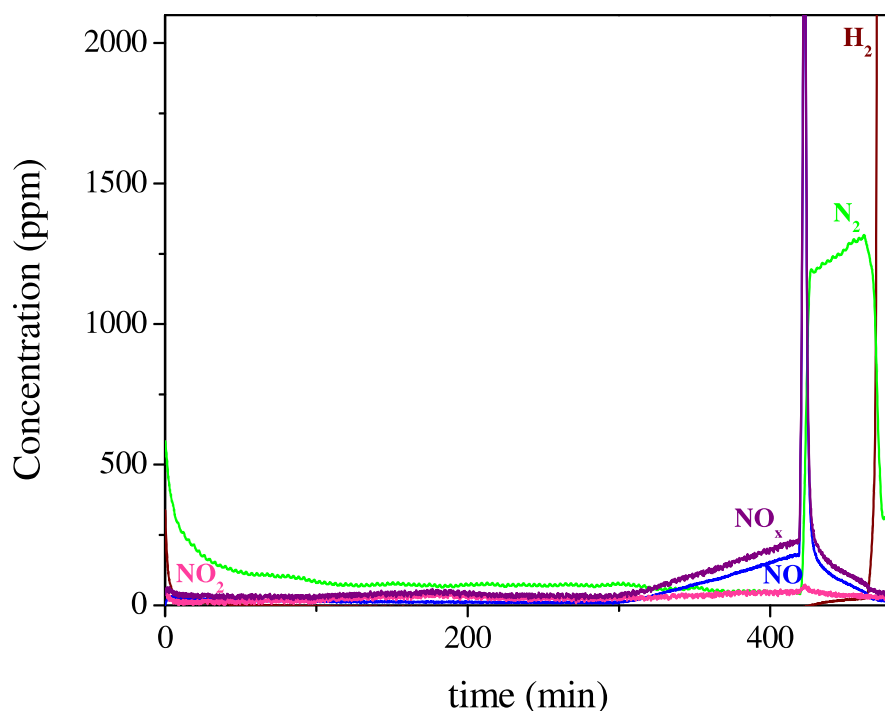


Figure 5.19. Storage-reduction cycles for Pt-Ba-K/ Al_2O_3 -M + Cu-SAPO-150-30-M at 350°C with lean-rich periods of 7-1h with a hydrogen concentration of 1% in $\text{H}_2\text{O}+\text{CO}_2$.

Similar species and processes took place in these conditions; however, there were small differences in the parameters. The amount of NO_x removed during the lean phase was also close to 0.26mmol per gram of NSR monolith because it depends on the temperature and the time of the period, since the catalyst is completely regenerated in each cycle. Only nitrogen was detected as the main product without the formation of other undesired compounds. The NO slip was also detected in these conditions,

although it was lower than at lower hydrogen concentrations, obtaining a conversion value of 96% and the total regeneration of the catalyst in 1 hour.

Finally, the same experiment was carried out using 2.5% of H₂ in the rich phase and the registered profiles are displayed in Figure 5.20.

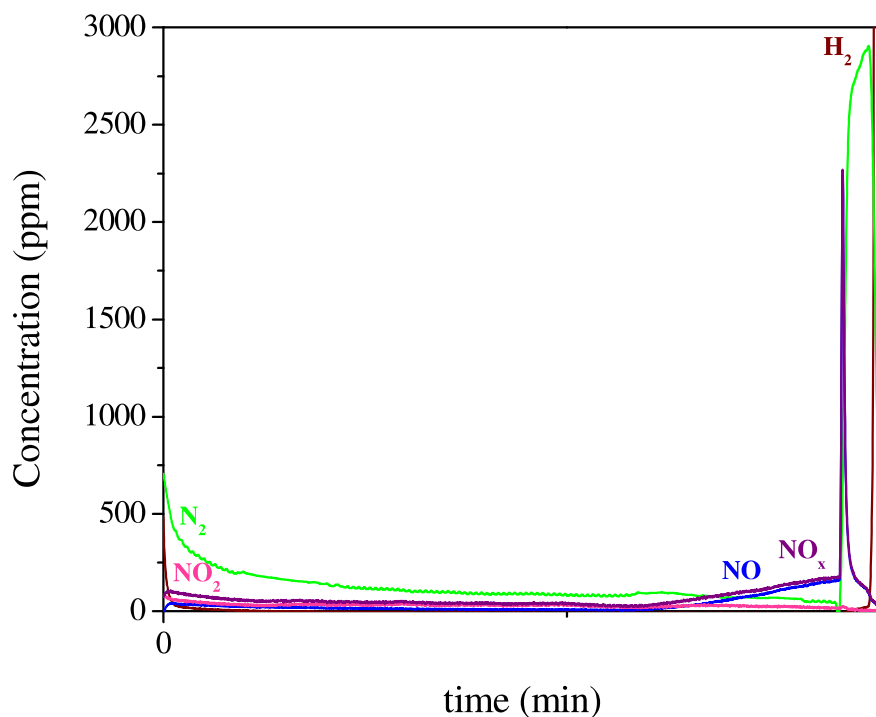


Figure 5.20. Storage-reduction cycles for Pt-Ba-K/Al₂O₃-M + Cu-SAPO-150-30-M at 350°C with lean-rich periods of 7-0.5h with a hydrogen concentration of 2.5% in H₂O+CO₂.

Total nitrogen selectivity, the combination of the NSR and SCR processes and 0.26mmol of removed NO_x per gram of NSR monolith were also observed. The NO slip was the lowest detected and conversion values of 98% were achieved. The high reductant concentration implied that the reduction of the time required for the total regeneration of the catalyst was 30 minutes. The influence of the hydrogen concentration was also studied by other authors [292] working with PtBaO/Al₂O₃ and Cu-CHA as NSR and SCR monoliths, respectively, and similar values in terms of selectivity, conversion and trends were observed.

The synthesized catalysts in monolith form presented morphological and structural properties similar to the powder catalysts. In terms of the NO_x removed per gram of monolith, the amount depended on the time of saturation and the operation temperature, although values comparable to those observed for powder catalysts were obtained. The

regeneration time, the NO slip and, in consequence, the conversion of the NO_x, are determined by the hydrogen content. For θ values around 1, the stoichiometric value is enough to achieve the regeneration in spite of the low conversion registered. As θ (ratio between the lean and rich phase times) increases, the concentration of hydrogen must also increase, since a higher amount of reducing agent is needed for the regeneration of the surface in less time. Similar trends were observed for the variation of θ in powder and in monolith. Hydrogen contents between 1 and 2.5% and θ values between 7 and 14 are enough to obtain conversions of around 98% and total selectivity to nitrogen in the whole operation range in the presence of water and CO₂.

5.5. Conclusions

A methodology of reproducible synthesis of NSR and SCR catalysts has been developed, obtaining structured catalysts that remove NO_x in light vehicles thus achieving zero emissions. The monoliths with 2wt% of active phase accomplish De-NO_x overall activity values similar to those raised by the catalysts in powder form. In spite of the low GHSV, the operation parameters provided conversion values around 97% with minimum NO slip ensuring zero emissions under laboratory scale conditions.



UNIVERSIDAD
DE MÁLAGA

6. Significance and future lines of research

In order to respond to the initial thesis title, taking NSR and SCR hybrid catalytic systems into account to ensure zero emissions at the outlet gas, the following conclusions were obtained:

- A multimetallic catalytic formulation was developed, combining Pt, Ba, K and Al_2O_3 with metal load of $5 \text{ at}\cdot\text{nm}^{-2}$, which allows simultaneous NO_x and soot removal operating in cyclic conditions and N_2 selectivity and conversion values higher than 80% in the whole range even in the presence of water and CO_2 . Furthermore, the function of each metal in the soot removal process was individualized.
- A reproducible and scalable one-pot synthesis process, with ultrasound, was carried out for a Cu-SAPO-34 material, with chabazite structure, all copper located inside the framework, forming hydrothermally stable reactive species and NH_3 -SCR capacity in *quasi*-real conditions, minimizing its N_2O production. Moreover, an insight into the reaction pathway was also performed, detecting Cu^{2+} species with different environment as the main species of the SCR process.
- The LNT-SCR hybrid system with volumetric ratio 1:1 and active phase load of 2 wt% produces high levels of mineralization to nitrogen without N_2O or NH_3 slip in *quasi*-real cyclic conditions tested in water and CO_2 . This opens the way towards the use of catalytic after-treatment systems for obtaining zero emissions.

Future lines of research

From the conclusions of this work, there are a series of open topics still to be addressed, and the following future lines of research are proposed:

- In spite of the low sulfur content in the exhaust, the sulfur resistance of the catalysts should be analyzed, fundamentally for SCR materials, since the NSR catalysts were previously studied in the presence of these compounds.
- The substitution of hydrogen in the reducing phase, using hydrocarbons similar to those employed in real conditions.
- Research into the behaviour of different diesel/petrodiesel blends and their cushioning by monoliths with the proposed formulations, as is being performed at present in an engine in which the outlet gas line has been bifurcated in order to introduce these monoliths.
- The scaling of the materials for their coupling in an engine in order to analyze on board emissions, similar to the real-world driving emissions (RDE) systems that are being introduced by current regulations.

7. References

- [1] Anuario Estadístico General, 2014. http://www.interior.gov.cl/n1396_08-07-2010.html.
- [2] I.S. Pieta, M. García-Diéguez, C. Herrera, M.A. Larrubia, L.J. Alemany, In situ DRIFT-TRM study of simultaneous NO_x and soot removal over Pt-Ba and Pt-K NSR catalysts, *J. Catal.* 270 (2010) 256–267. doi:10.1016/j.jcat.2010.01.003.
- [3] F. Dai, M. Meng, Y. Zha, Z. Li, T. Hu, Y. Xie, et al., Performance of Ce substituted hydrotalcite-derived mixed oxide catalysts Co_{2.5}Mg_{0.5}Al_{1-x%}Ce_{x%}O used for soot combustion and simultaneous NO_x-soot removal, *Fuel Process. Technol.* 104 (2012) 43–49. doi:10.1016/j.fuproc.2012.07.002.
- [4] W.F. Shangguan, Y. Teraoka, S. Kagawa, Kinetics of soot-O₂, soot-NO and soot-O₂-NO reactions over spinel-type CuFe₂O₄ catalyst, *Appl. Catal. B Environ.* 12 (1997) 237–247.
- [5] Q. Shen, G. Lu, C. Du, Y. Guo, Y. Wang, Y. Guo, et al., Role and reduction of NO_x in the catalytic combustion of soot over iron-ceria mixed oxide catalyst, *Chem. Eng. J.* 218 (2013) 164–172. doi:10.1016/j.cej.2012.12.010.
- [6] I. Atribak, I. Such-Basáñez, A. Bueno-López, A. García-García, Comparison of the catalytic activity of MO₂ (M = Ti, Zr, Ce) for soot oxidation under NO_x/O₂, *J. Catal.* 250 (2007) 75–84. doi:10.1016/j.jcat.2007.05.015.
- [7] A. Demirbas, Biofuels sources, biofuel policy, biofuel economy and global biofuel projections, *Energy Convers. Manag.* 49 (2008) 2106–2116. doi:10.1016/j.enconman.2008.02.020.
- [8] S.H. Park, C.S. Lee, Combustion performance and emission reduction characteristics of automotive DME engine system, *Prog. Energy Combust. Sci.* 39 (2013) 147–168. doi:10.1016/j.pecs.2012.10.002.
- [9] M.A. Peralta, M.S. Zanuttini, M.A. Ulla, C.A. Querini, Diesel soot and NO_x abatement on K/La₂O₃ catalyst: Influence of K precursor on soot combustion, *Appl. Catal. A Gen.* 399 (2011) 161–171. doi:10.1016/j.apcata.2011.03.046.
- [10] C.-B. Lim, H. Kusaba, H. Einaga, Y. Teraoka, Catalytic performance of supported precious metal catalysts for the combustion of diesel particulate matter, *Catal. Today.* 175 (2011) 106–111. doi:10.1016/j.cattod.2011.03.062.
- [11] R. Matarrese, L. Castoldi, L. Lietti, P. Forzatti, Soot combustion: Reactivity of alkaline and alkaline earth metal oxides in full contact with soot, *Catal. Today.* 136 (2008) 11–17. doi:10.1016/j.cattod.2008.03.022.
- [12] R. Matarrese, L. Castoldi, L. Lietti, Reaction between soot and stored NO_x over K-based LNT catalysts investigated by temperature programmed methods and labeling isotopic experiments, *Catal. Today.* 197 (2012) 228–235. doi:10.1016/j.cattod.2012.07.046.
- [13] Z. Wang, Q. Li, L. Wang, W. Shangguan, Simultaneous catalytic removal of NO_x and soot particulates over CuMgAl hydrotalcites derived mixed metal oxides, *Appl. Clay Sci.* 55 (2012) 125–130. doi:10.1016/j.clay.2011.11.003.
- [14] Q. Li, M. Meng, F. Dai, Y. Zha, Y. Xie, T. Hu, et al., Multifunctional hydrotalcite-derived K/MnMgAlO catalysts used for soot combustion, NO_x storage and simultaneous soot-NO_x removal, *Chem. Eng. J.* 184 (2012) 106–112. doi:10.1016/j.cej.2012.01.009.
- [15] V.G. Milt, C.A. Querini, E.E. Miró, M.A. Ulla, Abatement of diesel exhaust pollutants: NO_x adsorption on Co,Ba,K/CeO₂ catalysts, *J. Catal.* 220 (2003) 424–432. doi:10.1016/S0021-9517(03)00285-9.
- [16] Y. Wei, Z. Zhao, J. Liu, S. Liu, C. Xu, A. Duan, et al., Multifunctional catalysts of three-dimensionally ordered macroporous oxide-supported Au@Pt core-shell nanoparticles with high catalytic activity and stability for soot oxidation, *J. Catal.* 317 (2014) 62–74. doi:10.1016/j.jcat.2014.05.014.
- [17] M.E.A. Fahd, Y. Wenming, P.S. Lee, S.K. Chou, C.R. Yap, Experimental investigation of the performance and emission characteristics of direct injection diesel engine by water emulsion diesel under varying engine load condition, *Appl. Energy.* 102 (2013) 1042–1049. doi:10.1016/j.apenergy.2012.06.041.

- [18] A.J. Torregrosa, A. Broatch, B. Plá, L.F. Mónico, Impact of Fischer-Tropsch and biodiesel fuels on trade-offs between pollutant emissions and combustion noise in diesel engines, *Biomass and Bioenergy*. 52 (2013) 22–33. doi:10.1016/j.biombioe.2013.03.004.
- [19] I. Barabás, A. Todoruț, D. Băldean, Performance and emission characteristics of an CI engine fueled with diesel-biodiesel-bioethanol blends, *Fuel*. 89 (2010) 3827–3832. doi:10.1016/j.fuel.2010.07.011.
- [20] M. Canakci, A. Erdil, E. Arcaklioğlu, Performance and exhaust emissions of a biodiesel engine, *Appl. Energy*. 83 (2006) 594–605. doi:10.1016/j.apenergy.2005.05.003.
- [21] D.B. Hulwan, S. V. Joshi, Performance, emission and combustion characteristic of a multicylinder DI diesel engine running on diesel-ethanol-biodiesel blends of high ethanol content, *Appl. Energy*. 88 (2011) 5042–5055. doi:10.1016/j.apenergy.2011.07.008.
- [22] G.R. Kannan, R. Karvembu, R. Anand, Effect of metal based additive on performance emission and combustion characteristics of diesel engine fuelled with biodiesel, *Appl. Energy*. 88 (2011) 3694–3703. doi:10.1016/j.apenergy.2011.04.043.
- [23] M. Cortés-Reyes, C. Herrera, M.A. Larrubia, J.A. Auñón, M. González, L.J. Alemany, Impact of New Biofuels on Pollutant Production and Motor Performance and Study of DeNO_x Technologies to Achieve Zero, *Int. J. Innov. Res. Sci. Eng. Technol.* 5 (2016) 13082–13088. doi:10.15680/IJIRSET.2016.0507177.
- [24] H. Omidvarborna, A. Kumar, D.-S. Kim, NO_x emissions from low-temperature combustion of biodiesel made of various feedstocks and blends, *Fuel Process. Technol.* 140 (2015) 113–118. doi:10.1016/j.fuproc.2015.08.031.
- [25] R.D. Lanjekar, D. Deshmukh, A review of the effect of the composition of biodiesel on NO_x emission, oxidative stability and cold flow properties, *Renew. Sustain. Energy Rev.* 54 (2016) 1401–1411. doi:10.1016/j.rser.2015.10.034.
- [26] J.M. Dias, J.M. Araújo, J.F. Costa, M.C.M. Alvim-Ferraz, M.F. Almeida, Biodiesel production from raw castor oil, *Energy*. 53 (2013) 58–66. doi:10.1016/j.energy.2013.02.018.
- [27] D.C. Rakopoulos, C.D. Rakopoulos, E.G. Giakoumis, A.M. Dimaratos, M.A. Founti, Comparative environmental behavior of bus engine operating on blends of diesel fuel with four straight vegetable oils of Greek origin: Sunflower, cottonseed, corn and olive, *Fuel*. 90 (2011) 3439–3446. doi:10.1016/j.fuel.2011.06.009.
- [28] P.S. Monks, C. Granier, S. Fuzzi, A. Stohl, M.L. Williams, H. Akimoto, et al., Atmospheric composition change – global and regional air quality, *Atmos. Environ.* 43 (2009) 5268–5350. doi:10.1016/j.atmosenv.2009.08.021.
- [29] V.I. Pârvulescu, P. Grange, B. Delmon, Catalytic removal of NO, *Catal. Today*. 46 (1998) 233–316. doi:10.1016/S0920-5861(98)00399-X.
- [30] R.G. Derwent, The long range transport of ozone within Europe and its control, *Environ. Pollut.* 63 (1990) 299–318.
- [31] S. V. Krupa, R.N. Kickert, The Greenhouse effect: Impacts of ultraviolet-B (UV-B) radiation, carbon dioxide (CO₂), and ozone (O₃) on vegetation, *Environ. Pollut.* 61 (1989) 263–393. doi:10.1016/0269-7491(89)90166-8.
- [32] G. Mazzearella, F. Ferraraccio, M. V. Prati, S. Annunziata, A. Bianco, A. Mezzogiorno, et al., Effects of diesel exhaust particles on human lung epithelial cells: An in vitro study, *Respir. Med.* 101 (2007) 1155–1162. doi:10.1016/j.rmed.2006.11.011.
- [33] R.M. Heck, R.J. Farrauto, Automobile exhaust catalysts, *Appl. Catal. A Gen.* 221 (2001) 443–457.
- [34] Normativa emisiones <https://www.dieselnet.com//standards/eu/ld.php>.
- [35] G. Archer, Dieselgate : Who ? What ? How ?, *Transport&Environment* (2016).
- [36] I. Malpartida García, Un estudio del proceso de almacenamiento seguido de reducción, NSR, para la eliminación de NO_x en fuentes móviles, PhD Thesis (2006), University of Malaga.
- [37] C. Ciardelli, I. Nova, E. Tronconi, D. Chatterjee, B. Bandl-Konrad, M. Weibel, et al., Reactivity of NO/NO₂-NH₃ SCR system for diesel exhaust aftertreatment: Identification of the reaction network as a function of temperature and NO₂ feed content, *Appl. Catal.*

- B Environ. 70 (2007) 80–90. doi:10.1016/j.apcatb.2005.10.041.
- [38] M. Colombo, I. Nova, E. Tronconi, Detailed kinetic modeling of the NH_3 -NO/NO₂ SCR reactions over a commercial Cu-zeolite catalyst for Diesel exhausts after treatment, *Catal. Today*. 197 (2012) 243–255. doi:10.1016/j.cattod.2012.09.002.
- [39] S. Brandenberger, O. Kröcher, A. Tissler, R. Althoff, The State of the Art in Selective Catalytic Reduction of NO_x by Ammonia Using Metal-Exchanged Zeolite Catalysts, 2008. doi:10.1080/01614940802480122.
- [40] P. Forzatti, Present status and perspectives in de-NO_x SCR catalysis, *Appl. Catal. A Gen.* 222 (2001) 221–236.
- [41] B. Pereda-Ayo, U. De La Torre, M.J. Illán-Gómez, A. Bueno-López, J.R. González-Velasco, Role of the different copper species on the activity of Cu/zeolite catalysts for SCR of NO_x with NH₃, *Appl. Catal. B Environ.* 147 (2014) 420–428. doi:10.1016/j.apcatb.2013.09.010.
- [42] M. Koebel, M. Elsener, M. Kleemann, Urea-SCR: a promising technique to reduce NO_x emissions from automotive diesel engines, *Catal. Today*. 59 (2000) 335–345. doi:10.1016/S0920-5861(00)00299-6.
- [43] L.J. Alemany, L. Lietti, N. Ferlazzo, P. Forzatti, G. Busca, E. Giamello, et al., Reactivity and physicochemical characterisation of V₂O₅-WO₃/TiO₂ De-NO_x Catalysts, *J. Catal.* 155 (1995) 117–130.
- [44] B. Guan, R. Zhan, H. Lin, Z. Huang, Review of state of the art technologies of selective catalytic reduction of NO_x from diesel engine exhaust, *Appl. Therm. Eng.* 66 (2014) 395–414. doi:10.1016/j.applthermaleng.2014.02.021.
- [45] Z.G. Liu, N.A. Ottinger, C.M. Creemeens, Methods for quantifying the release of Vanadium from engine exhaust aftertreatment catalysts, *SAE Int. J. Engines*. 5 (2012) 663–671. doi:10.4271/2012-01-0887.
- [46] Database of Zeolite Structures, [Http://www.iza-Structure.org/databases/](http://www.iza-Structure.org/databases/).
- [47] M. Colombo, I. Nova, E. Tronconi, A comparative study of the NH₃-SCR reactions over a Cu-zeolite and a Fe-zeolite catalyst, *Catal. Today*. 151 (2010) 223–230. doi:10.1016/j.cattod.2010.01.010.
- [48] P.S. Metkar, M.P. Harold, V. Balakotaiah, Experimental and kinetic modeling study of NH₃-SCR of NO_x on Fe-ZSM-5, Cu-chabazite and combined Fe- and Cu-zeolite monolithic catalysts, *Chem. Eng. Sci.* 87 (2013) 51–66. doi:10.1016/j.ces.2012.09.008.
- [49] P. Boroń, L. Chmielarz, J. Gurgul, K. Łątka, B. Gil, B. Marszałek, et al., Influence of iron state and acidity of zeolites on the catalytic activity of FeHBEA, FeHZSM-5 and FeHMOR in SCR of NO with NH₃ and N₂O decomposition, *Microporous Mesoporous Mater.* 203 (2015) 73–85. doi:10.1016/j.micromeso.2014.10.023.
- [50] U. De La Torre, B. Pereda-Ayo, J.R. González-Velasco, Cu-zeolite NH₃-SCR catalysts for NO_x removal in the combined NSR-SCR technology, *Chem. Eng. J.* 207–208 (2012) 10–17. doi:10.1016/j.cej.2012.06.092.
- [51] J. Dědeček, L. Čapek, P. Sazama, Z. Sobalík, B. Wichterlová, Control of metal ion species in zeolites by distribution of aluminium in the framework: From structural analysis to performance under real conditions of SCR-NO_x and NO, N₂O decomposition, *Appl. Catal. A Gen.* 391 (2011) 244–253. doi:10.1016/j.apcata.2010.06.026.
- [52] X. Cheng, X.T. Bi, A review of recent advances in selective catalytic NO_x reduction reactor technologies, *Particuology*. 16 (2014) 1–18. doi:10.1016/j.partic.2014.01.006.
- [53] M. Rutkowska, Z. Piwowska, E. Micek, L. Chmielarz, Hierarchical Fe-, Cu- and Co-Beta zeolites obtained by mesotemplate-free method. Part I: Synthesis and catalytic activity in N₂O decomposition, *Microporous Mesoporous Mater.* 209 (2015) 54–65. doi:10.1016/j.micromeso.2014.10.011.
- [54] M. Colombo, I. Nova, E. Tronconi, NO₂ adsorption on Fe- and Cu-zeolite catalysts: The effect of the catalyst red-ox state, *Appl. Catal. B Environ.* 111–112 (2012) 433–444. doi:10.1016/j.apcatb.2011.10.031.
- [55] P. Chen, D. Rauch, P. Weide, S. Schönebaum, T. Simons, M. Muhler, et al., The effect of Cu and Fe cations on NH₃-supported proton transport in DeNO_x-SCR zeolite catalysts, *Catal. Sci. Technol.* (2016). doi:10.1039/C6CY00452K.

- [56] P.S. Metkar, V. Balakotaiah, M.P. Harold, Experimental and kinetic modeling study of NO oxidation: Comparison of Fe and Cu-zeolite catalysts, *Catal. Today*. 184 (2012) 115–128. doi:10.1016/j.cattod.2011.11.032.
- [57] O. Mihai, C.R. Widyastuti, S. Andonova, K. Kamasamudram, J. Li, S.Y. Joshi, et al., The effect of Cu-loading on different reactions involved in NH₃-SCR over Cu-BEA catalysts, *J. Catal.* 311 (2014) 170–181. doi:10.1016/j.jcat.2013.11.016.
- [58] S. Shwan, J. Jansson, J. Korsgren, L. Olsson, M. Skoglundh, Kinetic modeling of H-BEA and Fe-BEA as NH₃-SCR catalysts—Effect of hydrothermal treatment, *Catal. Today*. 197 (2012) 24–37. doi:10.1016/j.cattod.2012.06.014.
- [59] Y. Cheng, C. Lambert, D.H. Kim, J.H. Kwak, S.J. Cho, C.H.F. Peden, The different impacts of SO₂ and SO₃ on Cu/zeolite SCR catalysts, *Catal. Today*. 151 (2010) 266–270. doi:10.1016/j.cattod.2010.01.013.
- [60] M. Shen, H. Wen, T. Hao, T. Yu, D. Fan, J. Wang, et al., Deactivation mechanism of SO₂ on Cu/SAPO-34 NH₃-SCR catalysts: structure and active Cu²⁺, *Catal. Sci. Technol.* 5 (2015) 1741–1749. doi:10.1039/c4cy01129e.
- [61] J.H. Kwak, D. Tran, S.D. Burton, J. Szanyi, J.H. Lee, C.H.F. Peden, Effects of hydrothermal aging on NH₃-SCR reaction over Cu/zeolites, *J. Catal.* 287 (2012) 203–209. doi:10.1016/j.jcat.2011.12.025.
- [62] P.G. Blakeman, E.M. Burkholder, H.-Y. Chen, J.E. Collier, J.M. Fedeyko, H. Jobson, et al., The role of pore size on the thermal stability of zeolite supported Cu SCR catalysts, *Catal. Today*. 231 (2014) 56–63. doi:10.1016/j.cattod.2013.10.047.
- [63] T. Blasco, A. Corma, J. Martínez-Triguero, Hydrothermal stabilization of ZSM-5 catalytic-cracking additives by phosphorus addition, *J. Catal.* 237 (2006) 267–277. doi:10.1016/j.jcat.2005.11.011.
- [64] R. Martínez-Franco, M. Moliner, C. Franch, A. Kustov, A. Corma, Rational direct synthesis methodology of very active and hydrothermally stable Cu-SAPO-34 molecular sieves for the SCR of NO_x, *Appl. Catal. B Environ.* 127 (2012) 273–280. doi:10.1016/j.apcatb.2012.08.034.
- [65] Y.J. Kim, J.K. Lee, K.M. Min, S.B. Hong, I.-S. Nam, B.K. Cho, Hydrothermal stability of CuSSZ13 for reducing NO_x by NH₃, *J. Catal.* 311 (2014) 447–457. doi:10.1016/j.jcat.2013.12.012.
- [66] L. Ma, Y. Cheng, G. Cavataio, R.W. McCabe, L. Fu, J. Li, In situ DRIFTS and temperature-programmed technology study on NH₃-SCR of NO_x over Cu-SSZ-13 and Cu-SAPO-34 catalysts, *Appl. Catal. B Environ.* 156–157 (2014) 428–437. doi:10.1016/j.apcatb.2014.03.048.
- [67] D. Wang, Y. Jangjou, Y. Liu, M.K. Sharma, J. Luo, J. Li, et al., A comparison of hydrothermal aging effects on NH₃-SCR of NO_x over Cu-SSZ-13 and Cu-SAPO-34 catalysts, *Appl. Catal. B Environ.* 165 (2015) 438–445. doi:10.1016/j.apcatb.2014.10.020.
- [68] A. Beretta, E. Tronconi, L.J. Alemany, J. Svachula, P. Forzatti, Effect of morphology of honeycomb SCR catalysts on the reduction of NO_x and the oxidation of SO₂, *New Dev. Sel. Oxid. II*. (1994) 869–876.
- [69] G. Busca, Chapter 7 – Zeolites and Other Structurally Microporous Solids as Acid – Base Materials, in: *Heterog. Catal. Mater.*, 2014: pp. 197–249.
- [70] J.Q. Chen, A. Bozzano, B. Glover, T. Fuglerud, S. Kvisle, Recent advancements in ethylene and propylene production using the UOP/Hydro MTO process, *Catal. Today*. 106 (2005) 103–107. doi:10.1016/j.cattod.2005.07.178.
- [71] S. Li, Z. Zong, S.J. Zhou, Y. Huang, Z. Song, X. Feng, et al., SAPO-34 Membranes for N₂/CH₄ separation: Preparation, characterization, separation performance and economic evaluation, *J. Memb. Sci.* 487 (2015) 141–151. doi:10.1016/j.memsci.2015.03.078.
- [72] S. Li, M.A. Carreon, Y. Zhang, H.H. Funke, R.D. Noble, J.L. Falconer, Scale-up of SAPO-34 membranes for CO₂/CH₄ separation, *J. Memb. Sci.* 352 (2010) 7–13. doi:10.1016/j.memsci.2010.01.037.
- [73] K. Agarwal, M. John, S. Pai, B.L. Newalkar, R. Bhargava, N. V. Choudary, SAPO-34 assisted C3 separation: Modeling and simulation, *Microporous Mesoporous Mater.* 132

- (2010) 311–318. doi:10.1016/j.micromeso.2010.02.024.
- [74] S. Askari, R. Halladj, M. Sohrabi, An overview of the effects of crystallization time, template and silicon sources on hydrothermal synthesis of SAPO-34 molecular sieve with small crystals, *Rev. Adv. Mater. Sci.* 32 (2012) 83–93.
- [75] M. Fischer, Water adsorption in SAPO-34: elucidating the role of local heterogeneities and defects using dispersion-corrected DFT calculations, *Phys. Chem. Chem. Phys.* 17 (2015) 25260–25271. doi:10.1039/C5CP04189A.
- [76] M. Zokaie, U. Olsbye, K.P. Lillerud, O. Swang, A computational study on heteroatom distribution in zeotype materials, *Microporous Mesoporous Mater.* 158 (2012) 175–179. doi:10.1016/j.micromeso.2012.03.005.
- [77] D.W. Fickel, E. D’Addio, J.A. Lauterbach, R.F. Lobo, The ammonia selective catalytic reduction activity of copper-exchanged small-pore zeolites, *Appl. Catal. B Environ.* 102 (2011) 441–448. doi:10.1016/j.apcatb.2010.12.022.
- [78] A.M. Beale, F. Gao, I. Lezcano-Gonzalez, C.H.F. Peden, J. Szanyi, Recent advances in automotive catalysis for NO_x emission control by small-pore microporous materials, *Chem. Soc. Rev.* 44 (2015) 7371–7405. doi:10.1039/c5cs00108k.
- [79] W. Shan, H. Song, Catalysts for the selective catalytic reduction of NO_x with NH₃ at low temperature, *Catal. Sci. Technol.* 5 (2015) 4280–4288. doi:10.1039/c5cy00737b.
- [80] D. Wang, L. Zhang, J. Li, K. Kamasamudram, W.S. Epling, NH₃-SCR over Cu/SAPO-34 – Zeolite acidity and Cu structure changes as a function of Cu loading, *Catal. Today.* 231 (2014) 64–74. doi:10.1016/j.cattod.2013.11.040.
- [81] J. Ma, Z. Si, X. Wu, D. Weng, Y. Ma, Optimizing the crystallinity and acidity of H-SAPO-34 by fluoride for synthesizing Cu/SAPO-34 NH₃-SCR catalyst, *J. Environ. Sci.* 41 (2016) 244–251. doi:10.1016/j.jes.2015.05.024.
- [82] J. Wang, T. Yu, X. Wang, G. Qi, J. Xue, M. Shen, et al., The influence of silicon on the catalytic properties of Cu/SAPO-34 for NO_x reduction by ammonia-SCR, *Appl. Catal. B Environ.* 127 (2012) 137–147. doi:10.1016/j.apcatb.2012.08.016.
- [83] J. Xue, X. Wang, G. Qi, J. Wang, M. Shen, W. Li, Characterization of copper species over Cu/SAPO-34 in selective catalytic reduction of NO_x with ammonia: Relationships between active Cu sites and de-NO_x performance at low temperature, *J. Catal.* 297 (2013) 56–64. doi:10.1016/j.jcat.2012.09.020.
- [84] L. Wang, W. Li, G. Qi, D. Weng, Location and nature of Cu species in Cu/SAPO-34 for selective catalytic reduction of NO with NH₃, *J. Catal.* 289 (2012) 21–29. doi:10.1016/j.jcat.2012.01.012.
- [85] P.N.R. Vennestrøm, A. Katerinopoulou, R.R. Tiruvalam, A. Kustov, P.G. Moses, P. Concepcion, et al., Migration of Cu Ions in SAPO-34 and Its Impact on Selective Catalytic Reduction of NO_x with NH₃, *ACS Catal.* 3 (2013) 2158–2161. doi:10.1021/cs400499p.
- [86] U. Deka, I. Lezcano-Gonzalez, S.J. Warrender, A.L. Picone, P.A. Wright, B.M. Weckhuysen, et al., Changing active sites in Cu-CHA catalysts: deNO_x selectivity as a function of the preparation method, *Microporous Mesoporous Mater.* 166 (2013) 144–152. doi:10.1016/j.micromeso.2012.04.056.
- [87] A.L. Picone, S.J. Warrender, A.M.Z. Slawin, D.M. Dawson, S.E. Ashbrook, P.A. Wright, et al., A co-templating route to the synthesis of Cu SAPO STA-7, giving an active catalyst for the selective catalytic reduction of NO, *Microporous Mesoporous Mater.* 146 (2011) 36–47. doi:10.1016/j.micromeso.2011.04.039.
- [88] G. Busca, L. Lietti, G. Ramis, F. Berti, Chemical and mechanistic aspects of the selective catalytic reduction of NO_x by ammonia over oxide catalysts: A review, *Appl. Catal. B Environ.* 18 (1998) 1–36. doi:10.1016/S0926-3373(98)00040-X.
- [89] F. Gao, J.H. Kwak, J. Szanyi, C.H.F. Peden, Current understanding of Cu-Exchanged Chabazite molecular sieves for use as commercial diesel engine DeNO_x catalysts, *Top. Catal.* 56 (2013) 1441–1459. doi:10.2800/51626.
- [90] L. Xie, F. Liu, L. Ren, X. Shi, F. Xiao, H. He, Excellent performance of one-pot synthesized Cu-SSZ-13 catalyst for the selective catalytic reduction of NO_x with NH₃, *Environ. Sci. Technol.* 48 (2014) 566–572. doi:10.1021/es4032002.

- [91] S.A. Bates, A.A. Verma, C. Paolucci, A.A. Parekh, T. Anggara, A. Yezerets, et al., Identification of the active Cu site in standard selective catalytic reduction with ammonia on Cu-SSZ-13, *J. Catal.* 312 (2014) 87–97. doi:10.1016/j.jcat.2014.01.004.
- [92] T.V.W. Janssens, H. Falsig, L.F. Lundegaard, P.N.R. Vennestrøm, S.B. Rasmussen, P.G. Moses, et al., A consistent reaction scheme for the selective catalytic reduction of nitrogen oxides with ammonia, *ACS Catal.* 5 (2015) 2832–2845. doi:10.1021/cs501673g.
- [93] T. Yu, T. Hao, D. Fan, J. Wang, M. Shen, W. Li, Recent NH₃-SCR Mechanism Research over Cu/SAPO-34 Catalyst, *J. Phys. Chem. C.* 118 (2014) 6565–6575.
- [94] Y. Duan, J. Wang, T. Yu, M. Shen, J. Wang, The role and activity of various adsorbed ammonia species on Cu/SAPO-34 catalyst during passive-SCR process, *RSC Adv.* 5 (2015) 14103–14113. doi:10.1039/c4ra13984d.
- [95] T. Yu, J. Wang, M. Shen, W. Li, NH₃-SCR over Cu/SAPO-34 catalysts with various acid contents and low Cu loading, *Catal. Sci. Technol.* 3 (2013) 3234–3241. doi:10.1039/C3CY00453H.
- [96] C. Niu, X. Shi, F. Liu, K. Liu, L. Xie, Y. You, et al., High hydrothermal stability of Cu-SAPO-34 catalysts for the NH₃-SCR of NO_x, *Chem. Eng. J.* 294 (2016) 254–263. doi:10.1016/j.cej.2016.02.086.
- [97] M.P. Ruggeri, I. Nova, E. Tronconi, J. a. Pihl, T.J. Toops, W.P. Partridge, In-situ DRIFTS measurements for the mechanistic study of NO oxidation over a commercial Cu-CHA catalyst, *Appl. Catal. B Environ.* 166–167 (2015) 181–192. doi:10.1016/j.apcatb.2014.10.076.
- [98] J. Wang, H. Cui, X. Dong, H. Zhao, Y. Wang, H. Chen, et al., N₂O formation in the selective catalytic reduction of NO_x with NH₃ on a CeMoO_x catalyst, *Appl. Catal. A Gen.* 505 (2015) 8–15. doi:10.1016/j.cattod.2014.07.035.
- [99] A. Adamski, W. Zając, F. Zasada, Z. Sojka, Copper ionic pairs as possible active sites in N₂O decomposition on CuO_x/CeO₂ catalysts, *Catal. Today.* 191 (2012) 129–133. doi:10.1016/j.cattod.2012.01.022.
- [100] M.H. Groothaert, K. Lievens, H. Leeman, B.M. Weckhuysen, R.A. Schoonheydt, An operando optical fiber UV-vis spectroscopic study of the catalytic decomposition of NO and N₂O over Cu-ZSM-5, *J. Catal.* 220 (2003) 500–512. doi:10.1016/j.jcat.2003.08.009.
- [101] M. Fu, C. Li, P. Lu, L. Qu, M. Zhang, Y. Zhou, et al., A review on selective catalytic reduction of NO_x by supported catalysts at 100–300 °C—catalysts, mechanism, kinetics, *Catal. Sci. Technol.* 4 (2014) 14–25. doi:10.1039/c3cy00414g.
- [102] K. Leistner, L. Olsson, Deactivation of Cu/SAPO-34 during low-temperature NH₃-SCR, *Appl. Catal. B Environ.* 165 (2015) 192–199. doi:10.1016/j.apcatb.2014.09.067.
- [103] L. Wang, J.R. Gaudet, W. Li, D. Weng, Migration of Cu species in Cu/SAPO-34 during hydrothermal aging, *J. Catal.* 306 (2013) 68–77. doi:10.1016/j.jcat.2013.06.010.
- [104] W. Su, Z. Li, Y. Peng, J. Li, Correlation of the changes in framework and active Cu sites for typical Cu/CHA Zeolite (SSZ-13 and SAPO-34) during hydrothermal aging, *Phys. Chem. Chem. Phys.* 17 (2015) 29142–29149. doi:10.1039/c5cp05128b.
- [105] F. Gao, E.D. Walter, N.M. Washton, J. Szanyi, C.H.F. Peden, Synthesis and evaluation of Cu/SAPO-34 catalysts for NH₃-SCR 2: Solid-state ion exchange and one-pot synthesis, *Appl. Catal. B Environ.* 162 (2015) 501–514. doi:10.1016/j.apcatb.2014.07.029.
- [106] X. Liu, X. Wu, D. Weng, Z. Si, R. Ran, Evolution of copper species on Cu/SAPO-34 SCR catalysts upon hydrothermal aging, *Catal. Today.* (2016). doi:10.1016/j.cattod.2016.05.021.
- [107] B.I. Palella, M. Cadoni, A. Frache, H.O. Pastore, R. Pirone, G. Russo, et al., On the hydrothermal stability of CuAPSO-34 microporous catalysts for N₂O decomposition: A comparison with CuZSM-5, *J. Catal.* 217 (2003) 100–106. doi:10.1016/S0021-9517(03)00033-2.
- [108] J. Wang, D. Fan, T. Yu, J. Wang, T. Hao, X. Hu, et al., Improvement of low-temperature hydrothermal stability of Cu/SAPO-34 catalysts by Cu²⁺ species, *J. Catal.* 322 (2015) 84–90. doi:10.1016/j.jcat.2014.11.010.

- [109] T. Yu, J. Wang, M. Shen, J. Wang, W. Li, The influence of CO₂ and H₂O on selective catalytic reduction of NO by NH₃ over Cu/SAPO-34 catalyst, *Chem. Eng. J.* 264 (2015) 845–855. doi:10.1016/j.cej.2014.12.017.
- [110] U. De La Torre, B. Pereda-Ayo, M. Moliner, J.R. González-Velasco, A. Corma, Cu-zeolite catalysts for NO_x removal by selective catalytic reduction with NH₃ and coupled to NO storage/reduction monolith in diesel engine exhaust aftertreatment systems, *Appl. Catal. B Environ.* 187 (2016) 419–427. doi:10.1016/j.apcatb.2016.01.020.
- [111] I. Nova, L. Lietti, P. Forzatti, Mechanistic aspects of the reduction of stored NO_x over Pt–Ba/Al₂O₃ lean NO_x trap systems, *Catal. Today.* 136 (2008) 128–135. doi:10.1016/j.cattod.2008.01.006.
- [112] U. Elizundia, D. Duraiswami, B. Pereda-Ayo, R. López-Fonseca, J.R. González-Velasco, Controlling the selectivity to N₂O over Pt/Ba/Al₂O₃ NO_x storage/reduction catalysts, *Catal. Today.* 176 (2011) 324–327. doi:10.1016/j.cattod.2010.11.075.
- [113] I. Malpartida, M.A. Larrubia Vargas, L.J. Alemany, E. Finocchio, G. Busca, Pt–Ba–Al₂O₃ for NO_x storage and reduction: Characterization of the dispersed species, *Appl. Catal. B Environ.* 80 (2008) 214–225. doi:10.1016/j.apcatb.2007.11.035.
- [114] L. Castoldi, N. Artioli, R. Matarrese, L. Lietti, P. Forzatti, Study of DPNR catalysts for combined soot oxidation and NO_x reduction, *Catal. Today.* 157 (2010) 384–389. doi:10.1016/j.cattod.2010.03.022.
- [115] J.Y. Luo, W.S. Epling, New insights into the promoting effect of H₂O on a model Pt/Ba/Al₂O₃ NSR catalyst, *Appl. Catal. B Environ.* 97 (2010) 236–247. doi:10.1016/j.apcatb.2010.04.007.
- [116] L. Castoldi, L. Lietti, I. Nova, R. Matarrese, P. Forzatti, F. Vindigni, et al., Alkaline- and alkaline-earth oxides based Lean NO_x Traps: Effect of the storage component on the catalytic reactivity, *Chem. Eng. J.* 161 (2010) 416–423. doi:10.1016/j.cej.2009.10.065.
- [117] P. Forzatti, L. Lietti, N. Gabrielli, A kinetic study of the reduction of NO_x stored on Pt–Ba/Al₂O₃ catalyst, *Appl. Catal. B Environ.* 99 (2010) 145–155. doi:10.1016/j.apcatb.2010.06.011.
- [118] P. Forzatti, L. Castoldi, I. Nova, L. Lietti, E. Tronconi, NO_x removal catalysis under lean conditions, *Catal. Today.* 117 (2006) 316–320. doi:10.1016/j.cattod.2006.05.055.
- [119] W.P. Partridge, J.-S. Choi, NH₃ formation and utilization in regeneration of Pt/Ba/Al₂O₃ NO_x storage-reduction catalyst with H₂, *Appl. Catal. B Environ.* 91 (2009) 144–151. doi:10.1016/j.apcatb.2009.05.017.
- [120] L. Lietti, I. Nova, P. Forzatti, Role of ammonia in the reduction by hydrogen of NO_x stored over Pt–Ba/Al₂O₃ lean NO_x trap catalysts, *J. Catal.* 257 (2008) 270–282. doi:10.1016/j.jcat.2008.05.005.
- [121] Z. Liu, J. Li, A.S.M. Junaid, Knowledge and know-how in improving the sulfur tolerance of deNO_x catalysts, *Catal. Today.* 153 (2010) 95–102. doi:10.1016/j.cattod.2010.01.061.
- [122] H. Imagawa, N. Takahashi, T. Tanaka, S. Matsunaga, H. Shinjoh, Improved NO_x storage-reduction catalysts using Al₂O₃ and ZrO₂–TiO₂ nanocomposite support for thermal stability and sulfur durability, *Appl. Catal. B Environ.* 92 (2009) 23–29. doi:10.1016/j.apcatb.2009.07.027.
- [123] I.S. Pieta, M. García-Diéguez, M.A. Larrubia, L.J. Alemany, W.S. Epling, Sn-modified NO_x storage/reduction catalysts, *Catal. Today.* 207 (2013) 200–211. doi:10.1016/j.cattod.2012.04.016.
- [124] L.F. Liotta, A. Macaluso, G.E. Arena, M. Livi, G. Centi, G. Deganello, A study of the behaviour of Pt supported on CeO₂–ZrO₂/Al₂O₃–BaO as NO_x storage–reduction catalyst for the treatment of lean burn engine emissions, *Catal. Today.* 75 (2002) 439–449.
- [125] M. Casapu, J.-D. Grunwaldt, M. Maciejewski, A. Baiker, S. Eckhoff, U. Gobel, et al., The fate of platinum in Pt/Ba/CeO₂ and Pt/Ba/Al₂O₃ catalysts during thermal aging, *J. Catal.* 251 (2007) 28–38. doi:10.1016/j.jcat.2007.07.019.
- [126] B. Pereda-Ayo, U. De La Torre, M.P. González-Marcos, J.R. González-Velasco, Influence of ceria loading on the NO_x storage and reduction performance of model Pt–Ba/Al₂O₃ NSR catalyst, *Catal. Today.* 241 (2015) 133–142.

- doi:10.1016/j.cattod.2014.03.044.
- [127] L. Castoldi, I. Nova, L. Lietti, P. Forzatti, Study of the effect of Ba loading for catalytic activity of Pt–Ba/Al₂O₃ model catalysts, *Catal. Today*. 96 (2004) 43–52. doi:10.1016/j.cattod.2004.05.006.
- [128] B. Pereda-Ayo, D. Divakar, R. López-Fonseca, J.R. González-Velasco, Influence of platinum and barium precursors on the NSR behavior of Pt–Ba/Al₂O₃ monoliths for lean-burn engines, *Catal. Today*. 147 (2009) S244–S249. doi:10.1016/j.cattod.2009.07.027.
- [129] B. Pereda-Ayo, R. López-Fonseca, J.R. González-Velasco, Influence of the preparation procedure of NSR monolithic catalysts on the Pt–Ba dispersion and distribution, *Appl. Catal. A Gen.* 363 (2009) 73–80. doi:10.1016/j.apcata.2009.04.043.
- [130] M. Matti Maricq, Chemical characterization of particulate emissions from diesel engines: A review, *J. Aerosol Sci.* 38 (2007) 1079–1118. doi:10.1016/j.jaerosci.2007.08.001.
- [131] B.R. Stanmore, J.F. Brilhac, P. Gilot, The oxidation of soot: a review of experiments, mechanisms and models, *Carbon N. Y.* 39 (2001) 2247–2268.
- [132] J.P.A. Neeft, M. Makkee, J.A. Moulijn, Diesel particulate emission control, *Fuel Process. Technol.* 47 (1996) 1–69. doi:10.1016/0378-3820(96)01002-8.
- [133] S. Ye, Y.H. Yap, S.T. Kolaczkowski, K. Robinson, D. Lukyanov, Catalyst "light-off" experiments on a diesel oxidation catalyst connected to a diesel engine-Methodology and techniques, *Chem. Eng. Res. Des.* 90 (2012) 834–845. doi:10.1016/j.cherd.2011.10.003.
- [134] K. Krishna, M. Makkee, Soot oxidation over NO_x storage catalysts: Activity and deactivation, *Catal. Today*. 114 (2006) 48–56. doi:10.1016/j.cattod.2006.02.009.
- [135] V. Rico Pérez, A. Bueno-López, Catalytic regeneration of Diesel Particulate Filters: Comparison of Pt and CePr active phases, *Chem. Eng. J.* 279 (2015) 79–85. doi:10.1016/j.cej.2015.05.004.
- [136] C. Lee, J.-I. Park, Y.-G. Shul, H. Einaga, Y. Teraoka, Ag supported on electrospun macro-structure CeO₂ fibrous mats for diesel soot oxidation, *Appl. Catal. B Environ.* 174–175 (2015) 185–192. doi:10.1016/j.apcatb.2015.03.008.
- [137] M. Schejbal, M. Marek, M. Kubíček, P. Kočí, Modelling of diesel filters for particulates removal, *Chem. Eng. J.* 154 (2009) 219–230. doi:10.1016/j.cej.2009.04.056.
- [138] R. López-Fonseca, U. Elizundia, I. Landa, M.A. Gutiérrez-Ortiz, J.R. González-Velasco, Kinetic analysis of non-catalytic and Mn-catalysed combustion of diesel soot surrogates, *Appl. Catal. B Environ.* 61 (2005) 150–158. doi:10.1016/j.apcatb.2005.04.016.
- [139] X. Guo, M. Meng, F. Dai, Q. Li, Z. Zhang, Z. Jiang, et al., NO_x-assisted soot combustion over dually substituted perovskite catalysts La_{1-x}K_xCo_{1-y}Pd_yO_{3-δ}, *Appl. Catal. B Environ.* 142–143 (2013) 278–289. doi:10.1016/j.apcatb.2013.05.036.
- [140] L. Castoldi, R. Matarrese, L. Lietti, P. Forzatti, Intrinsic reactivity of alkaline and alkaline-earth metal oxide catalysts for oxidation of soot, *Appl. Catal. B Environ.* 90 (2009) 278–285. doi:10.1016/j.apcatb.2009.03.022.
- [141] H. Shimokawa, Y. Kurihara, H. Kusaba, H. Einaga, Y. Teraoka, Comparison of catalytic performance of Ag- and K-based catalysts for diesel soot combustion, *Catal. Today*. 185 (2012) 99–103. doi:10.1016/j.cattod.2011.10.030.
- [142] A. Yezerets, N.W. Currier, D.H. Kim, H.A. Eadler, W.S. Epling, C.H.F. Peden, Differential kinetic analysis of diesel particulate matter (soot) oxidation by oxygen using a step-response technique, *Appl. Catal. B Environ.* 61 (2005) 120–129. doi:10.1016/j.apcatb.2005.04.014.
- [143] S.J. Jelles, R.R. Krul, M. Makkee, J.A. Moulijn, The influence of NO_x on the oxidation of metal activated diesel soot, *Catal. Today*. 53 (1999) 623–630. doi:10.1016/S0920-5861(99)00150-9.
- [144] A. Setiabudi, M. Makkee, J.A. Moulijn, The role of NO₂ and O₂ in the accelerated combustion of soot in diesel exhaust gases, *Appl. Catal. B Environ.* 50 (2004) 185–194. doi:10.1016/j.apcatb.2004.01.004.
- [145] J.P.A. Neeft, M. Makkee, J.A. Moulijn, Catalysts for the oxidation of soot from diesel exhaust gases. I. An exploratory study, *Appl. Catal. B Environ.* 8 (1996) 57–78. doi:10.1016/0926-3373(95)00057-7.

- [146] D. Uner, M.K. Demirkol, B. Dernaika, A novel catalyst for diesel soot oxidation, *Appl. Catal. B Environ.* 61 (2005) 334–345. doi:10.1016/j.apcatb.2005.05.011.
- [147] A. Setiabudi, M. Makkee, J.A. Moulijn, An optimal NO_x assisted abatement of diesel soot in an advanced catalytic filter design, *Appl. Catal. B Environ.* 42 (2003) 35–45. doi:10.1016/S0926-3373(02)00213-8.
- [148] Q. Li, M. Meng, N. Tsubaki, X. Li, Z. Li, Y. Xie, et al., Performance of K-promoted hydrotalcite-derived CoMgAlO catalysts used for soot combustion, NO_x storage and simultaneous soot-NO_x removal, *Appl. Catal. B Environ.* 91 (2009) 406–415. doi:10.1016/j.cej.2012.01.009.
- [149] R. López-Fonseca, I. Landa, U. Elizundia, M.A. Gutiérrez-Ortiz, J.R. González-Velasco, Thermokinetic modeling of the combustion of carbonaceous particulate matter, *Combust. Flame.* 144 (2006) 398–406. doi:10.1016/j.combustflame.2005.08.012.
- [150] J.-O. Müller, B. Frank, R.E. Jentoft, R. Schlögl, D.S. Su, The oxidation of soot particulate in the presence of NO₂, *Catal. Today.* 191 (2012) 106–111. doi:10.1016/j.cattod.2012.03.010.
- [151] N. Artioli, R. Matarrese, L. Castoldi, L. Lietti, P. Forzatti, Effect of soot on the storage-reduction performances of PtBa/Al₂O₃ LNT catalyst, *Catal. Today.* 169 (2011) 36–44. doi:10.1016/j.cattod.2010.10.062.
- [152] L. Castoldi, R. Matarrese, L. Lietti, P. Forzatti, Simultaneous removal of NO_x and soot on Pt–Ba/Al₂O₃ NSR catalysts, *Appl. Catal. B Environ.* 64 (2006) 25–34. doi:10.1016/j.apcatb.2005.10.015.
- [153] W.S. Epling, L.E. Campbell, A. Yezerets, N.W. Currier, J.E. Parks II, Overview of the fundamental reactions and degradation mechanisms of NO_x storage/reduction catalysts, *Catal. Rev. Sci. Eng.* 46 (2004) 163–245. doi:10.1081/cr-200031932.
- [154] R. Matarrese, L. Castoldi, L. Lietti, P. Forzatti, High performances of Pt-K/Al₂O₃ versus Pt-Ba/Al₂O₃ LNT catalysts in the simultaneous removal of NO_x and soot, *Top. Catal.* 42–43 (2007) 293–297. doi:10.1007/s11244-007-0194-y.
- [155] S.S. Mulla, S.S. Chaugule, A. Yezerets, N.W. Currier, W.N. Delgass, F.H. Ribeiro, Regeneration mechanism of Pt/BaO/Al₂O₃ lean NO_x trap catalyst with H₂, *Catal. Today.* 136 (2008) 136–145. doi:10.1016/j.cattod.2008.01.007.
- [156] I.S. Pieta, W.S. Epling, M. García-Diéguez, J.Y. Luo, M.A. Larrubia, M.C. Herrera, et al., Nanofibrous Pt-Ba Lean NO_x trap catalyst with improved sulfur resistance and thermal durability, *Catal. Today.* 175 (2011) 55–64. doi:10.1016/j.cattod.2011.02.045.
- [157] I. Atribak, A. Bueno-López, A. García-García, Uncatalysed and catalysed soot combustion under NO_x+O₂: Real diesel versus model soots, *Combust. Flame.* 157 (2010) 2086–2094. doi:10.1016/j.combustflame.2010.04.018.
- [158] K. Yoshida, S. Makino, S. Sumiya, G. Muramatsu, R. Helferich, Simultaneous Reduction of NO_x and Particulate Emissions from Diesel Engine Exhaust, *SAE Tech. Pap.* (1989) 892046. doi:10.4271/892046.
- [159] B.A.A.L. van Setten, M. Makkee, J.A. Moulijn, Science and technology of catalytic diesel particulate filters, *Catal. Rev.* 43 (2001) 489–564. doi:10.1081/CR-120001810.
- [160] J.J. Yu, Y.X. Tao, C.C. Liu, Z.P. Hao, Z.P. Xu, Novel NO trapping catalysts derived from Co-Mg/X-Al (X=Fe, Mn, Zr, La) hydrotalcite-like compounds., *Environ. Sci. Technol.* 41 (2007) 1399–404. doi:10.1021/es061538t.
- [161] A. Fritz, V. Pitchon, The current state of research on automotive lean NO_x catalysis, *Appl. Catal. B Environ.* 13 (1997) 1–25. doi:10.1016/S0926-3373(96)00102-6.
- [162] Z. Li, M. Meng, Q. Li, Y. Xie, T. Hu, J. Zhang, Fe-substituted nanometric La_{0.9}K_{0.1}Co_{1-x}Fe_xO_{3-δ} perovskite catalysts used for soot combustion, NO_x storage and simultaneous catalytic removal of soot and NO_x, *Chem. Eng. J.* 164 (2010) 98–105. doi:10.1016/j.cej.2010.08.036.
- [163] H. Lin, Y. Li, W. Shangguan, Z. Huang, Soot oxidation and NO_x reduction over BaAl₂O₄ catalyst, *Combust. Flame.* 156 (2009) 2063–2070. doi:10.1016/j.combustflame.2009.08.006.
- [164] S. Matsumoto, DeNO_x catalyst for automotive lean-burn engine, *Catal. Today.* 29 (1996) 43–45. doi:10.1016/0920-5861(95)00259-6.

- [165] N. Miyoshi, S. Matsumoto, K. Katoh, T. Tanaka, J. Harada, N. Takahashi, et al., Development of New Concept Three-Way Catalyst for Automotive Lean-Burn Engines, SAE Tech. Pap. 950809 (1995). doi:10.4271/950809.
- [166] R. Matarrese, L. Castoldi, N. Artioli, E. Finocchio, G. Busca, L. Lietti, On the activity and stability of Pt-K/Al₂O₃ LNT catalysts for diesel soot and NO_x abatement, Appl. Catal. B Environ. 144 (2014) 783–791. doi:10.1016/j.apcatb.2013.08.012.
- [167] L. Castoldi, E. Aneggi, R. Matarrese, R. Bonzi, J. Llorca, A. Trovarelli, et al., Silver-based catalytic materials for the simultaneous removal of soot and NO_x, Catal. Today. 258 (2015) 405–415. doi:10.1016/j.cattod.2015.02.024.
- [168] M.E. Gálvez, S. Ascaso, R. Moliner, M.J. Lázaro, Me (Cu, Co, V)-K/Al₂O₃ supported catalysts for the simultaneous removal of soot and nitrogen oxides from diesel exhausts, Chem. Eng. Sci. 87 (2013) 75–90. doi:10.1016/j.ces.2012.10.001.
- [169] B.S. Sánchez, C.A. Querini, E.E. Miró, Potassium effect on the thermal stability and reactivity of NO_x species adsorbed on Pt,Rh/La₂O₃ catalysts, Appl. Catal. A Gen. 392 (2011) 158–165. doi:10.1016/j.apcata.2010.11.003.
- [170] M. Cortés-Reyes, M.C. Herrera, I.S. Pieta, M.A. Larrubia, L.J. Alemany, In situ TG-MS study of NO_x and soot removal over LNT model catalysts, Appl. Catal. A Gen. 523 (2016) 193–199. doi:10.1016/j.apcata.2016.06.004.
- [171] I.S. Pieta, The model and modified NSR catalysts for simultaneous PM and NO_x removal from diesel exhaust, 2011.
- [172] I.S. Pieta, M. García-Diéguez, M.A. Larrubia, L.J. Alemany, W.S. Epling, Nanofiber alumina supported lean NO_x Trap: Improved Sulfur Tolerance and NO_x Reduction, Top. Catal. 56 (2013) 50–55. doi:10.1007/s11244-013-9928-1.
- [173] L. Castoldi, L. Righini, R. Matarrese, L. Lietti, P. Forzatti, Mechanistic aspects of the release and the reduction of NO_x stored on Pt-Ba/Al₂O₃, J. Catal. 328 (2015) 270–279. doi:10.1016/j.jcat.2015.02.005.
- [174] M.E. Gálvez, S. Ascaso, I. Tobías, R. Moliner, M.J. Lázaro, Catalytic filters for the simultaneous removal of soot and NO_x: Influence of the alumina precursor on monolith washcoating and catalytic activity, Catal. Today. 191 (2012) 96–105. doi:10.1016/j.cattod.2011.12.012.
- [175] L. Xu, R.W. McCabe, LNT+in situ SCR catalyst system for diesel emissions control, Catal. Today. 184 (2012) 83–94. doi:10.1016/j.cattod.2011.12.005.
- [176] B. Pereda-Ayo, D. Duraiswami, J.R. González-Velasco, Control of NO_x storage and reduction in NSR bed for designing combined NSR–SCR systems, Catal. Today. 172 (2011) 66–72. doi:10.1016/j.cattod.2011.01.043.
- [177] L. Castoldi, R. Bonzi, L. Lietti, P. Forzatti, S. Morandi, G. Ghiotti, et al., Catalytic behaviour of hybrid LNT/SCR systems: Reactivity and in situ FTIR study, J. Catal. 282 (2011) 128–144. doi:10.1016/j.jcat.2011.06.002.
- [178] A. Lindholm, H. Sjövall, L. Olsson, Reduction of NO_x over a combined NSR and SCR system, Appl. Catal. B Environ. 98 (2010) 112–121. doi:10.1016/j.apcatb.2010.05.019.
- [179] F. Can, X. Courtois, S. Royer, G. Blanchard, S. Rousseau, D. Duprez, An overview of the production and use of ammonia in NSR+SCR coupled system for NO_x reduction from lean exhaust gas, Catal. Today. 197 (2012) 144–154. doi:10.1016/j.cattod.2012.07.032.
- [180] R. Bonzi, L. Lietti, L. Castoldi, P. Forzatti, NO_x removal over a double-bed NSR–SCR reactor configuration, Catal. Today. 151 (2010) 376–385. doi:10.1016/j.cattod.2010.02.003.
- [181] P. Forzatti, L. Lietti, The reduction of NO_x stored on LNT and combined LNT–SCR systems, Catal. Today. 155 (2010) 131–139. doi:10.1016/j.cattod.2008.11.023.
- [182] E.C. Corbos, M. Haneda, X. Courtois, P. Marecot, D. Duprez, H. Hamada, Cooperative effect of Pt–Rh/Ba/Al and CuZSM-5 catalysts for NO_x reduction during periodic lean-rich atmosphere, Catal. Commun. 10 (2008) 137–141. doi:10.1016/j.catcom.2008.06.014.
- [183] E.C. Corbos, M. Haneda, X. Courtois, P. Marecot, D. Duprez, H. Hamada, NO_x abatement for lean-burn engines under lean–rich atmosphere over mixed NSR–SCR

- catalysts: Influences of the addition of a SCR catalyst and of the operational conditions, *Appl. Catal. A Gen.* 365 (2009) 187–193. doi:10.1016/j.apcata.2009.06.008.
- [184] F. Can, X. Courtois, S. Berland, M. Seneque, S. Royer, D. Duprez, Composition dependent performance of alumina-based oxide supported WO_3 catalysts for the NH_3 -SCR reaction and the NSR + SCR coupled process, *Catal. Today.* 257 (2015) 41–50. doi:10.1016/j.cattod.2015.03.024.
- [185] Y. Zheng, Y. Liu, M.P. Harold, D. Luss, LNT-SCR dual-layer catalysts optimized for lean NO_x reduction by H_2 and CO, *Appl. Catal. B Environ.* 148–149 (2014) 311–321. doi:10.1016/j.apcatb.2013.11.007.
- [186] Y. Liu, Y. Zheng, M.P. Harold, D. Luss, Lean NO_x reduction on LNT-SCR dual-layer catalysts by H_2 and CO, *Appl. Catal. B Environ.* 132–133 (2013) 293–303. doi:10.1016/j.apcatb.2012.10.034.
- [187] U. De La Torre, M. Urrutxua, B. Pereda-Ayo, J.R. González-Velasco, On the Cu species in Cu/beta catalysts related to DeNO_x performance of coupled NSR-SCR technology using sequential monoliths and dual-layer monolithic catalysts, *Catal. Today.* 273 (2016) 72–82. doi:10.1016/j.cattod.2016.02.054.
- [188] B.M. Shakya, M.P. Harold, V. Balakotaiah, Modeling and analysis of dual-layer NO_x storage and reduction and selective catalytic reduction monolithic catalyst, *Chem. Eng. J.* 237 (2014) 109–122. doi:10.1016/j.cej.2013.10.008.
- [189] M. Al-Harbi, W.S. Epling, Effects of different regeneration timing protocols on the performance of a model NO_x storage/reduction catalyst, *Catal. Today.* 151 (2010) 347–353. doi:10.1016/j.cattod.2009.12.004.
- [190] H.M. Rietveld, A profile refinement method for nuclear and magnetic structures peak shape, *J. Appl. Crystallogr.* 2 (1969) 65–71. doi:10.1107/S0021889869006558.
- [191] A. Lindholm, N.W. Currier, J. Dawody, A. Hidayat, J. Li, A. Yezerets, et al., The influence of the preparation procedure on the storage and regeneration behavior of Pt and Ba based NO_x storage and reduction catalysts, *Appl. Catal. B Environ.* 88 (2009) 240–248. doi:10.1016/j.apcatb.2008.10.004.
- [192] J.F. Moulder, W.F. Stickle, P.E. Sobol, K.D. Bomben, *Handbook of X-ray Photoelectron Spectroscopy*, 1992.
- [193] R. Buchel, R. Strobel, F. Krumeich, A. Baiker, S.E. Pratsinis, Influence of Pt location on BaCO_3 or Al_2O_3 during NO_x storage reduction, *J. Catal.* 261 (2009) 201–207. doi:10.1016/j.jcat.2008.11.016.
- [194] I. Malpartida, M.O. Guerrero-Pérez, M.C. Herrera, M.A. Larrubia, L.J. Alemany, MS-FTIR reduction stage study of NSR catalysts, *Catal. Today.* 126 (2007) 162–168. doi:10.1016/j.cattod.2007.05.014.
- [195] J.A. Anderson, B. Bachiller-Baeza, M. Fernández-García, Role of Pt in Pt/Ba/ Al_2O_3 NO_x storage and reduction traps, *Phys. Chem. Chem. Phys.* 5 (2003) 4418–4427. doi:10.1039/b305809n.
- [196] E. Fridell, M. Skoglundh, S. Johansson, G. Smedler, NO_x Storage in Barium-Containing Catalysts, *J. Catal.* 183 (1999) 196–209.
- [197] L. Lietti, P. Forzatti, I. Nova, E. Tronconi, NO_x Storage Reduction over Pt-Ba/ γ - Al_2O_3 Catalyst, *J. Catal.* 204 (2001) 175–191. doi:10.1006/jcat.2001.3370.
- [198] L. Castoldi, L. Lietti, P. Forzatti, S. Morandi, G. Ghiotti, F. Vindigni, The NO_x storage-reduction on PtK/ Al_2O_3 Lean NO_x Trap catalyst, *J. Catal.* 276 (2010) 335–350. doi:10.1016/j.jcat.2010.09.026.
- [199] W.S. Epling, A. Yezerets, N.W. Currier, The effect of exothermic reactions during regeneration on the NO_x trapping efficiency of a NO_x storage/reduction catalyst, *Catal. Letters.* 110 (2006) 143–148. doi:10.1007/s10562-006-0102-2.
- [200] I. Nova, L. Lietti, L. Castoldi, E. Tronconi, P. Forzatti, New insights in the NO_x reduction mechanism with H_2 over Pt-Ba/ γ - Al_2O_3 lean NO_x trap catalysts under near-isothermal conditions, *J. Catal.* 239 (2006) 244–254. doi:10.1016/j.jcat.2006.01.013.
- [201] C.D. DiGiulio, V.G. Komvokis, M.D. Amiridis, In situ FTIR investigation of the role of surface isocyanates in the reduction of NO_x by CO and C_3H_6 over model Pt/BaO/ Al_2O_3 and Rh/BaO/ Al_2O_3 NO_x storage and reduction (NSR) catalysts, *Catal. Today.* 184 (2012)



- 8–19. doi:10.1016/j.cattod.2011.11.022.
- [202] T.J. Toops, D.B. Smith, W.P. Partridge, Quantification of the in situ DRIFT spectra of Pt/K/γ-Al₂O₃ NO_x adsorber catalysts, *Appl. Catal. B Environ.* 58 (2005) 245–254. doi:10.1016/j.apcatb.2004.10.021.
- [203] Y. Ji, T.J. Toops, J.A. Pihl, M. Crocker, NO_x storage and reduction in model lean NO_x trap catalysts studied by in situ DRIFTS, *Appl. Catal. B Environ.* 91 (2009) 329–338. doi:10.1016/j.apcatb.2009.06.002.
- [204] C. Sedlmair, K. Seshan, A. Jentys, J.A. Lercher, Elementary steps of NO_x adsorption and surface reaction on a commercial storage-reduction catalyst, *J. Catal.* 214 (2003) 308–316. doi:10.1016/S0021-9517(02)00085-4.
- [205] Z. Liu, J.A. Anderson, Influence of reductant on the thermal stability of stored NO_x in Pt/Ba/Al₂O₃ NO_x storage and reduction traps, *J. Catal.* 224 (2004) 18–27. doi:10.1016/j.jcat.2004.01.020.
- [206] B.R. Kromer, L. Cao, L. Cumarantunge, S.S. Mulla, J.L. Ratts, A. Yezerets, et al., Modeling of NO oxidation and NO_x storage on Pt/BaO/Al₂O₃ NO_x traps, *Catal. Today.* 136 (2008) 93–103. doi:10.1016/j.cattod.2008.02.013.
- [207] B.I. Mosqueda-Jiménez, A. Jentys, K. Seshan, J.A. Lercher, On the surface reactions during NO reduction with propene and propane on Ni-exchanged mordenite, *Appl. Catal. B Environ.* 46 (2003) 189–202. doi:10.1016/S0926-3373(03)00212-1.
- [208] A.L. Kustov, M. Makkee, Application of NO_x storage/release materials based on alkali-earth oxides supported on Al₂O₃ for high-temperature diesel soot oxidation, *Appl. Catal. B Environ.* 88 (2009) 263–271. doi:10.1016/j.apcatb.2008.11.013.
- [209] I. Nova, L. Castoldi, L. Lietti, E. Tronconi, P. Forzatti, F. Prinetto, et al., NO_x adsorption study over Pt–Ba/alumina catalysts: FT-IR and pulse experiments, *J. Catal.* 222 (2004) 377–388. doi:10.1016/j.jcat.2003.11.013.
- [210] Y. Su, M.D. Amiridis, In situ FTIR studies of the mechanism of NO_x storage and reduction on Pt/Ba/Al₂O₃ catalysts, *Catal. Today.* 96 (2004) 31–41. doi:10.1016/j.cattod.2004.05.005.
- [211] L. Kubiak, L. Castoldi, L. Lietti, S. Andonova, L. Olsson, Mechanistic investigation of the reduction of NO_x over Pt- and Rh-Based LNT Catalysts, *Catalysts.* 6 (2016) 1–14. doi:10.3390/catal6030046.
- [212] N. Nejar, M. Makkee, M.J. Illán-Gómez, Catalytic removal of NO_x and soot from diesel exhaust: Oxidation behaviour of carbon materials used as model soot, *Appl. Catal. B Environ.* 75 (2007) 11–16. doi:10.1016/j.apcatb.2007.03.009.
- [213] M. Lapuerta, F.J. Martos, J.M. Herreros, Effect of engine operating conditions on the size of primary particles composing diesel soot agglomerates, *Aerosol Sci.* 38 (2007) 455–466. doi:10.1016/j.jaerosci.2007.02.001.
- [214] D. Uy, M.A. Ford, D.T. Jayne, A.E. O'Neill, L.P. Haack, J. Hargas, et al., Characterization of gasoline soot and comparison to diesel soot: Morphology, chemistry, and wear, *Tribol. Int.* 80 (2014) 198–209. doi:10.1016/j.triboint.2014.06.009.
- [215] K. Hayashida, S. Nagaoka, H. Ishitani, Growth and oxidation of graphitic crystallites in soot particles within a laminar diffusion flame, *Fuel.* 128 (2014) 148–154. doi:10.1016/j.fuel.2014.03.008.
- [216] A. Sadezky, H. Muckenhuber, H. Grothe, R. Niessner, U. Pöschl, Raman microspectroscopy of soot and related carbonaceous materials: Spectral analysis and structural information, *Carbon N. Y.* 43 (2005) 1731–1742. doi:10.1016/j.carbon.2005.02.018.
- [217] M. Patel, C.L. Azanza Ricardo, P. Scardi, P.B. Aswath, Morphology, structure and chemistry of extracted diesel soot—Part I: Transmission electron microscopy, Raman spectroscopy, X-ray photoelectron spectroscopy and synchrotron X-ray diffraction study, *Tribol. Int.* 52 (2012) 29–39. doi:10.1016/j.triboint.2012.03.004.
- [218] G. Levi, O. Senneca, M. Causà, P. Salatino, P. Lacovig, S. Lizzit, Probing the chemical nature of surface oxides during coal char oxidation by high-resolution XPS, *Carbon N. Y.* 90 (2015) 181–196. doi:10.1016/j.carbon.2015.04.003.

- [219] H. Wang, J. Liu, Z. Zhao, Y. Wei, C. Xu, Comparative study of nanometric Co-, Mn- and Fe-based perovskite-type complex oxide catalysts for the simultaneous elimination of soot and NO_x from diesel engine exhaust, *Catal. Today*. 184 (2012) 288–300. doi:10.1016/j.cattod.2012.01.005.
- [220] D. Fino, S. Bensaid, M. Piumetti, N. Russo, A review on the catalytic combustion of soot in Diesel particulate filters for automotive applications: From powder catalysts to structured reactors, *Appl. Catal. A Gen.* 509 (2016) 75–96. doi:10.1016/j.apcata.2015.10.016.
- [221] K.I. Hadjiivanov, Identification of Neutral and Charged N_xO_y Surface Species by IR Spectroscopy, *Catal. Rev. Sci. Eng.* 42 (2000) 71–144. doi:10.1081/CR-100100260.
- [222] F. Prinetto, G. Ghiotti, I. Nova, L. Lietti, E. Tronconi, P. Forzatti, FT-IR and TPD Investigation of the NO_x Storage Properties of BaO/Al₂O₃ and Pt–BaO/Al₂O₃ Catalysts, *J. Phys. Chem. B*. 105 (2001) 12732–12745. doi:10.1021/jp012702w.
- [223] M. Cortés-Reyes, C. Herrera, M.Á. Larrubia, L.J. Alemany, Intrinsic reactivity analysis of soot removal in LNT-catalysts, *Appl. Catal. B Environ.* 193 (2016) 110–120. doi:10.1016/j.apcatb.2016.04.014.
- [224] B. Dernaika, D. Uner, A simplified approach to determine the activation energies of uncatalyzed and catalyzed combustion of soot, *Appl. Catal. B Environ.* 40 (2003) 219–229.
- [225] K.J.A. Raj, B. Viswanathan, Catalytic combustion of diesel soot particles on potassium and sodium titanates, *Indian J. Chem.* 49A (2010) 1174–1181.
- [226] D.B. Anthony, J.B. Howard, H.C. Hottel, H.P. Meissner, Rapid devolatilization and hydrogasification of bituminous coal, *Fuel*. 55 (1976) 121–128. doi:10.1016/0016-2361(76)90008-9.
- [227] V. Vand, A theory of the irreversible electrical resistance changes of metallic films evaporated in vacuum, *Proc. Phys. Soc.* 55 (1943) 222. doi:10.1088/0959-5309/55/3/308.
- [228] K. Hashimoto, K. Miura, T. Watanabe, Kinetics of thermal regeneration reaction of activated carbons used in waste water treatment, *AIChE J.* (1982).
- [229] R. Brukh, S. Mitra, Kinetics of carbon nanotube oxidation, *J. Mater. Chem.* 17 (2007) 619–623. doi:10.1039/b609218g.
- [230] R. López-Fonseca, I. Landa, U. Elizundia, M.A. Gutiérrez-Ortiz, J.R. González-Velasco, A kinetic study of the combustion of porous synthetic soot, *Chem. Eng. J.* 129 (2007) 41–49. doi:10.1016/j.cej.2006.10.029.
- [231] S. Ascaso, M.E. Gálvez, P. Da Costa, R. Moliner, M.J. Lázaro, On the influence of the alumina precursor in Fe-K/Al₂O₃ structured catalysts for the simultaneous removal of soot and NO_x: From surface properties to reaction mechanism, *Comptes Rendus Chim.* 17 (2014) 681–686. doi:10.1016/j.crci.2013.08.001.
- [232] F. Bin, C. Song, G. Lv, X. Li, X. Cao, J. Song, et al., Characterization of the NO-soot combustion process over the La_{0.8}Ce_{0.2}Mn_{0.7}Bi_{0.3}O₃ catalyst, *Proc. Combust. Inst.* 35 (2015) 2241–2248. doi:10.1016/j.proci.2014.08.028.
- [233] M.R. Díaz-Rey, M. Cortés-Reyes, C. Herrera, M.A. Larrubia, N. Amadeo, M. Laborde, et al., Hydrogen-rich gas production from algae-biomass by low temperature catalytic gasification, *Catal. Today*. 257 (2014) 177–184. doi:10.1016/j.cattod.2014.04.035.
- [234] A. Lindholm, N.W. Currier, E. Fridell, A. Yezerets, L. Olsson, NO_x storage and reduction over Pt based catalysts with hydrogen as the reducing agent. Influence of H₂O and CO₂, *Appl. Catal. B Environ.* 75 (2007) 78–87. doi:10.1016/j.apcatb.2007.03.008.
- [235] S. Morandi, F. Prinetto, G. Ghiotti, L. Castoldi, L. Lietti, P. Forzatti, et al., The influence of CO₂ and H₂O on the storage properties of Pt–Ba/Al₂O₃ LNT catalyst studied by FT-IR spectroscopy and transient microreactor experiments, *Catal. Today*. 231 (2014) 116–124. doi:10.1016/j.cattod.2013.12.036.
- [236] F. Frola, F. Prinetto, G. Ghiotti, L. Castoldi, I. Nova, L. Lietti, et al., Combined in situ FT-IR and TRM analysis of the NO_x storage properties of Pt–Ba/Al₂O₃ LNT catalysts, *Catal. Today*. 126 (2007) 81–89. doi:10.1016/j.cattod.2006.10.010.

- [237] W.S. Epling, J.E. Parks, G.C. Campbell, A. Yezerets, N.W. Currier, L.E. Campbell, Further evidence of multiple NO_x sorption sites on NO_x storage/reduction catalysts, *Catal. Today*. 96 (2004) 21–30. doi:10.1016/j.cattod.2004.05.004.
- [238] L. Masdrag, X. Courtois, F. Can, D. Duprez, Effect of reducing agent (C₃H₆, CO, H₂) on the NO_x conversion and selectivity during representative lean/rich cycles over monometallic platinum-based NSR catalysts. Influence of the support formulation, *Appl. Catal. B Environ.* 146 (2014) 12–23. doi:10.1016/j.apcatb.2013.06.006.
- [239] R.J. Hendershot, R. Vijay, C.M. Snively, J. Lauterbach, High-throughput study of the influence of H₂O and CO₂ on the performance of nitrogen storage and reduction (NSR) catalysts, *Appl. Surf. Sci.* 252 (2006) 2588–2592. doi:10.1016/j.apsusc.2005.06.041.
- [240] S. Askari, R. Halladj, Effects of ultrasound-related variables on sonochemically synthesized SAPO-34 nanoparticles, *J. Solid State Chem.* 201 (2013) 85–92. doi:10.1016/j.jssc.2013.02.026.
- [241] P.N. Panahi, A. Niaei, D. Salari, S.M. Mousavi, G. Delahay, Ultrasound-assistant preparation of Cu-SAPO-34 nanocatalyst for selective catalytic reduction of NO by NH₃, *J. Environ. Sci.* 35 (2015) 135–143. doi:10.1016/j.jes.2015.01.032.
- [242] M. Chorghand, M. Haghghi, S. Saedy, S. Aghamohammadi, Efficient hydrothermal synthesis of nanostructured SAPO-34 using ultrasound energy: Physicochemical characterization and catalytic performance toward methanol conversion to light olefins, *Adv. Powder Technol.* 25 (2014) 1728–1736. doi:10.1016/j.apt.2014.06.022.
- [243] M. Chorghand, M. Haghghi, S. Aghamohammadi, The Beneficial Use of Ultrasound in Synthesis of Nanostructured Ce-Doped SAPO-34 Used in Methanol Conversion to Light Olefins, *Ultrason. Sonochem.* 21 (2014) 1827–1838. doi:10.1016/j.ultsonch.2014.03.011.
- [244] T. Álvaro-Muñoz, C. Márquez-Álvarez, E. Sastre, Use of different templates on SAPO-34 synthesis: Effect on the acidity and catalytic activity in the MTO reaction, *Catal. Today*. 179 (2012) 27–34. doi:10.1016/j.cattod.2011.07.038.
- [245] Y. Cui, Q. Zhang, J. He, Y. Wang, F. Wei, Pore-structure-mediated hierarchical SAPO-34: Facile synthesis, tunable nanostructure, and catalysis applications for the conversion of dimethyl ether into olefins, *Particuology*. 11 (2013) 468–474. doi:10.1016/j.partic.2012.12.009.
- [246] C. Petitto, G. Delahay, Selective catalytic reduction of NO_x by NH₃ on Cu-SAPO-34 catalysts: Influence of silicium content on the activity of calcined and hydrotreated samples, *Chem. Eng. J.* 264 (2015) 404–410. doi:10.1016/j.cej.2014.11.111.
- [247] F. Marzpour Shalmani, R. Halladj, S. Askari, An investigation of the crystallization kinetics of zeotype SAPO-34 crystals synthesized by hydrothermal and sonochemical methods, *Ultrason. Sonochem.* 29 (2016) 354–362. doi:10.1016/j.ultsonch.2015.10.011.
- [248] G. Liu, P. Tian, J. Li, D. Zhang, F. Zhou, Z. Liu, Synthesis, characterization and catalytic properties of SAPO-34 synthesized using diethylamine as a template, *Microporous Mesoporous Mater.* 111 (2008) 143–149. doi:10.1016/j.micromeso.2007.07.023.
- [249] A.K. Singh, R. Yadav, A. Sakthivel, Synthesis, characterization, and catalytic application of mesoporous SAPO-34 (MESO-SAPO-34) molecular sieves, *Microporous Mesoporous Mater.* 181 (2013) 166–174. doi:10.1016/j.micromeso.2013.07.031.
- [250] S. Askari, Z. Sedighi, R. Halladj, Rapid synthesis of SAPO-34 nanocatalyst by dry gel conversion method templated with morpholine: Investigating the effects of experimental parameters, *Microporous Mesoporous Mater.* 197 (2014) 229–236. doi:10.1016/j.micromeso.2014.06.028.
- [251] M. Colombo, G. Koltsakis, I. Nova, E. Tronconi, Modelling the ammonia adsorption-desorption process over an Fe-zeolite catalyst for SCR automotive applications, *Catal. Today*. 188 (2012) 42–52. doi:10.1016/j.cattod.2011.09.002.
- [252] M.P. Ruggeri, A. Grossale, I. Nova, E. Tronconi, H. Jirglova, Z. Sobalik, FTIR in situ mechanistic study of the NH₃-NO/NO₂ "Fast SCR" reaction over a commercial Fe-ZSM-5 catalyst, *Catal. Today*. 184 (2012) 107–114. doi:10.1016/j.cattod.2011.10.036.

- [253] H. Zhu, J.H. Kwak, C.H.F. Peden, J. Szanyi, In situ DRIFTS-MS studies on the oxidation of adsorbed NH₃ by NO_x over a Cu-SSZ-13 zeolite, *Catal. Today*. 205 (2013) 16–23. doi:10.1016/j.cattod.2012.08.043.
- [254] D. Wang, L. Zhang, K. Kamasamudram, W.S. Epling, In situ-DRIFTS study of selective catalytic reduction of NO_x by NH₃ over Cu-exchanged SAPO-34, *ACS Catal.* 3 (2013) 871–881. doi:10.1021/cs300843k.
- [255] A. Zecchina, L. Marchese, S. Bordiga, C. Paze, E. Gianotti, Vibrational spectroscopy of NH⁴⁺ ions in zeolitic materials: An IR study, *J. Phys. Chem. B*. 101 (1997) 10128–10135. doi:10.1021/jp9717554.
- [256] R. Martínez-Franco, M. Moliner, P. Concepcion, J.R. Thogersen, A. Corma, Synthesis, characterization and reactivity of high hydrothermally stable Cu-SAPO-34 materials prepared by “one-pot” processes, *J. Catal.* 314 (2014) 73–82. doi:10.1016/j.jcat.2014.03.018.
- [257] A. Turrina, E.C.V. Eschenroeder, B.E. Bode, J.E. Collier, D.C. Apperley, P.A. Cox, et al., Understanding the structure directing action of copper–polyamine complexes in the direct synthesis of Cu-SAPO-34 and Cu-SAPO-18 catalysts for the selective catalytic reduction of NO with NH₃, *Microporous Mesoporous Mater.* 215 (2015) 154–167. doi:10.1016/j.micromeso.2015.05.038.
- [258] Y. Cao, S. Zou, L. Lan, Z. Yang, H. Xu, T. Lin, et al., Promotional effect of Ce on Cu-SAPO-34 monolith catalyst for selective catalytic reduction of NO_x with ammonia, *J. Mol. Catal. A Chem.* 398 (2015) 304–311. doi:10.1016/j.molcata.2014.12.020.
- [259] J. Wang, Y. Huang, T. Yu, S. Zhu, M. Shen, W. Li, et al., The migration of Cu species over Cu-SAPO-34 and its effect on NH₃ oxidation at high temperature, *Catal. Sci. Technol.* 4 (2014) 3004–3012. doi:10.1039/c4cy00451e.
- [260] X. Xiang, M. Yang, B. Gao, Y. Qiao, P. Tian, S. Xu, et al., Direct Cu²⁺ ion-exchanged into as-synthesized SAPO-34 and its catalytic application in the selective catalytic reduction of NO with NH₃, *RSC Adv.* 6 (2016) 12544–12552. doi:10.1039/c5ra22868a.
- [261] T.T.H. Dang, H.-L. Zubowa, U. Bentrup, M. Richter, A. Martin, Microwave-assisted synthesis and characterization of Cu-containing AlPO₄-5 and SAPO-5, *Microporous Mesoporous Mater.* 123 (2009) 209–220. doi:10.1016/j.micromeso.2009.04.003.
- [262] V. Petranovskii, E. Stoyanov, V. Gurin, N. Katada, M.A. Hernandez, M. Avalos, et al., Formation of copper nanoparticles in mordenites with variable SiO₂/Al₂O₃ molar ratios under redox treatments, *Rev. Mex. Fis.* 59 (2013) 170–185.
- [263] A.K.S. Clemens, A. Shishkin, P.A. Carlsson, M. Skoglundh, F.J. Martínez-Casado, Z. Matej, et al., Reaction-driven Ion Exchange of Copper into Zeolite SSZ-13, *ACS Catal.* 5 (2015) 6209–6218. doi:10.1021/acscatal.5b01200.
- [264] M. Turco, G. Bagnasco, U. Costantino, F. Marmottini, T. Montanari, G. Ramis, et al., Production of hydrogen from oxidative steam reforming of methanol. I. Preparation and characterization of Cu/ZnO/Al₂O₃ catalysts from a hydrotalcite-like LDH precursor, *J. Catal.* 228 (2004) 43–55. doi:10.1016/j.jcat.2004.08.026.
- [265] P.J. Smeets, M.H. Groothaert, R.A. Schoonheydt, Cu based zeolites: A UV-vis study of the active site in the selective methane oxidation at low temperatures, *Catal. Today*. 110 (2005) 303–309. doi:10.1016/j.cattod.2005.09.028.
- [266] S. Andonova, E. Vovk, J. Sjöblom, E. Ozensoy, L. Olsson, Chemical deactivation by phosphorous under lean hydrothermal conditions over Cu/BEA NH₃-SCR catalysts, *Appl. Catal. B Environ.* 147 (2014) 251–263. doi:10.1016/j.apcatb.2013.08.041.
- [267] W. Grüenert, N.W. Hayes, R.W. Joyner, E. S. Spiro, M. Rafiq, H. Siddiqui, et al., Structure, chemistry, and activity of Cu-ZSM-5 catalysts for the selective reduction of NO_x in the presence of oxygen, *J. Phys. Chem.* 98 (1994) 10832–10846. doi:10.1021/j100093a026.
- [268] L. Ma, Y. Cheng, G. Cavataio, R.W. McCabe, L. Fu, J. Li, Characterization of commercial Cu-SSZ-13 and Cu-SAPO-34 catalysts with hydrothermal treatment for NH₃-SCR of NO_x in diesel exhaust, *Chem. Eng. J.* 225 (2013) 323–330. doi:10.1016/j.cej.2013.03.078.

- [269] S.A. Bates, W.N. Delgass, F.H. Ribeiro, J.T. Miller, R. Gounder, Methods for NH₃ titration of Brønsted acid sites in Cu-zeolites that catalyze the selective catalytic reduction of NO_x with NH₃, *J. Catal.* 312 (2014) 26–36. doi:10.1016/j.jcat.2013.12.020.
- [270] G. Centi, S. Perathoner, Nature of active species in copper-based catalysts and their chemistry of transformation of nitrogen oxides, *Appl. Catal. A Gen.* 132 (1995) 179–259. doi:10.1016/0926-860X(95)00154-9.
- [271] T. Yu, D. Fan, T. Hao, J. Wang, M. Shen, W. Li, The effect of various templates on the NH₃-SCR activities over Cu/SAPO-34 catalysts, *Chem. Eng. J.* 243 (2014) 159–168. doi:10.1016/j.cej.2014.01.008.
- [272] S. Ashtekar, S.V. V. Chilukuri, D.K. Chakrabarty, Small-Pore Molecular Sieves SAPO-34 and SAPO-44 with Chabazite Structure: A study of silicon incorporation, *J. Phys. Chem.* 98 (1994) 4878–4883. doi:10.1021/j100069a018.
- [273] L. Wang, W. Li, S.J. Schmieg, D. Weng, Role of Brønsted acidity in NH₃ selective catalytic reduction reaction on Cu/SAPO-34 catalysts, *J. Catal.* 324 (2015) 98–106. doi:10.1016/j.jcat.2015.01.011.
- [274] S. Bordiga, L. Regli, D. Cocina, C. Lamberti, M. Bjørgen, K.P. Lillerud, et al., Assessing the Acidity of High Silica Chabazite H – SSZ-13 by FTIR Using CO as Molecular Probe : Comparison with H – SAPO-34, *J. Phys. Chem. B.* 109 (2005) 2779–2784. doi:10.1021/jp045498w.
- [275] Y. Wei, D. Zhang, Z. Liu, B.-L. Su, Highly efficient catalytic conversion of chloromethane to light olefins over HSAPO-34 as studied by catalytic testing and in situ FTIR, *J. Catal.* 238 (2006) 46–57. doi:10.1016/j.jcat.2005.11.021.
- [276] K. Hadjiivanov, Identification and characterization of surface hydroxyl groups by Infrared Spectroscopy, 1st ed., Elsevier Inc., 2014. doi:10.1016/B978-0-12-800127-1.00002-3.
- [277] L. Domokos, L. Lefferts, K. Seshan, J.A. Lercher, The importance of acid site locations for n-butene skeletal isomerization on ferrierite, *J. Mol. Catal. A Chem.* 162 (2000) 147–157. doi:10.1016/S1381-1169(00)00286-7.
- [278] G. Busca, Acid catalysts in industrial hydrocarbon chemistry, *Chem. Rev.* 107 (2007) 5366–5410.
- [279] I. Halasz, B. Moden, A. Petushkov, J.-J. Liang, M. Agarwal, Delicate distinction between OH groups on proton-exchanged H-chabazite and H-SAPO-34 molecular sieves, *J. Phys. Chem. C.* 119 (2015) 24046–24055. doi:10.1021/acs.jpcc.5b09247.
- [280] A. Frache, B. Palella, M. Cadoni, R. Pirone, P. Ciambelli, H.O. Pastore, et al., Catalytic DeNO_x activity of cobalt and copper ions in microporous MeALPO-34 and MeAPSO-34, *Catal. Today.* 75 (2002) 359–365. doi:10.1016/S0920-5861(02)00065-2.
- [281] C. Tyrsted, E. Borfecchia, G. Berlier, K. Lomachenko, C. Lamberti, S. Bordiga, et al., Nitrate-nitrite equilibrium in the reaction of NO with Cu-CHA catalyst for NH₃-SCR, *Catal. Sci. Technol.* (2016) Manuscript in preparation. doi:10.1039/C6CY01820C.
- [282] K.A. Lomachenko, E. Borfecchia, C. Negri, G. Berlier, C. Lamberti, P. Beato, et al., The Cu-CHA deNO_x catalyst in action: temperature-dependent NH₃-SCR monitored by operando XAS and XES, *J. Am. Chem. Soc.* 138 (2016) 12025–12028. doi:10.1021/jacs.6b06809.
- [283] M.P. Ruggeri, T. Selleri, M. Colombo, I. Nova, E. Tronconi, Identification of nitrites/HONO as primary products of NO oxidation over Fe-ZSM-5 and their role in the Standard SCR mechanism: A chemical trapping study, *J. Catal.* 311 (2014) 266–270. doi:10.1016/j.jcat.2013.11.028.
- [284] F. Marchitti, I. Nova, E. Tronconi, Experimental study of the interaction between soot combustion and NH₃-SCR reactivity over a Cu-Zeolite SDPF catalyst, *Catal. Today.* 267 (2016) 110–118. doi:10.1016/j.cattod.2016.01.027.
- [285] S. Fan, J. Xue, T. Yu, D. Fan, T. Hao, M. Shen, et al., The effect of synthesis methods on Cu species and active sites over Cu/SAPO-34 for NH₃-SCR reaction, *Catal. Sci. Technol.* 3 (2013) 2357–2364. doi:10.1039/c3cy00267e.
- [286] M. Cortés-Reyes, M.C. Herrera, M.A. Larrubia, L.J. Alemany, Fast ultrasound assisted synthesis of Cu-SAPO-34 for SCR application, *Int. J. Innov. Res. Sci. Eng. Technol.* 5

- (2016) 5540–5550. doi:10.15680/IJIRSET.2016.0504189.
- [287] J. Hun Kwak, H. Zhu, J.H. Lee, C.H.F. Peden, J. Szanyi, Two different cationic positions in Cu-SSZ-13?, *Chem. Commun.* 48 (2012) 4758–4760. doi:10.1039/c2cc31184d.
- [288] A. Grossale, I. Nova, E. Tronconi, Ammonia blocking of the “Fast SCR” reactivity over a commercial Fe-zeolite catalyst for Diesel exhaust aftertreatment, *J. Catal.* 265 (2009) 141–147. doi:10.1016/j.jcat.2009.04.014.
- [289] C.-K. Seo, H. Kim, B. Choi, M.T. Lim, The optimal volume of a combined system of LNT and SCR catalysts, *J. Ind. Eng. Chem.* 17 (2011) 382–385. doi:10.1016/j.jiec.2010.10.033.
- [290] R. Zukerman, L. Vradman, M. Herskowitz, E. Liverts, M. Liverts, A. Massner, et al., Modeling and simulation of a smart catalytic converter combining NO_x storage, ammonia production and SCR, *Chem. Eng. J.* 155 (2009) 419–426. doi:10.1016/j.cej.2009.08.015.
- [291] B.M. Shakya, M.P. Harold, V. Balakotaiah, Effect of cycle time on NH₃ generation on low Pt dispersion Pt/BaO/Al₂O₃ catalysts: Experiments and crystallite-scale modeling, *Chem. Eng. J.* 230 (2013) 584–594. doi:10.1016/j.cej.2013.06.109.
- [292] U. De-La-Torre, B. Pereda-Ayo, M. Moliner, J.A. González-Marcos, A. Corma, J.R. González-Velasco, Optimal operating conditions of coupled sequential NO_x storage/reduction and Cu/CHA selective catalytic reduction monoliths, *Top. Catal.* (2016). doi:10.1007/s11244-016-0720-x.
- [293] B. Pereda-Ayo, U. De La Torre, M. Romero-Sáez, A. Aranzabal, J.A. González-Marcos, J.R. González-Velasco, Influence of the washcoat characteristics on NH₃-SCR behavior of Cu-zeolite monoliths, *Catal. Today.* 216 (2013) 82–89. doi:10.1016/j.cattod.2013.06.012.
- [294] D. Kuscer, I. Bantan, M. Hrovat, B. Malič, The microstructure, coefficient of thermal expansion and flexural strength of cordierite ceramics prepared from alumina with different particle sizes, *J. Eur. Ceram. Soc.* 37 (2017) 739–746. doi:10.1016/j.jeurceramsoc.2016.08.032.
- [295] R. Goren, H. Gocmez, C. Ozgur, Synthesis of cordierite powder from talc, diatomite and alumina, *Ceram. Int.* 32 (2006) 407–409. doi:10.1016/j.ceramint.2005.03.016.
- [296] B. Pereda-Ayo, J.A. Botas-Echevarría, J. González-Casablanca, M.P. González-Marcos, J.R. González-Velasco, Characterization of Pt and Ba over alumina washcoated monolith for NO_x storage and reduction (NSR) by FIB-SEM, *Catal. Today.* 216 (2013) 50–56. doi:10.1016/j.cattod.2013.06.010.
- [297] M. Cortés-Reyes, E. Finocchio, C. Herrera, M.Á. Larrubia, L.J. Alemany, G. Busca, A study of Cu-SAPO-34 catalysts for SCR of NO_x by ammonia, *Microporous Mesoporous Mater.* (accepted) doi:10.1016/j.micromeso.2016.11.032.
- [298] S. Ascaso, M.E. Gálvez, P. Da Costa, R. Moliner, M.J. Lázaro Elorri, Influence of gas hourly space velocity on the activity of monolithic catalysts for the simultaneous removal of soot and NO_x, *Comptes Rendus Chim.* 18 (2015) 1007–1012. doi:10.1016/j.crci.2015.03.017.